Mechanical Design Optimisation of a Tibial Insert for use in Instrumented Total Knee Replacement

Edgars Kelmers

Submitted in accordance with the requirements for the degree of
Doctor of Philosophy

The University of Leeds

Mechanical Engineering

November 2023

Intellectual Property and Publication Statements

The candidate confirms that the work submitted is his own, except where work which has formed part of jointly authored publications has been included. The contribution of the candidate and the other authors to this work has been explicitly indicated below. The candidate confirms that the appropriate credit has been given within the thesis where reference has been made to the work of others.

Publication

Some of the work in Chapter 1 (literature review) of the thesis has appeared in publication as follows:

Kelmers, E., Szuba, A., King, S.W., Palan, J., Freear, S., Pandit, H.G. and van Duren, B.H., 2022. Smart Knee Implants: An Overview of Current Technologies and Future Possibilities. Indian Journal of Orthopaedics, pp.1-8. https://doi.org/10.1007/s43465-022-00810-5

I was responsible for carrying out the literature search and review, manuscript conception, preparation and editing. The co-authors contributed with feedback and comments on the publication.

Patent application

Some of the work from Chapters 1 to 8 has appeared in patent application GB2210781.7, application title: An implantable device and charging module for powering the same, lodged on 22 July 2022.

Copyright statement

This copy has been supplied on the understanding that it is copyright material and that no quotation from the thesis may be published without proper acknowledgement.

The right of Edgars Kelmers to be identified as Author of this work has been asserted by Edgars Kelmers in accordance with the Copyright, Designs and Patents Act 1988.

Acknowledgements

I am saying thank you to:

1. Maria Irina Foanta for encouragement, support, and sponsorship. Without your help I would have never been able to pursue my dream to develop novel medical implants. Additionally, I want to say thank you to my family for supporting me in my studies and giving me complete freedom of choice on what to pursue in my life.
2. Thanks to Engineering and Physical Sciences Research Council (EPSRC) [EP/L014823/1] for providing my scholarship and funding my research. Additional thanks to everyone from University of Leeds who helped developing the Centre for Doctoral Training.
3. Hemant Pandit and Bernard H. van Duren for giving me the opportunity to be the first one joining the iSMART project since 06 December 2018. Thank you, Hemant, for supervising and giving advice from clinical aspect. Thank you, Ben, for supervising and giving advice both on clinical aspect and mechanical prototyping.
4. Louise Jennings for supervising and giving advice in experimental laboratory testing.
5. Ruth K. Wilcox for supervising and giving advice on FEA modelling.
6. Ksenija Vasiljeva (ORCID 0000-0002-2049-6491), thank you for being my studentship mentor. Whilst unofficially, you also did a great job as my fifth supervisor. Thank you also for the initial support on the iSMART project and for helping with the Arduino Uno circuit board development.
7. Medacta International and their engineers for providing CAD files and engineering advice. Additional thank you to Dario Allegretti, Enoc Vergari, Alessio Beccari, and Michele Scala for giving training during my internship in November 2021.
8. Thomas Carpenter for developing a custom circuit board and a custom MatLab code for strain gauge measurements for the iSMART project.
9. Marlene Mengoni, thank you for creating MSc module for advanced FEA (this module helped me to develop the necessary skills for my PhD) and thank you for giving advice on FEA modelling for my PhD research.
10. Alison Jones and Tod Stuart for giving sugestions during transfer viva.
11. Alison Jones and Stephen Mellon for giving sugestions during the PhD viva defence.
12. Claire Brocket and Antony Herbert: for the support and management of the CDT. Additional thank you to Claire for helping organising my internship to Switzerland in the middle of COVID-19 pandemic.
13. Phil Wood for giving advice on fixture design and manufacturing.
14. Tony Wiese, for giving access to the Electropulse E10000 materials testing machine. Without this equipment I would have not been able to test the fatigue safety of my implant design.
15. Camille Hamersley, for giving training on all metrology equipment.
16. Kevin Rhodes for teaching me good measurement practices for CMM.
17. Raelene Cowie for training on a knee simulator.
18. Laura Mandefield for teaching me about clinical statistics.
19. Andrew Stockdale, Samuel Burdon, Dec Issac, Keith Dyer, and Jane Cardie for helping in laboratory, with fixture manufacturing, and implant modification.
20. Graham Brown, Rhys Moore, and Luke Philips in manufacturing department for delivering my implants and fixtures in short time and with small tolerances.
21. PhD students from the iMBE CDT program for the daily support.
22. Some of this work was undertaken on ARC3, part of the High Performance Computing facilities at the University of Leeds, UK.
23. Myself, Edgars Kelmers, see my CV in the Appendix B.

Abstract

Total knee replacement (TKR) is the treatment of choice for patients with severe osteoarthritis and significant symptoms. Whilst TKR is overall seen as a successful procedure, there remains a need to improve recovery after surgery, increase implant longevity, detect failure early, reduce hospital visits, and increase overall patient satisfaction. Smart implants, with embedded sensor technologies, have the potential to provide the quantitative *in vivo* data to facilitate these goals.

The aim of this PhD research was to investigate how to modify a conventional tibial insert design to incorporate sensors and electronic components whilst ensuring patient safety. Several manufacturing methods were developed to address manufacturing and assembling challenges. Computational and experimental studies were carried out to analyse the structural strength, wear performance, and safety of a modified tibial insert. Additional experimental studies were performed to illustrate the feasibility and practical applications for making measurements with embedded strain gauge sensors. Previous studies on instrumented tibial inserts did not address manufacturing limitations nor safety concerns.

This study proposed a novel design approach, by positioning sensors and electronic circuits inside a capsule and only at the intercondylar area instead of under the articulating surfaces, to maintain original implant geometry and reduce the risk of tibial insert wear and deformation.

Computational and experimental studies indicated no significant difference in contact pressure, internal stresses, deformation, and wear rates when comparing modified and conventional tibial inserts. Fatigue to failure study indicated a failure mode, when debris was generated due to contact between the capsule and the metal tray.

Computational and experimental studies indicated that strain signal could be used to approximate the total axial force at different locations in anterior-posterior direction and to indirectly detect tibial tray fracture.

In conclusion, this PhD research has presented guidelines on how to design, manufacture, and test a smart tibial insert.

Table of Contents

List of Figures

List of Tables

List of Equations

Terminology

Figure T.1 Human anatomy planes.
Image re-used from public domain, courtesy of National Cancer Institute [1].

Abbreviations

Abbreviation	Full Meaning
ACL	Anterior cruciate ligament
A-A	Adduction-Abduction
A-P	Anterior-Posterior
ASTM	American Society for Testing and Materials
BCR	Bi-cruciate Ligament Retaining
BW	Body Weight
CI	Confidence Interval
CMM	Coordinate Measuring Machine
CoP	Centre of Pressure
CR	Posterior Cruciate Retaining
DoF	Degree of Freedom
FDA	Food and Drug Administration of the United States of America
F-E	Flexion-Extension
FEA	Finite Element Analysis
Fx, Fy, Fz	Force component of x-, y-, and z-axis.
GUR	trade name for UHMWPE powder owned by Celanese
HXLPE	Highly Cross Linked Ultra-High Molecular Weight Polyethylene
I-E	Internal-External
iSMART	Instrumented Sensor Module for Arthroplasty Treatment
ISO	International Organization for Standardization
KS6	Knee Simulator No. 6
M-L	Medial-Lateral
Mx, My, Mz	Moment component around x-, y-, and z-axis.
MC	Million cycles
NJR	National Joint Registry for England, Wales, Northern Ireland, the Isle of Man and the States of Guernsey
OA	Osteoarthritis
PCL	Posterior Cruciate Ligament
PEEK	Polyetheretherketone
PS	Posterior Stabilised
RSA	Roentgen stereophotogrammetric analysis
SD	Standard Deviation
S-I	Superior-Inferior
TKR	Total Knee Replacement
UHMWPE	Ultra-High Molecular Weight Polyethylene
UKR	Unicompartmental Knee Replacement
X, Y, Z	Translation components of x-, y-, and z-axis.
X°, Y°, Z°	Rotation components around x-, y-, and z-axis.

1   Literature Review

This chapter gives a review of a relevant literature regarding prevalence of knee joint replacement surgeries, knee joint anatomy and physiology, history of instrumented knee implant development, and experimental and computational test methods used to compare and assess knee implant designs. This chapter relates to research Objective 1 and Objective 2 defined in section 2.2.

1.1   Introduction

Knee osteoarthritis (OA) is a progressive disease, which causes knee joint degeneration, pain, and stiffness. Knee osteoarthritis greatly reduces a person's quality of life and can result in disability. Severe osteoarthritis cases can be treated with Unicompartmental Knee Replacement (UKR) or Total Knee Replacement (TKR). During UKR surgery only medial or lateral compartment is resurfaced, whilst during TKR surgery three compartments of the knee (medial, lateral, and patellofemoral) are resurfaced with metal, ceramic, or polymer components in various possible combinations. TKR is the prevalent procedure.

The demand for TKR surgeries is increasing due to changing patient demands and expectations, the prevalence of obesity and the ageing population [2]. Annually over 90,000 TKR surgeries are performed in the United Kingdom [3], over 600,000 in the USA [4] and over 1.3 million worldwide [5], which is expected to increase by over two thirds by 2050 [4, 6]. Overall, TKR is seen as effective treatment where approximately 82% of primary implants last for at least 25 years [7].

Even though TKR is considered a successful surgery, unsatisfactory device performance is common. There is a significant risk for implant failure within a patient`s lifetime. The younger the patient is, the higher the risk of failure [3, 8]. The Australian joint registry reports that 17.8% of primary TKRs fail within 18 years for patients under 55 years [8]. In the majority of cases failed implants require revision surgery, which is costly, associated with variable outcome, and higher morbidity and mortality. The United Kingdom National Joint Registry (NJR) reports that revision surgery has poorer clinical outcomes with 14,9% of revised TKRs failing at seven years [3]. Therefore, there is an unmet clinical need to understand the factors contributing to the failure of TKRs.

Implant instrumentation is one of the solutions being explored to improve the understanding of TKR failure. In the early 2000s D`Lima and Heinlein developed

instrumented tibial trays, which measured six load components and the medial-lateral ratio of the axial force in the tibiofemoral joint [9]. These instrumented tibial trays have been successfully used in clinical trials and have been providing *in vivo* data for various activities of daily living (level walking, downhill walking, stair walking, sitting down, standing up, squatting, running etc.). However, these instrumented tibial trays have several design limitations, such as, excessive bone removal, restricted data transfer, and they are limited to one implant type, which restricts accessibility to patients.

Since 2009, further development has been performed to design instrumented Ultra-High Molecular Weight Polyethylene (UHMWPE) tibial inserts, which allow bone preservation, data transfer, and adaptability to different implant types [10]. Over the years, various prototypes of instrumented tibial inserts have been made. These prototypes were modified tibial inserts, which had an internal cavity to enclose sensors and electronical components [10-12]. However, no research has been carried out to investigate the structural strength or wear performance of the modified UHMWPE inserts.

The aim of this research is to study the change in structural strength of a clinically available tibial insert, which is modified to incorporate a cavity. The cavity is required to accommodate sensors and electronics. Specifically, this research will investigate design and optimisation methods for the incorporation of a cavity within a UHMWPE tibial insert, how the incorporation of a cavity influences structural strength and wear, as well as the practical applications of sensor measurements.

1.2 Knee anatomy and physiology

1.2.1 Knee gross anatomy

The knee joint consists of three bones: tibia, femur, and patella. The articulation between these bones forms the patellofemoral and tibiofemoral joints. The bones are connected by tendons and ligaments (Figure 1.1). The knee joint is encapsulated by the synovial membrane, which is filled with synovial fluid. Centrally in the knee joint there is an anterior cruciate ligament (ACL) and posterior cruciate ligament (PCL). The femur has a medial and lateral condyle. The tibial articular surface is largely covered by medial and lateral menisci which increase the contact area between femur and tibia and act as shock absorbers. The menisci are separated by the intercondylar area [13]. The cruciate ligaments and the menisci are commonly removed during TKR surgery.
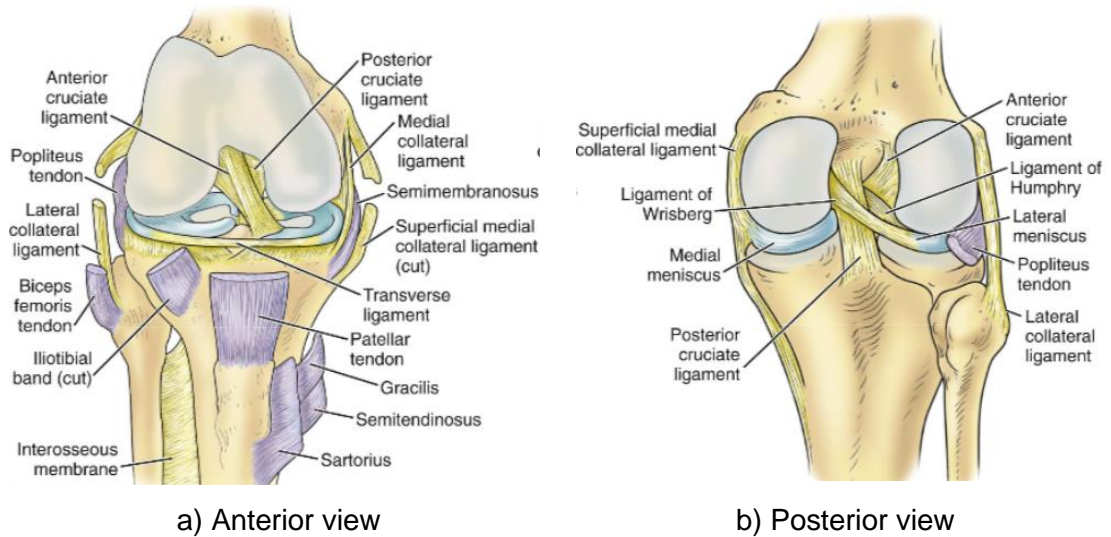
a) Anterior view   b) Posterior view
Figure 1.1 Knee anatomy.
Images used from book Insall & Scott Surgery of the Knee [13] with permission from
Elsevier.

1.2.2 Tibiofemoral joint kinematics and kinetics

The tibiofemoral joint has complex kinematics and kinetics. The joint can move in six
degrees of freedom (DoF) [14], as follows:

Three translation components (Figure 1.2):

- Medial Lateral (M-L), femur translation in X-axis
- Anterior Posterior (A-P), femur translation in Y-axis
- Superior Inferior (S-I), femur translation in Z-axis

Three rotation components (Figure 1.2):

- Flexion Extension (F-E), tibial rotation around X-axis
- Abduction Adduction (A-A), tibial rotation around Y-axis
- Internal External (I-E), tibial rotation around Z-axis
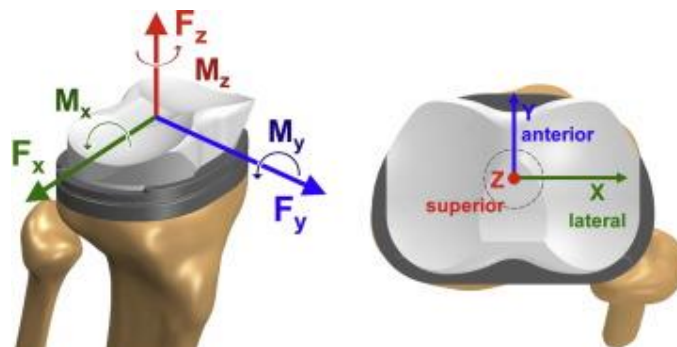
Figure 1.2 Tibiofemoral joint motion and loading axis for six degrees of freedom.
Image re-used from publication by Taylor et al., 2017 [14], open access license CC BY-
NC-ND 4.0.

The tibiofemoral joint is also loaded in all six DoF. The load distribution differs between the medial and lateral femoral condyle [15]. The latest studies have recorded 13 loading parameters to describe the joint kinematics and kinetics (3 translation, 3 rotation, 3 force, 3 moment components, and M-L force ratio) [14-16]. These parameters are necessary to estimate *in vivo* loading conditions for knee implants.

Multiple studies have shown that kinematics and kinetics are different for various daily activities, for example, walking, stair climbing, sitting and raising from a chair, squatting, and running. All daily activities contribute to the accumulated damage (wear and plastic deformation) of a UHMWPE tibial insert *in vivo* [17-19]. Table 1.1 provides a summary on available *in vivo* data for level walking.

Table 1.1 Summary of *in vivo* tibiofemoral joint load and motion data during level walking, mean (standard deviation).
Nomenclature: **"+"** = all data available, **"-"** = **N/A** = no available data, **DoF** = degree of freedom, **instrum.** = instrumented implant data,
inv. dyn. = inverse dynamics data, **CI** = confidence interval, **m** = male, **f** = female, max values showed in red.

	Taylor et al., 2017 [14]	Saxby et al., 2016 [20]	Bergmann et al., 2014 [21]	Messier et al. 2014 [22]	Kumar et al 2013 [23]	Worsley et al., 2013 [24]	Kutzner et al., 2011 [25]	Lundberg et al., 2011 [26]	Winby et al., 2009 [27]	D`Lima et al., 2008 [28]	Messier., 2005 [29]
Subjects	6 TKR	60 healthy	8 TKR	157 OA (stratified of 454)	12 healthy 16 OA	20 healthy 30 OA: 14 UKR+16 TKR	3 TKR	30 TKR	11 healthy	3 TKR	134 OA
Sex	5 m, 1 f	35 m, 25 f	6 m, 2 f	49 m, 108 f	healthy 6 m, 6 f OA: 8 m, 8 f	healthy: 9 m, 11 f OA: 14 m, 20 f	3 m	15 m, 15 f	-	2 m, 1 f	37 m, 105 f
Method	*instrum. *inv. dyn. *fluoroscopy	*inv. dyn.	*instrum. *inv. dyn.	*inv. dyn.	*inv. dyn.	*inv. dyn.	*instrum. *inv. dyn.	*inv. dyn.	*inv. dyn.	*instrum.	*inv. dyn.
Force 3 DoF	+	Fz	+	Fz, Fy	Fz	Fz, Fy	Fz	Fz	Fz	Fz	Fz, Fy
M-L force ratio	+	+	+	-	+	-	+	-	+	-	-
Moment 3 DoF	+	-	+	My, Mx	-	My, Mx	My	-	My	-	+
Translation 3 DoF	Y, Z	-	-	-	-	-	-	-	-	-	-
Angle 3 DoF	+	-	X°	-	-	-	-	-	-	-	-
Speed, m/s	-	1.44(0.22)	1.11	1.2(0.2)	healthy: 1.55 OA: 1.34	-	1.10-1.26	-	-	0.45-1.79	-
Mass, kg	88(12)	69.8(14)	91(4.5)	92.6(13.9)	healthy: 81.6(19.2) OA: 85.1(15.7)	healthy: 78(13) OA: 85(18)	98(1.9)	88(20)	-	78(4.6)	93.2
Age, years	68(5)	27.3(5.4)	70(1.8)	66 (6)	healthy: 59.5 (10.4) OA: 65.2 (9.5)	healthy: 62(6) OA: 64(10)	65(2.6)	65.6(9.15)	44(6.9)	77(4.1)	68.5
Peak Fz, BW	mean **2.74** max **3.73**	**2.83**(0.64)	average(75kg) **2.67** high(100kg) 3.43 extreme(100kg) **3.65**	mean **2.9**(0.96) min 1.36 max **6.95**	healthy **3.67** (95% CI 3.16, **4.17**) OA **3.50** (95% CI 3.06, **3.93**)	healthy: **3.4**(0.5) OA: **3.2**(0.6) UKR/TKR: **3.5**(0.6)	mean **2.11-2.49** One subject variation: **1.91-2.41**	**3.0**(0.7)	**3.9** (range 3.2–**4.9**)	Treadmill: 0.45 m/s: 2.23 0.89 m/s: 2.14 1.34 m/s: 2.42 1.79 m/s: **2.80** Floor walk: N/A: **2.60**	**3.16**
Raw data	web link	-	web link	-	-	-	-	-	-	-	-

Table 1.1 shows that all publications provide limited data on *in vivo* motion and loading conditions. All studies have recorded axial peak force F$_z$, which shows large intra-individual and inter-individual subject variation. However, most of the studies provide no motion data, therefore these studies cannot be used for computational or experimental test development for knee joint simulations. Data provided by Bergmann et al. [21] can be used for simplified tests where loading is synchronised with F-E angle. Data from Taylor et al. [14] provides a more comprehensive data set which takes into consideration implant motion in 5 DoF and loading in 6 DoF. Bergmann et al. [21] and Taylor et al. [14] results were collected for a small cohort of 6 to 8 subjects, but they show similarities with other study data on larger subject cohorts (Table 1.1).

Publications on other daily activities also reveal that data from Bergmann et al. [21] and Taylor et al. [14] studies are the most suitable for knee joint simulation test applications. Taylor et al. [14] provides data on 12 loading parameters for each of the 6 subjects (Figure 1.3). Bergmann et al. [21] provides worst case scenario loading data for a subject with mass of 100 kg. This data was derived from 8 loading parameters of 8 subjects (Figure 1.4).
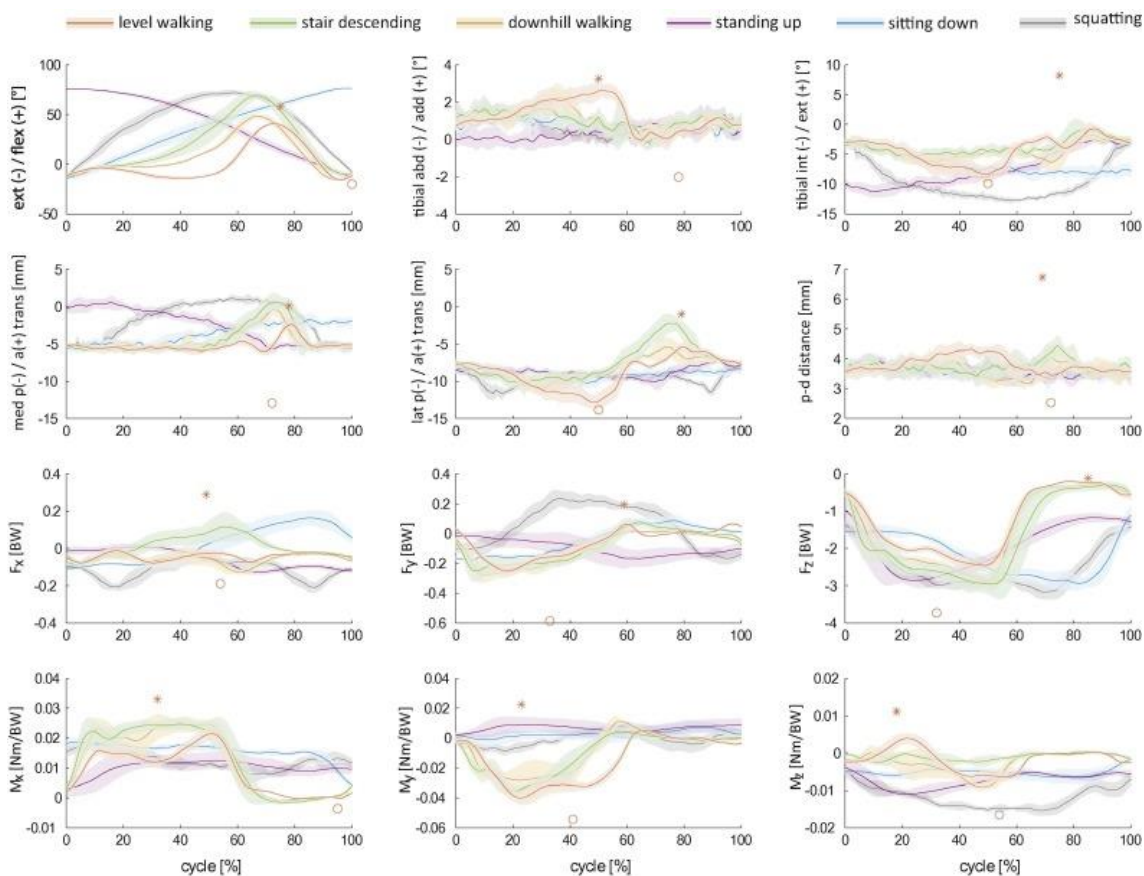
Figure 1.3 Example loading data from one subject with instrumented knee implant. The star (*) and the circle (°) symbols represent extreme values for level walking amongst all subjects and trials. Nomenclature: BW = body weight, M = moment, F = force, x,y,z = axis, p-d = Proximal-Distal = Superior-Inferior. Image re-used from publication by Taylor et al., 2017 [14], open access license CC BY-NC-ND 4.0.
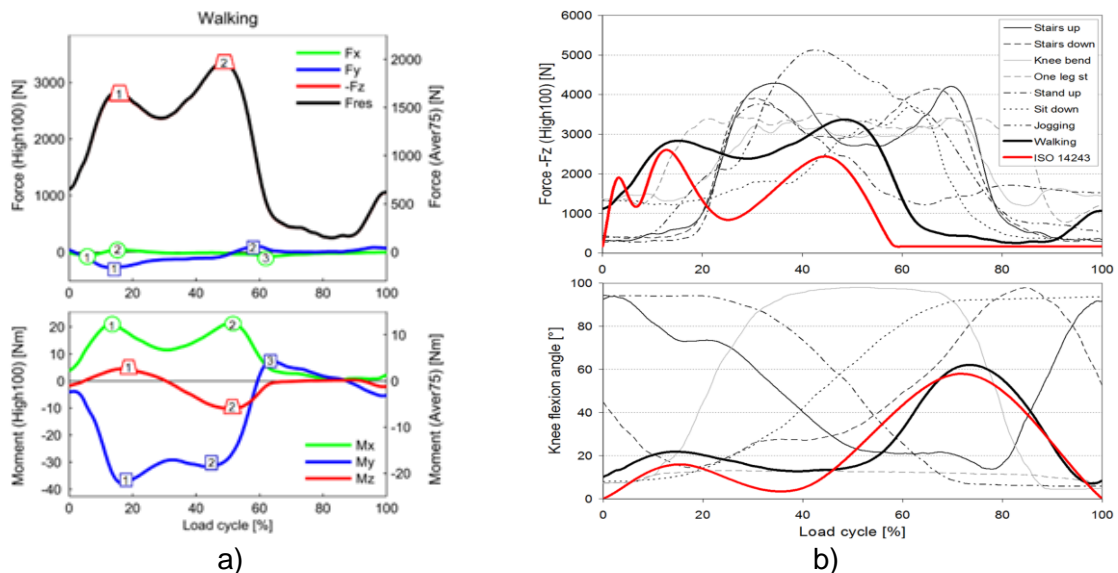
Figure 1.4 Example of combined data from eight subjects with instrumented knee implant on a) load components during level walking and b) axial reaction force and knee flexion angle during daily activities. Images re-used from publication by Bergmann et al., 2014 [21], open access license CC BY 4.0.

1.3 TKR implants

TKR implants have been incrementally improved since the 1960s [30]. Major improvement was made around 1998 by stopping performing tibial insert sterilisation with gamma radiation in air, which was causing accelerated surface fatigue, delamination, and wear of inserts [31]. A contemporary modular TKR system has 3 components (Figure 1.5). A metal femoral component is used to resurface the femoral condyles. A tibial insert, made of UHMWPE, serves as an articulation surface. A metal tibial plate resurfaces the tibial plateau. The metal components are most commonly made of cobalt-chromium or titanium alloys [32].

a) GMK Primary TKR CR knee system   b) metal femoral component

c) UHMWPE tibial insert   d) metal tibial tray
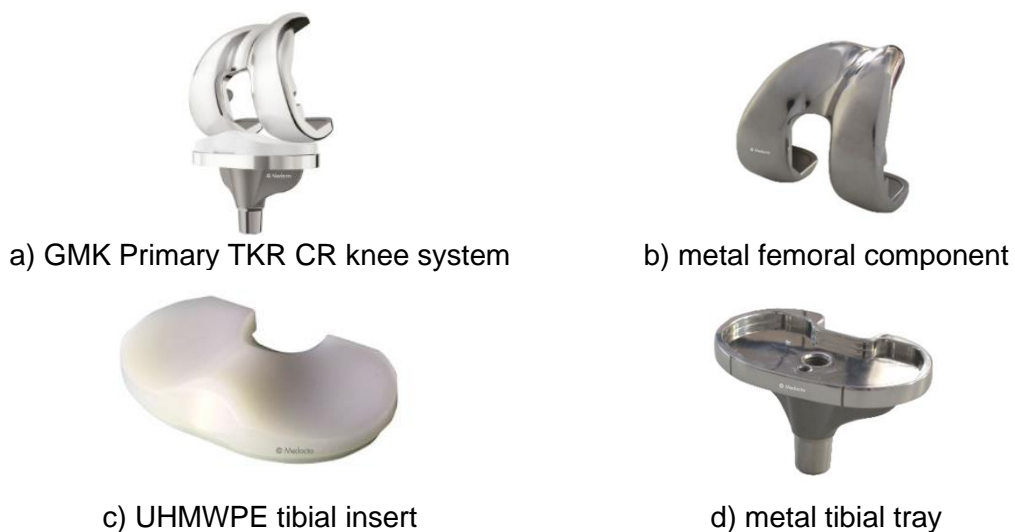
Figure 1.5 Medacta GMK Primary CR knee system.
Images reused from public domain Medacta.com [33] accessed 15-May-2020.

Tibial insert designs are available in a wide range, for example, with fixed or mobile bearing, posterior stabilised (PS), posterior cruciate ligament retaining (CR), bi-cruciate ligament retaining (BCR), for hinged TKR, with all-polyethylene tibial tray, or for a unicondylar replacement (UKR) [30]. The NJR report shows that in 2017 the most used implant design for primary surgeries was CR TKR with a fixed UHMWPE tibial insert (59.1%) (Figure 1.5c). The second most used design was PS TKR (21.0%) [3].

1.4 Instrumented knee implant history

Currently there are limited options for standards or widely accepted techniques for tracking knee implant performance *in vivo* [34]. Standard ISO 16087:2013 [35] describes how roentgen stereophotogrammetric analysis (RSA) could be used to assess the *in vivo* migration of metal implant components and bone, which could be used to approximate bone fracture, implant dislocation, and wear [35, 36]. However, this method comes with additional risks due to greater X-ray exposure dose and the necessity to embed additional metal marker beads into patient's bone [35].

Multiple attempts have been made to further improve *in vivo* implant analysis with the help of instrumented implants. This chapter gives an overview on the history of instrumented knee implant development and the advantages and disadvantages of each prototype.

1.4.1 Clinical need of instrumented TKR

The relevant literature identifies three clinical needs for TKR research, to investigate:

   i)   causes of failure;

   ii) the effect of different implant designs on knee kinetics and kinematics; and

   iii) the effect of different surgical approaches on clinical outcome.

Firstly, while TKR surgery is seen as a successful procedure, there is a significant risk for implant failure within a patient`s lifetime. The most frequent causes for TKR failure are loosening, infection, and instability [3, 8]. According to the 2019 Australian joint registry data, 3.6% of patients over the age of 75 experience primary TKR failure within the first 18 years, 7.0% between ages 65 and 74, 11.7% between ages 55 to 64, and 17.8% under the age of 55 [8]. The younger the patient is, the higher the failure risk [3, 8], which could be explained by more active life style and longer life expectancy [37]. Therefore, it is important to investigate how implant failure is affected by the TKR loads during prolonged use, and during the use by physically active patients.

Secondly, even though 80-90% of patients have overall satisfaction with their implants [38, 39] only 66% feel that their knee functions "normally" [38]. Furthermore, many

patients have post-surgery symptoms or functional problems, such as, ongoing pain (33%) or difficulties with rising from a chair (31%), getting out of a car (38%), or climbing stairs (54%) [38]. Therefore, it is important to investigate how different implant designs affect knee joint kinematics and kinetics [40-42].

Thirdly, there is no consensus between surgeons in relation to various surgical variables. For example, there is no mutual agreement on: whether mechanical or kinematic alignment should be performed [43]; whether cemented or cementless implants should be used [44]; whether patella should be resurfaced [45]; or which TKR design should be used (posterior cruciate retaining, posterior cruciate sacrificing, "medial pivot" etc.) [46, 47]. All these decisions affect knee joint kinematics and kinetics, but there is no direct way to measure them. Therefore, there is an unmet need to find solutions for measuring and recording clinical data, which would improve both surgeons' and engineers` decision making [21].

Implant instrumentation is one of the solutions being explored to improve the understanding of TKR performance *in vivo*. For example, *in vivo* load measurements could be related to implant wear, deformation, and stress distribution within the implant or the periprosthetic bone [48], which would further improve the understanding of implant failure modes, implant design, and surgical procedures.

The existing clinical trial studies of instrumented tibial trays have already been beneficial in creating more realistic TKR testing conditions. For example, ASTM F3141 [49] test standard was developed, which provides loading conditions for various activities of daily living.

In the future, many other applications could be further developed. Pressure and motion measurements would show if the implant is overloaded [50]. Temperature measurements could indicate infection [51], bone resorption, or component loosening [52]. A study by O'Connor and Kiourti [50] lists multiple potential applications: instrumented implants could provide alternative for the medical imaging to assess loosening, physiotherapists could use load measurements to suggest physical activities which avoid damaging the implant or harming the soft tissue around the knee, to diagnose implant failure, to alarm the patient of any problems, to sense bone formation, to validate *in vitro* experiments and mathematical models. In addition, correct implant placement could be assessed to improve surgical instrument design [9] or an internal memory could store relevant medical data [53].

1.4.2 Instrumented metal knee implant prototypes

Since 1996, a number of instrumented knee prototypes have been developed, but few have been tested in clinical studies [48], and only one (Juvenile Tumour System by Stanmore Implants) has been used for patient treatment [54]. *In vivo* studies have been performed only on 3 designs of instrumented knee implants, where sensors were always enclosed inside the metal components. In 2021 Zimmer Biomet was the first to commercialize a Persona IQ "smart" knee implants with embedded sensors and a telemetry system [55], however no evidence has yet been shown for providing any clinical benefit [56].

The first wireless design was a distal femoral replacement (used in two subjects), which measured longitudinal axial force and torque, and two bending moments in the shaft (Figure 1.6) [57]. This implant allowed only indirect estimation of knee joint forces.
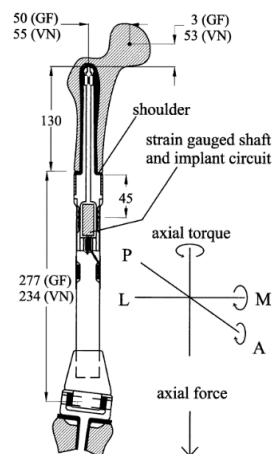
Figure 1.6 Instrumented femoral shaft.
Image re-used from Taylor & Walker, 2001 [57], with permission from Elsevier.

The second design was an instrumented tibial tray (used in one subject in 2005), which directly measured total compressive force and its centre of pressure (Figure 1.7) [58].
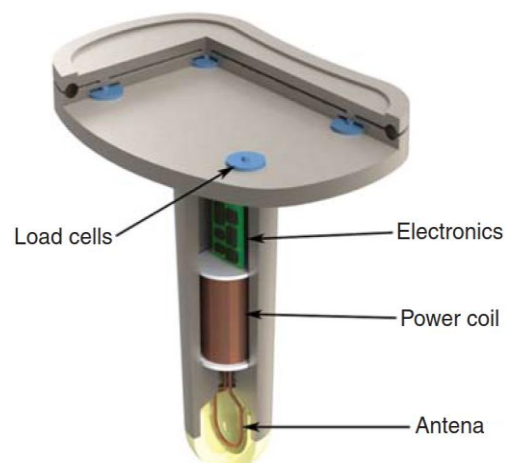
Figure 1.7 Instrumented tibial tray, which can measure axial compressive force.
Image re-used from Torrão et al., 2015 [9], with permission from Taylor & Francis.

The third design was an improved tibial tray (Figure 1.8), which could measure 6 load components (three orthogonal forces and three moments about the orthogonal axis). Two research groups developed their own design of the improved tibial tray, and both designs were used in clinical studies. D`Lima's design from 2007 [59] was used in three subjects and Heinlein design from 2008 [60] was used in nine subjects [9]. In order to get approval for clinical trials both D`Lima [61] and Heinlein [62] designs were proven to resist 10 million cycles of structural fatigue testing, according to test standard ASTM F1800 or "physiological tibial test" respectively.
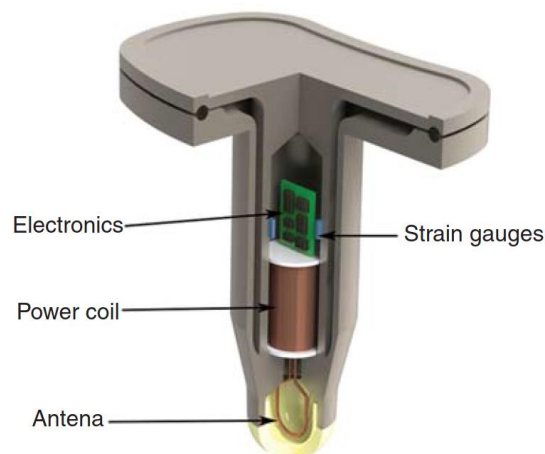
Figure 1.8 Instrumented tibial tray, which can measure 6 load components.
Image re-used from Torrão et al., 2015 [9], with permission from Taylor & Francis.

In 2013 a third research group attempted to develop new instrumented tibial tray design with integrated piezoelectric components, which could also harvest energy from walking (Figure 1.9) [63]. This design incorporated 6 force sensors to distinguish between medial, lateral, anterior, and posterior loading. Their design allowed for wireless data transfer. However, the tibial tray design was not suitable for implantation as the electronic components were not hermetically sealed. This design required modification of both tibial tray and tibial insert, which would cause alterations to surgical procedure. This prototype was not tested for structural fatigue resistance.
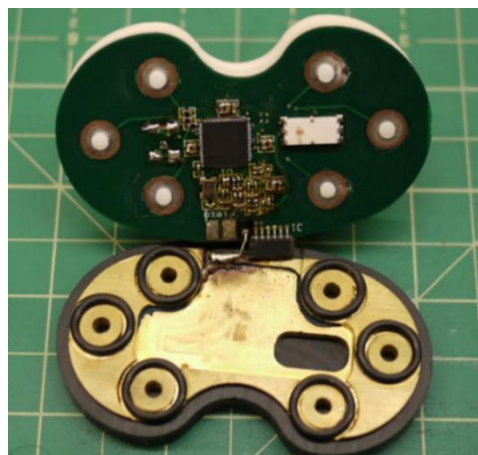
Figure 1.9 Instrumented tibial tray with piezoelectric components. Image reused from publication by Holmberg et al., 2013 [63] with permission from ASME.

In 2011 Stanmore Implants was the first to commercialize Juvenile Tumour System extendable implant. The Stanmore extendable implants do not contain any electronics but have an internal mechanism which allows implant extension *in vivo* [54]. The extendable implant has a telescopic rod connected to magnetically driven gear system which is activated by an external magnetic field. It follows that this implant lengthening technology is limited to use for patients requiring limb lengthening.
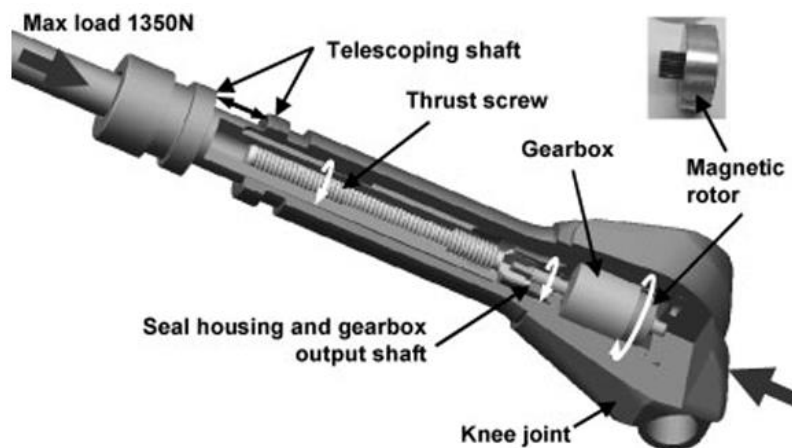
Figure 1.10 Juvenile Tumour System developed by Stanmore Implants. Image reused from publication by Meswania et al., 2008 [54] with permission from SAGE Publicatios.

In 2021 Zimmer Biomet in collaboration with Canary Medical was the first to commercialize and perform surgeries with a Persona IQ "smart" knee implants with embedded sensors and a telemetry system [55]. Its tibial stem has embedded 3-D accelerometer, a gyroscope, and a telemetry system with a claimed battery lifetime for at least 10 years [64]. The data from the sensors is used to measure steps per minute, average walking speed, stride length, distance travelled, tibial range of motion, and step count [56]. The data can be monitored by the patient and remotely by a health care professional [64].
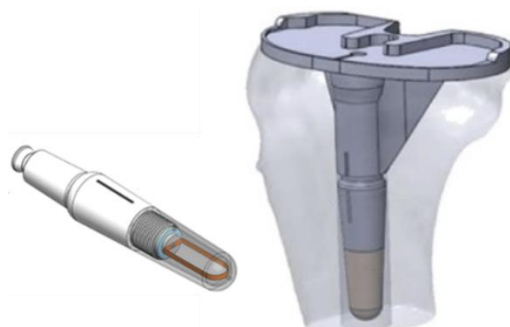
Figure 1.11 Persona IQ "smart" knee implant with canturio™*te* tibial stem. Image re-used from publication by Cushner et al., 2022 [65],open access license CC BY-NC-ND 4.0.

The instrumented tibial tray designs were only implanted in early 2000s for the purpose of clinical studies, and they have not been implanted in live patients ever since. In 2021 Zimmer Biomet started performing surgeries with their Persona IQ "smart" knee implants, but no clinical studies have been reported yet. One study shows that six Heinlein design implants have been successfully used for at least 16 years [14], but no publications give explanation why this design has not been commercialised for public use. However, the lack of clinical use could be explained due to four disadvantages of instrumented metal components.

Firstly, metal instrumented implants have larger dimensions compared to original implants. Instrumented tibial trays have an increased stem length and tray thickness to accommodate the electronics [66, 67]. Therefore, more bone must be resected than what is required for a conventional implant**.**

Secondly, metal walls obstruct electromagnetic signal. Due to low power for data transfer an inductive coupling was used [68]. This made the devices impractical to use outside laboratory [69]. In 2011 D`Lima et al. [70] resolved this issue by developing a portable telemetry system, but this solution was not adopted in the future studies.

Thirdly, the above-mentioned prototype designs are limited to a single design, which is impractical for most surgeons who are trained on other knee systems. This also limits the number of patients who could benefit from instrumented knee implants.

Fourthly, the high costs of manufacturing, the necessity of additional clinical studies, and regulatory approval hinders instrumented implant commercialisation [71, 72].

1.4.3 Instrumented UHMWPE implant prototypes

In order to resolve the disadvantages of instrumented metal components, some studies have been focused on instrumentation of UHMWPE components. Firstly, wireless signal goes through polymer much easier [68]. Secondly, commercial TKR tibial inserts have larger dimensions, which allows to modify them without increasing external dimensions. Retaining original insert design would allow to avoid additional bone resection and keep original surgery procedure [68]. Lastly, UHMWPE is easier to machine, which would allow to incorporate sensors in most existing knee designs [73]. Therefore, instrumented tibial inserts would be accessible to all surgeons and patients.

However, additional complications must be resolved before using instrumented tibial inserts. Firstly, UHMWPE compared to metal has poorer structural strength due to lower elastic modulus, hence a cavity could weaken the tibial insert and increase the failure risk due to deformation or fracture. Secondly, UHMWPE has non-linear elastic

and plastic deformation behaviour, which would complicate the measurement accuracy [68, 73].

Current prototypes of instrumented tibial inserts are underdeveloped and have never reached *in vivo* clinical trial stage. Multiple research groups have been focusing on developing novel sensors or energy harvesting units, but have not been able to create a usable system with a complete wireless circuit [68, 69, 74-76]. Only two research groups (Crescini et al. [10, 11] and Simoncini M. [12]) have developed a fully enclosed wireless system for tibial inserts

In 2009 and 2011 Crescini et al. [10, 11] developed two fully enclosed wireless tibial insert prototypes. Crescini et al. suggested to cut UHMWPE insert in half, then machine cavities for the electronic components, and in the end hermetically seal both halves by laser welding. The first prototype (Figure 1.12a) showed the potential to embed the electronics within the UHMWPE tibial insert while still retaining the original implant dimensions. This prototype used magnetoresistive sensors, which could measure load up to 12 kg in 1 axis [10]. The second prototype (Figure 1.12b) used a set of 3 magnetoresistors to distinguish medial and lateral axial compression force up to 3000 N [11]. To date, these are the only known fully sealed wireless instrumented tibial inserts, which worked in laboratory environment. Since 2011 no further development was reported. Neither computational models nor mechanical tests were performed to investigate the mechanical safety of these designs.

Both Crescini designs require laser welding assembly. However, this manufacturing technique may not be implemented by orthopaedic companies due to medical regulation restrictions. Medical Device Regulation 2017/745 Annex II paragraph 3(b) [77] requires from manufacturers to present complete information on manufacturing processes and their validation. Currently established manufacturing techniques are milling, turning, drilling, and direct compression moulding [78]. In order to implement laser welding, orthopaedic companies would need to change and re-validate their manufacturing processes. Manufacturing re-validation would require time and money and as such may not offer any economic benefit. Consequently, the suggested manufacturing method is a design limitation.
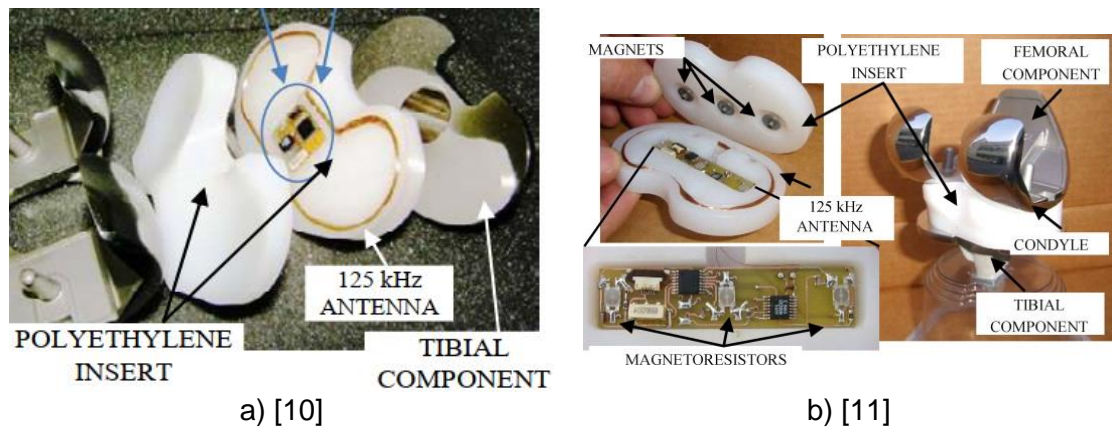
a) [10]   b) [11]

Figure 1.12 Fully sealed wireless instrumented tibial insert
with a) one sensor and b) three sensors. Images re-used from publication by Crescini
et al., 2009 [10], open access license CC BY-NC-ND 3.0, and from publication by
Crescini et al., 2011 [11], with permission from Elsevier.

In 2014 Simoncini M. [12] attempted to design an instrumented wireless tibial insert for use in primary surgeries (Figure 1.13). Simoncini modified tibial insert to have 12 mm minimum thickness, whilst also following suggestion from an orthopaedic company to maintain at least 3 mm thick walls. Additionally, the research suggested to use two phase direct compression moulding to encapsulate the electronics. At first, only the lower half of the tibial insert would be moulded. Then the encapsulated electronics would be placed on top of the lower part. Lastly, the upper part would be moulded over the electronics. Neither computational models nor mechanical tests were performed to investigate the mechanical safety of this design.

The design also considered a two-layer protection to isolate electronic components from bodily fluids. First protection is provided by the UHMWPE, which is already a waterproof material [12]. For secondary protection, it was suggested to cover electronics with bio-compatible polymer layer of Paralene C, Polyimide, or Pyralux. This research succeeded to make sensor readings with wired connection (Figure 1.13a), however a battery powered wireless configuration (Figure 1.13b) was not completed.

Even if the wireless prototype would have worked, this design would still be impractical. As already mentioned, the researchers developed a sensor infrastructure for an insert with 12 mm minimum thickness. However, surgeons would prioritise to use tibial inserts with the minimum thickness (for example, 6 mm thick), to sacrifice as little bone as possible during primary surgery [79, 80]. Consequently, the increased thickness of the suggested design is a design limitation.

a)   b)
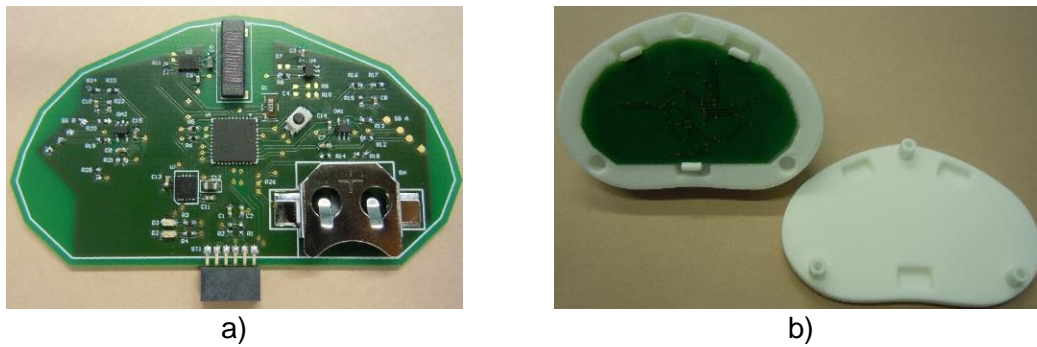
Figure 1.13 Instrumented tibial insert a) wired design, b) wireless design.
Images re-used from public domain thesis by Simoncini, 2014 [12].

The above mentioned two research groups showed that multiple designs and manufacturing techniques are available to develop fully sealed wireless tibial insert. However, their work has been mainly focused on solving electronic problems. Therefore, to date, no research has been conducted on mechanical problems to investigate the structural strength of instrumented UHMWPE tibial inserts.

1.4.4 Summary of instrumented knee implants

Instrumented implants have the potential to provide quantitative information on implant kinematics and kinetics. Instrumented UHMWPE tibial inserts could provide more benefits than instrumented metal tibial trays, since tibial insert does not shield wireless signal, is easier to modify, and can retain original dimensions.

The studies of instrumented metal and UHMWPE implants showed that several design aspects should be considered, such as:

i)   electronic components should be hermetically sealed;

ii)   the design should allow to distinguish medial, lateral, anterior, and posterior loading;

iii) the instrumented insert should retain external dimensions of original implant;

iv)   the prototypes must undergo and withstand *in vitro* tests to determine their resistance to damage, for example, wear, deformation, fracture.

The studies of instrumented UHMWPE tibial inserts have only investigated the development of electronic components and the general assembly. However, none of the studies addressed the UHMWPE tibial insert structural strength after mechanical modifications. It is crucial to perform mechanical design analysis to determine whether electronic components can be incorporated safely.

1.5 Tibial insert design

This chapter describes common *in vivo* failure modes of UHMWPE tibial insert. This chapter also provides a short analysis on the relevant geometrical features, such as, thickness, geometry, width, and cavity location.

1.5.1 Modern tibial insert failure modes

In the past, tibial inserts had a reduced life span due to severe wear or fracture [34]. Ever since orthopaedic companies took measures for the prevention of UHMWPE oxidation, the lifespan of the tibial insert has increased [31, 81]. Nevertheless, modern tibial inserts can still wear [82], plastically deform [17], fracture [83], and dislocate [84] (Figure 1.14).

a) Posterior delamination and fracture (HXLPE sterilised in gas plasma) [85]

b) Posterior plastic deformation and fracture (UHMWPE sterilised in nitrogen) [17]

c) Articular surface wear (HXLPE sterilised in gas plasma) [82]

d) Backside wear (gamma-inert sterilized UHMWPE) [86]

e) Tibial tray and insert fracture [83]

Image copying is restricted by copyright. See Fig. 8D in publication by Li. et al, 2016 [84] ([website link](#)).

f) Insert dislocation from the tray [84]

Figure 1.14 Failure modes of UHMWPE tibial inserts.
Images re-used from publication by Teeter et al., 2014 [85] with open access license CC BY 3.0, from publication by Popoola et al., 2010 [17] with permission from John Wiley & Sons, from publication by Spece et al., 2019 [82] with permission from Elsevier, from publication by Currier et al., 2015 [86] with permission from Elsevier, from publication by Kang & Lee, 2016 [83] with permission from SLACK INC.

The Australian and the United Kingdom (NJR) joint registries report that the main reasons for knee implant revision are loosening, infection and instability [3, 8]. The Australian joint registry also shows that the tibial insert wear of TKR and UKR is responsible only for 1.9% and 1.7% revisions respectively at a time frame of 18 years

[8]. Australian joint registry also shows that UKR tibial implant breakage is a cause for 0.6% revisions [8]. NJR shows that TKR fracture is a cause for 1.3% revisions at a time frame of 14.75 years [3]. Since the UKR tibial insert has a reduced width compared to the TKR, this may indicate that the width of UHMWPE component may not affect the implant performance, since the UHMWPE components of UKR and TKR show similar revision rates due to wear and fracture.

1.5.2 The importance of geometry

Tibial insert performance is affected by its geometry, for example, the insert thickness and the geometry of the articular surface.

Tibial insert thickness is a risk factor since reduced insert thickness increases the contact surface pressure [87-89] and increases the articular wear of UHMWPE [90]. Accordingly, ISO 21536 [91] standard and the Food and Drug Administration of the United States (FDA) [92] recommend to use a tibial insert of a minimum thickness of 6 mm in combination with a metal tibial tray.

The geometry of the tibial insert articular surface affects knee joint kinematics [40]. Ardestani et al. [41] parametric FEA study shows that joint kinematics and surface pressure are affected by articular geometry changes in various locations. The geometry of the tibial articular surface also affects quadriceps muscle force [42] and wear rate [93].

1.5.3 Tibial insert designs

Tibial inserts are available in various shapes and sizes. This research aims to modify tibial inserts by removing material unnecessary for structural support. As such, the focus is directed on designs of commercial tibial inserts which already incorporate a cavity, or which have UHMWPE components with a reduced width. Analysis of these designs will give an insight to successful modification approaches.

A number of currently sold knee systems have modified the intercondylar area of the insert. Some fixed bearing designs have a drilled hole for placing fixation bolts (Figure 1.15 a-b) [94, 95]. Some mobile bearing designs also have a cavity in S-I direction, which allows rotation around a metal peg (Figure 1.15 c) [96]. A cavity in A-P direction has been used for Zimmer Monoblock design (Figure 1.15 d), which was used to attach an impaction handle [97]. Zimmer Monoblock cavity was left empty after the completion of surgery [98].

a) SAIPH knee [94]

b) APEX knee [95]

c) Scorpio Plus SuperFlex PS
mobile bearing [96]
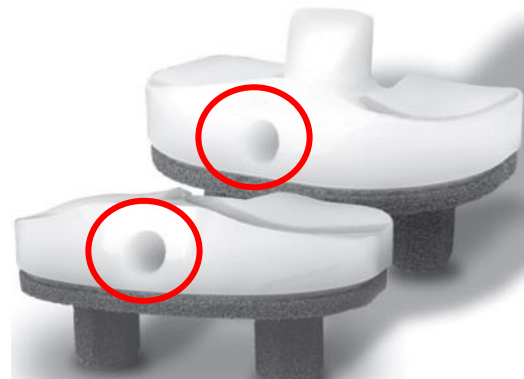
d) Zimmer Monoblock [97]

Figure 1.15 Tibial insert designs with a cavity in intercondylar area
(red circle highlights areas were UHMWPE has a cavity to hold bolts, pegs, or to help
seat the implant).
Images reused from public domain matortho.com [94] accessed 28-Jan-2020, from
public domain coringroup.com [95] accessed 28-Jan-2020, from publication by
Kobayashi et al., 2012 [96] with open access licence CC BY 2.0, from public domain
zimmerbiomet.com [97] accessed 15-May-2020.

Other knee systems have completely removed the intercondylar area of tibial insert and
instead use unicondylar tibial insert components. Figure 1.16 shows that separated
UHMWPE components have been implemented in UKR [99] and TKR designs [100,
101].

a) Oxford partial knee [99]

b) Vanguard XP knee [100]

c) iTotal patient-specific knee [101]

Figure 1.16 Knee implant designs which use unicondylar components (red circle highlights the area were the UHMWPE components are separated). Images reused from public domain biomet.com [99] accessed 28-Jan-2020, from public domain medicalexpo.com [100] accessed 28-Jan-2020, from public domain conformis.com [101] accessed 28-Jan-2020.

No published design rationales were found which describe the consequences of modifying the intercondylar area. However, since tibial insert design allows only contact between the tibial articular surface with the femoral condyles (Figure 1.17) [102], it could explain why it is common to modify or completely remove the intercondylar area as shown in Figure 1.15 and Figure 1.16. Accordingly, the intercondylar area could potentially serve as a safe place for a cavity, which accommodates sensors and electronic components.
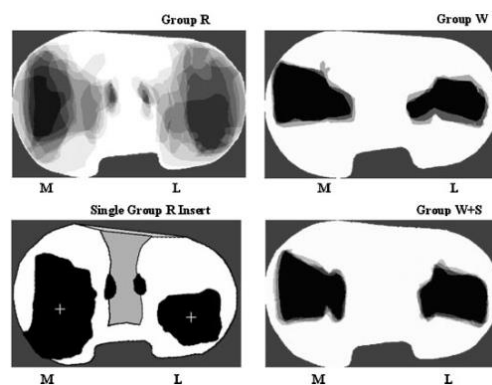
Figure 1.17 Overlaid wear areas of multiple retrieved and *in vitro* tested tibial inserts (groups: R – retrieved implants, W – *in vitro* walking, S – *in vitro* stair descent) [102]. Image reused from publication by Karman et al., 2009 with permission from John Wiley and Sons.

1.5.4 Summary

The design of UHMWPE tibial inserts has seen numerous alterations over decades of use. A review of clinically available designs shows that it is common to machine a cavity in the intercondylar area of UHMWPE tibial insert. Therefore, the intercondylar

area could potentially be safely utilised to house sensors and electronic components without compromising the performance and longevity of the implant.

1.6 Tibial insert methods of testing

Diverse physical and computational test methods have been developed to analyse implant performance. *In vitro* physical tests can provide a relatively close representation of real-life materials and *in vivo* environment, however testing requires a significant amount of time and components can be costly [103, 104]. Finite element analysis (FEA) computational models help with reducing testing time and cost, but they give a less accurate representation of material behaviour and *in vivo* environment [105]. This chapter analyses the physical and FEA tests for instrumented tibial inserts.

1.6.1 Physical tests

Physical tests aim to evaluate implants in a controlled and lifelike loading environment. Multiple test methods have been developed to emulate clinically observed implant damage. As such, they attempt to recreate wear, creep, dislocation, or fracture of tibial inserts. Therefore, *in vitro* tests are required prior to clinical studies [103]. While there is not a single test which could recreate all *in vivo* damage modes in all relevant areas, various test methods aim to recreate specific damage in specific location, as described in this section.

1.6.1.1 Knee simulator test

A knee simulator is a versatile test machine, which is used to apply lifelike loading environment on TKR implants. Most advanced knee simulators are capable of reproducing and measuring movement in six DoF and have multiple synchronised testing stations (Figure 1.1). A knee simulator is primarily used to inflict wear and plastic deformation to the articular surface of tibial insert [106]. However, it has also been used to inflict posterior edge fracture (Figure 1.19a) [17].

Figure 1.18 Example image of AMTI (AMTI, USA) knee simulator.
Images reused from public domain amti.biz [107] accessed 07-May-2023.

Standardised test methods are commonly used to compare different implant designs, and they provide minimum requirements that a product should fulfil. Knee simulator wear tests can be performed according to ISO 14243-1 [108], ISO 14243-3 [109] and ASTM F3141 [49] test standards. ISO 14243 tests provide motion and load profile for normal walking, while ASTM F3141 test provides additional profiles for daily activities, such as, stair climbing, turning, and sitting. Alternatively, non-standardised tests with modified scenarios can be used to apply more demanding loading profiles [17, 21, 110].

Non-standardised wear test by Popoola et al. [17] adopted various kinematic and kinetic waveforms to mimic activities of daily living, such as, raising from a chair, stair ascent, and deep squat. The study also implemented aging of the tibial insert based on the ASTM F2003 [111] standard. This test method was able to develop wear, creep, and fracture at the posterior edge of the gamma-inert sterilised tibial insert (Figure 1.19a). However, this test method was unable to recreate clinically observed damage to the Highly Cross Linked UHMWPE (HXLPE) inserts (Figure 1.19b) with complete fracture and removal of the posterior aspect as shown in Figure 1.14a. This test method may be of interest when testing the structural strength and wear resistance of instrumented tibial insert, since the damage could be close to the internal cavity.

a) Gamma-inert sterilised UHMWPE   b) Gas-plasma sterilised melt-annealed
                                                                       e-beam irradiated HXLPE
Figure 1.19 Tibial insert damage after adverse loading scenario test on the knee simulator. Images re-used from publication by Popoola et al., 2010 [17] with permission from John Wiley & Sons.

1.6.1.2 Posterior edge fatigue test

Popoola et al. [17] also designed a posterior edge fatigue test, which replicates damage caused by heel strike in ACL-deficient knee (Figure 1.20). This method applied a 2224 N constant force via medial femoral condyle on the tibial insert with a 7° slope. The femoral condyle was set to slide at 2 Hz frequency over the posterior edge of the insert with 10 mm stroke. As a result, this test method could create fatigue damage on the posterior edge of UHMWPE inserts (Figure 1.21a), but it did not inflict damage on the HXLPE inserts (Figure 1.21b). This test method may prove useful when testing instrumented tibial insert, since the damage could be near the cavity.
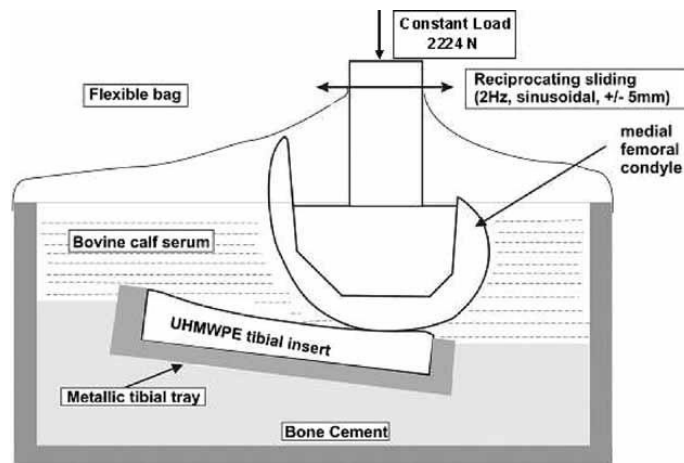
Figure 1.20 Posterior edge fatigue test setup. Image re-used from publication by Popoola et al., 2010 [17] with permission from John Wiley & Sons.
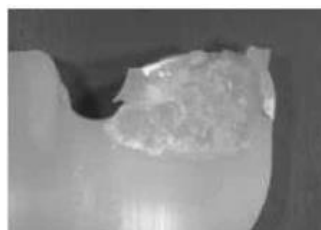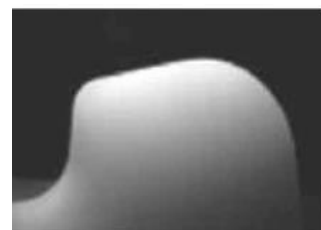
a) UHMWPE   b) HXLPE

Figure 1.21 Posterior edge fatigue test was able to damage a) UHMWPE component but was not capable to damage b) HXLPE component. Images re-used from publication by Popoola et al., 2010 [17] with permission from John Wiley & Sons.

1.6.1.3 High flexion deformation test

The ASTM F2777 [112] test standard allows a creep test to be performed on an artificially aged UHMWPE insert, while it is immersed in water at 37° temperature. In this method, as recommended by manufacturer, the femoral component is rotated at maximum flexion angle and positioned on the posterior edge of the inclined tibial component (Figure 1.22). Then cyclic downward load is applied through the femoral component with a maximum force of 2275 N. This test method is intended to simulate deformation and potential fracture at the posterior edge. This method could be used on instrumented tibial inserts, since inflicted damage could be close to the cavity.

Figure 1.22 ASTM F2777 component setup (red arrow shows the direction of load). Image reused from public domain endolab.org [113] accessed 19-Feb-2020.

1.6.1.4 Tibial tray fatigue test

The tibial tray fatigue test standard ASTM F1800 [114] was developed to test the fracture resistance of the metal tibial tray due to *in vivo* loading. This simplified test method approximately replicates clinically observed tibial tray fracture, when one half of tibial tray has lost bone support while still being subjected to *in vivo* loads. The test method requires fixation of one half of the tibial tray. Five million cycles of 900 N (per ASTM F2083 [115]) are then applied to the remaining unsupported half (Figure 1.23). The test is passed if no cracks can be observed under normal or corrected vision.
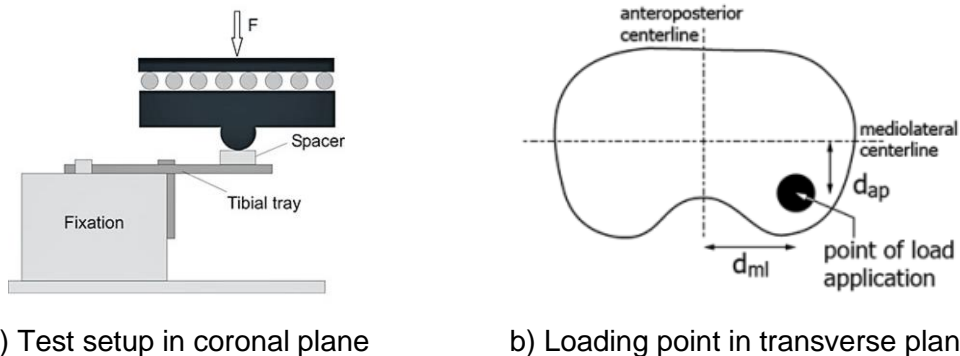
a) Test setup in coronal plane   b) Loading point in transverse plane
Figure 1.23 Tibial tray fatigue test setup per ASTM F1800-19. Image reused from standard ASTM F1800-19 [114] with permission from ASTM.
Note: d_{ml} - loading point distance from anteroposterior centreline,
d_{ap} - loading point distance from mediolateral centreline.

This test can be modified to accommodate the investigator's goal. For example, studies suggest applying maximum force of 2000 N or higher, to represent a more realistic worst-case scenario [116, 117]. Additionally, the point of load and loading environment can be changed per user requirements. An instrumented tibial insert could be placed inside the tibial tray. Therefore, this test method could potentially simulate clinically observed UHMWPE tibial insert fracture in A-P direction as shown in Figure 1.14e.

1.6.1.5 Physical test comparison

Table 1.2 shows a summary of relevant methods which could be used to assess the structural strength or wear resistance of UHMWPE tibial insert. These test methods can be used to compare the performance of the instrumented tibial insert with the original tibial insert.

Table 1.2 Physical tibial insert test comparison.

	Knee simulator test	Posterior edge fatigue test	High flexion deformation test	Tibial tray fatigue test
Damaged area	Articulating and bottom surface	Posterior edge	Posterior edge	Loading point and distal areas
Primary damage modes	Wear, plastic deformation.	Wear, plastic deformation.	Plastic deformation.	Fracture
Potential damage modes	Posterior edge fracture	Posterior edge fracture	-	-

1.6.2 Computational tests

1.6.2.1 Finite Element Analysis

Computational models can be used to simulate the mechanical behaviour of various structures and materials. Finite element analysis (FEA) is the most commonly used technique in solid mechanics for the analysis of components with complex shapes and material properties [105].

The FEA method divides complex geometry into multiple small elements of finite size, connected by nodes, and delivers approximate partial differential equation solutions [118]. The elements are typically formed out of triangles or rectangles and their three-dimensional analogues. To obtain reasonably accurate solutions, thousands of elements are usually needed. The FEA models can be used to analyse the structural behaviour, for example, deformation, stresses, and strains. FEA allows to investigate the influence on a number of variables, for example, applied loads, geometry, material properties, and boundary conditions. In order to relate displacements to forces, the FEA method applies energy principles of structural mechanics. For instance, the principle of virtual work is commonly used for linear and non-linear FEA models [118].

Modelling uncertainties and errors occur due to model assumptions and approximations of the mathematical formula representing the physical problem. Therefore, the FEA model accuracy must be checked with verification, sensitivity studies, and validation [119]. The checks can be qualitative and quantitative.

Qualitative observations of contour plots and deformed geometry provide a general assessment of whether the model shows reasonable results.

A calculation verification can be performed with a mesh convergence test. The mesh convergence test does not guarantee model accuracy, but it helps to make the result independent of mesh size. A computational prediction validation can be performed by comparing FEA model results to analytical solutions.

Sensitivity studies help to assess the influence of model inputs on model outputs and they should be performed before model validation. Sensitivity studies are useful for parametric optimisation and for designing a laboratory experiment.

Validation is required in order to check if FEA results accurately represent the experimental data (the "gold standard"). However, validation should not be confused with calibration, when FEA input parameters are altered until the computational results align with experimental data. It is recommended to validate the primary outputs of interest. When possible, it is also beneficial to validate other model outputs for

establishing a higher level of credibility [119]. Validation can be done at different levels, for example, by comparing with an analytical formula, with another FEA model, with results from another publication, with laboratory experiment data, or with patient data.

FEA can be used to analyse TKRs to reduce the testing time and costs [105]. FEA is commonly used to investigate the influence of specific implant design features [120, 121]. FEA can be used during initial design optimisation stages to identify fragile regions of the implant design and to reduce failure risk [120, 122]. FEA is particularly useful to analyse stress and strain distribution everywhere within the internal structure of the tibial insert, which cannot be achieved with physical tests [121, 122]. Therefore, FEA methods are gradually evolving to allow knee implant strength analysis. For example, two standardised FEA methods are available for metal knee components: ASTM F3161 [123] for femoral component and ASTM F3334 [124] for tibial tray. However, no FEA standards exist for UHMWPE components.

1.6.2.2 FEA models of cavities within UHMWPE

In the absence of FEA standards for UHMWPE component modelling only guidance from research publications could be used. Two studies by Pegg et al. [121] and Hasenkamp et al. were found, showing how internal stresses and strains are distributed within the UHMWPE tibial insert near a cavity.

A study by Pegg et al. [121] carried out a fracture risk analysis focusing on internal holes and embedded metal objects. Pegg et al. used the FEA method to analyse the internal stress distribution of a UKR UHMWPE insert (Figure 1.24).

In this study, the material model assumed isotropic J2-plasticity (simple elastic–plastic response), Poisson's ratio of 0.46, a density of 0.95 g/cm3, Young's modulus of 315 MPa, and a yield stress of 11 MPa. A symmetric constraint was applied to model one half of the UKR insert. The base of the insert was constrained in the z-axis, and the metal markers could not rotate. A friction coefficient of 0.07 was applied for all interactions except for the insert base. A sinusoidal cyclic compression force of 2400 N was applied in the z-axis at a frequency of 1 Hz. The model used quadratic tetrahedral elements (C3D10). The femoral component and the tibial tray were modelled as analytical rigid surfaces. The mesh convergence test was used to choose an overall mesh seed size of 1 mm with the areas of interest having a smaller mesh size of 0.3 mm [121].

The model was verified by comparing the kinetic energy to the inertial energy. Additionally, the explicit model was compared to an equivalent implicit quasi-static model, which showed no significant difference in stress distribution. A sensitivity study was performed by changing parameters of the friction, the insert thickness, the A-P and

S-I position of the metal markers, and the A-P radius of the femoral condyle. The model was validated with surface pressure measurements by using a pressure sensor with 572 sensels (Model 4000; Tekscan, Boston, USA); however, the experimental test was performed only with one specimen and the model did not account for UHMWPE creep. The results showed that increased marker dimensions and close proximity to the point of load increased tensile stresses, which have been related to clinically observed unicondylar insert fracture [121].

a) The maximum principal stresses distribution (MPa)   b) The von Mises stresses distribution (MPa)
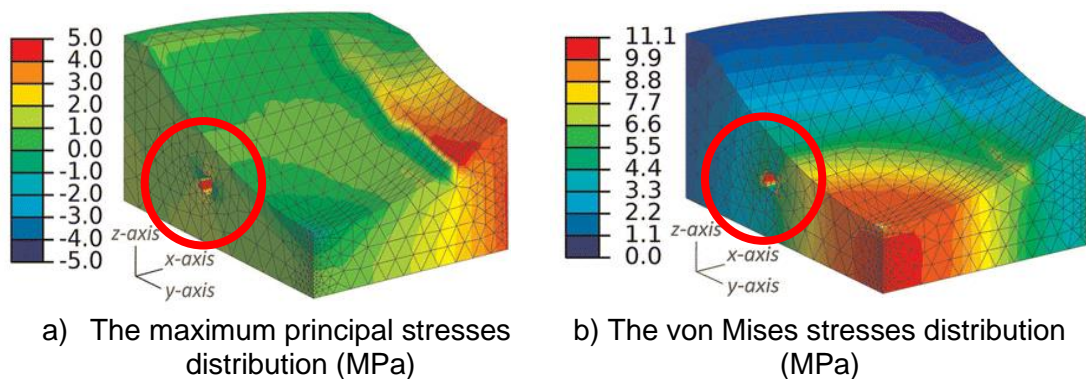
Figure 1.24 Internal stress distribution around the internal hole (red circle) within the posterior part of UKR insert. Images reused from publication by Pegg et al., 2013 [121] with permission from SAGE Publications.

A study by Hasenkamp et al. [122] analysed strain distribution within UHMWPE mobile-bearing tibial insert. Hasenkamp's et al. primary goal was to find an optimal location for strain gauges. However, the FEA model also showed strain distribution and strain increase near the guide pin hole (Figure 1.25).

Here, the material model assumed linear elastic UHMWPE properties with Poisson's ratio of 0.4 and Young's modulus of 340 MPa. The metal femoral and tibial components were modelled as a deformable part with linear elastic Co-Cr-Mo properties with Poisson's ratio of 0.3 and Young's modulus of 115 GPa. A symmetric constraint was applied to model one half of the TKR insert. The base of the insert had a fixed constraint. A compression force from 200 to 3100 N was applied in the z-axis. The model used tetrahedral elements. The mesh seed size varied from 0.1 to 1 mm.

A sensitivity study was performed by changing the force from 200 to 3100 N, which allowed to locate the regions of maximum and zero strain. The model was validated with one specimen by comparing the measured and simulated strain. The strain sensors provided good dynamic measurements within 1 s time window, but afterwards strain measurements were affected by UHMWPE creep.
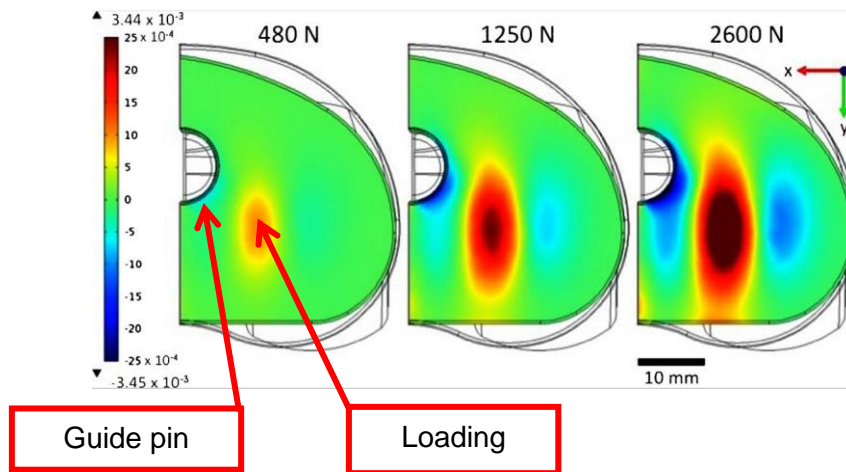
Figure 1.25 Internal strain distribution in the x-axis of a mobile-bearing tibial insert with a guide pin hole, for loads of different magnitudes. Image re-used from publication by Hasenkamp et al, 2013 [122] with open access licence CC BY.

The two studies showed that stress and strain outputs are useful for tibial insert design analysis. The studies showed that stress and strain concentrations are higher near the holes, which can lead to component fracture. Whilst the FEA models in both studies were validated, the model accuracy was reduced by the creep of UHMWPE.

1.6.2.3 UHMWPE material properties

In order to create an FEA model of a tibial insert it is important to understand the material properties of UHMWPE. UHMWPE has many beneficial properties; it is biocompatible due to its chemical inertness, additionally it has high lubricity, impact resistance, and abrasion resistance [125]. However, UHMWPE is difficult to model, since it has non-linear material properties, which are affected by manufacturing processes and the surrounding environment.

UHMWPE has a simple chemical composition, consisting of only hydrogen and carbon, which creates organised ethylene segments, which are further combined in polyethylene (Figure 1.26) [125].
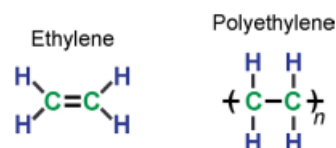
Figure 1.26 Chemical structure of ethylene and polyethylene. Image taken from book by Kurtz [125] with permission from Elsevier.

The simple UHMWPE chemical composition is deceptive, because it has a complex hierarchy at the molecular and super-molecular scale [125]. UHMWPE has both a chaotic amorphous region and a crystalline region with highly organised lamellas. Most solid UHMWPEs consist of about 50% crystalline, however the external and internal molecular structure can further change due to various manufacturing processes [125].

There are three manufacturing steps for an UHMWPE implant (Figure 1.27). First, a powder (i.e. resin or flake) is created from ethylene gas. Second, the powder is consolidated (i.e. converted) into a solid block (i.e. slab). Third, the block is machined into a final implant shape. Alternatively, a two-step process can be completed with direct compression moulding to mould the powder into the final implant shape. However, even direct compression moulding may still require a machining step to cut out additional features [78].

a) [78]
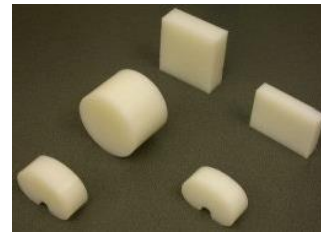
b) [126]

c) [78]

d) [127]

Figure 1.27 (a) UHMWPE resin, (b) consolidated slab, (c) machining step, (d) final product. Images taken from book by Kurtz, 2016 [78] with permission from Elsevier, from public domain acnis-titanium.com [126] accessed 06-Jan-2020, from public domain medacta.com [127] accessed 06-Jan-2020.

UHMWPE material properties differ due to multiple factors:

i)   Powder grade: GUR 1020 or 1050 [78];

ii) Consolidation process: compression moulding or ram extrusion [78];

iii) Sterilisation: with or without radiation [128];

iv) Thermal treatment: melting or annealing [128];

v)   Adding antioxidants: vitamin E or COVERNOX™ antioxidant [128];

vi) Ambient temperature [105];

vii) Loading rate [105];

viii) The amount of loading [105].

1.6.2.4 GUR 1020 material properties

This research will modify and test currently available (and in clinical use) tibial inserts (manufactured by Medacta Int, CSP, Lugano, Switzerland) made of compression moulded GUR 1020 and sterilised in ethylene oxide [129].

For small deformations within the elastic range, a simple material model can be used defining only Young`s modulus and Poisson`s ratio. Virgin GUR 1020 material usually has reported Young`s modulus under tension of 346 MPa [130], 424 MPa [130], 500 MPa [129], under compression of 421 MPa to 720 MPa [131] and Poisson`s ratio of 0.46 [128].

For large deformations an elastic-plastic material model should be used. Commonly used are engineering or true stress-strain curves (Figure 1.28).

a)

b)   c)
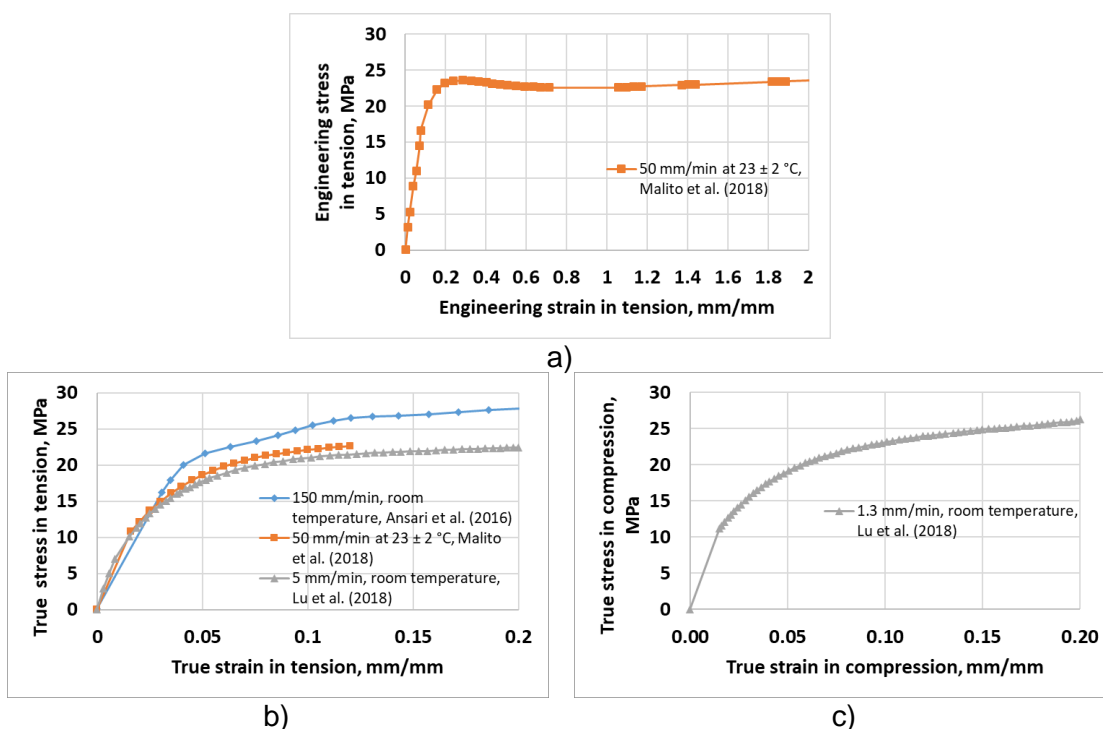
Figure 1.28 Virgin GUR 1020 a) engineering and b,c) true stress-strain relationship [128, 130, 132].

2   Aims and objectives

2.1 Research aims

The first aim of this research is to investigate how optimisation of different parameters, such as, location, shape, and size of a machined cavity, would affect the mechanical structural strength of modified UHMWPE knee insert. The second aim is to investigate how the structural strength of modified insert would change if the machined cavity held an embedded object. The third aim is to create a smart tibial insert prototype and investigate optimal sensor location.

2.2 Research objectives

1. Set out design requirements for the "smart" knee implant prototype.
2. Investigate what test methods are needed to analyse the structural strength and resistance to damage of a tibial insert with an internal cavity. Required steps:
    a. Review physiological environment.
    b. Review published test methods and test standards.
    c. Analyse which computational and physical tests allow for evaluation the strength of modified tibial insert.
3. Develop physical tests and computational models to compare different modified tibial insert designs.
4. Validate FEA model and reanalyse the advantages and limitations of computational and physical tests methods.
5. Perform parametric modelling to optimise internal cavity shape and location.
6. Perform tests on modified tibial insert.
7. Perform tests with embedded sensors and optimise smart knee implant prototype.

3   Design of an instrumented tibial insert

3.1 Introduction

This chapter relates to research Objective 1. Specifically, this chapter outlines the design requirements and presents a novel design idea, which would allow to modify a commercial UHMWPE tibial insert for the purpose of embedding sensors and electronics.

3.2 Design requirements

Table 3.1 identifies the design inputs for mechanical modification of commercial tibial inserts, which would satisfy the user of "smart" knee implants.

Table 3.1 User needs with corresponding design inputs for "smart" knee implant.

	User needs	Design input
1	Make measurements with sensors.	Cavity should accommodate strain gauges or other sensors.
2	Use existing tibial insert designs.	External tibial insert shape or tibial tray shape should not be changed. **Design assumption:** surgical procedure will not change if the implants retain their original external shape.
3	Retain insert`s thickness under femoral condyles.	Cavity should not be placed under the tibial articulating surface.
4	Withstand extreme physiological loading. For example, modified insert damage is similar to original insert damage.	Cavity should not be placed under the tibial articulating surface.
5	UHMWPE material around the cavity should not undergo plastic deformation during physiological loading.	Cavity shape, size, location should be optimized so there would be no plastic deformation on the cavity walls. **Design assumption**: cavity walls should not plastically deform to retain constant position of the internal components, to reduce the risk of fracture, and to simplify electronic calibration.
6	Retain the interlocking mechanism strength.	Cavity should not interfere with the locking mechanism.
7	Should be sterilisable.	Modified insert should be able to withstand normal clinical cleaning and sterilisation methods.
8	Feasible to manufacture.	Cavity should be machined with drilling or milling tools. Final cavity design should have assigned tolerances.
9	Be a stand-alone product.	Insert and sensor assembly should be done by a manufacturer and not by a surgeon during surgery to reduce surgical time.
10	Cavity should provide space for electronics.	Cavity volume should be maximised to fit more electronic components, while still satisfying other design needs.

3.3 Design concept

Over the years, various prototypes of instrumented tibial inserts have been developed both for UKR [76] and TKR [10-12, 69]. All existing prototypes have suggested placing sensors and electronic components in a cavity beneath the articular surface. However, this design approach has two limitations.

Firstly, a cavity would reduce the UHMWPE component thickness under the articular surface. ISO 21536 standard and FDA recommend to retain a minimum insert thickness of 6 mm under the load bearing area (the articular surface) [91, 92], because the thickness reduction will increase the articulating surface wear [90]. Additionally, the placement of a metal object under the articular surface may increase internal stresses, which can result in tibial insert fracture [121].

Secondly, the existing prototypes require uncommon manufacturing methods, such as, laser welding or direct compression moulding. Laser welding is not an established manufacturing technique [78], therefore orthopaedic companies would need to re-validate their manufacturing processes to comply with medical regulations [77]. Direct compression moulding is an established manufacturing method, but it is not widely used by all manufacturers [78].

This research proposes a novel design approach, by creating a cavity in the intercondylar area of the UHMWPE tibial insert. The literature review revealed that it could be safe to machine a cavity in the intercondylar area, since various commercial tibial inserts designs have modified or completely removed the intercondylar area, as shown in Figure 1.15 and Figure 1.16.

This design approach also resolves the two design limitations. Firstly, sensors placed in the intercondylar area would not reduce the UHMWPE thickness under the articular surface. Secondly, the cavity can be made by drilling or reaming, which is an available manufacturing method that saves costs. Thirdly, it is not required to attach the sensors directly to the UHMWPE. Instead, the sensors can be placed in a sealed capsule which is pressed inside the cavity with an interference fit.

This design proposal is based on the rationale, that the tibial articular surface has direct contact with the femoral condyles. Therefore, the UHMWPE material under the articular surface provides structural support, which is crucial for providing resistance against wear, deformation, and fracture. However, no literature was found, investigating whether the intercondylar area provides any structural support.

In this research project it is hypothesised that the intercondylar area provides minimal or no structural support (Figure 3.1). Accordingly, it is assumed that modification of the intercondylar area should not make a significant difference to the performance of the tibial insert, for example, by changing the resistance against wear, deformation, and fracture.
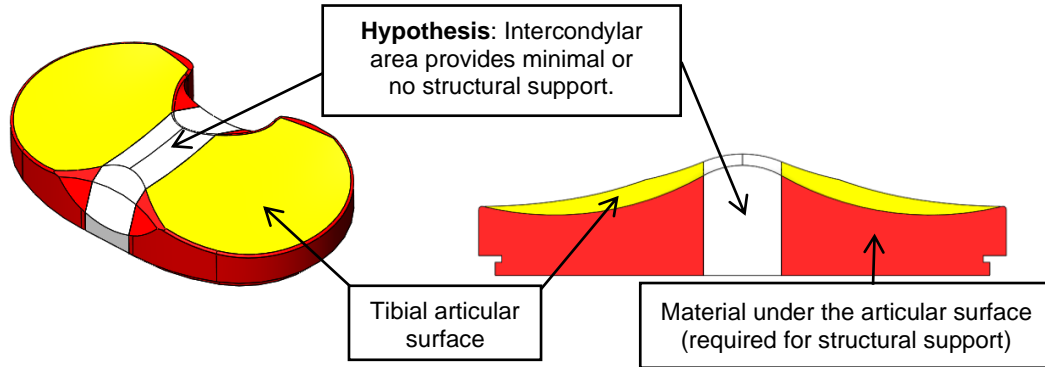
a) Tibial insert   b) Section view in coronal plane
Figure 3.1 Illustration of structural support for the TKR tibial insert
(tibial articular surface is shown in yellow, material required for structural support is shown in red, material not required for the structural support is shown in white).

4   Computational methods

The work presented in this chapter covers research Objective 3 and 4. Specifically, this chapter outlines the work on FEA model development and validation.

Computational modelling is advantageous for conducting parametric studies, since it is a faster and cheaper method than physical testing [105]. Computational modelling allows incremental changes to be made to the component geometry, component alignment, and applied loading conditions. This can be particularly useful to provide a greater understanding on how the shape, size, and location of an internal cavity would change the deformation patterns of the UHMWPE tibial insert.

This and the following chapters will present a combination between computational and experimental studies. FEA models were used in conjunction with experimental studies. It was not possible to arrange the chapters in the chronological order, therefore chronological order of computational and experimental studies is shown in Appendix A.

4.1   Sphere-on-plate model

4.1.1   Introduction

Finite element models of TKRs require advanced user expertise. Such complex models take a long time to develop, therefore it is beneficial to first create simplified FEA models which could help with exploring initial design ideas. To provide an initial understanding of the structural support provided by the tibial insert, a simplified model of a single tibial insert articulating surface was constructed. A sphere-on-plate model was developed using Abaqus software (Abaqus/CAE 2017, Simulia, USA), which could help with parametric modelling for a single tibial insert width described in section 4.1.5. Static FEA (Abaqus/Standard, implicit, static general) was used for modelling simplified geometry and material properties of TKR components under axial compression load. The outputs of interest were contact pressure and deformation of the UHMWPE component. Contact pressure predictions could indicate plastic deformation, while deformation could indicate change in stiffness of the overall structure.

4.1.2   FEA model setup

The sphere-on-plate model represents a simplified interaction between the medial femoral condyle and the tibial insert (Figure 4.1). The half-sphere represented a rigid medial condyle and was modelled as an analytical rigid body. The plate represented the tibial insert and was assigned a liner-elastic material property of UHMWPE GUR 1020, to allow validation with Hertzian contact analytical solution.

The plate was fixed on its base to restrict movement in all directions. The load was applied via a sphere in two steps: a displacement step brought the components into contact and a force step applied 2462 N in the normal direction to the plate to represent 73% medial condyle force ratio [15] of 3372 N total peak force during walking for a 100 kg person [21].). The mesh elements were set as linear, 3D stress, hexagonal (C3D8R), to reduce computational time. FEA model input parameters are summarised in Table 4.1.
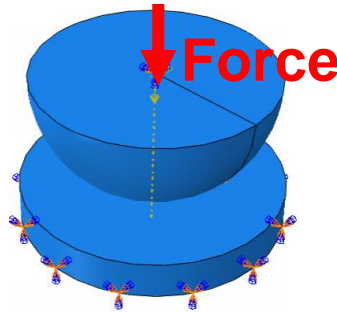
Figure 4.1 Sphere-on-plate FEA model.

Table 4.1 Static FEA inputs for the sphere-on-plate models.

Input	Value
Co-Cr-Mo component	
Sphere diameter	63.5 mm [133]
Young's modulus and Poisson's ratio	The FEA models used analytically rigid body. Young`s modulus of 210,000 MPa and Poisson`s ratio of 0.3 [134] was used for the Hertzian analytical formula.
UHMWPE component (GUR 1020)	
Plate diameter	70 mm [133]
Plate thickness	10 mm [133]
Young's modulus (linear elastic per Hertzian contact)	421 MPa [131]
Poisson's ratio (linear elastic per Hertzian contact)	0.46 [128]
Force (normal compressive force per Hertzian contact theory)	2462 N (73% medial condyle force ratio [15] of 3372 N total peak force during walking for a 100 kg person [21].)
Contact and boundary condition settings	
Friction between surfaces (frictionless per Hertzian contact)	0
Mesh element type	C3D8R: hexagonal mesh with reduced integration and linear shape function.
Contact interaction	* Normal behaviour had "hard" contact with default penalty constraint enforcement method and the penalty stiffness of 10 [135]. * Finite sliding. * Surface-to-surface.
Boundary conditions	* Encastre fixation at the bottom of the plate. * The metal component moves freely only in the loading direction
Loading steps	Step 1: displacement of 0.05 mm Step 2: force of 2462 N

4.1.3 Verification with mesh convergence test

The mesh convergence test must be conducted to verify FEA model calculations [119]. It allows to estimate the errors associated with model discretization. During the test the mesh is incrementally refined until the parameter of interest reaches a plateau, thus ensuring that further discretization would not be likely to make significant changes. The mesh was gradually refined from a course mesh into a fine mesh by doubling the number of elements until the peak contact pressure and peak displacement reached a plateau. The contact pressure was calculated because the node value can be compared to analytical Herzian contact pressure solution. The displacement was calculated because it was of interest for the parametric study since change in deformation would indicate a change in stiffness.

During the qualitative assessment, the FEA model showed maximum deformation and stress concentration directly under the sphere (Figure 4.2).
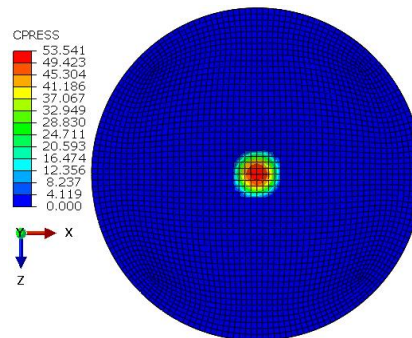
Figure 4.2 Top view of the sphere-on-plate model with mesh size of 1.25 mm. Contour plot of the contact pressure (MPa).

The mesh convergence results showed that plateau was reached at mesh size of 1.25 mm (Figure 4.3). Any further mesh refinement changed the peak contact pressure by less than ±2.9% and the peak displacement by less than ±0.9%. Mesh convergence results are shown in Table 4.2.

a)   b)
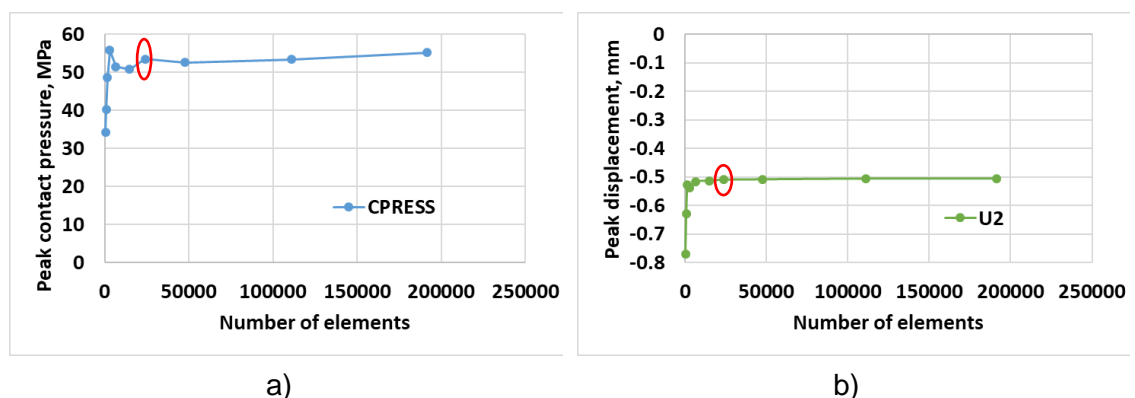
Figure 4.3 Sphere-on-plate mesh convergence test of a) the peak contact pressure and b) the peak displacement (the red circle highlights the results with chosen mesh size of 1.25 mm).

Table 4.2 Results of mesh convergence for the sphere-on-plate model
("-" sign denotes compression).

Global mesh size, mm	Number of elements	Peak contact pressure, MPa	Peak displacement, mm
5	416	34.28	-0.7711
4	924	40.24	-0.6283
3	1620	48.63	-0.528
2.5	2992	55.85	-0.5372
2	6520	51.46	-0.5171
1.5	14756	50.78	-0.5131
1.25	23936	53.54	-0.5101
1	47840	52.57	-0.5088
0.75	111020	53.39	-0.5063
0.625	191488	55.16	-0.5057

4.1.4 Validation with Hertzian contact theory

The Hertzian contact analytical solution can be used to validate simplified FEA contact model results. The Hertzian solution replicates non-adhesive interaction between two bodies. It assumes frictionless contact, purely elastic deformation, and continuous surfaces. The analytical formula is used to calculate the contact surface area and pressure, which are affected by the geometry and material properties of each object and the applied force. The contact radius a is shown in **Equation 1**, the maximum contact pressure P_{max} is shown in **Equation 2** [136]. The subscript 1 and 2 denotes the sphere and the plate respectively. The maximum pressure P_{max} occurs at the centre of the contact area and is equal to the principal stress component σ_z in the axial loading direction at 0 mm distance from the contact surface [136].

F: applied force
d: the diameter of the sphere
v: Poisson's ratio
E: Youngs modulus
a: contact radius
P_{max}: maximum pressure
σ: principal stress

$$a = \sqrt[3]{\frac{3F}{8} \frac{\frac{(1-v_1^2)}{E_1} + \frac{(1-v_2^2)}{E_2}}{\frac{1}{d}}}$$

Equation 1: Hertzian contact radius

$$P_{max} = \frac{3F}{2\pi a^2}$$
$$= \sigma_z \; at \; 0 \; mm \; distance \; from \; surface$$

Equation 2: Hertzian maximum contact pressure

For the given force, geometry, and material properties the Hertzian analytical solution for contact pressure was 51.19 MPa, which differed by 4.4% from the FEA prediction of 53.54 MPa (Figure 4.3).

4.1.5 FEA parametric test for the required minimum support

This research project aims to provide guidance on how to design a cavity at the intercondylar region for instrumented UHMWPE tibial inserts. The size of the cavity can be derived with a direct or an indirect method. The direct method is to find the maximum allowed cavity size. The indirect method is to find the minimum necessary support size. The direct method is more informative but time consuming, because parametric analysis would be required for every implant size and design. The indirect method can save time by providing first simplified approximations regardless of implant design, by finding the minimum necessary support width, which would serve as a guidance for any tibial insert size and design. Figure 4.4 illustrates the two primary dimensions of interest:

1. The maximum allowed width for the cavity;
2. The minimum necessary width for structural support.
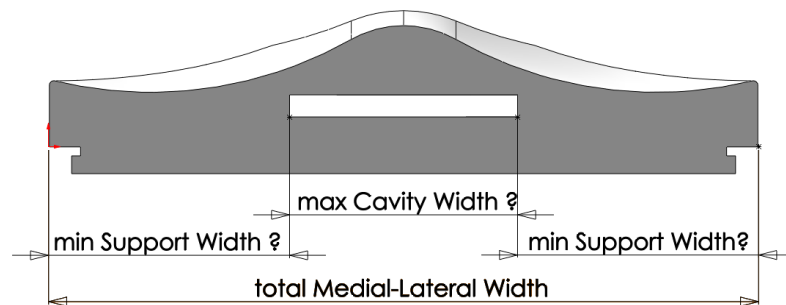
Figure 4.4 Cross section view of a tibial insert: ilustration of the maximum allowed width for the cavity and the minimum necessary width for the structural support.

Sphere-on-plate model (Figure 4.1) could be used to represent a unicondylar tibial insert or one articulating surface of the TKR tibial insert, allowing to approximate the cavity width indirectly. The aim of the parametric study is to find the minimum plate diameter, which provides sufficient structural stiffness. Then the radius of the plate can be used to approximately indicate the required support around the centre of pressure (CoP) as illustrated in Figure 4.5.
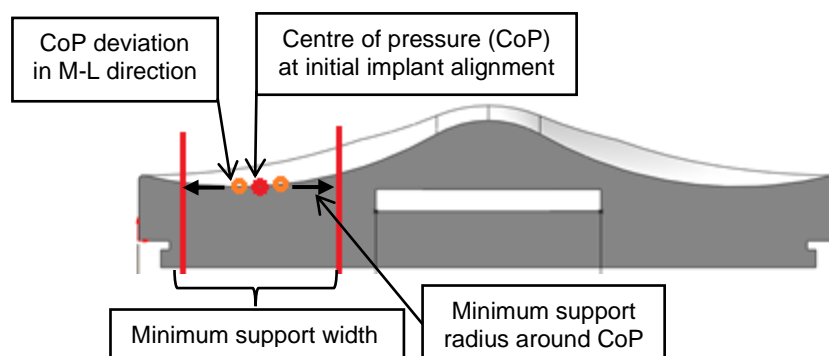
Figure 4.5 Minimum required support width could be approximated by combining information of the minimum support radius and the CoP deviation.
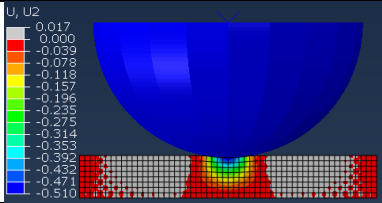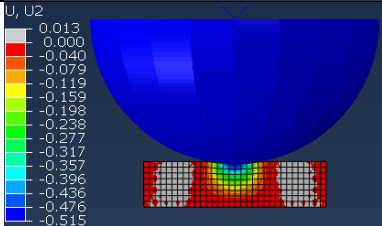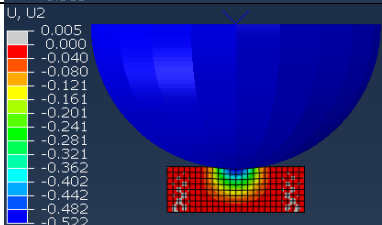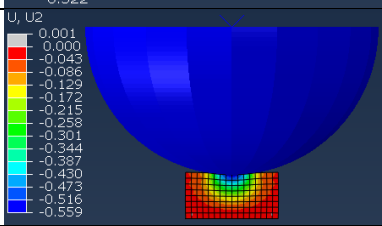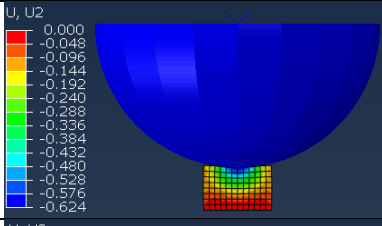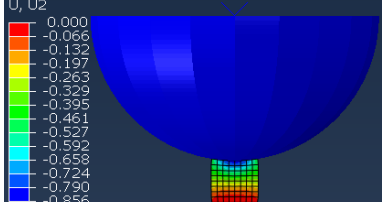
4.1.5.1 Materials and methods

A reduction in diameter would decrease the overall stiffness and provide less resistance against the deformation. However, it was unknown at what diameter a noticeable change in structural stiffness could be observed. Therefore, a parametric study was performed on the sphere-on-plate model (Figure 4.1) to observe the plate diameter influence on the contact pressure and the peak displacement. The FEA model setup remained unchanged with a mesh size of 1.25 mm, only the initial diameter of 70 mm was reduced to 40 mm, 30 mm, 20 mm, 15 mm, and 10 mm.

4.1.5.2 Results

The parametric study showed that reduction of the plate diameter caused an increase in contact pressure and displacement (Table 4.3.). All results were compared to the plate model with 70 mm diameter. The plate with 30 mm diameter showed minimal differences, since displacement did not differ by more than 2.3%. The plate with 20 mm diameter showed noticeable difference in peak displacement by 8.8%. The plate with 10 mm diameter showed noticeable difference in peak displacement by 40.4% and peak contact pressure by 13.2%.

Table 4.3 Parametric analysis of the plate diameter effect on the peak contact pressure and the peak displacement (the value in bracket is the difference in percentage with the 70 mm diameter model).

Plate diameter, mm	Contour plot of displacement in the loading direction	Peak contact pressure, MPa	Peak displacement, mm
70		53.54	-0.510
40		53.80 (0.5%)	-0.515 (1.0%)
30		53.84 (0.6%)	-0.522 (2.3%)
20		54.29 (1.4%)	-0.559 (8.8%)
15		55.26 (3.1%)	-0.624 (18.3%)
10		61.69 (13.2%)	-0.856 (40.4%)

4.1.5.3 Discussion

The parametric study of sphere-on-plate model was used to provide guidance for UHMWPE material behaviour and approximate the necessary support width for the tibial insert. This FEA model was limited by a simplified geometry, material properties, and a single loading case whilst in reality, there are various complex geometries, many

different material grades exist, and the load would change direction and magnitude and the contact region would alter.

The benefit of using a simplified model is that it is much easier to analyse the effect of one specific parameter, in this case, the support width. To make the model relevant, the "worst case" material and loading parameters were taken from existing literature, by choosing the smallest UHMWPE Young's modulus, the largest axial force (during walking) and a sphere geometry to increase the deformation. The axial force was used, since it is the dominant force component as shown in Bergmann et al. [21] and Taylor et al. [14] studies.

This model visualised that even the areas, which are not under direct contact, may provide some structural support. This is important for the instrumented tibial insert design, because material removal from the intercondylar area of the tibial insert may still affect the overall structural stiffness underneath the articular surface.

The parametric study also showed that at certain diameter there was minimal change in stress and displacement. The 40 mm and 30 mm diameter plates had similar structural stiffness to the 70 mm plate, since the displacement did not differ by more than 2.3%. While the displacement in plates with diameter of 20 mm and below differed by more than 8.8%. Therefore, a support width of 30 mm may provide sufficient structural stiffness, which falls within the range of commercial unicondylar tibial inserts, which have M-L width of 17.5 mm to 37.0 mm [137-139]. The suggested width of 30 mm is a rough approximation, because it does not take into account the deviation of centre of pressure as illustrated in Figure 4.5. Nevertheless, it gives the first indication to support the design hypothesis (illustrated in Figure 3.1 in Section 3.3) that the intercondylar area provides minimal or no structural support.

The sphere-on-plate model was limited to simplified geometry, material properties, and loading conditions. Therefore, further FEA models were developed with realistic geometry, elastic-plastic material properties and diverse loading scenarios, which are described in the next sections.

4.2 Static FEA model for TKR

As a preliminary step, a static FEA model was created, since static models are easier to replicate in laboratory conditions. Static FEA (Abaqus/Standard, implicit, static general) was used for modelling quasi-static loading of TKR under axial compression and to carry out mesh convergence. Then a quasi-static experimental test was performed to validate the static FEA model.

4.2.1 Geometry of components

The FEA model consisted of two parts: femoral component and tibial insert. Both parts had dimensions of clinically used GMK Primary knee implants (Medacta International, Switzerland): size S3/10 cruciate retaining tibial insert (with minimal thickness of 7 mm) and size 3 left femoral component. The tibial insert was defeatured with CAD software (SolidWorks® Premium 2019 SP3.0, Dassault Systèmes) by removing peripheral chamfers and fillets, to reduce computational time (see Figure 4.6).
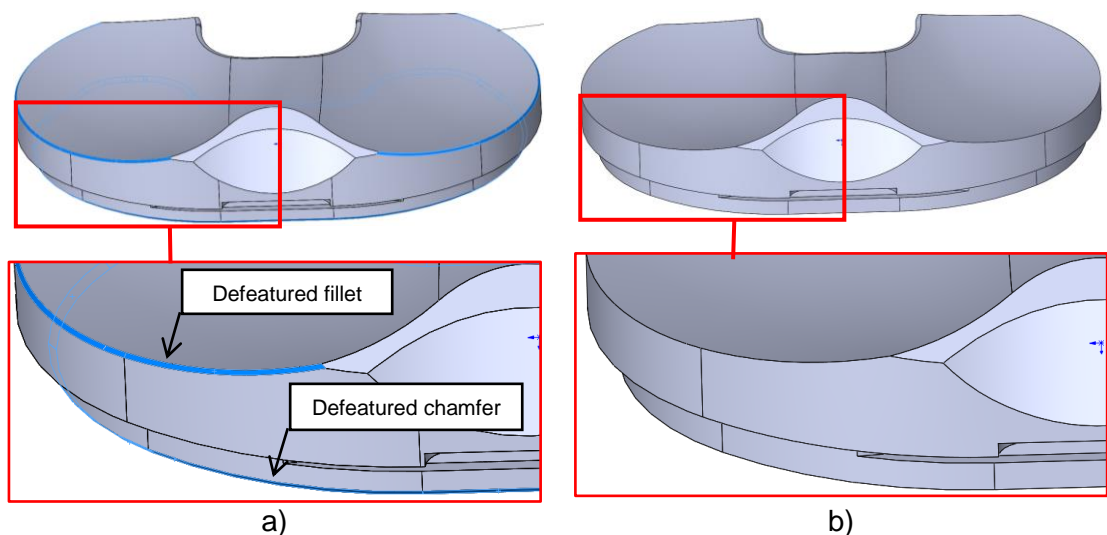
Figure 4.6. Tibial insert a) geometry with chamfers and fillets (highlighted in blue) and b) defeatured geometry without chamfers and fillets on the top and bottom faces.

4.2.2 Assembly alignment

Both parts were assembled together and aligned within SolidWorks. Femoral component was rotated at 0º flexion by ensuring that the insert base and femoral base were parallel. The condyles of the femoral components were aligned to match the dwell points of the tibial insert articulating surface (see Figure 4.7). Then the assembly was imported as Parasolid file .x_t into ABAQUS software. Tibial tray was not added to the model to reduce computational time.

Dwell point
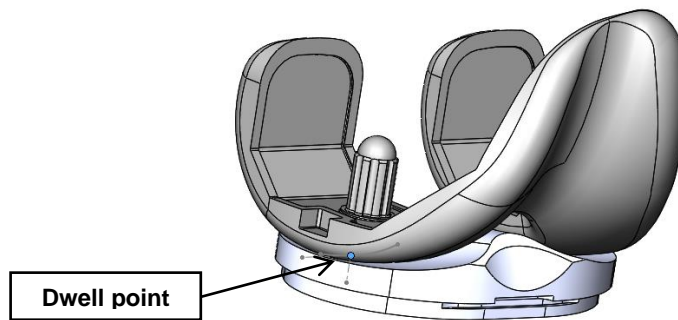
Figure 4.7. Femoral and Tibial part alignment at 0º flexion of the static ABAQUS model.

4.2.3 Material properties

The femoral component was modelled as a rigid shell, and the tibial insert was modelled as a deformable 3D part. The femoral component is made out of Co-Cr-Mo alloy with Young`s modulus of 210,000 MPa [140], whilst the tibial insert is made out of unirradiated GUR1020 UHMWPE with Young`s modulus of 748.2 MPa [132]. It was assumed that the femoral component will not deform due to its higher stiffness because both axial and flexural stiffness are directly proportional to Young`s modulus and the elastic modulus between the two materials differ by three orders of magnitude. The tibial insert was assigned linear elastic and non-linear plastic material properties. The elastic material properties were defined with Young`s modulus of 748.2 MPa [132] and Poison`s ratio of 0.459 [128]. The plastic properties were defined with compressive true stress-strain data (see Table 4.5) with yield stress of 11.22 MPa for virgin GUR1020 UHMWPE when loaded at a rate of 1.3 mm/min [132]. The material plasticity model was defined with the ABAQUS default isotropic von Mises yield surface criteria [141].

4.2.4 Contact interaction properties

Finite sliding tracking approach was used to allow unrestrained motion of the surfaces in contact. A surface-to-surface instead of node-to-surface contact pair discretization was used to improve result accuracy. The deformable tibial insert was defined as the slave surface (see Figure 4.8). Normal behaviour was defined as "hard" contact with default penalty constraint enforcement method and the penalty stiffness of 10 [135]. Tangential behaviour was defined as a penalty with friction coefficient of 0.04 [142].

a)   b)
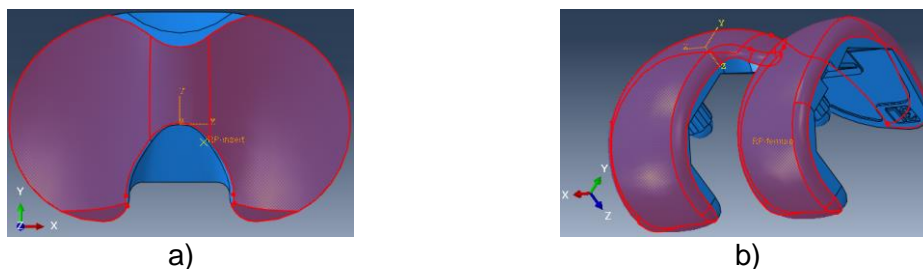
Figure 4.8. Contact properties were defined between a) slave and b) master surface (highlighted in red).

4.2.5 Boundary conditions

Tibial tray was not added to reduce computational time. The boundary conditions were defined to replicate the fixation within a test machine, when the tibial insert motion is fully restricted by a custom metal fixture with tibial tray dimensions as further described in section 4.2.11. The femoral component was assigned one reference point, which allowed motion only in axial I-S direction. The tibial insert was assigned a kinematic coupling constraint connecting the bottom face of the tibial insert to a single reference point, which had fixed translation and rotation in all directions (encastre fixation) (see Figure 4.9), because the tibial insert motion was restricted by a metal tray. This fixation approximation was used because no tibial tray was modelled. In reality, there could be a small gap between the tibial insert at the tibial tray side walls, which would allow for a micromotion or even the tibial insert being pushed out.
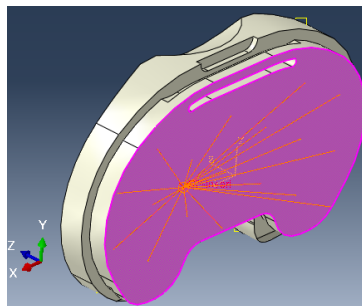
Figure 4.9. Tibial inserts with assigned kinematic coupling constraint at the bottom face to fixate translation and rotation in all directions.

4.2.6 Loading steps

Loading was completed in three steps: preload, load, and unload. In step 1, the femur was preloaded in displacement control with 0.05 mm downward displacement to initiate the contact between parts. In step 2, a compressive axial force of 5480 N at 0º flexion was applied to the femur. In step 3, the femur was un-loaded in displacement control to remove any contact.

4.2.7 Mesh element type

Since the femoral component was modelled as a discrete rigid shell, the femur was assigned with linear triangular mesh elements R3D3. The tibial insert had a complex geometry which could not be meshed entirely with hexahedral elements (see Figure 4.10). Therefore, the tibial insert was modelled as a 3D part with 10-node modified quadratic tetrahedral elements (C3D10M, where the 'M' stands for modified) (see Figure 4.11). C3D10M elements are the same as C3D10 elements, but with hourglass control and three additional displacement variables [143]. Hourglass modes are non-physical modes of distortion that can occur in solid elements with only one integration point [144]. Hourglass control applies internal forces to each element to resist the

deformation of the element. The hourglass control formulation provides improved coarse mesh accuracy with slightly higher computational cost and performs better for nonlinear material response at high strain levels [145]. Quadratic modified elements were chosen, because they can accurately calculate contact pressure for "hard" contact simulations [146]. The modified elements are designed to alleviate the shortcoming of regular elements: improve uniform contact pressure for the "hard" contact relationship, exhibit minimal shear and volumetric locking, and are robust during finite deformation [144].

a)   b)
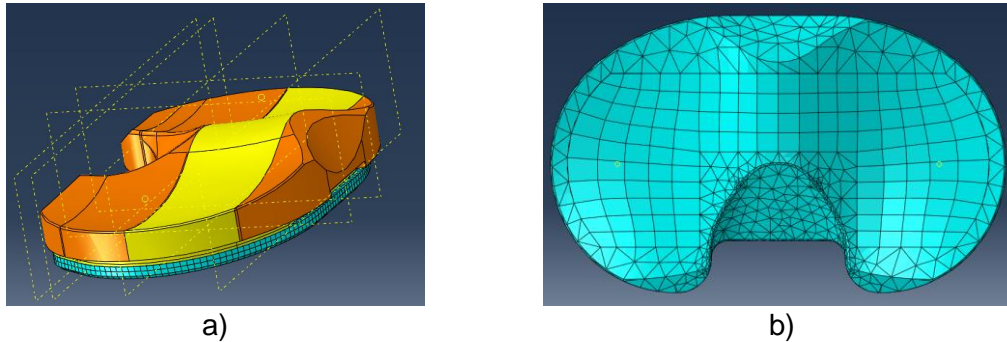
Figure 4.10. Example images of failed meshing attempts when tibial insert was divided in multiple segments and partially meshed with hexahedral elements.

a)   b)
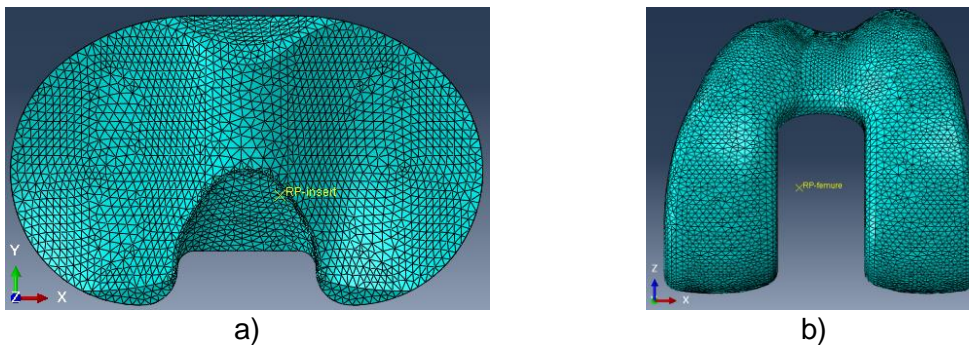
Figure 4.11. Successfully meshed a) tibial insert and b) femoral component with global seed size of 1.3 mm.

4.2.8 Mesh convergence check

The same mesh size was used both for the femur and the insert (global seed size ratio of 1:1) to reduce mesh sensitivity [147]. Mesh convergence analysis was performed with global seed size of 5.8 mm, 3.6 mm, 2.4 mm, 1.9 mm, 1.3 mm, 1.0 mm, and 0.8 mm to double the element number of the tibial insert with each meshing increment, which would approximately double the degrees of freedom in the model. Mesh convergence was compared by calculating peak contact pressure, peak von Mises stress, and peak axial deformation (see Figure 4.12). Mesh convergence was obtained with mesh size of 1.3 mm, because the change for peak contact pressure, peak von

Mises stress, and peak displacement was less than ±3.6%, ±2.7% and ±2.4% with more refined meshes (see Figure 4.13).

a)   b)

c)   d)
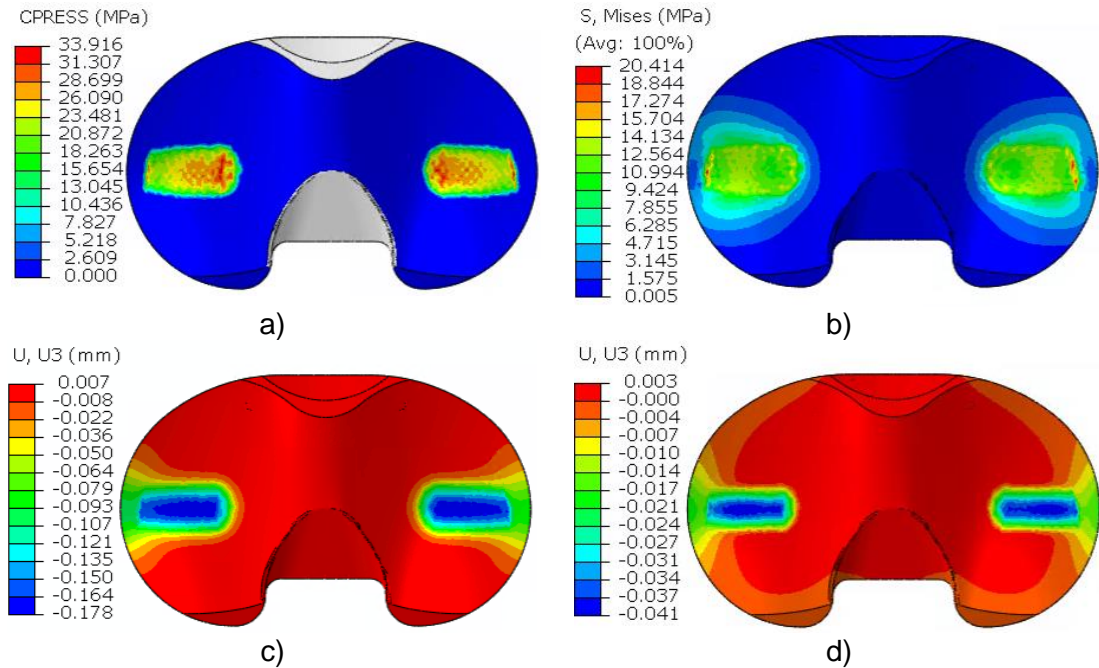
Figure 4.12. Static FEA model (mesh size of 1.3 mm) results for a) contact pressure, b) von Mises stress, c) axial deformation during loading, and d) axial deformation after un-loading.

a)   b)
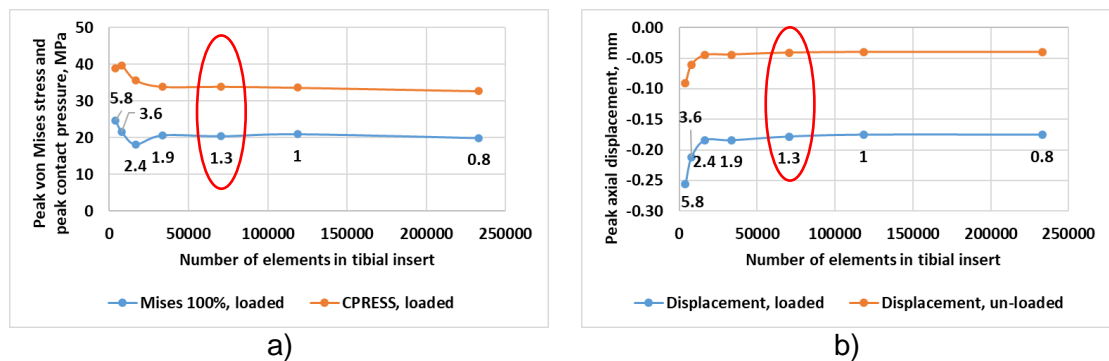
Figure 4.13. Mesh convergence check for a) maximum contact pressure (CPRESS) and von Mises stress during loading and b) maximum axial displacement during loading and after un-loading. The numbers near data points indicate the global seed size. The red circle highlights values for the mesh size of 1.3 mm at which the convergence was obtained.

4.2.9 Static FEA input parameter summary for TKR

The summary of FEA model input parameters is shown in Table 4.4.

Table 4.4. Summary of static FEA model input parameters for TKR.

Parameter	Inputs
Part geometry	3D geometry of clinically available implant: GMK Primary knee (Medacta International, Switzerland). Femoral component: size 3 left, original geometry. Tibial insert: size S3/10 cruciate retaining, defeatured geometry with removed chamfers and fillets.
Material properties	Material properties or unirradiated GUR1020 UHMWPE) when loaded at a rate of 1.3 mm/min [132]. Elastic: Young`s modulus of 748.2 MPa [132] and Poison`s ratio of 0.459 [128] Plastic: true stress-strain with yield stress of 11.22 MPa [132]. Plasticity model: isotropic von Mises yield surface criteria.
Solver	Abaqus/Standard (implicit), static general.
Loading steps	Step 1: pre-loading in displacement control at -0.05 mm absolute position. Step 2: loading in force control. Step 3: un-loading in displacement control to +0.5 mm absolute position.
Contact algorithm	Tracking approach: Finite sliding. Contact pair discretization: Surface-to-surface. Master surface = rigid femoral component. Slave surface = deformable tibial insert.
Contact conditions	Normal behaviour = "Hard" contact with penalty constraint enforcement and the penalty stiffness of 10 [135]. Tangential behaviour = Penalty with 0.04 friction coefficient [142].
Load	Compressive axial force of 5480 N applied at 0º flexion.
Boundary conditions	Bottom face of the tibial insert is connected to a reference point with kinematic coupling constraint. The tibial reference point is fully fixed to not allow any translation and rotation (encastre fixation).
Mesh	Femoral component: discrete rigid shell with linear triangular elements R3D3. Tibial insert: deformable 3D part, with a 10-node modified quadratic tetrahedral element, with hourglass control (C3D10M, where the 'M' stands for modified). Femur and tibia use the same global seed size for meshing.

Table 4.5. Published true stress-strain data for unirradiated GUR1020 UHMWPE plastic deformation at loading rate of 1.3 mm/min [132] (see Figure 1.28c).

Stress, MPa	Strain, mm/mm
11.22	0.000
12.11	0.003
13.08	0.006
14.05	0.009
15.05	0.013
16.05	0.017
17.33	0.024
18.12	0.028
19.19	0.036
20.24	0.044
21.16	0.054
22.05	0.065
23.02	0.083
24.12	0.110
25.04	0.144
26.24	0.185

4.2.10   Edge loading

An edge loading effect was observed in the FEA contour plots. A thin line with concentrated pressure could be seen on the top surface of the tibial insert both at the far medial and far lateral side (see Figure 4.14a). It was unusual to see an edge loading area, since the femoral condyle geometry seems to be fully conforming to the tibial insert articulating surface. Initially it was thought that the edge loading could be caused by the reduced tibial insert thickness since the tibia insert has a cut-out at the bottom face in order to fit into the metal tibial tray (see Figure 4.14b).
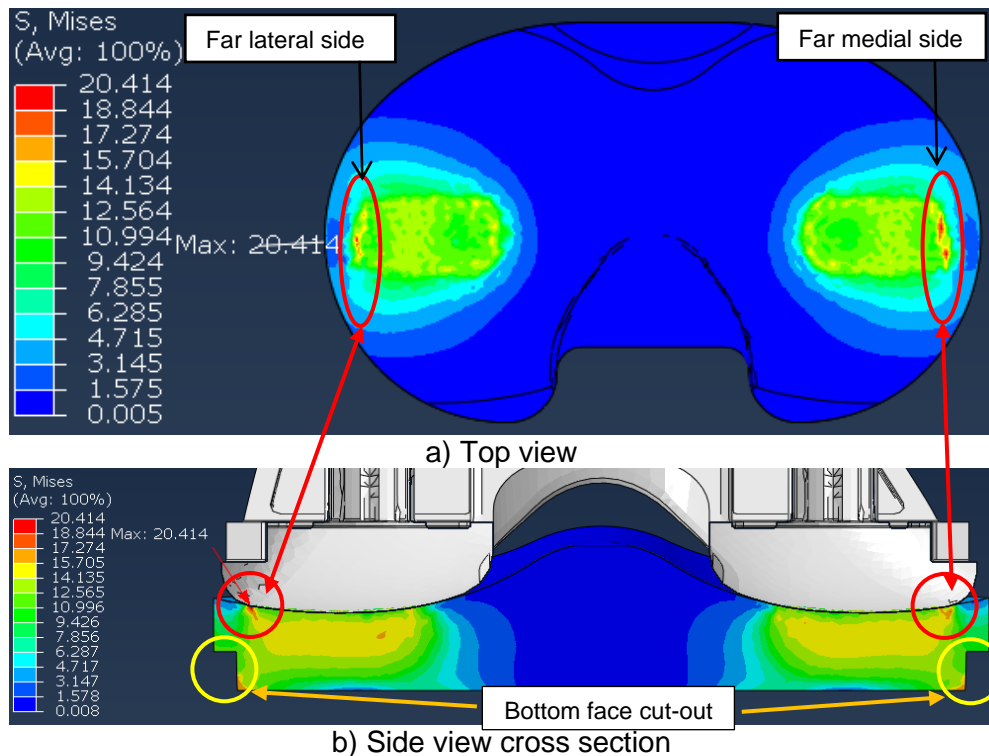
Figure 4.14. Edge loading line shown from a) a top view and b) a side view. The red circle highlights the edge loading line at the far medial and lateral side, the yellow circle highlights the cut-out at the bottom face of the tibial insert.

In order to confirm whether the edge loading is caused by the cut-out at the tibial insert bottom face, the FEA model was recalculated with a modified tibial insert geometry. The CAD model of the original tibial insert was modified by filling in the gap below the tibial insert (see Figure 4.15).
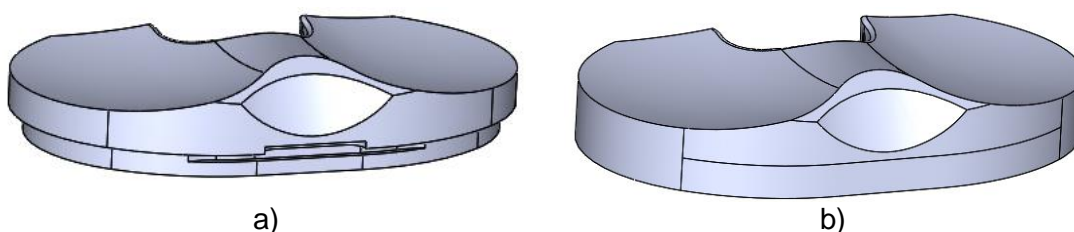
Figure 4.15. Illustration of tibial insert a) with a cut-out at the inferior face and b) without a cut-out at the inferior face

The FEA results for the insert without a cut-out still showed edge loading in exactly the same location. Edge loading effect could be observed as an increase in contact pressure, von Mises stress, and as the increase deformation on both articulating sides of the tibial insert (see Figure 4.16). This shows that the cut-out geometry feature in the tibial insert was not causing the edge loading effect.

a) Von Mises stress when loaded (top view)

b) Von Mises stress when loaded (side view cross section)

c) Axial deformation when loaded (top view)

d) Axial deformation when unloaded (top view)

e) Contact pressure when loaded (top view)
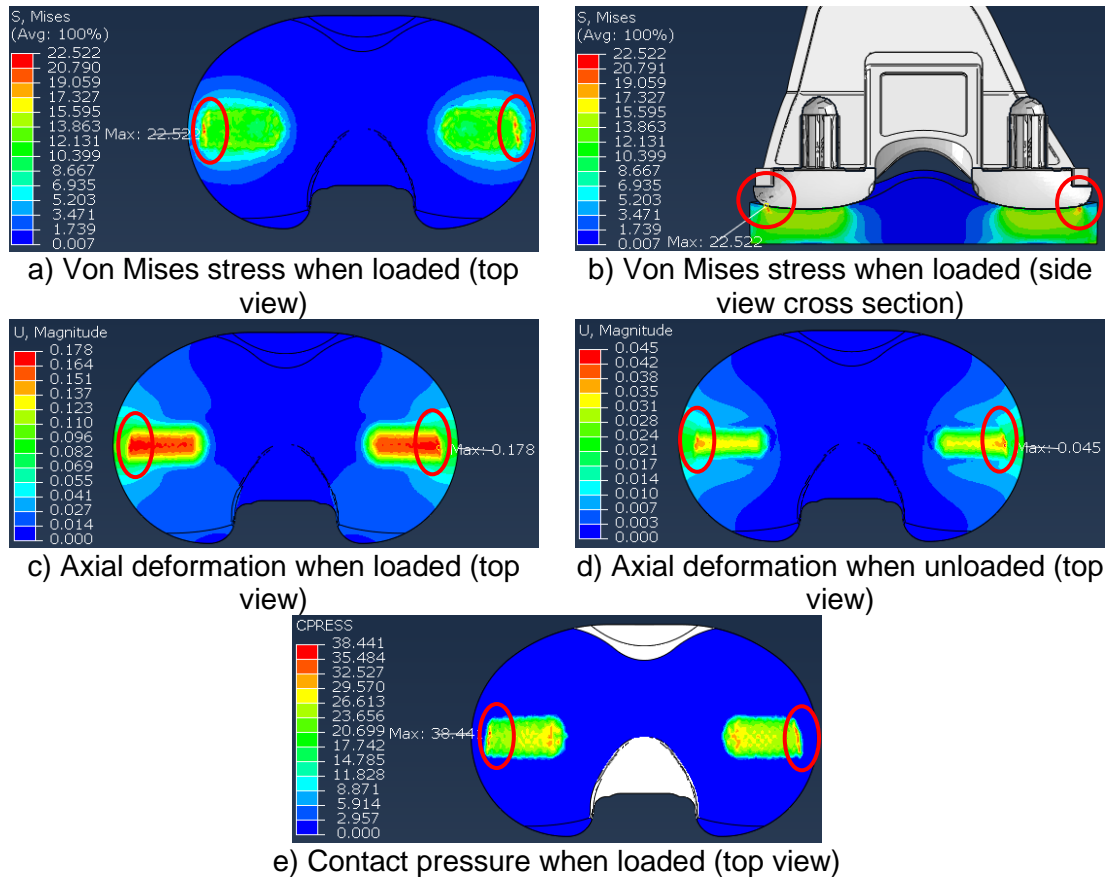
Figure 4.16. Static FEA model results of tibial insert without a bottom cut-out for a,b) von Mises stress, c) deformation during loading, and d) deformation after unloading, and e) contact pressure. Red circles highlight the areas with edge loading.

The edge loading is most probably caused by the unique geometry of the femoral component. When looking at the cross section of the femoral condyle, it can be observed that the condyle geometry consisting of multiple joint semi-circles, which are merged together. The femoral condyle has a small fillet on both sides in order to create rounded corners. When enlarging the image from Figure 4.16b, it can be observed the edge of the fillet is in a direct contact with the maximum stress point (see Figure 4.17). This indicates that edge loading is caused by the fillet of the femoral condyle. Existing literature shows that similar edge loading pattern has been previously observed with ZIMMER NK-II tibial insert, where the edge loading was caused by the flat bearing femur and insert design [148].
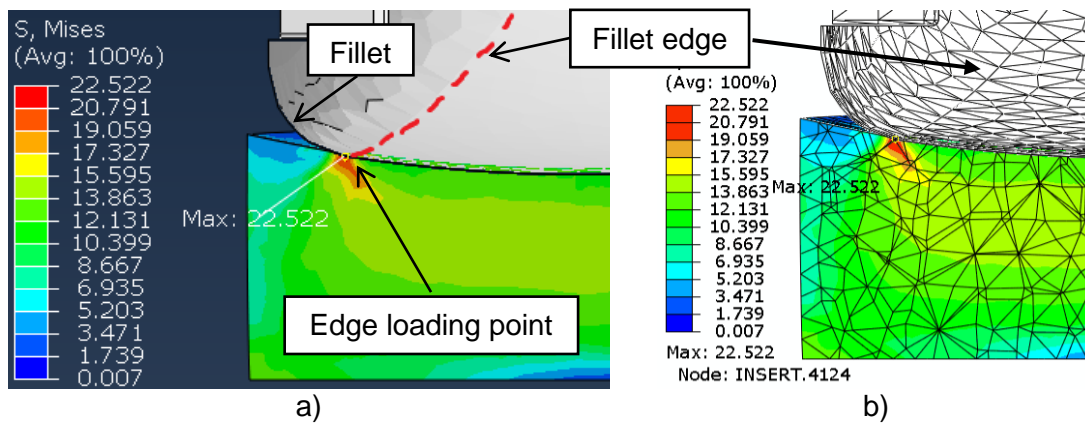
Figure 4.17. Edge loading image a) without mesh, and b) with mesh. Edge loading point is in a direct contact with the fillet edge of the femoral condyle. Red dashed line highlights the fillet edge.

The fillet edge is a physical geometrical feature as designed by the manufacturer, therefore for the purpose of this PhD project it cannot be measured or altered. A sensitivity study by changing the fillet radius could be completed in the future work.

4.2.11   Static FEA validation with Tekscan pressure film and a height gauge

An axial compression test was developed to replicate the static FEA loading scenario in controlled laboratory environment. The aim of the experimental test was to validate the predicted results of the static FEA model.

The experimental test was performed with Instron 3366 materials testing machine (Instron, USA), a dial height gauge DG-50M (Linear Tools, UK), and Tekscan pressure films (model 4000 with pressure range to 62 MPa; Tekscan, Boston, USA), I-scan software (Tekscan Inc., South Boston, MA) was used to analyse the Tekscan measurements. Instron machine was used to control the applied force and the loading rate, height gauge measurements were used to measure plastic deformation caused by a single loading cycle, and Tekscan pressure films were used to measure contact pressure on both articulating surfaces of the tibial insert.

A custom metal tibial tray fixture was used to ensure correct tibial insert position on the bed of the Instron machine (see Figure 4.18). The tibial tray fixture had a cut-out which matched the internal dimensions of the metal tibial tray. To ensure fixture alignment, a black permanent marker and a ruler with ±0.5 mm accuracy was used to draw thin centrelines on the Instron bed and on the metal tibial tray fixture. Then metal tibial fixture was centred on the Instron bed and firmly clamped to prevent any motion.

a)

b)   c)
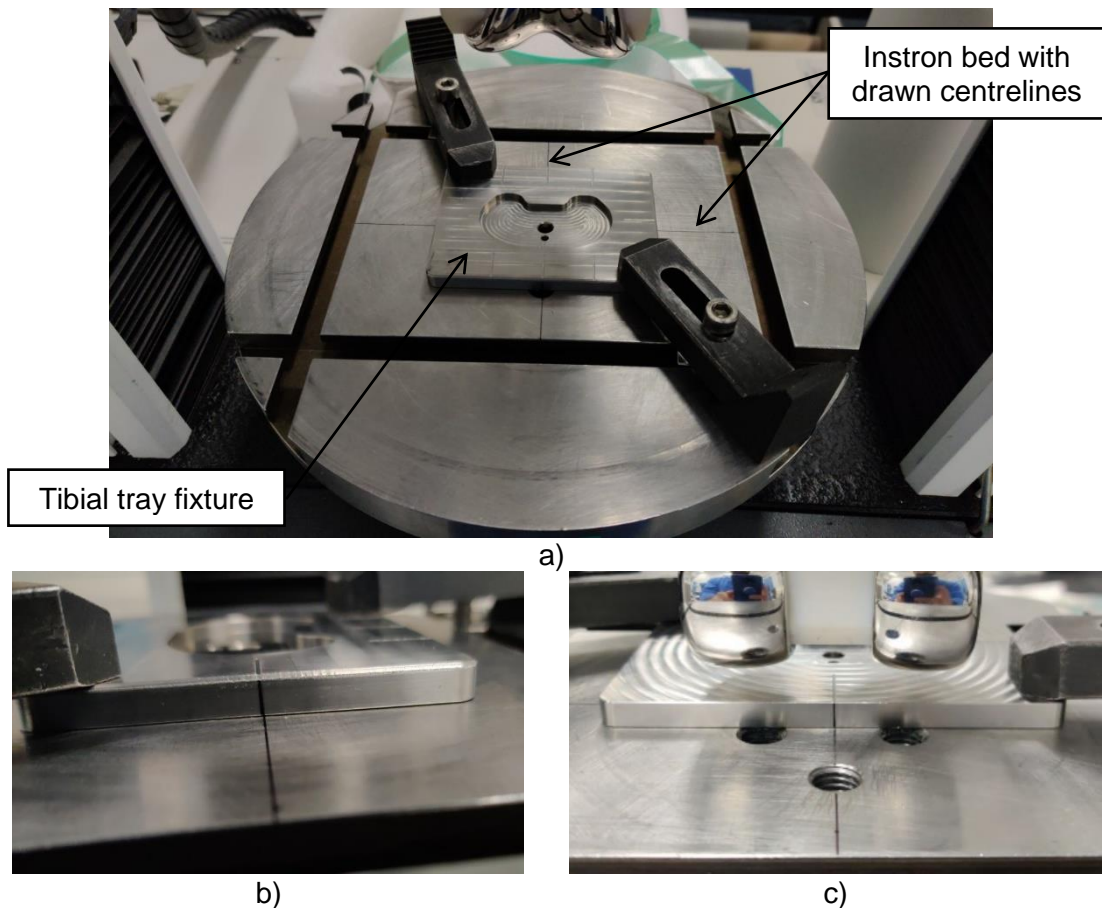
Figure 4.18. Tibial tray fixture position on the Instron machine bed. The fixture was centred by aligning centrelines of the a) Instron bed and b,c) the tibial tray fixture.

TekScan K-Scan 4000/9000psi pressure film (Tekscan Inc., USA) pressure sensor was placed on the tibial tray fixture. Tekscan pressure sensor had two separate pressure films to allow separate measurements on each side of the tibial insert articulating surface. Tekscan films were approximately aligned to be parallel to each other and at equal distance from the centre line (see Figure 4.19a). Both pressure films were taped to the table to reduce film movement during testing.

a)   b)
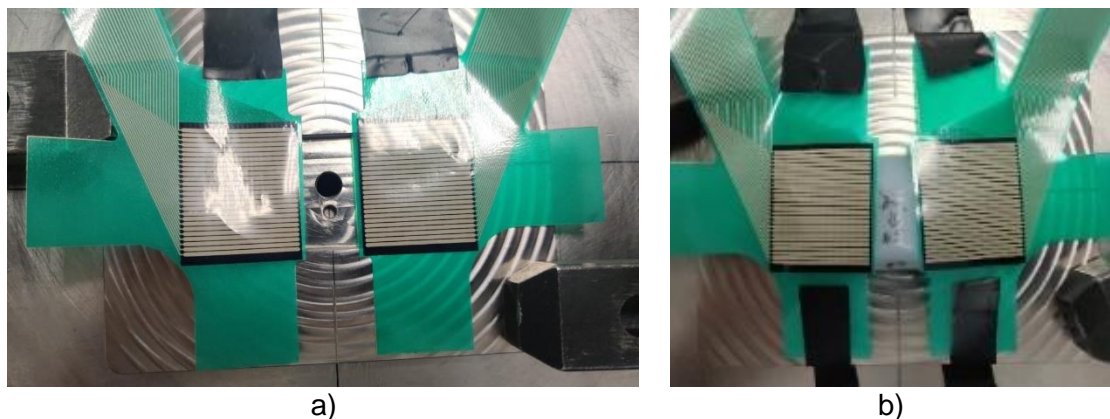
Figure 4.19. During the test setup on the Instron 3366 material testing machine a) at first the Tekscan pressure films taped onto the metal tray fixture (a ruler was used to ensure symmetrical position) then b) tibial insert was placed beneath the pressure films.

Dial height gauge measurements were used to measure plastic deformation of the tibial insert at the dwell point (see Figure 4.21). Plastic deformation was observed by measuring height at the same point before and immediately after loading with the Instron machine. To ensure measurement repeatability, the height gauge was used in a combination with a 3D printed fixture. Both the height gauge and the 3D printed fixture were clamped to the measuring table (see Figure 4.20). The 3D printed fixture had a cut-out to exactly match the bottom face of the tibial insert. At first, the insert was placed inside the 3D printed fixture and then positioned under the height gauge to find the dwell point. Once the lowest point was found on the lateral articulating surface, the 3D printed fixture was fixed in place with two clamps. When placed inside the 3D printed fixture, the tibial insert bottom face was laid flat on the measuring table. The 3D printed fixture only supported the side walls and did not affect the height of the tibial insert, since tibial insert was in contact with the table.

The height gauge accuracy was ±5 µm. Before testing, the height gauge measurement repeatability was confirmed with slip gauges. It was observed that the height gauge was always adding 0.01 mm to the nominal height of the slip gauge. After each measurement, the height gauge would always return to 0.00 mm height when lowering the plunger on the measuring table.
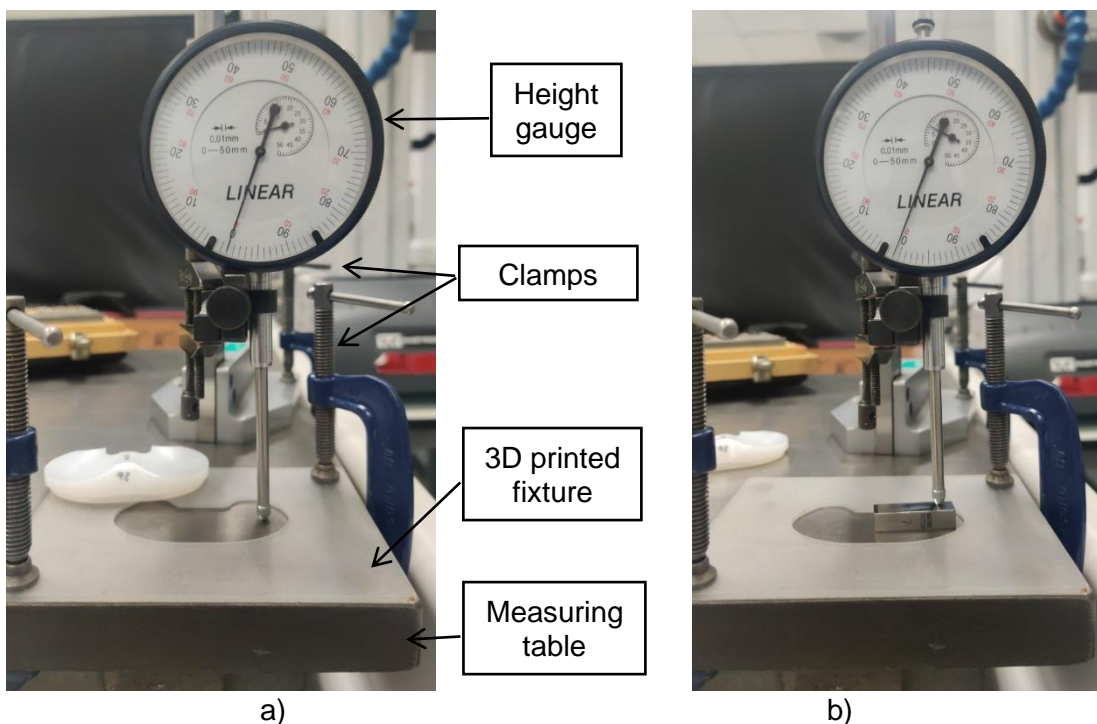
Figure 4.20. Example images of height gauge measurement at a) the table height (dial shows 0.00 mm) and b) the 7mm slip gauge height (dial shows 7.01 mm).

Figure 4.21. Example image of pre-test height gauge measurement of the lateral dwell point of the tibial insert (dial shows 7.010 mm).

After measuring the tibial insert height before loading, the tibial insert was placed in the Instron machine into the tibia tray fixture (see Figure 4.19b). Then the Tekscan pressure film was placed in between the insert and the femoral component to allow contact pressure measurements.

The femoral component was attached to Instron load cell. Instron was equipped with a 10 kN load cell with force accuracy ±1% of reading. During the compression test, the femoral component was aligned at 0° flexion and with the most distal points on the femoral condyle surface resting on the lowest points on the insert surface (see Figure 4.22). The insert was pre-loaded with a 10 N force for 60 seconds. Then the compressive force was ramped up to 5480 N [21] at the displacement rate of 1.3 mm/min [132]. A peak force of 5480 N was chosen, as it was the highest axial force ("Peak-100kg" jogging load) from all OrthoLoad "Standard Loads Knee Joint" data sets [21]. After reaching 5480 N, the force was immediately ramped down to 10 N at the rate of 1.3 mm/min and held for 60 seconds, after which the insert was immediately unloaded and removed. The 60 second hold was chosen as a precaution to have additional data before and after the loading to observe if the Instron machine can maintain the required loading. The applied loading profile is shown in Figure 4.23.

Tekscan sensitivity was set to "Low-3" to record the full pressure range without oversaturation. Both Instron load cell and Tekscan sensor recordings were started simultaneously and were performed at 50 Hz frequency. After testing, the Instron data was checked to find the exact frame number at which the force of 5480 N was applied. Then Tekscan recording was checked on the I-scan software, and the same frame was calibrated with force of 5480 N.
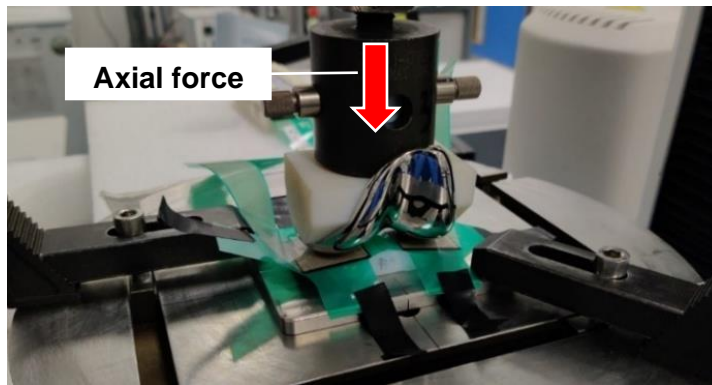
Figure 4.22. Axial compression test setup with Instron 3366 material testing machine and Tekscan pressure film.
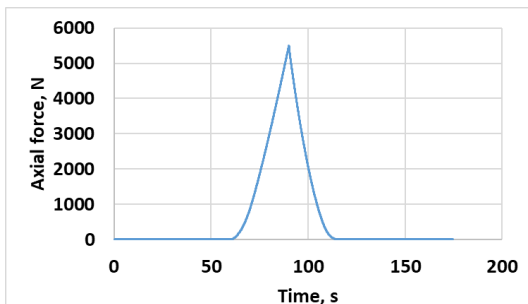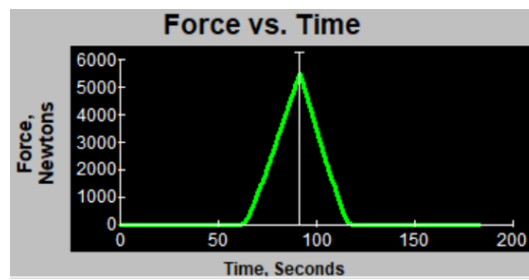
a) Instron 3366 plot   b) Tekscan plot

Figure 4.23. Example plots of a) Instron 3366 and b) Tekscan force versus time measurement.

Immediately after completing the single loading profile with Instron, the tibial insert was placed back under the height gauge (see Figure 4.24). The height was re-measured after several time interval, approximately after 30 minutes, 1 hour, and 17 hours [149], to check if the plastic deformation has remained.

a) Height before loading is 7.01 mm.

b) Height immediately after loading is 6.98 mm.

c) Height one hour after loading remained 6.98 mm.

Figure 4.24. Example images of tibial insert height measurement at the lateral dwell point a) before loading b) immediately after loading, and b) one hour after loading. of pre-test height gauge measurement of the lateral dwell point of the tibial insert (dial shows 7.010 mm).

4.2.11.1   Results

The test was performed on two unused tibial insert specimens (insert No. 5 and insert No. 6). No more than two specimens were used, because the Tekscan results looked similar between the two specimens, which indicated that the test method is repeatable. Height gauge measurements were used to calculate tibial insert plastic deformation, and Tekscan measurements were used to measure contact pressure and contact area. Result summary is shown in Table 4.7.

4.2.11.1.1 Height gauge results

The heigh gauge measurements showed that plastic deformation can occur even after a single loading cycle, as it was predicted by the static FEA model (see Figure 4.25e). The height gauge measurements showed that both tibial insert specimens (No. 5 and No. 6) were plastically deformed by 0.030 mm (height gauge accuracy ±0.005 mm) at the lateral dwell point (see Table 4.6) immediately after loading with the Instron machine. The height measurements were repeated at multiple time points, but no change in height due to elastic relaxation was observed either after 1 hour or 24 hours. Static FEA model predicted plastic deformation 0.038 mm (mesh convergence accuracy ±0.001 mm), which differ by 21% from the experimental results.

a) Insert No. 5. Undeformed= 7.010 mm.   b) Insert No. 5. Deformed= 6.980 mm.   c) Insert No. 6. Undeformed= 7.005 mm.   d) Insert No. 6. Deformed= 6.985 mm.

e)
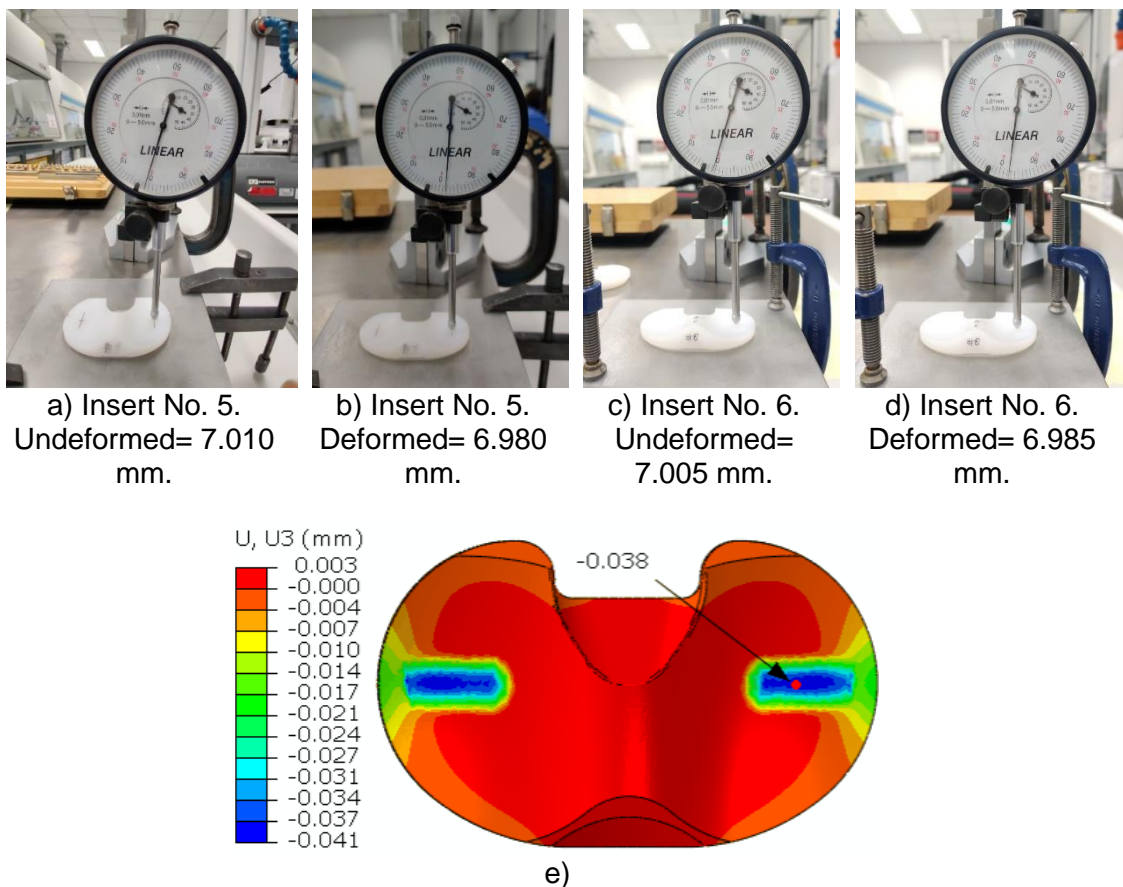
Figure 4.25. Lateral dwell point (red dot) height measured a,b) on insert specimen No. 5, c,d) on insert specimen No. 6 before and after loading with 5480 N on the Instron machine, and e) plastic deformation predicted by static FEA model.

Table 4.6. Permanent plastic deformation measured at the lateral dwell point, which was caused by a single cycle loading with 5480 N force.

	Plastic deformation measured at the lateral dwell point, mm		
	FEA prediction	Insert No. 5	Insert No. 6
Immediately after test	0.038	0.030	0.030
After 30 min	-	0.030	0.030
After 1 hour	-	0.030	-*
After 24 hours	-	-*	0.030
Difference from FEA	0%	21%	21%

*Note: measurement was not taken.

4.2.11.1.2 Tekscan results

The Tekscan pressure film measurements showed a good agreement with the static FEA model prediction (see Figure 4.26). The peak contact pressure for inserts No. 5 and No. 6 was 32.4 MPa and 31.9 MPa respectively at the far edge under the lateral. The static FEA model predicted a peak contact pressure of 33.92 MPa (mesh convergence accuracy ±1.22 MPa) at the far edge under the medial condyle, which differed from the experimental test by 4% and 6% respectively. The total contact area measured on inserts No. 5 and No. 6 was 269 mm^2 and 263 mm^2 respectively. Literature shows that Tekscan 4000 sensor could overestimate contact area by 11.7% to 20.0% [150]. The static FEA model predicted a contact area of 242 mm^2, which was lower than the experimental test by 10% and 8% respectively.

a) Insert No. 5 loaded with 5480 N

b) Insert No. 6 loaded with 5480 N

c) static FEA model loaded with 5480 N
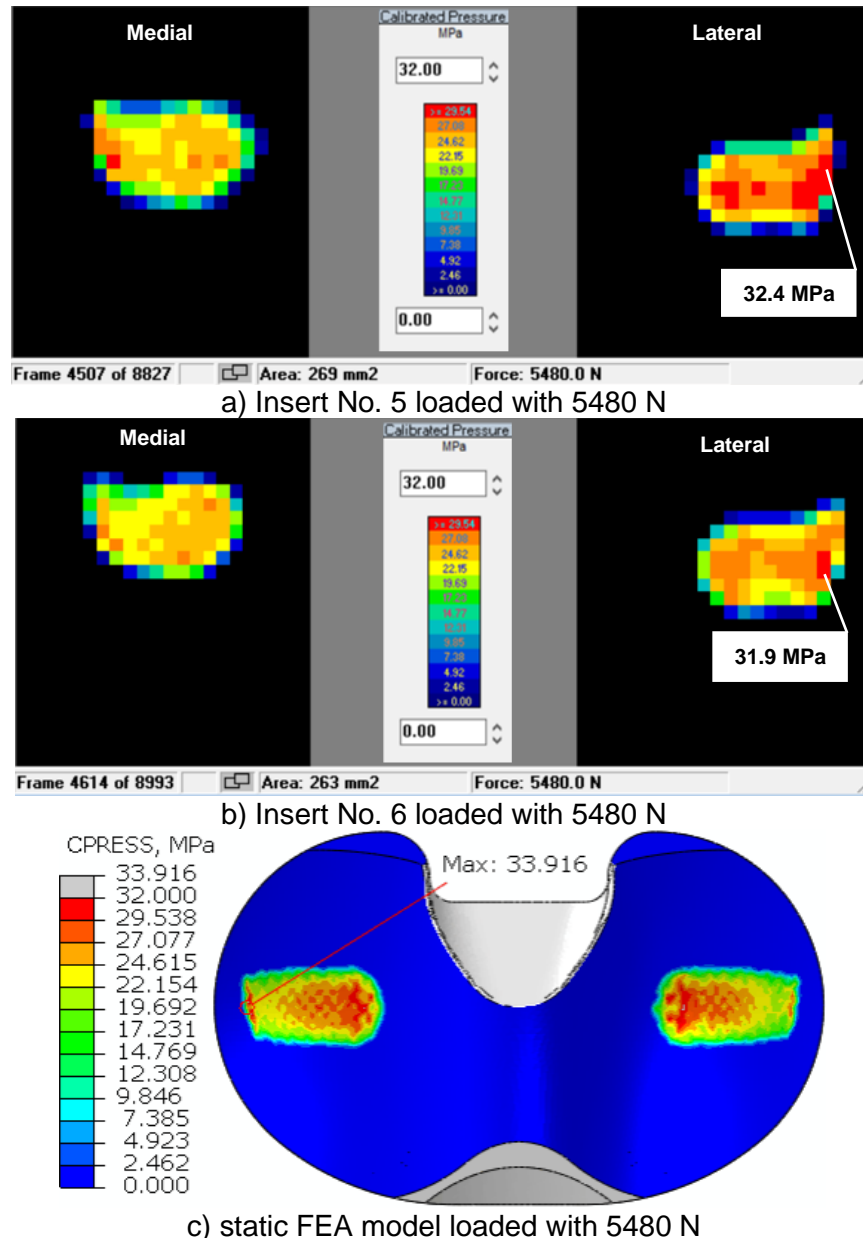
Figure 4.26. Contact pressure measured with the Tekscan K-Scan 4000 pressure film on a) insert No. 5, b) insert No. 6, and c) predicted by the static FEA model.

Both Tekscan and static FEA pressure contour plots showed similar contour geometry (see Figure 4.27). Tekscan pressure contour plots also showed pressure distribution, which was similar to the FEA predictions. In particular, Tekscan films recorded peak pressure points on the far medial and far lateral side of the tibial insert, which was also predicted by the FEA model and was indicating the edge loading effect.
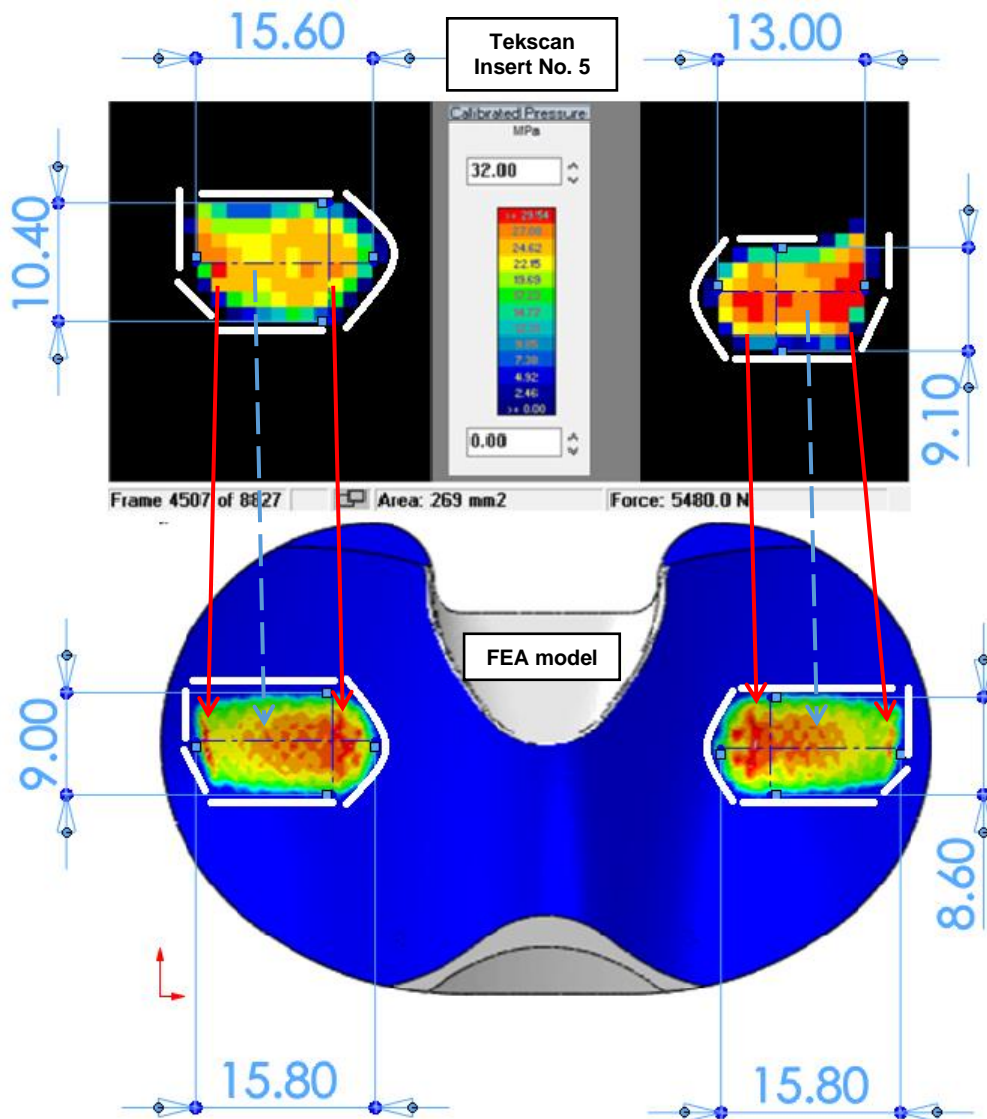
Figure 4.27. Comparison of contact pressure contour maps between Tekscan (insert No. 5) measurement and static FEA prediction. White lines outline the approximate contour geometry. Red arrows indicate the locations of peak pressure points. Blue dashed arrows point out that the central area has lower pressure. Note: images were scaled to the same size and measured in SolidWorks.

Table 4.7. Comparison of experimental measurements and static FEA predictions.

	Total contact area, mm²	Difference from FEA	Max contact pressure, MPa	Difference from FEA	Z-axis displacement, mm	Difference from FEA
Insert No. 5	269	10%	32.4	4%	-0.030	21%
Insert No. 6	263	8%	31.9	6%	-0.030	21%
Static FEA prediction	242	-	33.9	-	-0.038	-

4.2.11.2   Discussion

The test results showed good agreement between the static FEA model predictions and the experimental measurements.

Firstly, the static FEA model predicted a unique loading pattern with edge loading on the far medial and lateral side, which was also experimentally observed on Tekscan film measurements with both specimens. The Tekscan pressure contour closely replicated the predicted contact contour and the contact area differed by no more than 10% from the static FEA prediction. Tekscan sensors are prone to overestimate the area, because even if a small corner is pressed, the entire sensel square will be used in area calculation. Literature shows that K-scan 4000 film could overestimate contact area up to 20% [150], therefore the FEA prediction falls within this range. Additionally, the Tekscan film resolution is limited by square sensels with size of 1.3x1.3 mm. The FEA model provided a higher resolution because it used a quadratic shape function with an intermediate node, therefore all nodes were approximately within 0.65 mm distance between each other.

Secondly, the peak contact pressures for both insert specimens differed by up to 6% from the static FEA prediction. The Tekscan sensors showed smaller pressure, which could be related to the overestimation of the contact area. Other studies have achieved results within 10% of the predicted value for contact area and contact pressure measurements [121, 151].

Thirdly, the laboratory experiment measured 30 μm deformation with +/-5 μm accuracy, which was close to the static FEA prediction of 38 μm. This FEA model was considered as being sufficiently accurate since it predicted plastic deformation at a micron scale, which was experimentally confirmed. In comparison, a different study achieved 8% accuracy by implementing a dynamic nonlinear viscoelastic FEA model with time-dependent relaxation [152].

The proposed static FEA model was considered to be valid for the intended purpose, which is to guide design decisions before performing laboratory tests. The FEA predictions were close to the laboratory experiment results and showed realistic deformation pattern, which indicate that appropriate material properties were chosen. Therefore, this FEA model was further used to analyse different changes in the implant geometry or different loading scenarios.

4.2.12   Sensitivity study of insert bottom support

Whilst performing the experimental test, a small gap was noticed between the metal tibial tray fixture and the bottom side faces on the tibial insert (see Figure 4.28).
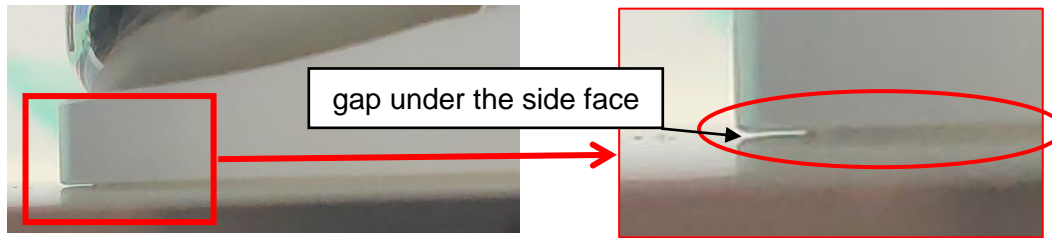
Figure 4.28. Example image of the gap between the top surface of the metal tray fixture and the bottom surface of the tibial insert side wall. The red circle highlights that the gap can be seen across the entire with of the tibial insert.

The gap height was approximately 0.2 mm, when the tibial insert was unloaded. However, when insert was loaded with force of 5480 N, the gap height reduced to approximately 0.1 mm (see Figure 4.29). Similar gap sizes of 0.15 to 0.20 mm were observed also when tibial inserts were fitted inside the tibial trays. Such gap size was reasonable, since it is commonly acceptable to manufacture parts with a fine tolerance of 0.1 mm when trying to achieve dimensions between 6 to 30 mm [153, 154].

| a) | b) |
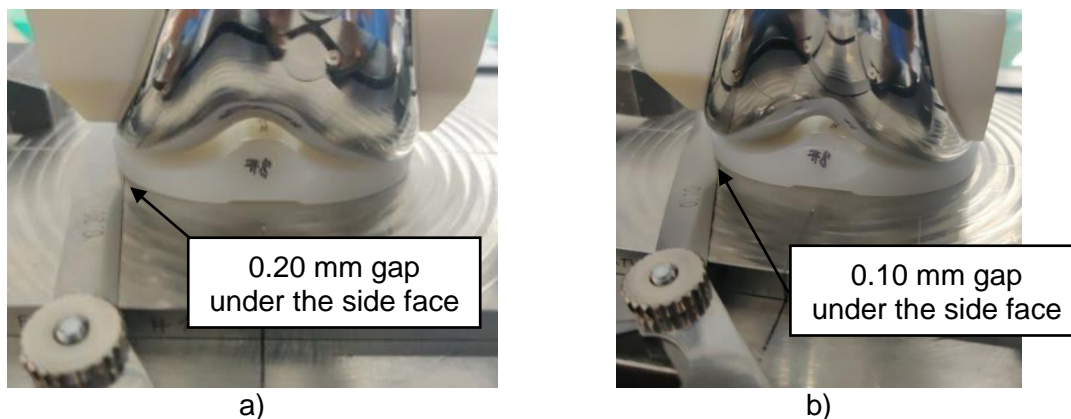
Figure 4.29. Feeler gauge measurements at the gap between the top surface of the metal tray fixture and the bottom surface of the tibial insert side wall, showed gap size of a) 0.20 mm when loaded with 10 N and c) 0.10 mm when loaded with 5480 N.

A sensitivity study was performed to analyse whether boundary conditions with different gap height could change FEA model results. Four FEA models were created to simulate different supports provided by the metal tibial tray: no support under the side face (see Figure 4.30a), with 0 mm gap, with 0.05 mm gap, and with 0.10 mm gap (see Figure 4.30b-c). In order to simulate a gap between the top surface of the tibial tray, an analytical rigid plane (modelled as a circle) was created and positioned below the tibial insert (see Figure 4.30c,d). A second surface-to-surface contact pair was

created between the side face of the tibial insert and the rigid plane, which used contact properties already defined for the femoral component.

a) no support below the side face
(taken from Figure 4.9).

b) 0 mm gap.

c) 0.05 mm gap.
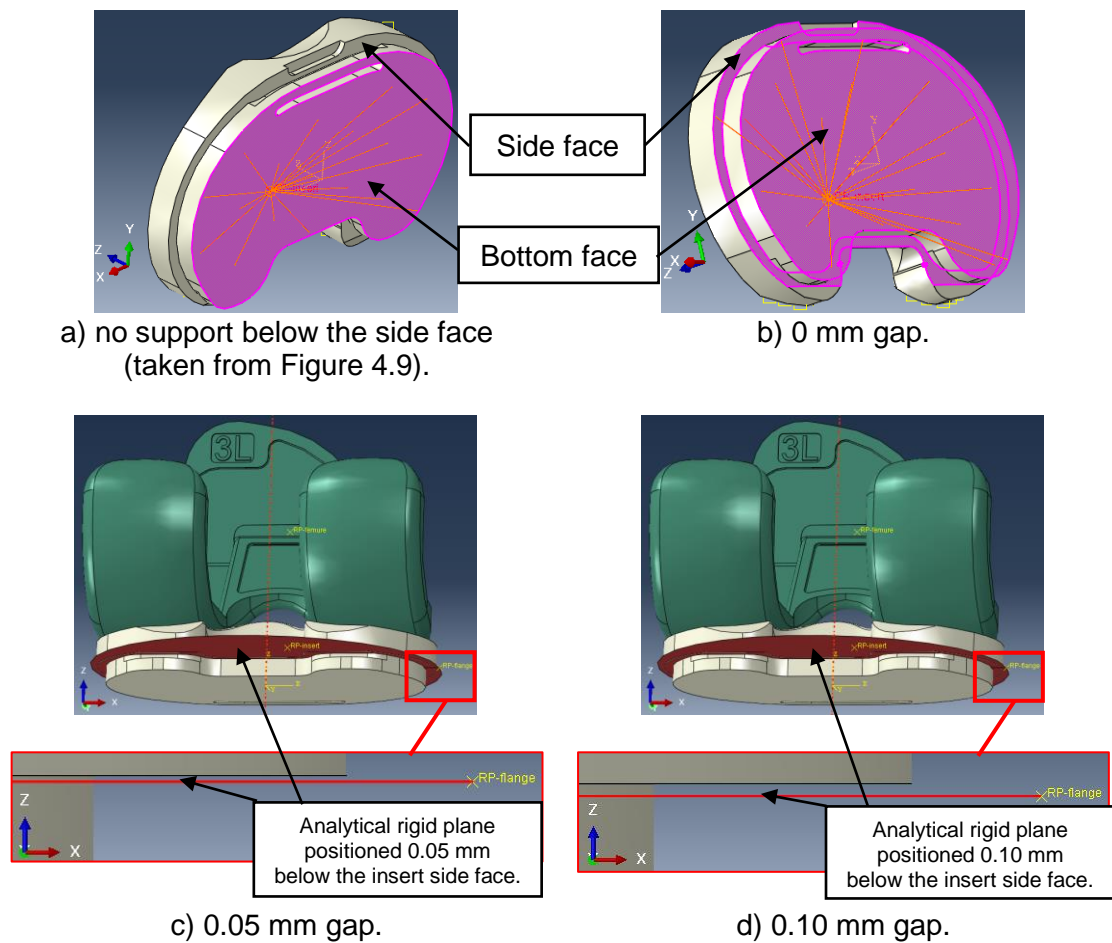
d) 0.10 mm gap.

Figure 4.30. FEA model sensitivity study was performed with four different boundary conditions mimicking the support provided by the tibial tray, where the tibial insert had a) no support b) 0 mm gap, c) 0.05 mm gap, and d) 0.10 mm gap below the side face. In all models the bottom face of the tibial insert was fully fixed.

The sensitivity analysis for boundary conditions with no support, 0 mm gap, 0.05 mm gap, and 0.10 mm gap below the side face showed peak contact pressure of 33.9 MPa, 39.6 MPa, 35.2 MPa, and 33.9 MPa respectively. Identical contact pressure contour plot was shown for the boundary condition with no support (Figure 4.31a) and with 0.10 mm gap below the side face (Figure 4.31d).

a) With no support.
(same as Figure 4.26c)

b) With 0 mm gap.

c) With 0.05 mm gap.
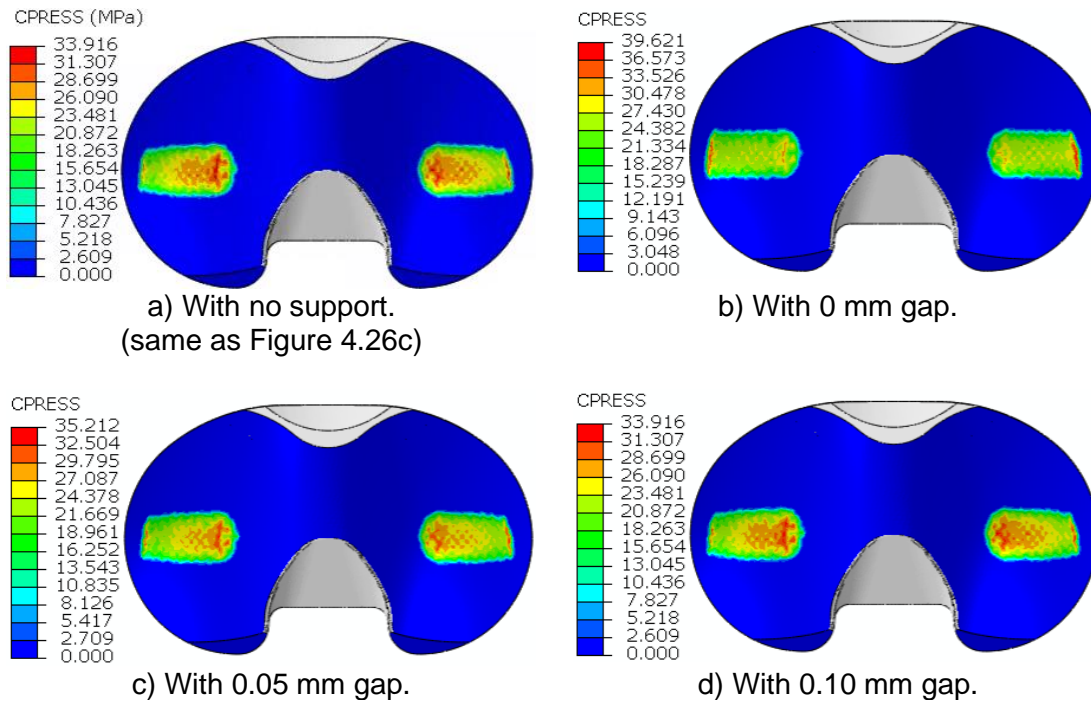
d) With 0.10 mm gap.

Figure 4.31. Sensitivity study results showing contact pressure (unit: MPa) for different boundary conditions when the tibial insert had a) no support b) 0 mm gap, c) 0.05 mm gap, and d) 0.10 mm gap below the side face.

The FEA models with 0.05 mm and 0.10 mm gap revealed deformation of the tibial insert side walls (see Figure 4.32). Furthermore, the model with 0.05 mm gap showed that the gap gets completely closed by compressing the tibial insert against the top face of the tibial tray (see Figure 4.32a), whilst the models with a 0.10 mm gap retained a small gap when loaded with 5480 N, showing a deformation similar to experimental observations in Figure 4.29. This could explain why the model with no support and with 0.10 mm gap showed smaller peak contact pressure. Since the side face of the tibial insert was not restricted, the tibial insert had a free space to deform, which would allow the insert to conform better with the femoral condyle geometry, thus reducing the contact pressure.
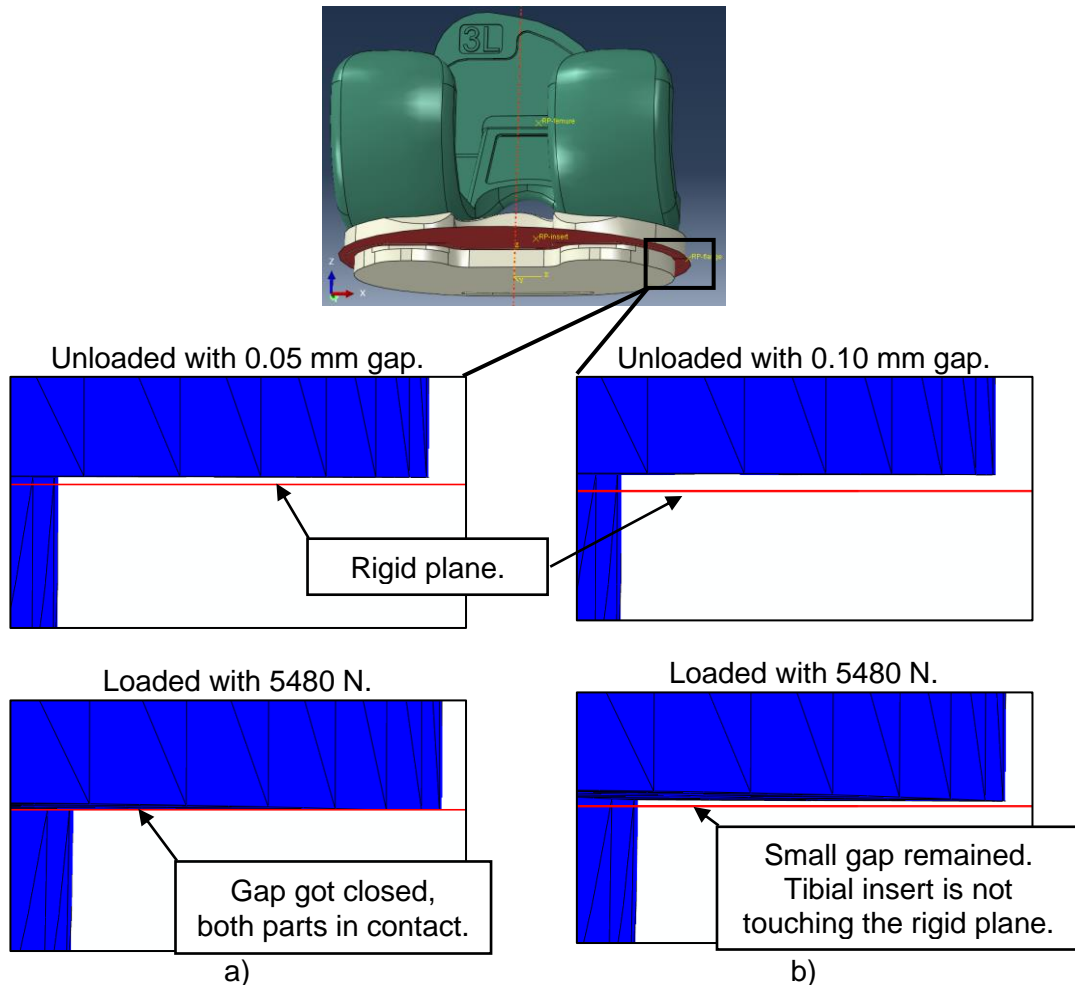
Figure 4.32. Enlarged FEA model side view visualising the gap closure at the bottom side face on the tibial insert with a) full gap closure for the 0.05 mm gap and d) partial gap closure for the 0.10 mm gap after applying force of 5480 N.

The sensitivity study showed that models with a gap of 0.10 mm or higher provide results similar to the experimental measurements under axial loading. The use of 0.10 mm or higher gap did not affect the results for the static FEA model. However, in the more advanced FEA models with daily activity loading the tibial insert could show even larger deformation of the side face. Therefore, a gap of 0.20 mm (as experimentally observed in Figure 4.29a) will be implemented in the further FEA with daily activity loading.

4.2.13   Limitations

The plastic deformation validation was limited to one measurement point (at the tibial insert dwell point). This validation method with a dial height gauge provided a benefit of a quick measurement with accessible measuring tool. However, dial gauge measurements are susceptible to human error, for example, if the dial gauge is

accidentally moved or the gauge tip is rapidly released, causing the dial tip to penetrate the tibial insert surface and cause additional deformation. Therefore, this method could be further improved by performing CMM measurement of the entire tibial insert surface, since CMM can control the applied force, have higher accuracy, and can measure the entire tibial insert geometry.

The contact pressure validation was limited by the resolution of Tekscan 4000 film with a sensel size of 1.3 mm^2. Unfortunately, Tekscan does not provide pressure films with a smaller sensel size which could also resist the required contact pressure of around 40 MPa.

The material properties of UHMWPE could vary due to various factors described in section 1.6.2.3. The static FEA model could be further improved by performing sensitivity study with various material properties, for example, by repeating the FEA simulations with different true stress-strain data from available literature shown in Figure 1.28. However, ideally material properties should be obtained by performing experimental tensile tests with the exact material sample.

Further studies could implement additional validation method by comparing experimental and computational strain results.

Static FEA model validation is useful to quickly assess the material properties and FEA input parameters. However, static FEA model does not fully represent the dynamic loading conditions, where inertia and change in loading rate could affect the results. Additionally, the static FEA material model does not consider the viscoelastic properties of UHMWPE, which could also affect the deformation predictions.

4.2.14   Conclusion

In order to obtain realistic predictions with FEA it is important to perform FEA validation with experimental tests. This chapter described a testing method for axial compression of TKR, which allows validation of static FEA models for contact pressure and plastic deformation. When compared to the experimental results the static FEA model predicted peak contact pressure with 6% accuracy, contact area with 10% accuracy, and plastic deformation at the dwell point with 21% accuracy. The static FEA model also showed realistic deformation patterns which were observed during the laboratory experiment.

During FEA sensitivity analysis it was discovered that it is important to model the gap between the side faces of the tibial insert and the tibial tray. During experimental testing it was observed that the height of the side gap is reduced due to tibial insert

deformation. The static FEA model predicted that the tibial tray restricts insert deformation and therefore affects the stress and deformation patterns.

4.3 Daily activity FEA knee models for knee simulator

When designing new medical products, it is important to consider worst-case scenarios by modelling various daily activities at high loading conditions. Therefore, FEA modelling was used to analyse TKR performance during a full gait cycle of seven daily activities (walking, jogging, pivot turn, crossover turn, stairs ascend, stair descend, and sit to stand to sit). FEA models replicated standardised loading conditions used for the knee simulator. Further details of the simulator set-up are described in Chapter 8. The FEA models of daily activities recreated test conditions published by the ISO 14243 standards [108, 109], ASTM F3141 standard [49], and OrthoLoad data base [155]. Daily activity scenario for walking in displacement control per ISO 14243-3 was performed with static FEA. Per ISO 14243-3 the tibial insert motion was controlled by applying A-P displacement and I-E rotation.

The remaining daily activity scenarios required simulations in load control instead of displacement control. The load control scenarios controlled tibial insert motion by applying A-P force, and M-L force, and I-E torque with additional non-linear springs to simulate soft tissue constraints. The contact mechanics for the load control scenarios could not be solved with static FEA, since the static solver could not calculate complex non-linear conditions caused by A-P force, M-L force, and I-E torque in combination with non-linear plastic material properties and non-linear spring constraints.

The remaining daily activity models with dynamic load control parameters were modelled with dynamic FEA. Abaqus allows to create dynamic simulations with explicit or implicit solver. For both the explicit and the implicit solver the equilibrium is defined in terms of the external forces, the internal element forces, and the nodal accelerations. The two solvers mainly differ in the manner how nodal accelerations are calculated. Explicit solver is using mass matrix and is conditionally stable, whist implicit solver is using both stiffness and mass matrix and is unconditionally stable [156]. The explicit dynamic solver is more suitable for dynamic effects caused at high speed and within short time interval, usually in milliseconds, for example, stress wave caused by a blast or impact [157]. The implicit dynamic solver is more suitable for dynamic models at slower speeds and longer time interval of around 1 second and would normally require shorter computational time with stable solutions. The implicit solver is also beneficial because it can be used together with static pre-loading and un-loading steps. In this study the FEA models were not intended to simulate impact conditions, therefore implicit dynamic solver was chosen to simulate the motion of the TKR components

within the knee simulator. A preliminary check showed that dynamic implicit solver results were no different to static solver when simulating ISO 14243-3 in displacement control.

Since dynamic FEA models required large computational resources, the modelling was undertaken on ARC3, part of the High Performance Computing facilities at the University of Leeds, UK [158]. The FEA simulations were run on 12 cores of Intel Xeon E5-2650v4 CPU with 64GB RAM memory [159].

4.3.1 Dynamic FEA input parameters

The dynamic implicit FEA model assembly consisted of three parts: femoral component, tibial insert, and a rigid plane. All dynamic models implemented input parameters and mesh size from the static FEA model (described in Table 4.4). Additionally, all dynamic models were further updated by adding material density to tibial insert, spring constraints, and loading profiles specific for each daily activity. A rigid plane was needed to simulate contact with the tibial tray. Spring constraints were needed to recreate the boundary conditions of a knee simulator testing machine (see Figure 4.33). The rigid plane had 5 cm radius and was positioned 0.20 mm (gap per Figure 4.29a) below the tibial insert side edge to simulate a gap between the tibial insert and the tibial tray.
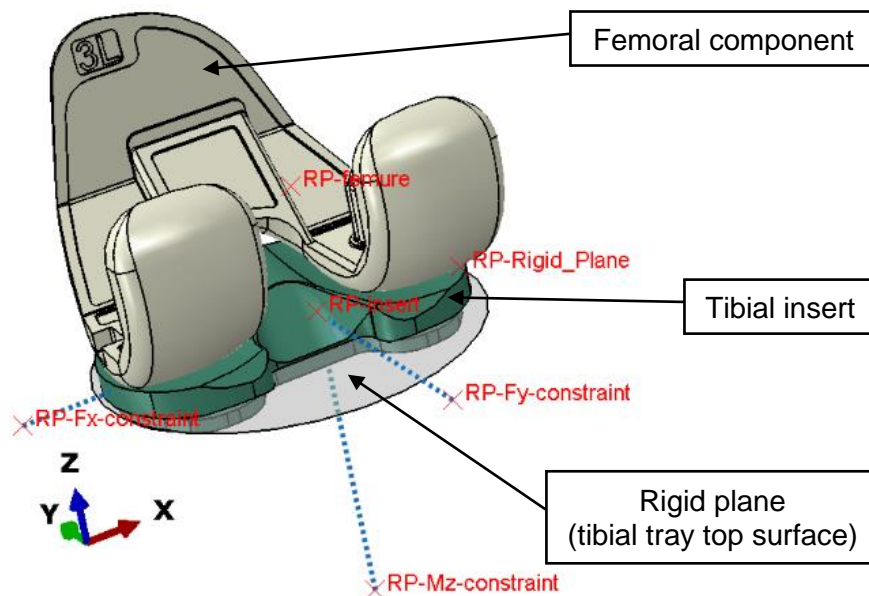
Figure 4.33. Dynamic FEA model representation with assembled parts, reference points, and soft tissue constraints for the cruciate retaining knee implant. Red crosses are the reference points, blue dotted lines are the soft tissue spring constraints.

4.3.2 Step definition

Loading was completed in four steps: pre-displacement, preload, load, and unload. In step 1, the femur was preloaded in displacement control with a downward axial displacement and F-E rotation to initiate the contact between the parts and to align the component as required for each daily activity simulation. In step 2, the femur applied the forces and torques to initiate the load needed for each daily activity simulation. In step 3, an amplitude profile for motion and loading was applied to the tibial insert and the femoral component to simulate one full gait cycle. The loading profile amplitude for ISO models consisted of 101 loading points (from 0 to 1 second with 0.01 s increments) and for ASTM and OrthoLoad models consisted of 201 loading points (from 0 to 1 second with 0.005 s increments). Steps 2 and 3 were defined as implicit dynamic simulation to successfully complete the simulation. In step 4, the femoral component was un-loaded in displacement control to remove any contact between the femoral component and the tibial insert.

4.3.3 Boundary conditions

Reference points (RP) were used to apply motion, loading, and attach spring wires. For ISO FEA models, the femoral component and the tibial insert had a reference point defined per ISO 14243 standard [108, 109]. The femoral component had a reference point defined at intersecting imaginary planes at 30° and 60° of flexion. The tibial insert had a reference point defined directly below the reference point of the femoral component at the height of the dwell point. Both femoral and tibial reference points were offset in the medial direction by 7% of the tibial insert overall M-L width (see Figure 4.34).

For ASTM and OrthoLoad FEA models the centre of rotation for the femoral component and the tibial insert were defined per ASTM F3141-17a [49] standard. The tibial insert had a reference point defined at the height of the dwell point and coaxial with the tibial tray stem. The femoral component had a reference point defined at intersecting imaginary planes at 30° and 60° of flexion and at the midpoint of both condyles (see Figure 4.35).

For both ISO and ASTM models the femoral component was free to move only in the direction of axial translation and F-E rotation. The tibial insert was free to move in the loading directions (A-P translation, M-L translation, I-E rotation, A-A rotation) as specifically required for each ISO and ASTM standard.

a)   b)
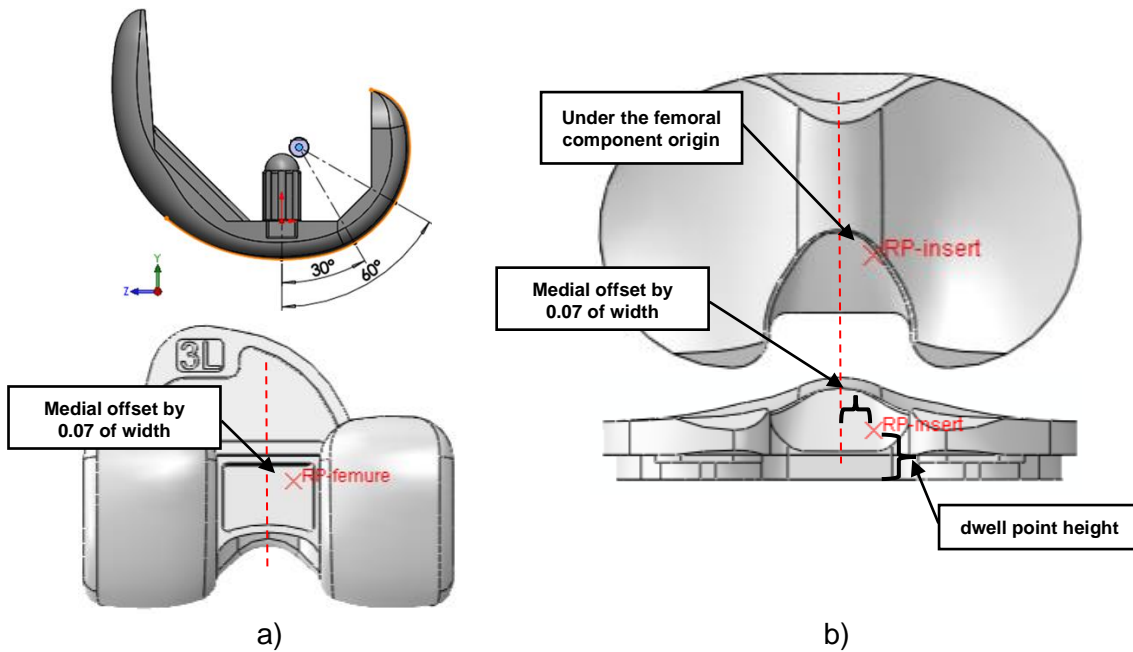
Figure 4.34. Centre of rotation at reference points (RP) for the left a) femoral component and b) tibial insert used for the FEA models per ISO 14243 standard.

a)   b)
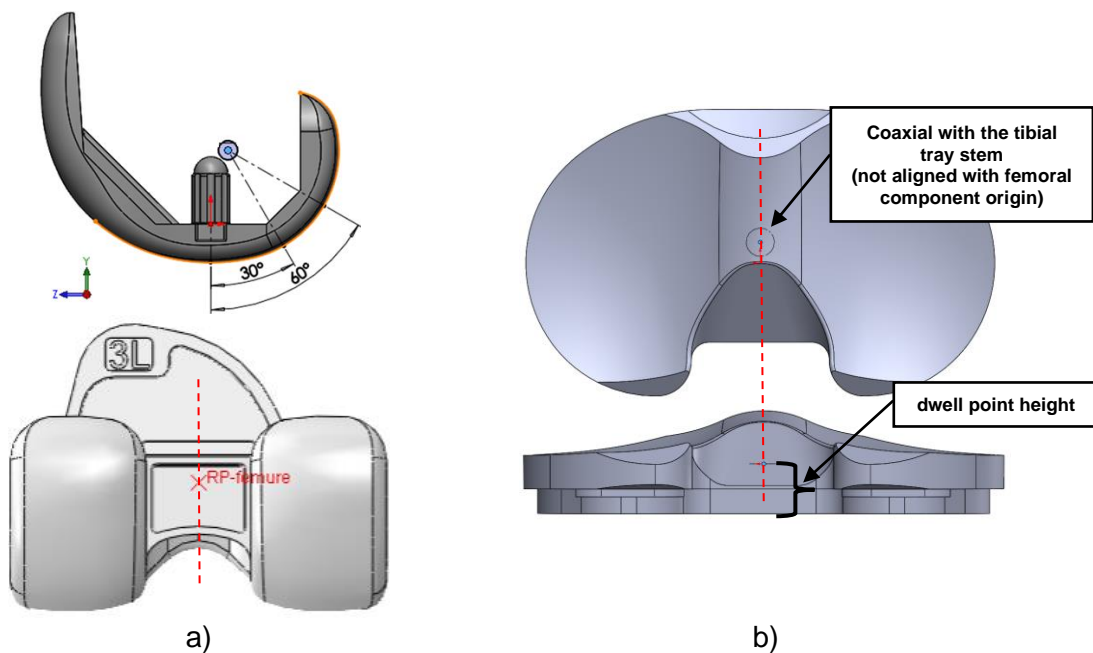
Figure 4.35. Centre of rotation at reference points (RP) for a) femoral component and b) tibial insert used for the FEA models per ASTM F3141-17a standard and OrthoLoad data.

4.3.4 Input profiles for motion and loading

In total nine FEA models were created to simulate loading conditions for various daily activities. Two models recreated ISO 14243-3:2014 [109] and ISO 14243-1:2009 [108] input profiles for walking in displacement and load control respectively. Additional, six input profiles were taken from ASTM F3141-17a [49] to simulate worst case conditions

with heavy loading for a 100 kg subject during walking, pivot turn, crossover turn, stairs ascend, stair descend, and sit to stand to sit. The ninth loading profile for jogging was created by combining OrthoLoad Peak-100kg force and torque data [155] with flexion angle data from Miller et al. 2014 [160]. Standardised loading conditions were chosen, because standards are well described and widely available. The jogging profile was added, because it is an activity with the highest recorded axial force [21].

The ISO and ASTM models simulated only one full gait cycle from heal to heal. The jogging model simulated only the stance phase from heel to toe-off. All nine FEA models replicated loading condition for *in vitro* knee simulator testing and were normalised to 0-100% loading phase with the cycle time of 1 second.

Walking model per ISO 14243-3:2014 [109] was executed as a static FEA model because it had input profile parameters for displacement control. The remaining eight models were executed as dynamic implicit FEA models. The dynamic analysis differs from static by including inertial forces in the equation of equilibrium and by adding damping to the internal forces [161]. The dynamic implicit solver with the default moderate dissipation application tends to improve convergence behaviour without significantly degrading solution accuracy [162].

In order to execute dynamic implicit models a mass density of 9.34×10^{-10} tonne/mm^3 [132] was assigned to the tibial insert made of GUR1020 UHMWPE. To simplify the FEA model, no mass properties were added to simulate femoral component or surrounding fixtures (further described in Section 4.3.7). The dynamic implicit solver added the effect of inertia to the tibial insert; however, the inertia effects were relatively small since the tibial insert had a mass of around 17.25 g (further described in Section 4.3.7). The input profiles for displacement and load control are shown in Figure 4.36 and Figure 4.37 respectively.

a)   b)
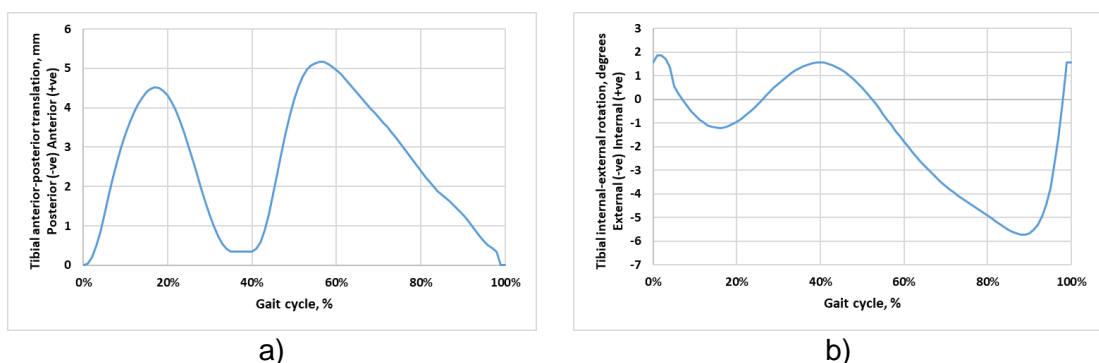
Figure 4.36. ISO 14243-3:2014 displacement control input profile for a) A-P translation and b) I-E rotation.
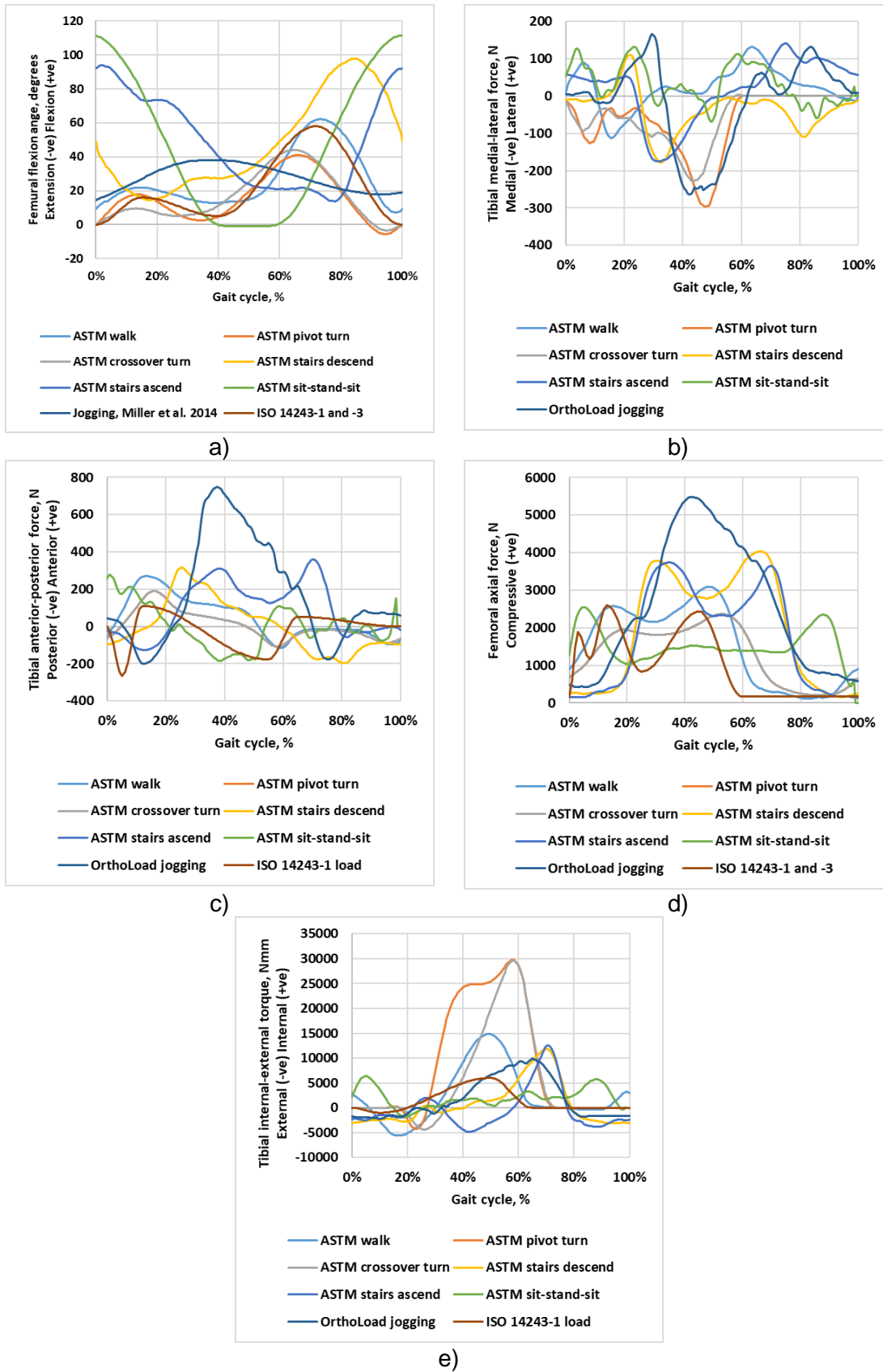
Figure 4.37. Displacement and loading control input profiles for a) flexion angle, b) M-L force, c) A-P force, d) axial force, and e) I-E torque.

4.3.5 Spring definition

All dynamic implicit FEA models required soft tissue constraints, which were modelled as spring constraints for anterior-posterior translation, medial-lateral translation, and internal-external rotation motion. The added springs acted as the soft tissue by preventing the tibial insert from translating or rotating too far, the same way as it is achieved in knee simulator testing machines.

Initially all dynamic FEA models were modelled with soft tissue spring stiffness values defined in ISO 14243-1 standard [108], since ASTM and OrthoLoad data do not define soft tissue constraints. However, whilst running computational simulations, it was discovered that ISO spring profiles do not provide sufficient restrictions when modelling ASTM and OrthoLoad daily activities with high loading. The FEA simulations of ASTM and OrthoLoad daily activities failed, because the femoral component would slip off the tibial insert either in the posterior or medial direction (see Figure 4.38). The observed femoral component dislocation was caused by the applied large forces and torques, which could not be restricted by the ISO [108] defined soft tissue spring constraints.

a) Posterior dislocation   b) Medial dislocation
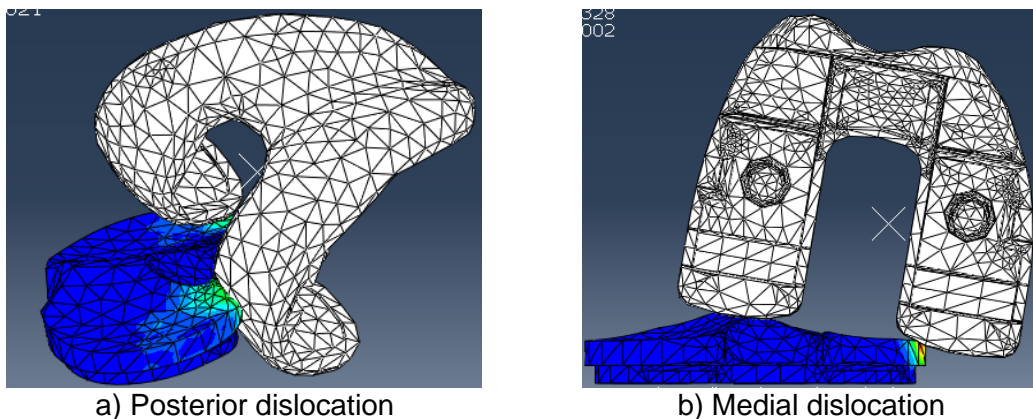
Figure 4.38. Example images of femoral component slipping of the tibial insert in the a) posterior or b) lateral direction when performing FEA models with spring stiffness taken from ISO 14243-1 standard. (Note: mesh size of 5.8 mm was used to reduce computational time when checking for problems in the model.)

Since the applied loading profiles were obtained from OrthoLoad [155] studies with live human subjects, it was considered that the applied loads are realistic. Human subjects in OrthoLoad [155] studies were able to exert high loads without dislocating their joints, which indicated that the soft tissue constraints defined in the ISO 14243-1 standard [108] were unrealistic for high loading scenarios. Therefore, existing literature was researched to find soft tissue constraints which would not allow implant dislocation (see Figure 4.39). Additionally, for all dynamic FEA models an A-P spring gap of ±2.5 mm and I-E spring gap of ±6° was assumed based on the ISO 14243-1:2009 standard [108]. The stair ascent model required an additional M-L spring with spring gap of ±1.5 mm [163]. The applied soft tissue constraints for each dynamic FEA model are listed in Table 4.8.
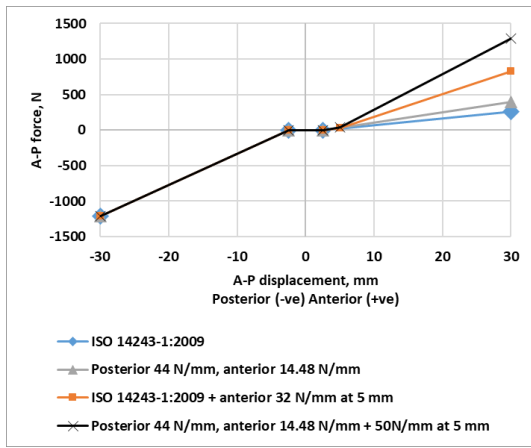
a)
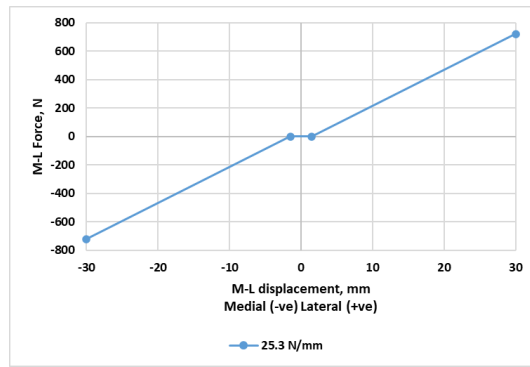
b)
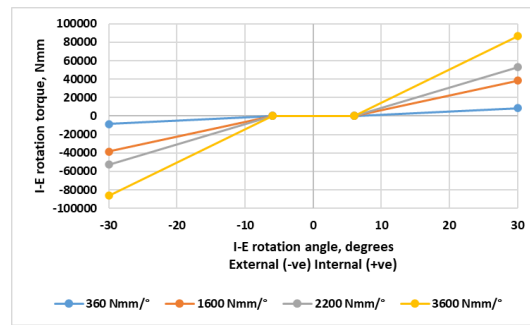
c)

Figure 4.39. Soft tissue constraints were defined with spring stiffness for a)
A-P translation, b) M-L translation, and c) I-E rotation.

Table 4.8. Soft tissue stiffness constraints in A-P, I-E, and M-L direction for all daily activity FEA models (differences from ISO 14243-1:2009 are highlighted in yellow).

Loading profile	A-P translation stiffness N/mm	I-E rotation stiffness Nmm/°	M-L translation stiffness N/mm
Static FEA (displacement control)			
Walking per ISO 14243-3:2014 [109]	None	None	None
Dynamic implicit FEA (load control)			
Walking per ISO 14243-1:2009 [108]	**Anterior:** 0 - 2.5 mm: 0 [108] > 2.5 mm: 9.3 [108] **Posterior:** 0 - 2.5 mm: 0 [108] > 2.5 mm: 44 [108]	0º - 6º: 0 [108] > 6º: 360 [108]	None
Walking (Heavy-100kg) per ASTM F3141-17a [49]			None
Stair ascent (Heavy-100kg) per ASTM F3141-17a [49]			0 - 1.5 mm: 0 [163] >1.5 mm: 25.3 [164]
Stair descent (Heavy-100kg) per ASTM F3141-17a [49]		0º - 6º: 0 [108]	None
Crossover turn (100kg) per ASTM F3141-17a [49]		> 6º: 1600 [165]	None
Pivot turn (100kg) per ASTM F3141-17a [49]	**Anterior:** 0 - 2.5 mm: 0 [108] > 2.5 mm: 14.48 [166] **Posterior:** 0 - 2.5 mm: 0 [108] > 2.5 mm: 44 [108]	0º - 6º: 0 [108] > 6º: 2200 [165]	None
Sit-stand-sit (Heavy-100kg) per ASTM F3141-17a [49]	**Anterior:** 0 - 2.5 mm: 0 [108] 2.5 - 5.0 mm: 9.3 [108] > 5.0 mm: 32 [167] **Posterior:** 0 - 2.5 mm: 0 [108] > 2.5 mm: 44 [108]	0º - 6º: 0 [108] > 6º: 1600 [165]	None
Jogging (Peak-100kg) per OrthoLoad [155], with flexion angle from Miller et al. 2014 [160]	**Anterior:** 0 - 2.5 mm: 0 [108] > 2.5 mm: 14.48 [166] > 5.0 mm: 50 [165] **Posterior:** 0 - 2.5 mm: 0 [108] > 2.5 mm: 44 [108]	0º - 6º: 0 [108] > 6º: 3600 [165]	None

4.3.6 Results of daily activity FEA models

The contact pressure, Von Mises stress, and plastic deformation distribution was different between all nine daily activity FEA models (see Figure 4.40 to Figure 4.43).

Walking simulations with ISO displacement and load control predicted the smallest contact areas and peak contact pressures of 41.2 MPa and 38.2 MPa respectively. All other models, which simulated loads caused by a 100 kg subject, predicted larger contact areas and larger peak contact pressures ranging between 46.7 MPa to 64.9 MPa (see Figure 4.40).
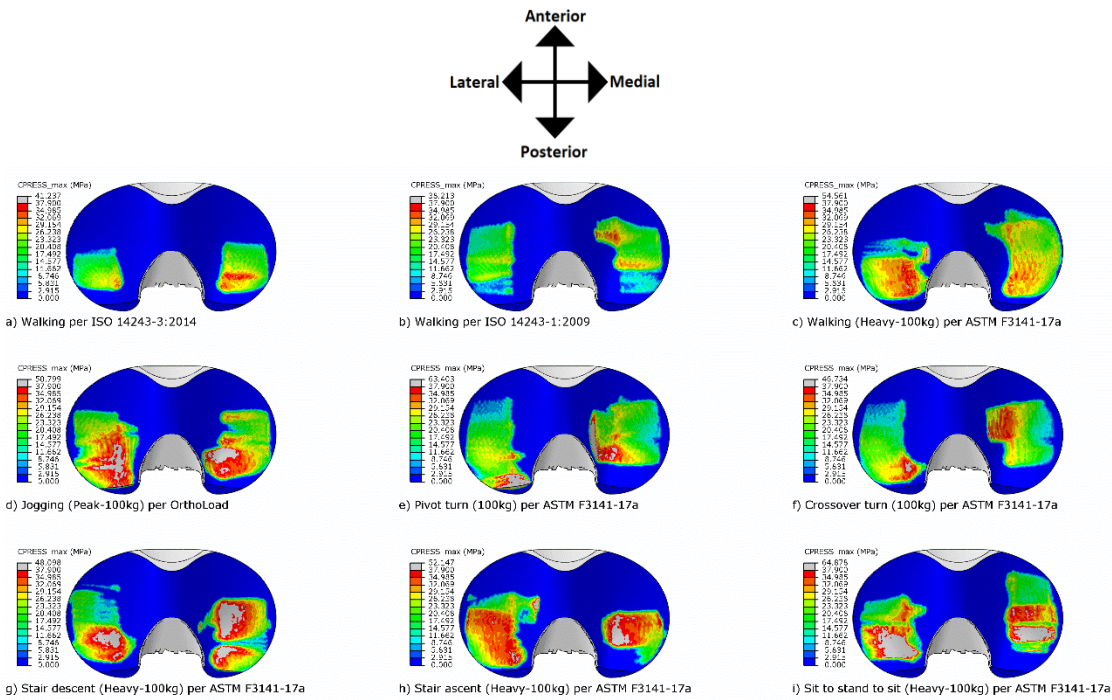
Figure 4.40. Nine daily activity FEA model showing maximum contact pressure (MPa) value overlapping across all frames of one full loading cycle.

Walking simulations with ISO displacement and load control predicted the smallest peak axial plastic deformation of 0.09 mm and 0.04 mm respectively. All other models, which simulated loads caused by a 100 kg subject, predicted larger peak plastic deformation ranging between 0.17 mm to 1.04 mm (see Figure 4.41).
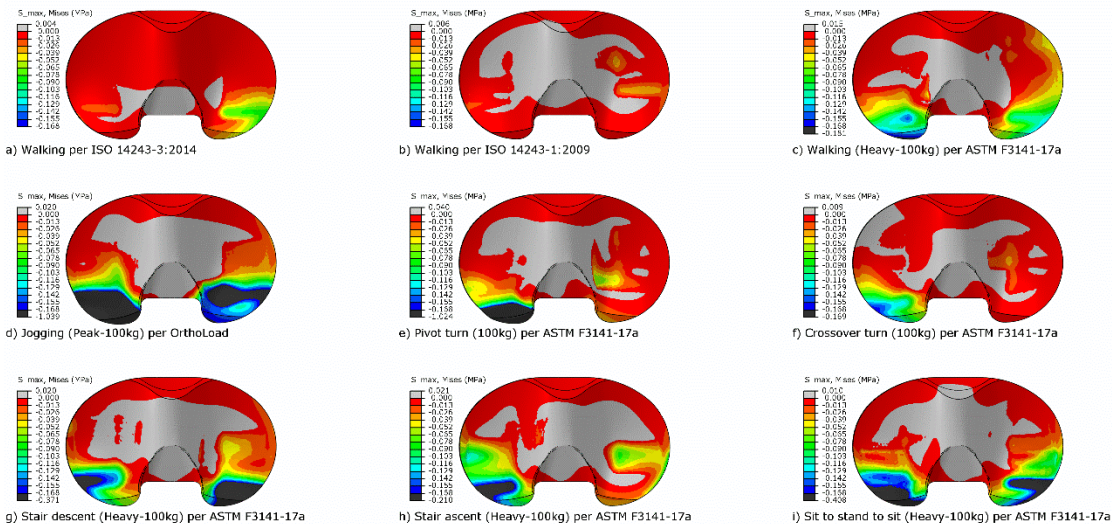
Figure 4.41. Nine daily activity FEA model showing axial plastic deformation (mm) after completing one full loading cycle and un-loading.

Walking simulations with ISO displacement and load control predicted the smallest peak Von Mises stress of 24.2 MPa and 22.2 MPa respectively. All other models, which simulated loads caused by a 100 kg subject, predicted larger peak Von Mises stress ranging between 26.7 MPa to 45.4 MPa (see Figure 4.42).
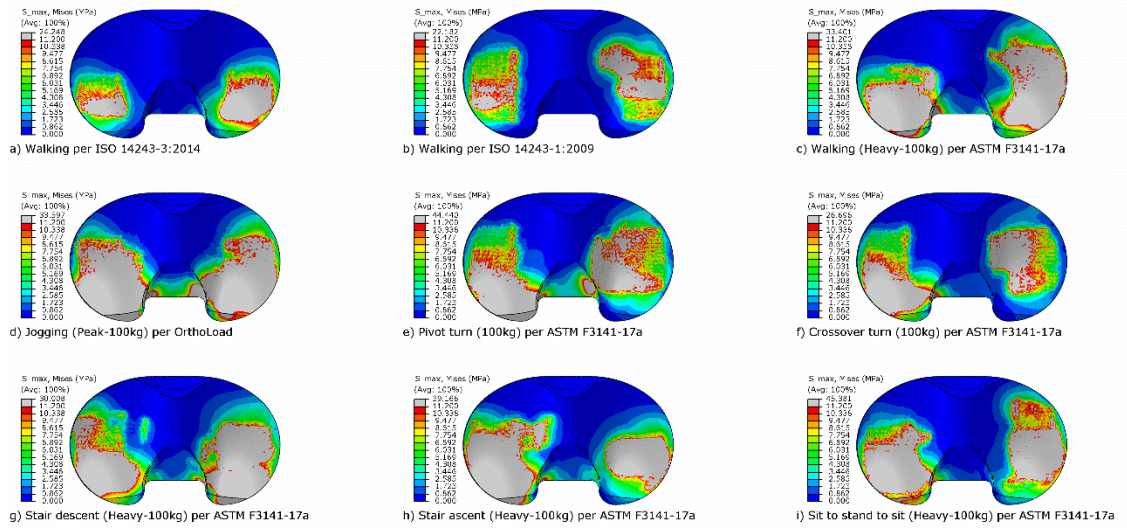
Figure 4.42. Nine daily activity FEA model showing maximum Von Mises stress (MPa) value overlapping across all frames of one full loading cycle. The grey area shows values above the true yield stress of 11.2 MPa.

A video was created to simultaneously visualise a full loading cycle synchronized for all nine daily activity FEA models. Example frame images at 0%, 25%, and 50% loading cycle for contact pressure are shown in Figure 4.43.

Video 1 shows the contact pressure contour plot for every 0.5% increment of the full loading cycle. These are the same contour plots, which were overlapped and shown in Figure 4.40. Video 1 allows to observe the full range of motion for the tibial insert and contact pressure differences at specific frames, which visualises the differences between the nine daily activity loading cycles.

It can be observed that FEA models per ASTM standard display larger tibial insert translation and rotation compared to the ISO standard. Furthermore, the ASTM models apply loading closer to the intercondylar area of the tibial insert, which is relevant to analyse for the proposed tibial insert modification with a drilled hole at the intercondylar area. The ISO and ASTM models show large differences, since ASTM models apply larger loads and also add an additional M-L force component. Consequently, all of the ASTM models show higher contact pressure values compared to ISO models. Some of the ASTM models even show areas of point loading, which were caused by the M-L force (see stair ascent at 0% and 85% gait).
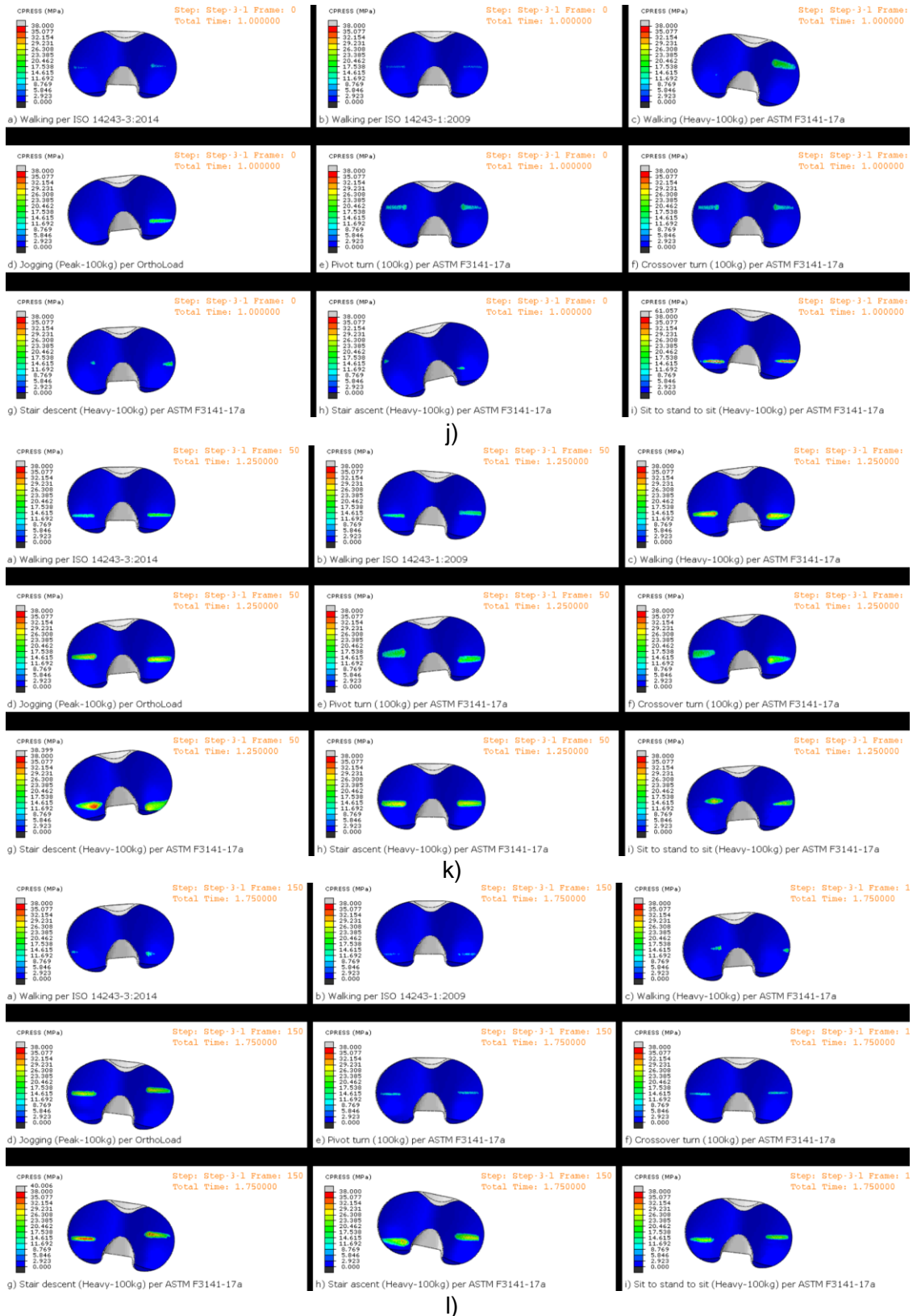
Figure 4.43. Contact pressure (MPa) comparison for 9 daily activity FEA models at j) 0%, k) 25%, and l) 50% of loading cycle. Full loading cycle is shown in a separate video file named "Video 1, CPRESS, original unmodified tibial insert, GMK Primary size 3 left.avi".

The computational time for all daily activity FEA models ranged between 4 to 96 hours (see Table 4.9). The total computational time for all nine models was approximately 457 hours.

Table 4.9. Computational time required to execute daily activity FEA models with mesh size of 1.3 mm.

Loading profile	Hours
Walking (displacement control) per ISO 14243-3:2014 [109]	4
Walking per ISO 14243-1:2009 [108]	32
Pivot turn (100kg) per ASTM F3141-17a [49]	33
Crossover turn (100kg) per ASTM F3141-17a [49]	37
Jogging (Peak-100kg) per OrthoLoad [155], with flexion angle taken from Miller et al. 2014 [160]	47
Sit-stand-sit (Heavy-100kg) per ASTM F3141-17a [49]	67
Stair ascent (Heavy-100kg) per ASTM F3141-17a [49]	70
Stair descent (Heavy-100kg) per ASTM F3141-17a [49]	72
Walking (Heavy-100kg) per ASTM F3141-17a [49]	96
Total:	457 hours ≈ 19 days

4.3.7 Sensitivity analysis of inertia effect

In this study, to simplify the FEA models, no mass was added to the femoral component and the surrounding fixtures to simulate the inertia effects in the knee simulator. However, a sensitivity study was performed with one model (ISO 14243-1 in load control) to visualise the potential effect of added mass.

Only one parameter was changed, by increasing the density of tibial insert from 9.34×10^{-10} tonne/mm^3 to 2.71×10^{-7} tonne/mm^3 to change tibial insert component mass from 17.25 g to approximately 5 kg. The 5 kg represented the approximate mass of knee simulator fixtures under the tibial insert. This FEA model did not simulate realistic mass distribution, it only served as an example to analyse the potential inertia effect.

4.3.7.1 Results

FEA model with the artificially added 5 kg mass showed larger areas of applied contact pressure, Von Mises stress, and plastic deformation, which were expanded both in A-P and M-L direction (Figure 4.44).
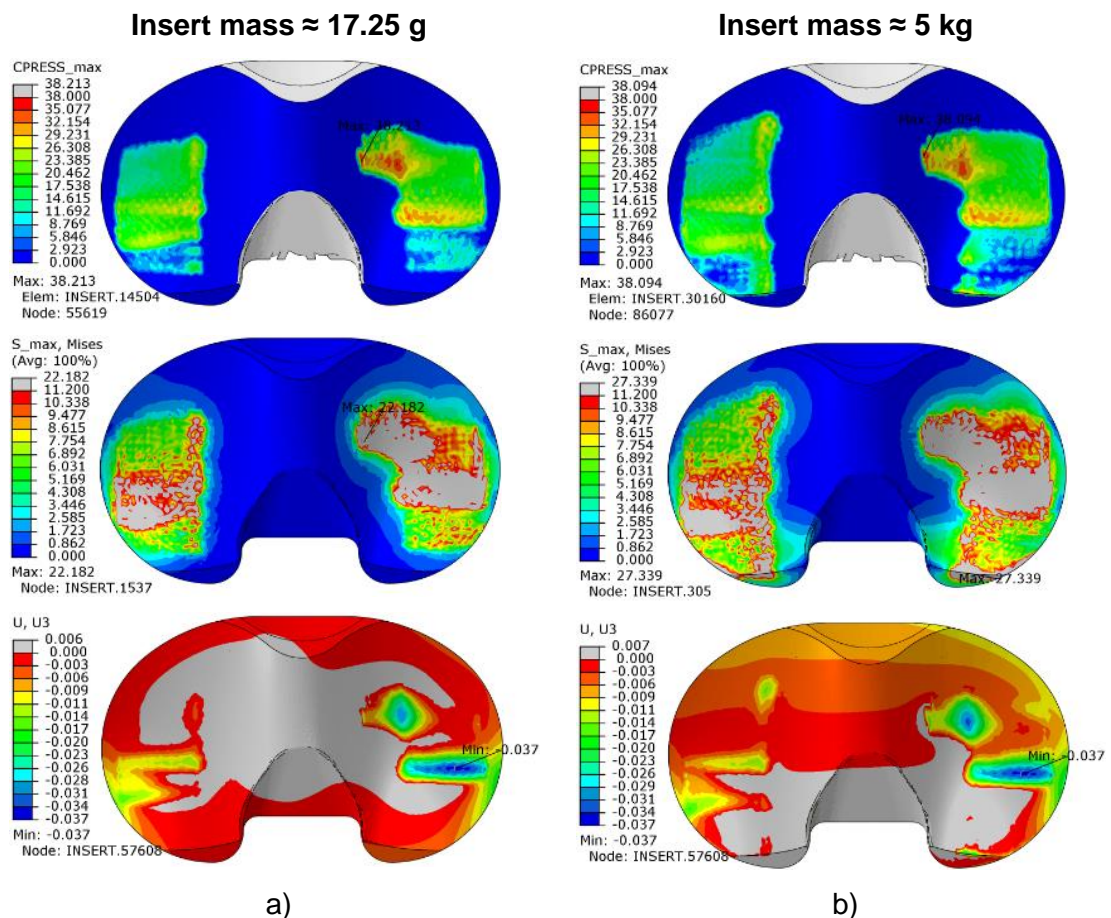
Figure 4.44. Comparison of contact pressure (MPa), Von Mises stress (MPa), and axial plastic deformation (mm) for FEA simulation of ISO 14243-1 in load control with tibial insert mass of a) 17.25 g and b) 5 kg.

4.3.8 Discussion

It was not possible to validate any of the dynamic FEA models with a laboratory experiment due to technical issues with a knee simulator (further described in Section 8.3.1). It was only possible to make indirect comparison with other published FEA models, with validation study results for the static FEA, and experimental knee simulator study results in displacement control.

Only one publication by Wang et al. [167] was found to present six FEA models per ASTM F3141 standard. These models had several differences in boundary conditions: they used only linear elastic material properties, implemented centre of rotation per ISO instead of ASTM standard, used average instead of heavy loading data, used different implant geometry (left posterior stabilised TKR with a central post) and had no reference to a clinical implant design, used different spring constraints by combining ISO 14243-1:2009 with additional A-P stiffness of 32N/mm after exceeding ±5 mm displacement and I-E stiffness of 790 Nmm/° after exceeding ±12° rotation. Due to the many differences, the presented models on daily activities cannot be quantitatively compared. Wang et al. [167] presented wear depth plots, where wear was calculated as a function of contact pressure and sliding distance. Whilst not directly comparable, some similarities could be observed for the location of the peak contact area and peak wear area (see Table 4.10), because both contact pressure and wear depth plots showed peak values near the intercondylar area. Wang et al. [167] did not provide sufficient information to directly compare contact pressures.

Table 4.10. Qualitative comparison for the location of the peak contact pressure areas presented in this thesis and the peak wear areas presented in study by Wang et al. [167] for the FEA models with ASTM F3141 loading for daily activities.

Contact pressure (CR insert) per ASTM F3141 taken from Figure 4.40	Wear depth (PS insert with moderate lip) per ASTM F3141 taken from Wang et al. [167]
3.Walking (Heavy-100kg) per ASTM F3141-17a	
5.Pivot turn (100kg) per ASTM F3141-17a	
6.Crossover turn (100kg) per ASTM F3141-17a	
7.Stair descent (Heavy-100kg) per ASTM F3141-17a	
8.Stair ascent (Heavy-100kg) per ASTM F3141-17a	
9.Sit to stand to sit (Heavy-100kg) per ASTM F3141-17a	

Amongst all nine daily activity models, the dynamic FEA per ISO 14243-1 showed the smallest peak contact pressure, Von Mises stress, and plastic deformation values, and had the most similarities to the static FEA model for axial compression with 5480 N force. A comparison between static FEA and dynamic FEA at one frame is shown Figure 4.45. The validation study under axial conditions had shown that static FEA model predicts contact pressure and plastic deformation close to experimental observations. The dynamic FEA models re-used the same material properties and applied axial load via a rigid femoral component shell as it was done in the static FEA. Accordingly, dynamic FEA models should give realistic predictions regarding axial deformation. The biggest difference between the static and dynamic models was the addition of inertia to the tibial insert component, which affects tibial insert kinematics and therefore also the contact areas (as shown in Figure 4.44). Consequently, dynamic FEA models were not validated for the sliding distance and loading patterns created by dynamic forces.

a)   b)
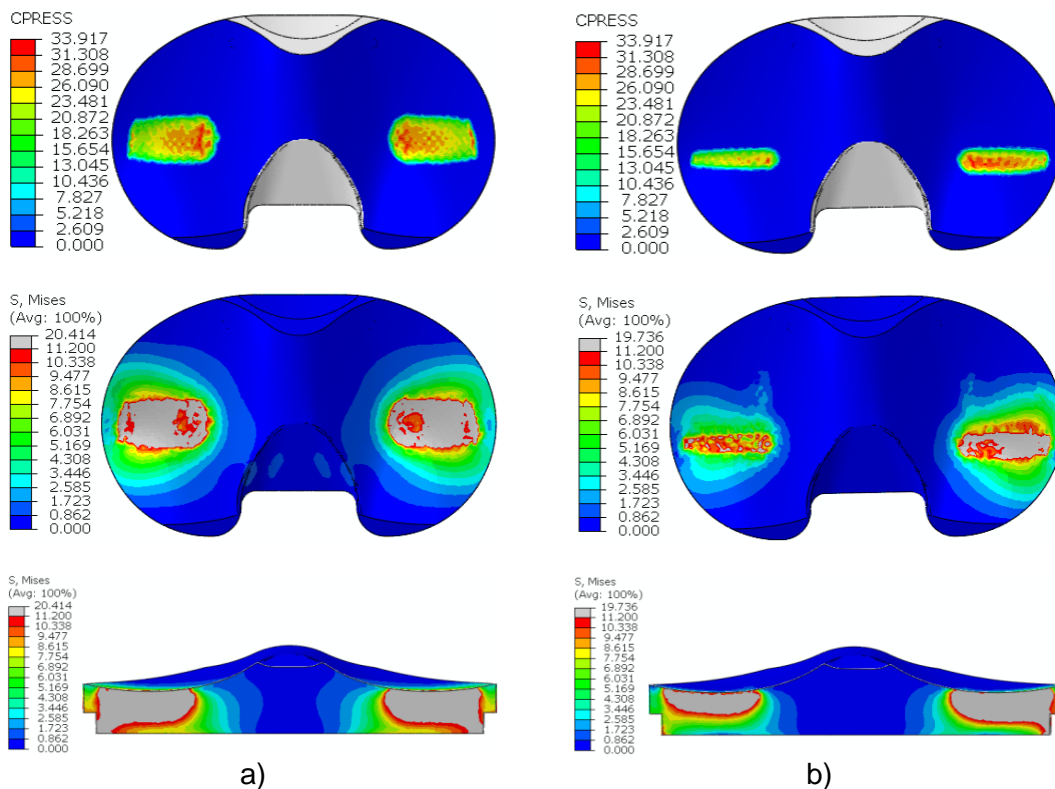
Figure 4.45. Comparison of contact pressure (MPa) and Von Mises stress (MPa) between FEA models for a) axial compression with 5480 N at 0° flexion and b) a single frame from ISO 14243-1 in load control with 2600 N at 15.3° flexion.

In this study an attempt was made to validate the dynamic FEA model for ISO 14243-1. However, due to technical problems a knee simulator study could be performed only with simplified simulation condition for ISO 14243-1 in displacement control (calculated with FEA) instead of load control (see detailed description in Section 8.3.1). Whilst direct comparison was not possible, some similarities could be seen between the FEA

predictions and the experimental simulation. For example, CMM measurements showed deeper wear scars on the medial side compared to lateral, which corresponds to the dynamic FEA model prediction of larger contact pressure on the medial side. CMM measurements also showed minimal surface deviation at the intercondylar. A few tibial inserts showed backside wear due to contact with the top rim of the tibial tray, which was predicted by both static and dynamic FEA.

Dynamic daily activity FEA models per ASTM and OrthoLoad showed large contact pressure, Von Mises stress, and axial deformation close to the posterior area. These FEA predictions correspond to other published experimental and retrieval studies, showing that modern tibial inserts are still subjected to plastic deformation and fracture at the posterior area or anterior dislocation caused by posterior forces (see Figure 1.14).

A number of studies have performed joint simulator wear tests [17, 19, 168] or computational models [169] on TKR loading for activities of daily living. However, these studies did not report what soft tissue constraints were used, which makes it impossible to recreate their published testing conditions. During this PhD research it was discovered that soft tissue constraints taken from ISO 14243-1:2009 standard [108] cannot be applied to daily loading conditions per ASTM F3141-17a [49], because ISO [108] spring values would not prevent femoral component dislocation. Therefore, this PhD research has presented potential spring constraint values for a number of different activities of daily living, which could be recreated both with experimental and computational tests (see Table 4.8). The soft tissue constraints used in this PhD research were taken either from ISO 14243-1:2009 standard [108] or from clinical data [163-166]. A few other publications can be used to find alternative values for motion restraints, for example, ASTM F3141-17a standard [49] gives references to many clinical studies regarding soft tissue constraints. Wear test study by Liu et al. [148] implemented motion restraints from ISO 14243-1:2009 but did not apply A-P and I-E spring gap to avoid implant luxation. Computational study by Wang et al. [167] implemented motion restraints from ISO 14243-1, 2009 and added additional restraint for A-P motion of 32 N/mm if displacement exceeded 5 mm, and for I-E motion of 790 Nmm/° if angular rotation exceeded ±12°. A computational study by Shu et al. [43] implemented spring constraints from ISO 14243-1: 2009, but excluded M-L forces.

The daily activity FEA models showed peak contact pressures ranging from 38.2 MPa to 64.9 MPa for axial joint force of up to 5480 N. In comparison, other computational publications which applied true stress-strain material properties reported maximum contact pressures ranging from 29 to 62 MPa [148, 169-173] for axial joint force of up to 3000 N during walking. All ASTM and OrthoLoad models showed larger peak

contact pressure, larger Von Mises stress, and larger area of plastic deformation compared to both ISO models. High contact pressure does not necessary indicate implant failure, since UHMWPE can withstand contact stresses that exceed the yield stress [170], and the true ultimate tensile stress for virgin GUR 1020 UHMWPE is up to 188 MPa [128, 130]. Nevertheless, a number of wear studies have reported that loading from daily activities can increase the wear rate [17, 148, 174]. Therefore, FEA models with ASTM [49] and OrthoLoad [155] loading profiles are more beneficial for modelling worst case loading scenarios when compared to the ISO 14243 loading profiles.

4.3.9 Daily Activity FEA model assumptions and limitations

The daily activity FEA models were created to simulate the experimental joint simulator conditions, however there are some differences between the FEA models and the experimental tests. For example, the FEA model did not consider the mass or the friction of the fixtures used for the joint simulator, to reduce model complexity. However, the lack of mass and friction would likely result in different kinematics, which would further result in different contact pressure, internal stress, and deformation patterns as shown in Figure 4.44.

To simplify FEA models and allow simultaneous comparison of FEA gait videos for each model at gait increments of 0.5%, all daily activity models were models with the same time period of 1.0 second, whilst ASTM F3141-17a [49] standard suggested various time periods from 1.16 s to 2.45 s. FEA models with different time periods could give different results due to difference in inertia. No further sensitivity analysis was performed on analysing the effect of different time periods due to time limitation of this PhD research; therefore, it should be addressed in the future work.

4.3.10   Conclusion

In order to create FEA models for daily activity loading scenarios with cruciate retaining TKR it is important to choose realistic soft tissue constraint parameters. This chapter described which soft tissue spring constraint parameters could be applied both for experimental joint simulators and computational FEA models for following activities: walking, jogging, pivot turn, crossover turn, stairs ascend, stair descend, and sit to stand to sit.

In total nine FEA models of daily activity were created by using loading data from ISO 14243-1:2009 standard [108], ISO 14243-3:2014 standard [109], ASTM F3141-17a

standard [49], and OrthoLoad data base [155]. The location and magnitude of deformation and stresses varied amongst all nine FEA models. In particular FEA models per ISO standard predicted the smallest tibial insert deformation and material stresses. Therefore, the results of this research indicate that all loading patterns should be considered before performing either experimental or computational studies.

5   Instrumented tibial insert design

5.1 Introduction

The work presented in this chapter covers research Objective 3 to 5. Specifically, this chapter outlines the work on FEA model development, validation, and optimisation of smart knee implant prototype.

When designing an instrumented tibial insert it is important to choose where to position electronic components, in which direction to align sensors, and which manufacturing process to use. This section describes the fundamental design assumptions and design optimisation for the instrumented tibial insert, such as, hole diameter, hole depth, capsule shape, and use of strain gauges.

Both computational and experimental methods were used to analyse and compare different design ideas. FEA studies were useful for analysing different design concepts without the need to physically manufacture and test every design idea. Primarily simplified static FEA models were used for design optimisation studies, due to the benefit of reduced computational time. Dynamic FEA models were performed to show the differences between the original and modified tibial insert under daily activity scenarios. Experimental studies were used for analysing a few chosen design concepts in a more realistic environment and for validating the static FEA model predictions.

5.2 Static FEA (insert with a through hole)

5.2.1 Introduction

This PhD research proposed a novel design concept to place electronic components only at the intercondylar area of the tibial insert to retain the structural integrity under the articulating surfaces (previously described in Section 3.3). At first, it was of interest to perform static FEA models to analyse the effect of adding a hole. A hole was needed to provide an empty space for electronics. Therefore, it was of interest to see if adding a hole would change internal stresses or deformation under the articulating surfaces, since it could affect the long-term wear performance.

5.2.2 Method

In order to simplify the manufacturing process, it was decided to drill or mill a hole at the intercondylar area instead of using laser welding [10, 11] or compression moulding [12] of two separate parts. Inside this hole, a capsule containing sensors would be placed. Therefore, a through hole with diameter of 10 mm was created at the intercondylar area at 6.5 mm height from the bottom face, leaving about 1.5 mm thick

wall at the top and the bottom face (see Figure 5.1). The 10 mm diameter was chosen because it was the largest diameter hole which could be drilled in the GMK Primary size 3/10 tibial insert with the available machining equipment.
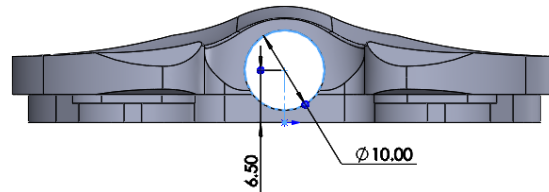
Figure 5.1. Tibial insert with a thru hole at the intercondylar area.

A static FEA model, with a compressive axial force of 5480 N (maximum force from OrthoLoad jogging Peak100 [155]) applied at the dwell point with 0º flexion (previously described in Section 4.2), was repeated to check whether insert with a drilled hole will exhibit larger deformation or larger Von Mises stress under the articulating surface compared to the original tibial insert design. No additional mesh convergence tests were performed. Mesh size of 1.3 mm was used for the modified insert to retain approximately the same element size and element location as in the original insert and allow relative comparison.

5.2.3 Results

No major differences were observed between the original and the drilled insert under axial compression (Figure 5.2). The contour plots showed almost identical magnitude and distribution of the deformation and internal stress. Both original and drilled insert displayed maximum plastic deformation of 0.041 mm, therefore showing 0% difference for the maximum values. The maximum Von Mises stress was 20.41 MPa for the original insert and 20.36 MPa for the drilled insert, therefore showing 0.003% difference for the maximum values. Von Mises stresses did not show any stress raisers caused by the hole. Stresses near the hole were below true yield stress of 11.2 MPa, therefore indicating no signs of plastic deformation. The FEA mesh convergence check in Section 4.2.8 showed that that FEA results could differ by ±2.7% for von Mises stress and ±2.4% for axial deformation. Therefore, differences shown in Figure 5.2 were assumed to be negligible.

a) Von Mises stress (MPa) when Loaded with 5480 N

b) Axial deformation (mm) after un-loading

c) Von Mises stress (MPa) when Loaded with 5480 N

d) Axial deformation (mm) after un-loading
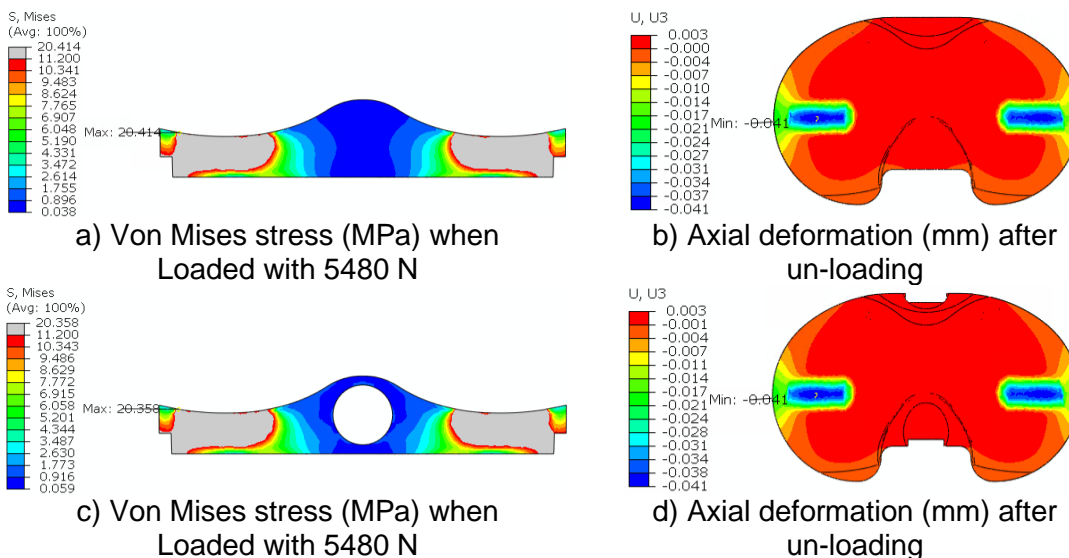
Figure 5.2. Static FEA models show minimal difference between a,b) original insert and c,d) insert with a 10 mm thru hole when axially loaded with force of 5480 N and after unloading. Gray area shows stress above the true yield stress of 11.2 MPa.

5.2.4 Discussion

The static FEA model under simplified axial compression showed no major difference between the original and modified tibial insert design. Result differences for both Von Mises and axial deformation contour plots between the two designs were below the mesh convergence accuracy. The maximum Von Mises stress was slightly smaller for the insert with a hole, but the slight difference could have been caused due to re-meshing the modified insert. FEA model with a hole showed no stress raises and no signs of plastic deformation near the hole. Therefore, it was decided to keep the hole diameter of 10 mm for the following studies.

5.3 Design of the capsule with electronics

5.3.1 Introduction

After adding a hole, it was of interest to analyse the effect of embedding a rigid object within the tibial insert. In order to design an instrumented tibial insert it is important to consider how to seal the electronic components to ensure patient safety. During this research it was decided that all electronic components will be placed within a sealed capsule.

One of the concerns was that a rigid capsule could create stress concentration points potentially leading to a fracture, for example, if the capsule had a geometry with sharp edges. A published study with a hip implant liner showed that geometry with notches or grooves could increase fracture risk [175], and another study with an unicondylar insert advised using spherical ball markers instead of cylindrical wire markers to prevent insert fracture [121]. Therefore, a static FEA study was performed to compare a few potential capsule shapes and whether the capsule shape would create any stress concentration points.

5.3.2 Materials and methods

5.3.2.1 Capsule shape

To decide which capsule shape should be used, an FEA study was performed comparing three different capsule geometries: cylinder shape, bullet shape, and pill shape capsule (see Figure 5.3). Cylinder capsule provided the largest useful volume, but also had two sharp edges. The bullet and pill shape capsule had less useful volume, but they would have one or two rounded edges. Capsule was 17 mm long and had the same diameter as the hole.

a)   b)   c)
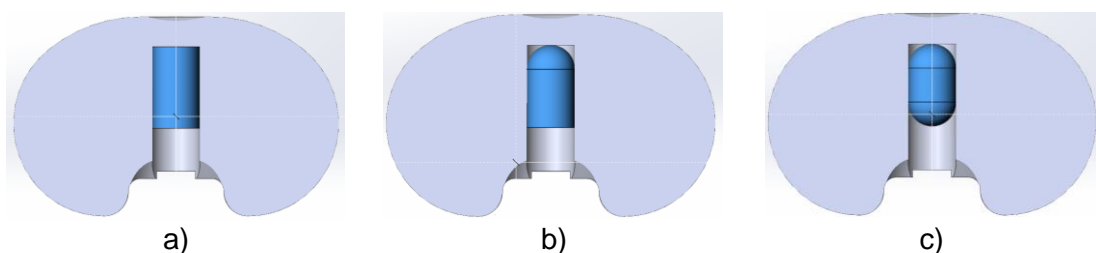
Figure 5.3. Three capsule designs with a) cylinder, b) bullet, and c) pill shape, and their location within a tibial insert with posteriorly drilled flat end hole.

To prevent damaging the anterior locking mechanism, it was decided not to drill a through hole. Instead, a hole would be milled from the posterior direction. The hole would be milled to a depth which maintains at least 1 mm thick wall from the anterior locking mechanism. A flat bottom mill bit was chosen to simplify the milling procedure

on a non-flat surface. Mill bits with conical and round bottom were excluded, since they could deviate from the straight course when milling into a surface with a slope.

5.3.2.2 FEA parameters for insert with a capsule

A static FEA model parameters were similar to the previously described model in Section 4.2. The tibial insert with embedded capsule was compressed by applying an axial force of 5480 N at the dwell point via the femoral component with 0º flexion (see Figure 5.4).
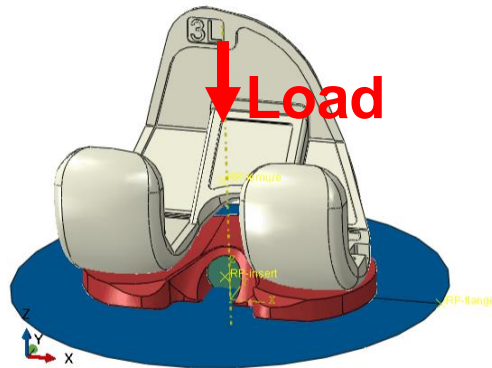
Figure 5.4. Example image of FEA model assembly with embedded capsule.

During this PhD research it was discovered that electronics and strain gauges could be moulded into any capsule shape by using a bone cement (further described in Section 6.4). Therefore, the capsule was assigned linear elastic material properties for bone cement material made of polymethyl methacrylate (PMMA) with Young`s modulus of 2280 MPa and Poison`s ratio of 0.3 [176].

The capsule was modelled as a deformable body. The capsule was modelled as a 3D part with C3D10M elements with a mesh size of 1.3 mm same as the insert.

Surface-to-surface contact was defined between all walls of the drilled hole and of the capsule (see Figure 5.5). Normal behaviour was defined as "hard" contact with default penalty constraint enforcement method and the penalty stiffness of 10 [135]. Tangential behaviour was defined as a penalty with friction coefficient of 0.297 [177].

a)   b)
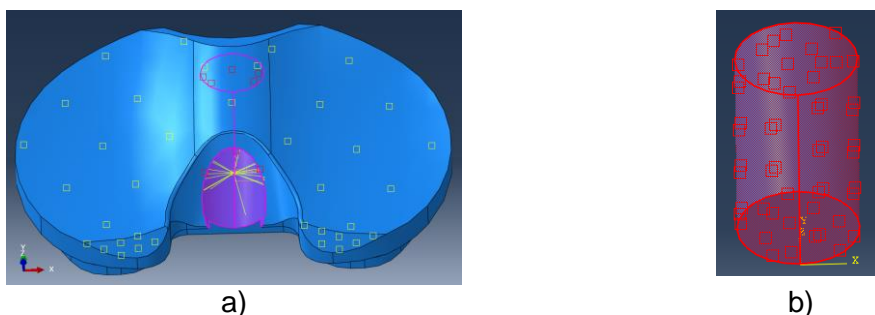
Figure 5.5. Example images of surface-to-surface contact surfaces between all a) insert walls and all b) capsule walls.

The FEA model could not initiate the first pre-displacement step without defining any boundary condition on the capsule. Therefore, a boundary condition was defined by selecting a single point on the capsule and restricting translation either in M-L or A-P direction (see Figure 5.6) during the first pre-displacement step to initiate contact. Then this boundary condition was removed for the subsequent loading step.

a)   b)   c)
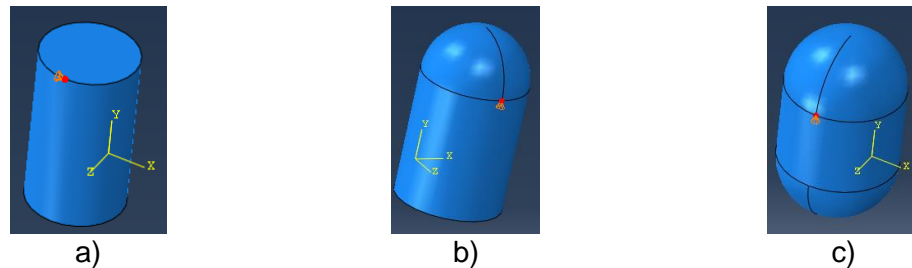
Figure 5.6. Example images of node fixation for the a) cylinder, b) bullet, and c) pill capsule.

5.3.3 Results

Three FEA models were completed with the three different capsule designs, where an axial force of 5480 N was applied to the tibial insert at the dwell point. The Von Mises stress contour plots revealed that the stresses on the walls of the hole were below the true yield stress of 11.2 MPa for all three-capsule design (see Figure 5.7 and Figure 5.8). The cylinder capsule showed slightly higher maximum stress on the insert's internal hole wall of around 2.5 MPa compared to the other two capsule designs.

a)   b)   c)
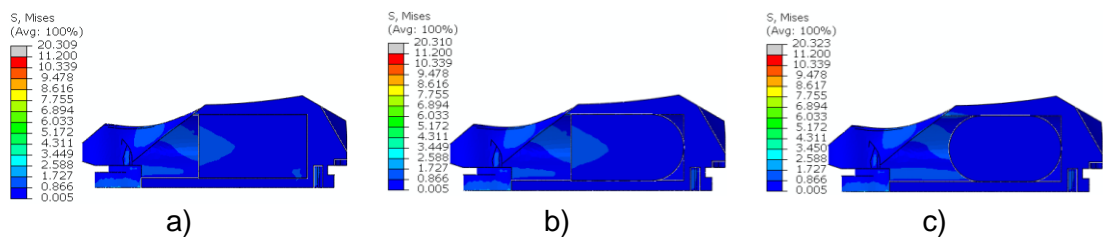
Figure 5.7. Side cut view with Von Mises stress (MPa) contour plot for the FEA models with a) cylinder, b) bullet, and c) pill capsule. Yield stress of 11.2 MPa was not exceeded on the tibial insert hole walls for any model when insert was compressed with axial force of 5480 N.

a)   b)   c)
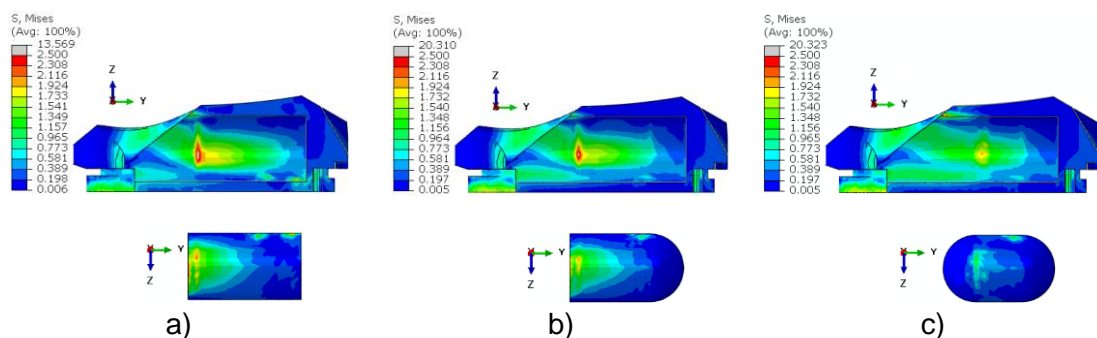
Figure 5.8. Side cut view with Von Mises stress (MPa) contour plot for the FEA models with a) cylinder, b) bullet, and c) pill capsule. Images show contact surfaces between insert and capsule.

The FEA models also revealed that the capsule is compressed mainly in the Medial-Lateral (M-L) direction, which could be explained with Poisson effect. More specifically, when the tibial insert is axially compressed in S-I direction, its material is simultaneously expanding in the transverse plane both in M-L and A-P direction. Figure 5.9 shows larger compressive microstrains of ≈-0.00080 in M-L direction, and smaller tensile microstrains of ≈+0.00035 in A-P and S-I direction. Accordingly, insert expansion is resisted by the capsule and the capsule gets compressed in the M-L direction from both sides. Therefore, the primary compressive force applied by the femoral component is creating a secondary compressive force applied to the capsule (see Figure 5.9). The secondary force could be experimentally approximated, for example, by measuring the capsule deformation with strain gauges. Therefore, potentially the primary force could also be approximated if it was proportional to the strain gauges signal. Accordingly, for optimal strain recordings the strain gauges should be positioned inside the capsule, parallel to the transverse plane, and aligned in M-L direction (see Figure 5.10). For example, 7 mm wide strain gauges could be used which would cover most of the capsule surface in the M-L direction.
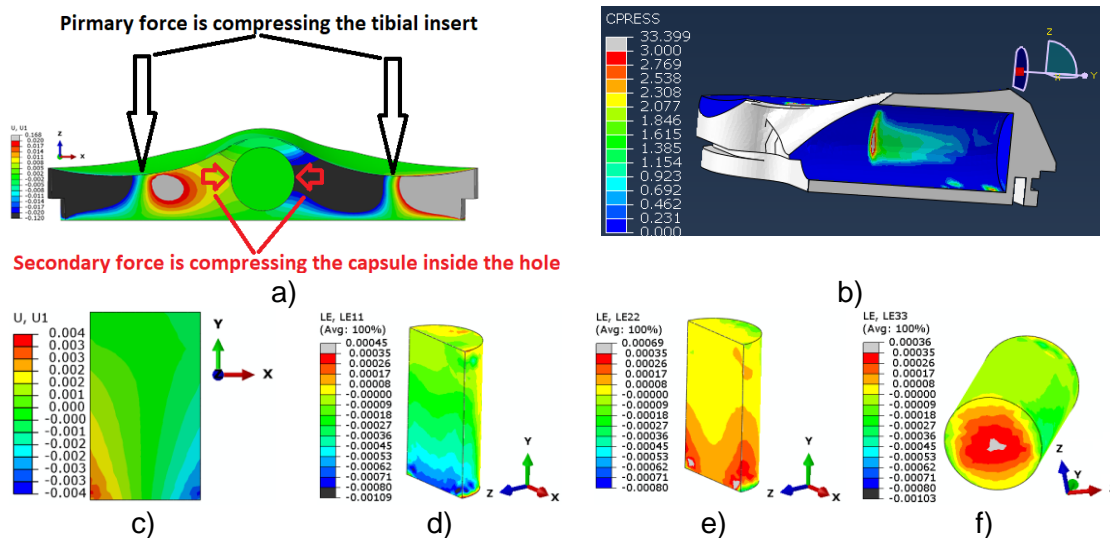
Figure 5.9. Figure a) of displacement (mm) illustrates how the primary force is causing material expansion in M-L direction, therefore creating a secondary force applied to the capsule. Figure b) shows that contact pressure (MPa) is applied mainly in M-L direction. Figure c) of displacement (mm) shows M-L capsule compression. Strain plot d) in M-L direction shows the largest strains when comparing with strains in e) A-P direction and f) S-I direction.
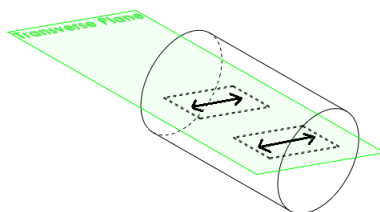
Figure 5.10. Strain gauges positioned inside the capsule, paralel to the transverse plane, and aligned in M-L direction. Arrows illustrate strain gauge alignment in M-L direction.

5.3.4 Discussion

Before conducting the FEA models with three different capsule shapes it was anticipated that the cylindrical capsule could show higher stresses on the walls of the hole. The cylindrical capsule indeed caused the highest Von Mises stresses, the bullet shape capsule showed slightly lower stresses, and the pill shape capsule created the lowest stresses. However, the maximum stresses created by the cylinder capsule were around 2.5 MPa, which is well below the yield stress of 11.2 MPa. Therefore, the bullet and pill shape capsules showed no practical benefits with their rounded edges. The cylinder shape capsule provides the biggest volume for housing electronics, therefore it was considered as the most optimal shape for encapsulating electronic components for the current research purposes. However, this conclusion was made only with a simplified FEA model under axial loading.

In the future research the capsule shape should be re-evaluated with more complex FEA models simulating daily loading scenarios. Different loading scenarios might potentially reveal whether the thin hole wall is impinged between the femoral component and the capsule, or whether the sharp cylindrical edges are causing stress concentrations above the yield stress. Additionally, in this research it was assumed that the capsule and the hole have identical diameter. Therefore, it would be of interest to further analyse stress differences due to various interference or clearance fits with the capsule.

The FEA model with capsules also allowed to gain better understanding about the capsule deformation mechanics. Since FEA models predicted that the capsule would be mainly compressed in M-L direction, it was decided that for optimal strain recordings the strain gauges should be positioned inside the capsule, paralel to the transverse plane, and aligned in M-L direction. This was also experimentally confirmed and further described in Section 6.5.

5.4 Static FEA (insert with a posterior hole and a metal capsule)

5.4.1 Introduction

After improving the insert design, by drilling posterior hole and using a cylindrical capsule, it was of interest to investigate different capsule material, for example, a capsule made of metal. It was of interest to see if there could be changes in contact pressure or plastic deformation if an object with high stiffness was placed in the middle of the insert, since a similar study with an unicondylar insert have reported insert fracture due to embedded metal marker wires [121].

5.4.2 Materials and Methods

A static FEA model parameters were similar to the previously described model in Section 5.3.2.2. The tibial insert with embedded capsule was compressed by applying an axial force of 5480 N at the dwell point via the femoral component with 0º flexion (see Figure 5.4).

Three FEA models were made to compare the effect of drilling posterior hole and using a metal capsule: original insert with no modifications, insert with an empty posterior hole, insert with a posterior hole and embedded metal cylinder.

Stainless steel material SS316 was chosen, because it is widely available medical grade material with large Young`s modulus of 193,000 MPa [134]. Poisson`s ratio was assumed to be 0.3 [134] and coefficient of friction on the UHMWPE contact surface was assumed to be 0.06 [178]. A metal cylinder with length of 15 mm and diameter of 10 mm (Figure 5.11) was placed inside the tibial insert (as shown in Figure 5.3a). Chamfers of 0.5 mm and 45° were created to remove sharp edges and make it easier to insert the capsule inside the hole.
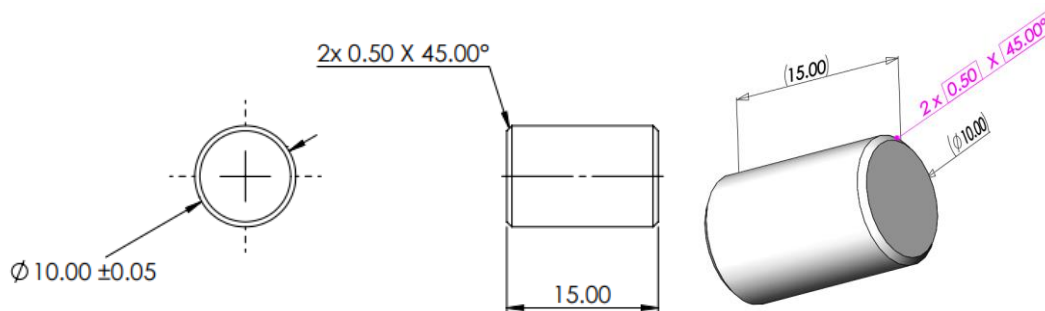
Figure 5.11. Dimension of the SS316 cylinder capsule.

5.4.3 Results

No major differences were observed between the three FEA models under simple axial loading with 5480 N. The contour plots showed almost identical distribution of the contact pressure and deformation. All three models displayed maximum plastic deformation of 0.041 mm. Maximum contact pressure for the drilled insert and the insert with a capsule was 34.44 MPa and 34.40 MPs respectively compared to original insert of 33.92 MPa, but the maximum difference of 1.5% was considered as minimal since the FEA mesh convergence check in Section 4.2.8 showed that that contact pressure results could differ by ±3.6%.
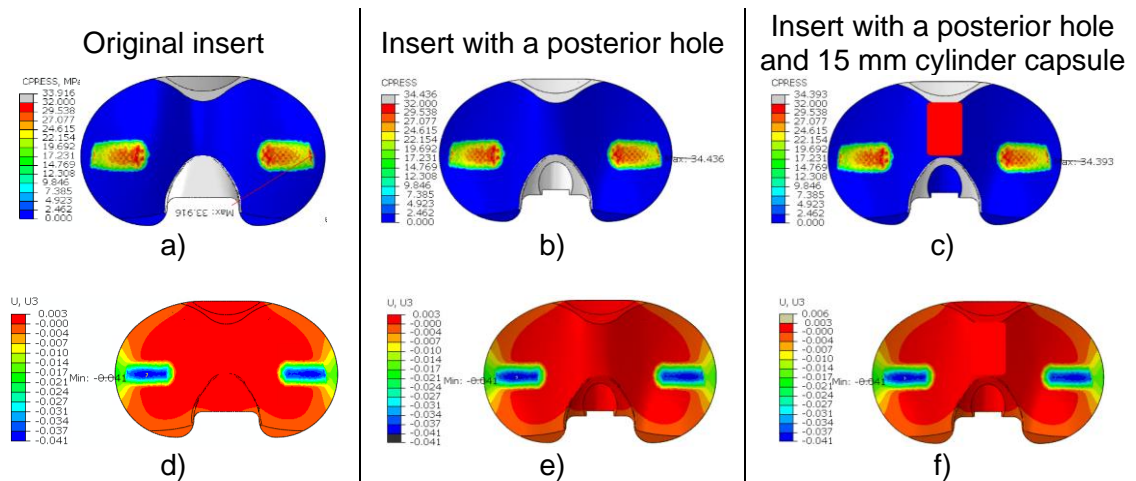
Figure 5.12. FEA results showing a,b,c) contact pressure (MPa) under axial force of 5480 N, and d,e,f) axial plastic displacement (mm) after un-loading for original insert, insert with a posterior hole, and insert with a posterior hole and a 15 mm SS316 cylinder capsule.

5.4.4 Static FEA validation of the insert with a posterior hole and a metal capsule

This experimental study had two aims. First, to perform relative comparison between the original tibial insert and two insert modifications. Second, to compare experimental results with the FEA predictions.

The null hypothesis for this study was that there is no significant difference between the mean values obtained from original insert and any insert modification.

5.4.4.1 Method

A laboratory experiment was performed to confirm the FEA predictions with the drilled insert and the embedded capsule. Literature search on FEA validation showed that other publications used between 1 to 10 specimens per group [121, 168, 179-182], with majority of studies using just 1 specimen per group. For this study a sample size of n=3 was chosen as acceptable for a small pilot study. More specimens per group were not chosen due to the cost of the specimens and budget limitations. An axial compression test with Instron 3366 material testing machine was repeated (previously described in Section 4.2.11) on three implant groups each consisting of 3 specimens (Figure 5.13):

1. 3x unmodified original inserts: No. 8 to 10 (+1 control insert No. 7 used for height gauge measurements),
2. 3x inserts with a drilled posterior hole: No. 11 to 13,
3. 3x inserts with a drilled posterior hole and a metal cylinder made of SS316: No. 14 to 16.

Figure 5.13. Specimens used for FEA validation study: original inserts, inserts with a posterior hole, and inserts with a posterior hole and a metal cylinder.

It was of interest to see whether drilling a hole or placing a metal cylinder would give different results from the original tibial insert regarding the contact pressure and axial deformation. Student`s unpaired two sample two-tail t-test was carried out to test for significant statistical differences with p<0.05 being taken for significance to reject the null hypothesis (calculated in Excel, Microsoft 365, version 2304).

Since n=3 was considered a small sample size, this study was used as a pilot study to provide preliminary data. Therefore, the results were used to approximate a required sample size for future studies per **Equation 3** [183], assuming normal distribution with confidence level of α=0.05 with two tails and power of (1-β)=0.80.

n: sample size per group
σ: standard deviation per group
μ: mean per group*
Z: Z-value
$Z_{1-\alpha/2}$(when α=0.05)=1.960 [183]
$Z_{1-\beta}$(when β=0.2)=0.842 [183]

$$n = (\sigma_1^2 + \sigma_2^2)\frac{(Z_{1-\alpha/2} + Z_{1-\beta})^2}{(\mu_1 - \mu_2)^2}$$

Equation 3:
Sample size

*Note: If known, difference between two group means (μ_1-μ_2) should be replaced with a "clinically important difference" (d) [184].

5.4.4.2 Results

Tekscan contact area showed that during experimental testing the fixtures were slightly misaligned on the Instron material testing machine, which resulted in slightly different contact area and shape under the two condyles. The contact area under the lateral condyle was slightly larger and more elongated compared to the measurements on the medial side (see Table 5.2).
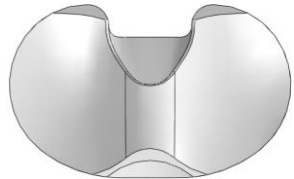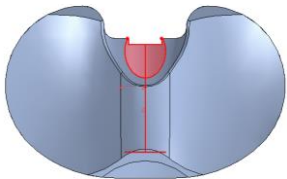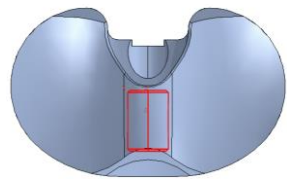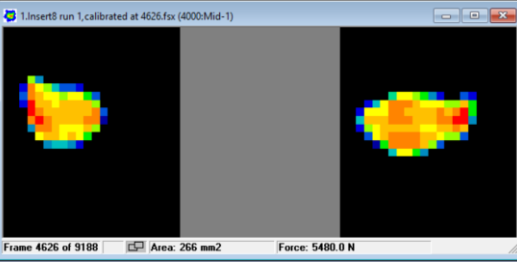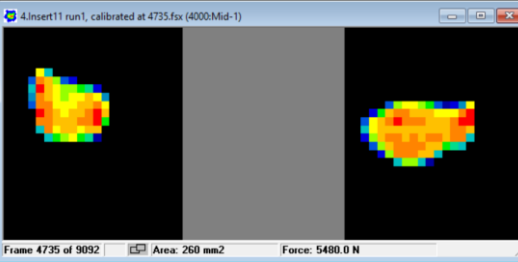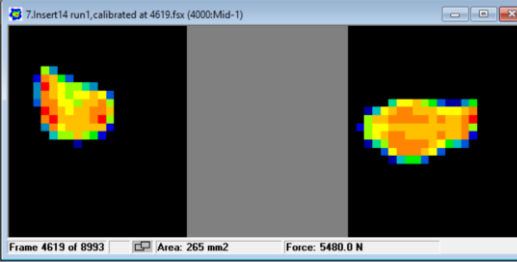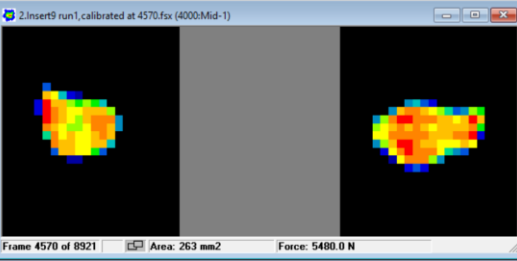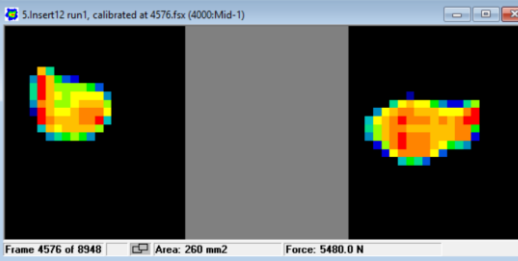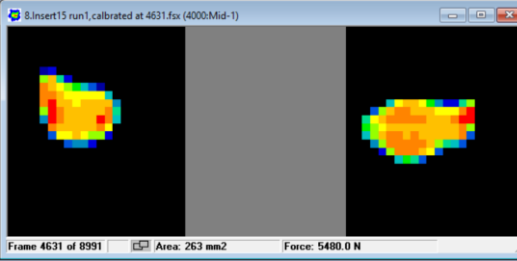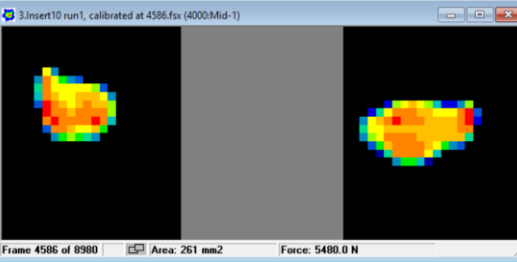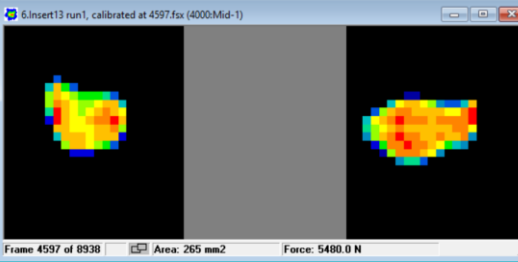
The results per group and its specimens are organised in tables in the specific order as listed in Table 5.1.

Table 5.1. Specimen results per each group are shown in the following order.

	Group 1	**Group 2**	**Group 3**
	Original insert	Insert with hole	Insert with hole and cylinder
Specimen 1	No.8	No.11	No.14
Specimen 2	No.9	No.12	No.15
Specimen 3	No.10	No.13	No.16

Overall, the FEA results differed from the laboratory measurements by up to 15% in peak contact pressure, up to 8% in total contact area, and up to 43% in plastic deformation at the dwell point which is presented in Table 5.3, Table 5.4, and Table 5.5 respectively.

Table 5.2. Tekscan measurements under axial compressions of 3 tibial insert groups: original insert, insert with a posterior hole, and insert with a posterior hole and a 15 mm long cylinder made of SS316.

Tekscan measurements showed mean peak contact pressure of 30.23 MPa (SD±0.43), 30.45 MPa (SD±1.62), and 29.20 MPa (SD±0.94) for original tibial insert, insert with a hole, and insert with a cylinder inside the hole respectively (see Table 5.3). Student's unpaired two sample t-test showed no statistically significant difference when comparing original insert and insert with a hole (p=0.84) or original insert and insert with a cylinder inside the hole (p=0.16).

Table 5.3. Tekscan measurements of peak contact pressure for 3 tibial insert groups.

	Group 1	Group 2	Group 3
	Original	With hole	With hole and cylinder
	MPa	MPa	MPa
Specimen 1	30.47	31.82	28.82
Specimen 2	29.74	28.66	30.27
Specimen 3	30.49	30.86	28.5
Group mean	30.23	30.45	29.20
Group standard deviation	0.43	1.62	0.94
Student`s unpaired two sample t-test with group 1	-	p=0.84	p=0.16
FEA prediction	33.92	34.44	34.39
Difference between FEA and group mean	11%	12%	15%
Delta of means with group 1	-	0.21	1.04
Approximated required sample size (n) with group 1	-	485	8

Tekscan measurements showed mean total contact area of 263 mm^2 (SD±2.5), 262 mm^2 (SD±2.9), and 265 mm^2 (SD±1.5) for original tibial insert, insert with a hole, and insert with a cylinder inside the hole respectively (see Table 5.4). Student`s unpaired two sample t-test showed no statistically significant difference when comparing original insert and insert with a hole (p=0.49) or original insert and insert with a cylinder inside the hole (p=0.48).

Table 5.4. Tekscan measurements of total contact area for 3 tibial insert groups.

	Group 1	Group 2	Group 3
	Original	With hole	With hole and cylinder
	mm^2	mm^2	mm^2
Specimen 1	266	260	265
Specimen 2	263	260	263
Specimen 3	261	265	266
Group Mean	**263**	**262**	**265**
Group Standard Deviation	**2.5**	**2.9**	**1.5**
Student`s unpaired two sample t-test with group 1	-	**p=0.49**	**p=0.48**
FEA prediction	242	243	243
Difference between FEA and group mean	8%	7%	8%
Delta of means with group 1	-	1.7	1.3
Approximated required sample size (n) with group 1	-	42	39

Dial height gauge measurements showed mean axial plastic deformation of 25.0 µm (SD±5.0), 21.7 µm (SD±2.9), and 26.7 µm (SD±7.6) for original tibial insert, insert with a hole, and insert with a cylinder inside the hole respectively (see Table 5.5). Student`s unpaired two sample t-test showed no statistically significant difference when comparing original insert and insert with a hole (p=0.37) or original insert and insert with a cylinder inside the hole (p=0.77). Control specimen measurements showed that repeatability of daily measurements was within 10 µm (see Table 5.6).

Table 5.5. Dial height gauge measurements of axial plastic deformation at the dwell point for 3 tibial insert groups after >17 hours.

	Group 1	Group 2	Group 3
	Original	With hole	With hole and cylinder
	Δ, µm	Δ, µm	Δ, µm
Specimen 1	30	20	20
Specimen 2	25	25	25
Specimen 3	20	20	35
Group Mean	**25.0**	**21.7**	**26.7**
Group Standard Deviation	**5.0**	**2.9**	**7.6**
Student`s unpaired two sample t-test with group 1	-	**p=0.37**	**p=0.77**
FEA prediction	38	38	38
Difference between FEA and group mean	34%	43%	30%
Delta of means with group 1	-	3.3	1.7
Approximated required sample size (n) with group 1	-	24	236

Table 5.6. Height gauge measurement repeatability with control specimen No.7.

Measurement day	Control specimen No.7 Dwell point height, mm
Day 1: specimen No.8	7.010
Day 2: specimen No.9	7.010
Day 3: specimen No.10	7.000
Day 4: specimen No.11	7.000
Day 5: specimen No.12	7.000
Day 6: specimen No.13	7.000
Day 7: specimen No.14	7.000
Day 8: specimen No.15	7.000
Day 9: specimen No.16	7.000
Maximum deviation between all measurements	0.010

5.4.5 Discussion

In this study the laboratory result comparison of the three tibial insert groups was not affected by the misalignment of the fixtures. The fixtures were aligned and firmly clamped to the Instron test machine bed before starting the test. During the testing the fixtures were never moved. Therefore, all 9 test specimens were aligned and loaded under the same conditions, which allowed direct comparison of experimental results between the specimens and groups.

The experimental results showed similar mean values with overlapping standard deviation between the three design groups when comparing the peak contact pressure, total contact area, or plastic deformation of the dwell point. The experimental results indicated that under axial loading conditions the modified inserts did not show major differences compared to the original insert, which was also predicted by the FEA models (from Figure 5.12). Therefore, it was decided to keep the hole diameter of 10 mm for the following studies.

FEA predictions showed larger differences from the laboratory experiments, compared to the previous validation study described in section 4.2.11. This study showed differences in total contact area of up to 8%, in peak contact pressure of up to 15%, and axial plastic deformation of up to 43%. Differences between the FEA and experimental results could have been caused by fixture misalignment, Tekscan film accuracy, differences in hole diameter, or differences in interference/clearance fit with the metal cylinder. FEA sensitivity analysis was not performed to study these variations.

Tekscan pressure measurements revealed asymmetrical contact areas between the two articulating surfaces, which was probably caused by fixture misalignment.

Accordingly, the fixture misalignment, could have increased the differences between the experimental and FEA results. It was unknown which part of the fixturing was misaligned on the Instron test machine. It could have been the misalignment of the metal tray fixture, the misalignment of the femoral component, or combination of both.

The pressure and contact area measurements were also affected by Tekscan measurement accuracy. Due to large sensel size, Tekscan 4000 films are prone to overestimate the contact area and underestimate the contact pressure. In this study the contact pressure was underestimated by up to 15% and contact area was overestimated by up to 8% when comparing experimental results with FEA predictions. Similar studies have shown that contact area was overestimated by up to 20% [150], and contact pressure was underestimated by up to 10% [121, 151].

FEA sensitivity analysis of component misalignment was not performed, since the main purpose of the FEA models was to predict whether there would be any difference between the groups. FEA models predicted that under the same loading conditions there would be no distinguishable difference between the contact pressure or plastic deformation on all three tibial insert groups.

No justification was found in literature on what sample size would be acceptable for FEA validation and group comparison. The small sample size of (n=3) may not have been sufficient to correctly accept the null hypothesis. Therefore, the result data were used to approximate the required sample size ranging from 8 to 485 specimens per group. The sample size formula assumed that the difference between the two-group means is significant, which is likely not to be the case. For example, height gauge measurement comparison between group 1 and group 3 had a mean difference of 1.7µm which is a minuscule dimension incapable of being distinguished by the measuring tool. If 1.7 µm would be replaced with a measurable difference of 10 µm as shown in Table 5.6, then the sample number approximation would drastically reduce from 236 to 7 required specimens per group. Unfortunately, no literature was found on clinically important difference which would have helped to improve the sample size approximation.

5.5 Strain pattern analysis with static FEA

5.5.1 Introduction

After finalising some aspects of the design for the hole and the capsule, it was of interest to analyse the potential benefits of using strain gauges. Specifically, it was of

interest to analyse whether different loading scenarios could be detected and recognised by measuring changes in strain within the capsule.

5.5.2 Methods

This study reused static FEA model parameters similar to the previously described model in Section 5.3.2.2. The parameters for tibial insert, femoral component, and capsule were not changed. Only cylindrical capsule was used. The capsule had PMMA material properties and had identical diameter with the hole, which can be achieved by pouring a self-curing liquid resin inside the hole. Femoral component remained always at 0º flexion (see Figure 5.4). Different loading scenarios were compared by changing the axial force, by changing the loading location in A-P direction, and by adding A-A moment to create different condyle pressure. Strain response was analysed for the M-L deformation at the middle of the capsule in the transverse plane, where the strain gauges would be placed as shown in Figure 5.10.

The changing strain patterns within the capsule were analysed by performing three FEA studies with different loading scenarios:

1) with different axial loading;
2) with the same axial loading applied at different locations in A-P direction;
3) with different condyle pressure applied at different locations in A-P direction.

The first FEA test (see section 5.5.3.1) was performed to investigate if it would be possible to indirectly measure the applied axial force by measuring the strain response within the capsule. In this FEA model an axial force from 500 N to 5000 N was applied at the dwell points.

The second FEA test (see section 5.5.3.2) was performed to investigate if it would be possible to recognise in which location the tibial insert is loaded, if the force was applied at different location in the A-P direction. An FEA model was created by applying axial force of 5480 N in three locations:

1. 5 mm anterior from the dwell point,
2. at the dwell point, and
3. 5 mm posterior from the dwell point.

The third FEA test (see section 5.5.3.3) was performed to investigate if it would be possible to recognise what is the condyle pressure ratio when different loads are applied to the medial and lateral articulating surface. An FEA model was created by applying axial force of 5480 N together with A-A moment of 50740 Nmm (maximum moment from OrthoLoad jogging Peak100 [155]). The A-A moment was used instead of simply applying two different forces, because there was no experimental simulator

available which could simultaneously apply two different forces. The load was applied in three locations:

1. 5 mm anterior from the dwell point,
2. at the dwell point, and
3. 5 mm posterior from the dwell point.

5.5.3 Results

5.5.3.1 Strain response to changing axial loading

The FEA models showed that the increase of the axial force on the femoral component also increased the contact pressure and strain deformation on the embedded capsule at the posterior area (see Table 5.7). When looking at the capsule cut in half in the transverse plane, the capsule showed ≈-0.1 microstrains under 500 N force, and up to ≈-0.7 microstrains under 5000 N force. Therefore, theoretically it could be possible to approximate the axial force applied by the femoral component, by measuring the strain deformation of the embedded capsule. The approximate relationship between the M-L strain and the axial force is plotted in Figure 5.14.
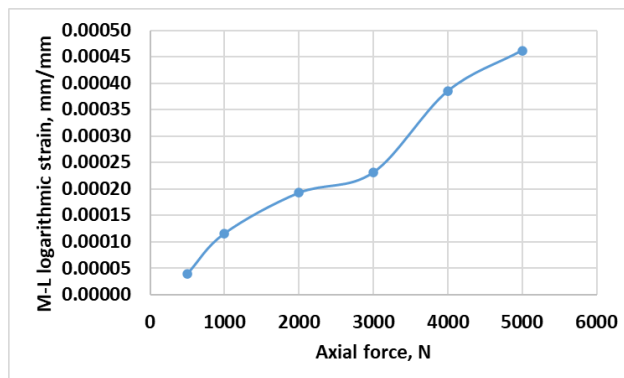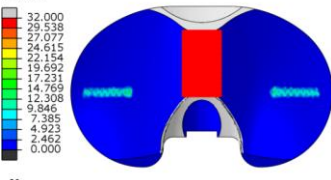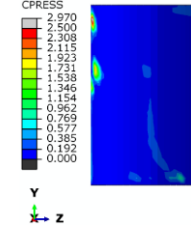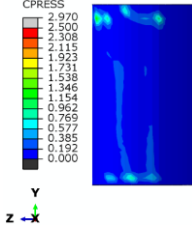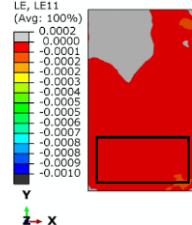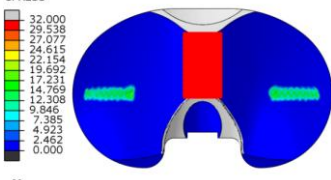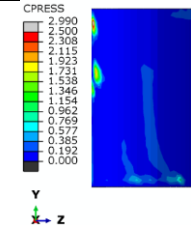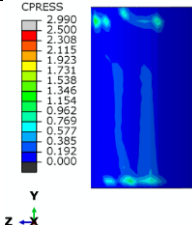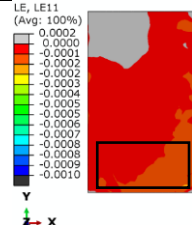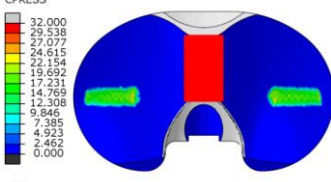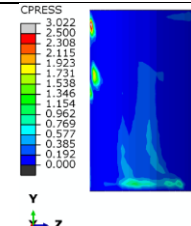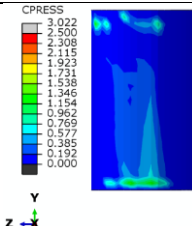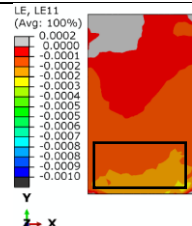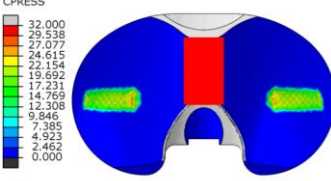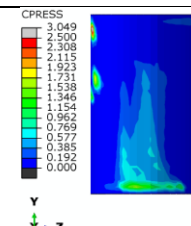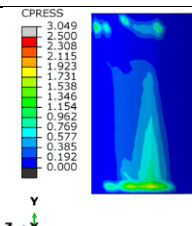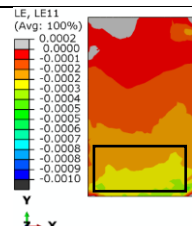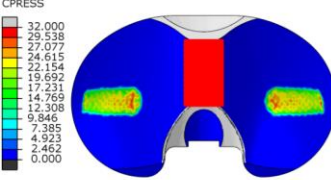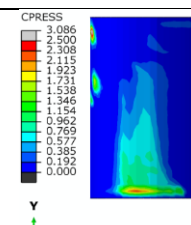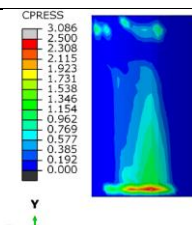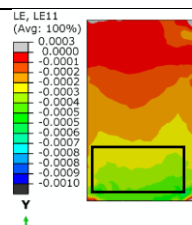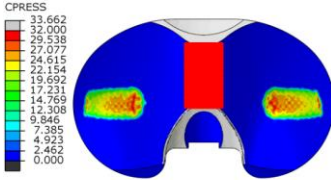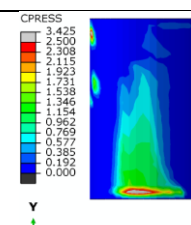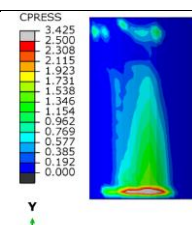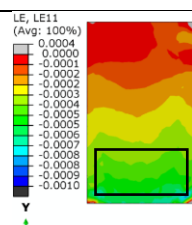
Figure 5.14. Plot showing approximate relation between the M-L logarithmic strain and the axial force as illustrated in Table 5.7.

Table 5.7. FEA model results showing contact pressure and strain changes of the embedded capsule when tibial insert is axially loaded from 500 N to 5000 N. Black rectangles highlight strain differences near the posterior edge. The strain is shown inside the capsule, which is cut in half in the transverse plane.

Tibial insert Applied axial force	Cylinder capsule Contact pressure, MPa		Cylinder capsule M-L strain
Top view (capsule in red)	Lateral view	Medial view	Superior cut view
500 N			
1000 N			
2000 N			
3000 N			
4000 N			
5000 N			

5.5.3.2 Strain response to loading at different A-P locations

The FEA models showed that axial force applied in the anterior, dwell, and posterior location will also change the contact pressure location on the capsule, which also affected the location of the maximum strain within the embedded capsule (see Figure 5.15 and Table 5.8). Therefore, theoretically it could be possible to approximate the tibial insert loading location in A-P direction, by measuring the strain deformation of the embedded capsule if two or more strain gauges were used.
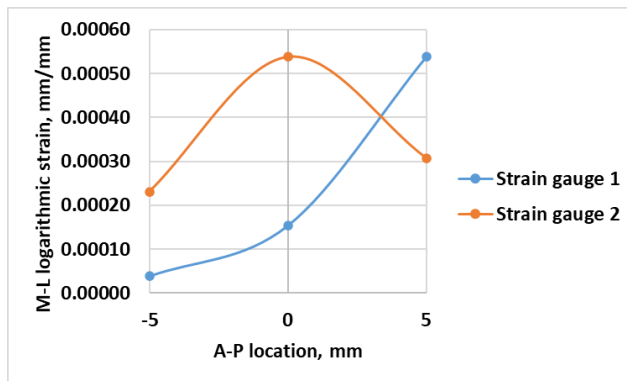
Figure 5.15. Plot showing approximate relation between the M-L logarithmic strain and the axial force applied at different A-P location as illustrated in Table 5.8).

Table 5.8. FEA model results showing changes in contact pressure and strain at the embedded capsule when tibial insert is axially loaded with 5480 N in three different locations in the A-P direction. Black rectangles illustrate that two strain gauges potentially could show different signal combinations depending on the loading location.

Tibial insert Loading location	Cylinder capsule Contact pressure, MPa	Cylinder capsule M-L strain
Top view (capsule in red)	Lateral view	Superior cut view
5 mm anterior from dwell point		
At the dwell point		
5 mm posterior from dwell point		

5.5.3.3 Strain response to different condyle pressure

The FEA models showed no obvious differences between the medial and the lateral loading applied to the embedded capsule. The capsule showed almost identical contact pressure and strain contour plot whether the insert was loaded on the lateral or medial side (see Table 5.9 and Table 5.10). The capsule only showed differences in strain patterns which were caused due to load applied at different A-P locations, but no differences could be observed due to different condyle pressure.

The inability to distinguish differences between the medial and lateral pressure could be explained by the Newton's third law, because on a stationary object for every action force there will be equal and opposite reaction force. Since the capsule is fixed within the tibial insert and the tibial insert is fixed within the tibial tray, then the M-L force applied to the capsule should always equalise. Therefore, it should not be possible to approximate the differences of tibial insert condyle pressure, by measuring strain deformation at the embedded intercondylar capsule.

Table 5.9. Capsule contact pressure and strain, when tibial insert is loaded in three different locations with axial force of 5480 N and negative A-A moment -50740 Nmm. Black rectangles illustrate two strain gauges.

Tibial insert Loading location	Cylinder capsule Contact pressure, MPa		Cylinder capsule M-L strain
Top view (capsule in red)	Lateral view	Medial view	Superior cut view
5 mm anterior from dwell point			
Dwell point			
5 mm posterior from dwell point			
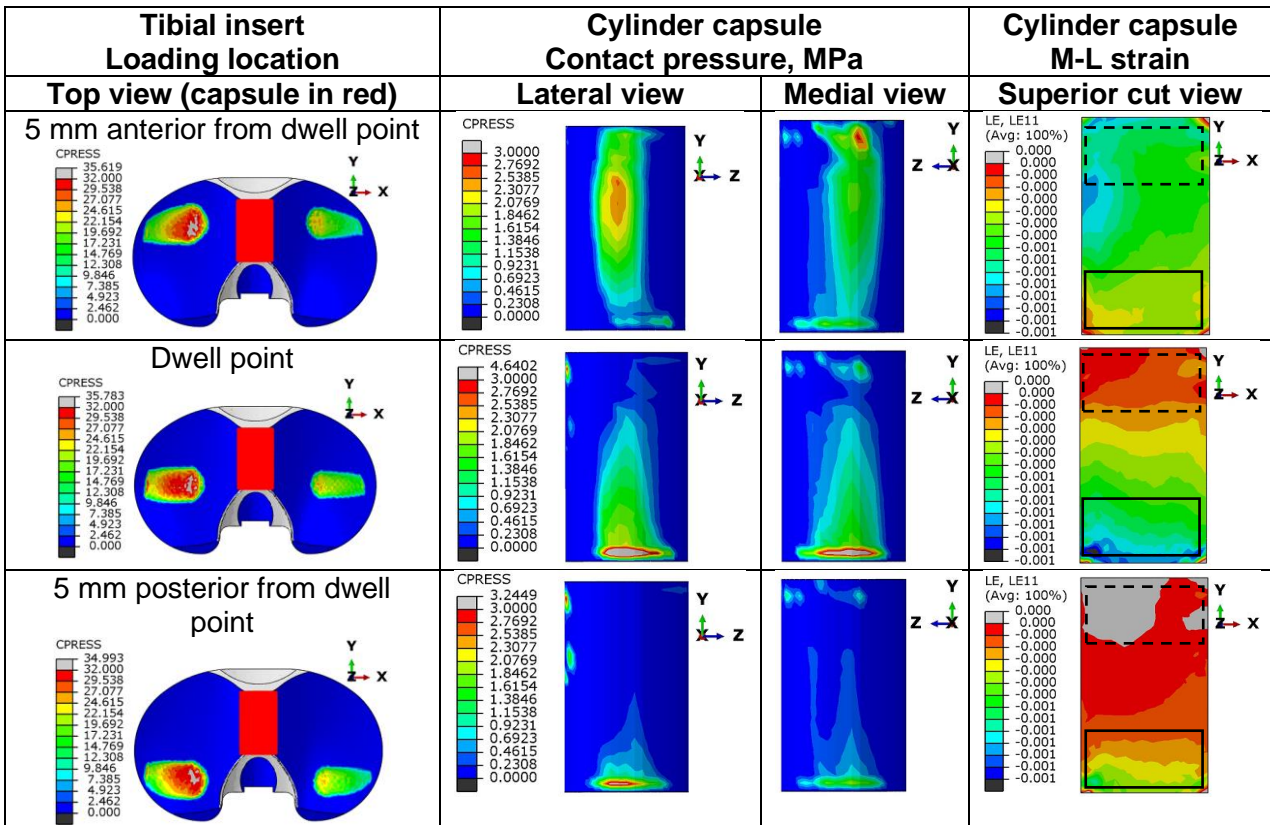
Table 5.10. Capsule contact pressure and strain, when tibial insert is loaded in three different locations with axial force of 5480 N and positive A-A moment 50740 Nmm. Black rectangles illustrate two strain gauges.

Tibial insert Loading location	Cylinder capsule Contact pressure, MPa		Cylinder capsule M-L strain
Top view (capsule in red)	Lateral view	Medial view	Superior cut view
5 mm anterior from dwell point			
Dwell point			
5 mm posterior from dwell point			
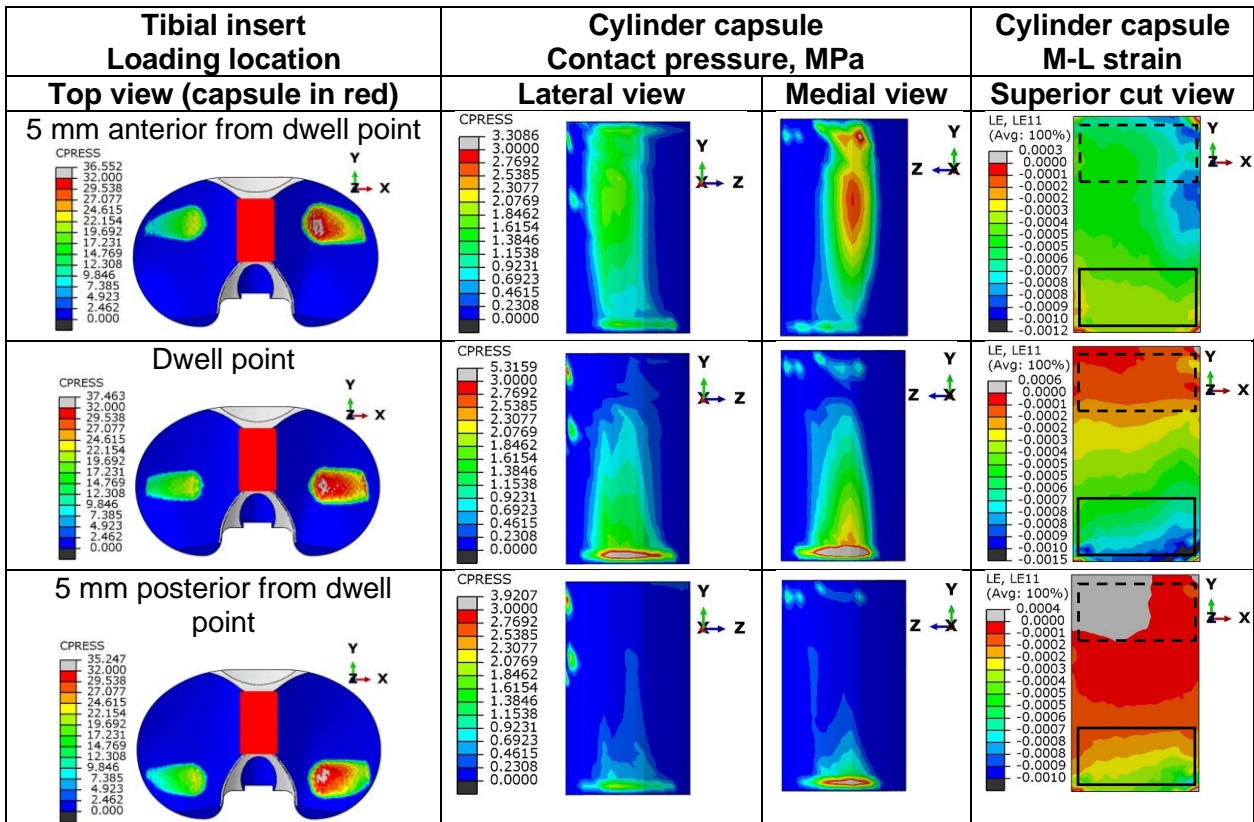
5.5.4 Discussion

Strain gauges could be potentially used to distinguish some of the loading scenarios, for example, to approximate axial force or to distinguish loading applied in different A-P locations. However, there are several limitations, which would make it difficult to calibrate strain signal against applied forces.

Initially, when the tibial insert will be plastically deforming the strain response will not be linear. However, if tibial insert would settle at a final shape due to strain hardening effect, the strain signal could become linear. Due to tibial insert's material creep, the strain gauges would stay constantly pre-loaded, therefore strain gauges would start showing signal strength only after exceeding a certain force threshold. Therefore, strain gauges are likely to be insensitive to relatively small forces, which need to be further investigated. An experimental study on instrumented tibial insert with embedded strain gauges under the articulating surfaces have shown the strain signal non-linearity and insensitivity due to material creep [122]. Clinically, it could be beneficial to distinguish forces with a certain accuracy, for example, if strain gauges could distinguish applied forces with 50 N accuracy, then it could allow record forces during manual clinical tests such as varus-valgus test.

The differences in hole size or interference/clearance fit (both capsule fit within the insert, and insert fit within the tibial tray) would affect strain signal strength and maybe also signal pattern. Capsule made of stiffer materials would show weaker strain signal. Additionally, it is unknown how the strain patterns would change with complex loading scenarios, for example, when the contact area would change due to femur flexion, or when both femoral condyles would apply load at different A-P and M-L coordinates due to I-E rotation.

5.6 Daily activity FEA (insert with a through hole)

5.6.1 Introduction

After comparing static FEA models, the next task was to compare the original and drilled insert with daily activity FEA models (described in previous Section 4.3). The limitation of static FEA models is that only a single axial force was applied at the dwell points, therefore no direct loading was applied at the walls of the drilled 10 mm hole. In comparison, dynamic FEA models take long computational time, but they can simulate a more realistic loading, which would be also applied directly at the walls of the drilled hole in the intercondylar area.

It must be noted that the dynamic FEA models were not validated, because there was limited literature to compare with and, due to technical issues, it was also not feasible to perform experimental knee simulator study in load control, as further described in Section 8.3.1 about experimental knee simulator study. The dynamic FEA models were performed with modified tibial insert design with a drilled through hole to show potential benefits and necessity for using dynamic FEA models for design optimisation studies.

5.6.2 Methods

The daily activity FEA models (previously described in Section 4.3) were repeated on a tibial insert with a drilled hole but without an internal capsule. Only the tibial insert geometry was changed, whilst all other FEA model parameters remained. The tibial insert had a through hole with diameter of 10 mm created at the intercondylar area at 6.5 mm height from the bottom face, leaving about 1.5 mm thick wall at the top and the bottom face (see Figure 5.1). Insert with a through hole was chosen, to represent the worst case scenario, to simplify the FEA model, and to represent the design chosen for the experimental knee simulator study (further described in Section 8.2).

5.6.3 Results

Figure 5.16 shows qualitatively that both original and drilled tibial inserts exhibit similar contour plots. Since the plotted contact areas and contact pressure patterns are similar, it could be assumed that also the wear rates would be identical. Full loading cycle is shown in Video 1 and Video 2.

j) Taken from Figure 4.40

k)
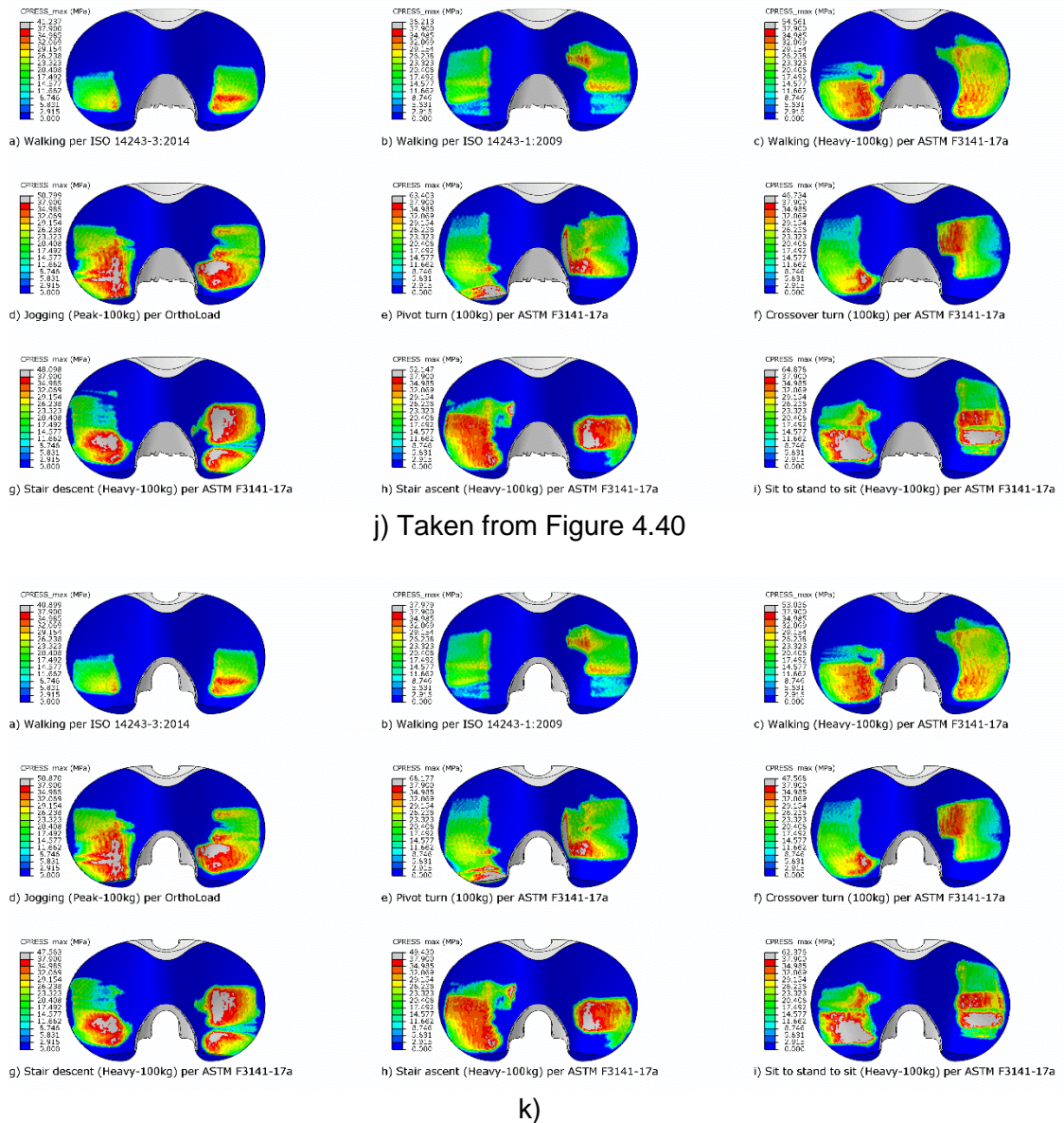
Figure 5.16. FEA contact pressure comparison between j) original tibial insert and k) tibial insert with a 10 mm through hole. Both designs show nine daily activity FEA models with maximum contact pressure value overlapping across all frames of one full loading cycle. Full loading cycle is shown in separate video files named "Video 1, CPRESS, original unmodified tibial insert, GMK Primary size 3 left.avi" and "Video 2, CPRESS, modified tibial insert with a hole, GMK Primary size 3 left.avi").

Von Mises stress contour plots for the drilled tibial insert (see Figure 5.17) were almost identical to the contour plots for the original tibial insert (see Figure 4.42). Both FEA models with ISO walking load showed the smallest stresses on the internal walls of the 10 mm hole. FEA models with jogging and pivot turn loading showed the largest stresses on the internal walls of the hole, in particular, the yield stress was exceeded at the posterior edge of the hole, which indicated plastic deformation.
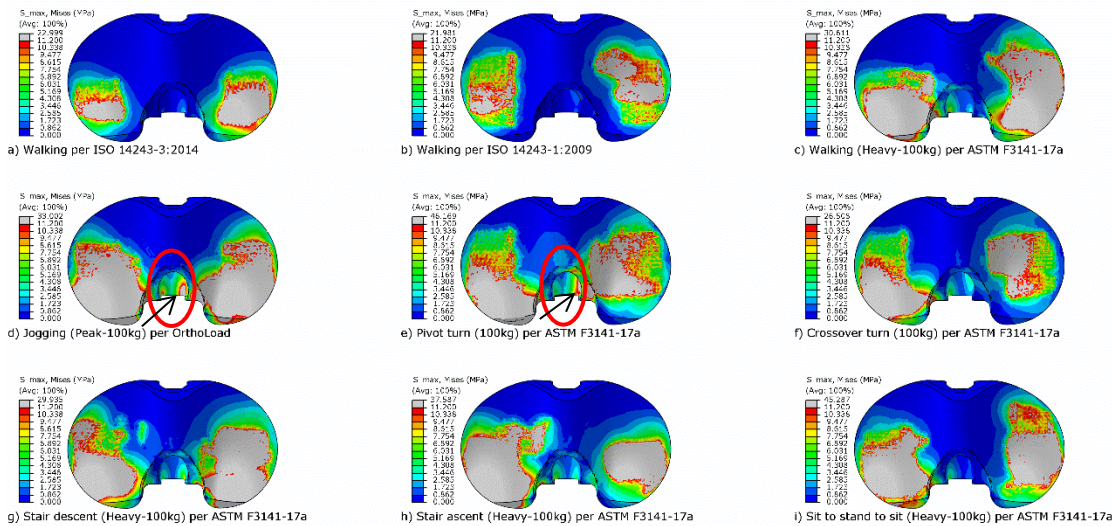
Figure 5.17. FEA Von Mises stress models for the tibial insert with a 10 mm through hole. Nine daily activity FEA model showing maximum Von Mises stress value overlapping across all frames of one full loading cycle. The grey area shows values above the true yield stress of 11.2 MPa. Red circle with black arrow highlights the areas where yield stress was exceeded at the posterior edge of the drilled hole for the jogging and pivot turn loading.

5.6.4 Discussion

The daily activity FEA models for the tibial insert with a 10 mm hole showed small differences from the original tibial insert when qualitatively comparing locations of the contact pressure and Von Mises stress contour plots. This indicated that the tibial insert with a 10 mm hole could have similar wear rates to the original tibial insert.

However, there might be problems with placing capsule with electronics inside the drilled hole. Jogging and pivot turn models indicated that plastic deformation could occur at the posterior end of the drilled hole. Such deformation could potentially lead to difficulties with reliable sensor measurements, for example, strain gauge measurements could become inaccurate due to plastic deformation. Additionally, if the 10 mm hole would be left unsealed at the anterior and posterior end, then after repetitive loading the capsule with electronics could potentially be pushed out of the tibial insert, since clinical cases have been reported with pushed out tibial locking bolt [185-187]. Therefore, further studies must be performed to assess the safety of the proposed instrumented tibial insert design.

5.7 Conclusion

Static FEA models were used as a parametric analysis tool which helped to optimise the instrumented tibial insert design. Whilst dynamic FEA models were not validated, they were still useful to illustrate the potential differences between various daily loading scenarios. Created FEA models helped with recognising potential problems and making following suggestions for design improvement:

1) A posterior drilled hole would be preferred over anterior drilled hole to prevent damaging anterior locking mechanism (as per design requirements in section 3.2).
2) In ideal scenario the capsule should be secured both from the anterior and posterior side to prevent the capsule from being pushed out (concluded from Figure 5.17).
3) A cylindrical shaped capsule provides the largest useful volumetric space for housing electronics (concluded from Figure 5.8).
4) Axial static FEA loading showed no Von Mises stress above yield stress near the cylindrical capsule walls (concluded from Figure 5.8)., however FEA models with daily activity loading should be further improved and considered for future design decisions.
5) The capsule is compressed in M-L direction; therefore, strain gauges should be also aligned in the M-L direction (concluded from Figure 5.9).
6) Strain gauges, positioned in the intercondylar area, could help with approximating the total axial force and distinguishing the loading location in the A-P direction, but would not be able to distinguish difference between the medial and lateral condyle pressure, which should be further considered (concluded from Table 5.11 to Table 5.10).
7) The strain gauge accuracy could be affected by the plastic deformation of the drilled hole walls, which should be further considered (concluded from Figure 5.17).

The experimental results with 3 different tibial insert groups under axial compression gave further indications that a tibial insert could retain its structural strength even if a hole was drilled at the intercondylar area and a rigid object was placed inside the hole.

5.8 Limitations and future work

In all FEA studies presented in Section 5 no mesh convergence analysis was not performed for the capsule, because it was decided to keep a matching mesh size of 1.3 mm for all components to reduce computational time. Since 1.3 mm was a suitable mesh size for the tibial insert with 7 mm thickness under direct loading, then it was also seen sufficient for a capsule with 10 mm thickness. In this FEA study it was only of interest to observe overall deformation patterns of the capsule and make relative comparison between the models. The absolute values for the capsule measurements were of less importance, since these values were not experimentally compared.

Only static FEA model could be validated with laboratory experiments. Further work must be done to validate dynamic FEA models. The described dynamic FEA models of daily activities could not be validated, because there was limited literature to compare with. It was also not feasible to perform validation with knee simulator study in load control, as further described in Section 8.3.1 about knee simulator testing.

The current study showed that Instron test machine in combination with Tekscan pressure film could be used to validate static FEA models without using a knee simulator. In the described method an axial load was applied at 0° flexion in a single location. However, this validation method could be further improved, for example, by changing the loading location in A-P direction or I-E rotation, changing the femoral flexion angle, or simultaneously applying axial force with tibial torque (this can be achieved with Electropulse E10,000 materials testing machine).

Parametric modelling and design optimisation with FEA could be also further expanded. For example, it could be of interest to analyse the effect of tibial component misalignment, the effect of femoral condyle radius to reduce edge loading effect, or the effect of cavity dimensions to gain more empty volume for electronics.

6   Experimental strain gauge study

6.1 Introduction

This chapter relates to research Objective 1 (fulfil the design requirements), Objective 3 (develop test methods), Objective 6 (testing with modified insert), and Objective 7 (testing with sensors and prototype optimisation). Specifically, this chapter outlines the preliminary physical test results, which investigate the feasibility of the first design requirement: to perform sensor measurements from within the hole at the intercondylar area. This study describes the use of strain gauge sensors.

This chapter presents a combination between computational and experimental studies. FEA models were used in conjunction with experimental studies. It was not possible to arrange the chapter in the chronological order, therefore chronological order of computational and experimental studies is shown in Appendix A.

6.2 Proof of concept with UHMWPE shells

At first a simplified test method was developed to investigate the proposed design concept to place sensors in a hole at the intercondylar area of the tibial insert. Specifically, the aim was to answer the following two questions:

- i)   Is it possible to indirectly approximate a force applied to the articular surface, if the sensors are placed within the intercondylar area?
- ii)   Is it possible to make measurements through a capsule, which is placed inside a hole with an interference fit?

6.2.1 Specimen preparation

This test used a 20 x 45 x 75 mm rectangular block with a cylindrical hole and a capsule made of two cylindrical half shells (Figure 6.1). The block simulated a simplified geometry of tibial insert with a cavity placed in the intercondylar area. The half shells were used, because it was the only possible way to attach strain gauges on the internal walls. The block and shells were machined out of UHMWPE GUR 1120 material (non-medical grade equivalent of GUR 1020).

Figure 6.1 Rectangular block with a cylindrical hole and two cylindrical half shells.

The hole within the block was machined to 10 mm diameter. Diameter of 10 mm was chosen, since it provided sufficient space to insert commercial strain gauges. Two half capsules were machined to have outer diameter of 9.8 mm, inner diameter of 6 mm, and length of 20 mm. Even though, in theory there should have been a free fit with a 0.2 mm gap, some amount of force was needed to press in the half shells into the hole. This indicated that there was some interference fit, most likely caused by manufacturing imprecisions. The effect of interference was not investigated.

Both shells had one strain gauge attached (120 Ω resistance) to the internal surface at 90° to the longitudinal axis (Figure 6.2). The strain gauges were attached with Loctite Super glue "All plastics" (Henkel, Germany). The strain gauges were used to detect the deformation of the cylindrical cavity walls.
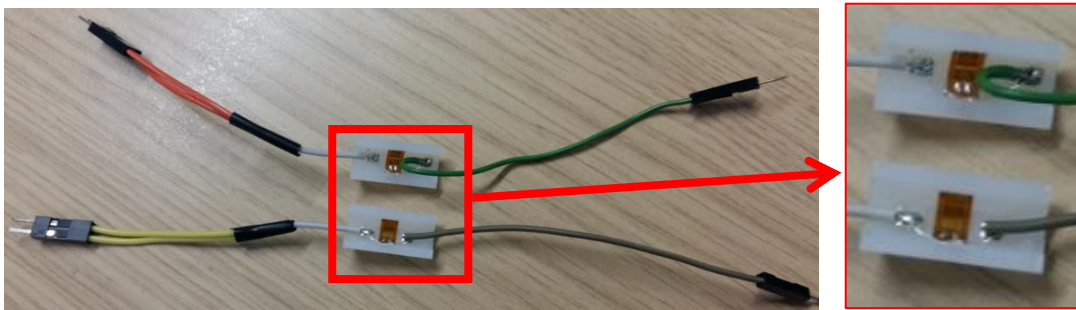
Figure 6.2 The internal surface of the half capsules with attached strain gauges at 90° to the longitudinal axis (aligned in S-I direction).

After attaching the strain gauges, both shells were pressed inside the block. The shells were placed the middle of the hole and were rotated to face one half of the block (Figure 6.3).
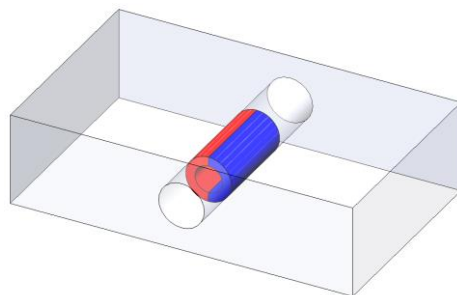
Figure 6.3 Two half shells (red and blue) placed in the middle of the cylindrical hole.

6.2.2 Test setup

Axial compression tests were performed to observe the strain gauge response. The test equipment setup is shown in Figure 6.4. The compression tests were performed using Instron 3366 (Instron®, USA) materials testing machine. The applied force and displacement were controlled and recorded by the Instron computer. The block with the embedded strain gauges was placed on the base plate, which was connected to the

test machine`s bed. The block was compressed with the top plate, which was connected to the load cell and the displacement actuator. Strain gauges with resistance of 120 Ω and resistor of 120 Ω were used for the three-wire quarter bridge strain gauge circuit. The strain gauge signal was passed through a load cell amplifier HX711 and measured with the Arduino Uno board (v1.8.12, © 2020 Arduino, Arduino LLC, USA) as shown in Figure 6.5.The signal was recorded on the laptop with the Processing 3 (version 3.4, Processing Foundation 501©(3), USA) computer program. Help with Arduino Uno and Processing 3 was received from Dr. Ksenija Vasiljeva[1] [188].
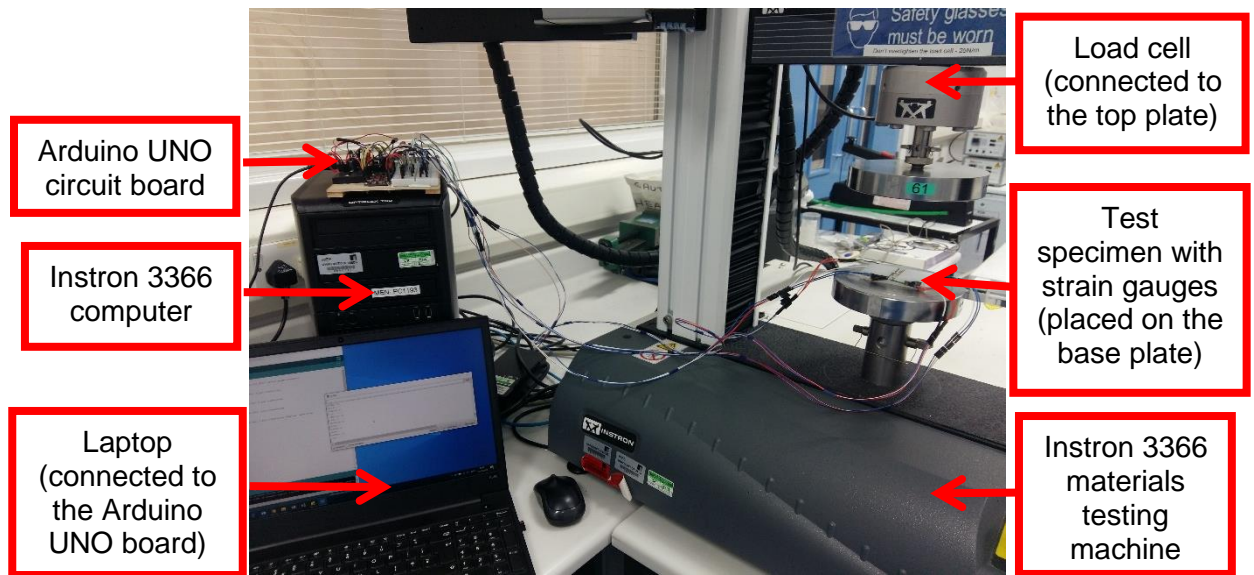
Figure 6.4 Test equipment setup.
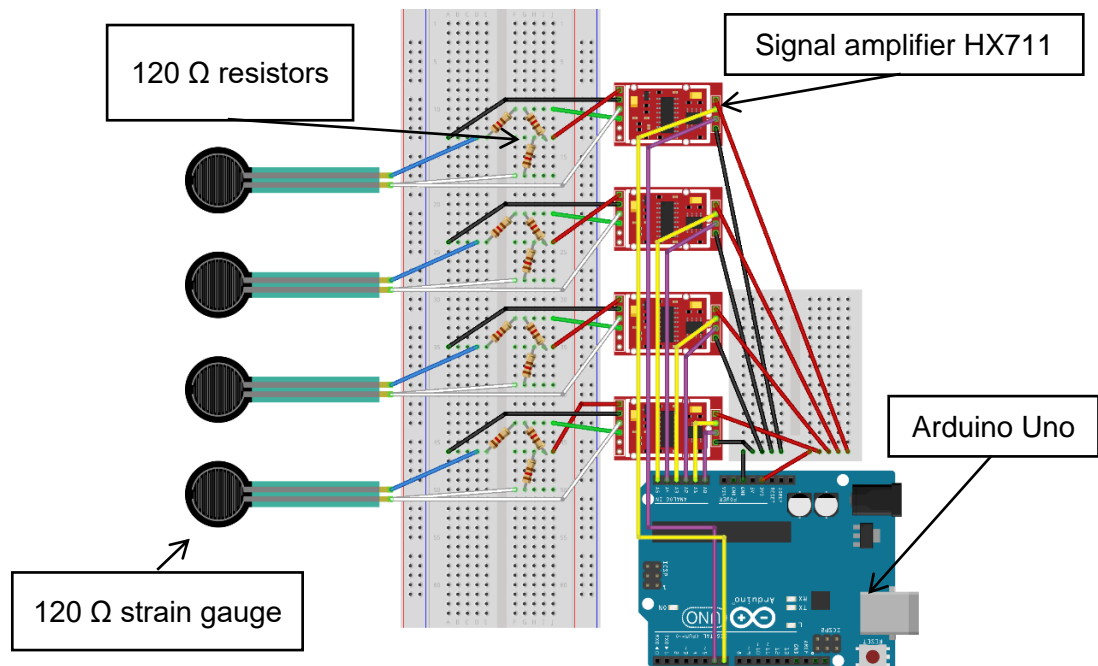
Figure 6.5 Arduino Uno circuit board setup with four strain gauges.

---

[1] The Arduino circuit board and the Processing script for recording strain signal was provided by Dr. Ksenija Vasiljeva from the iSMART project team (LIRMM, University of Leeds).

Two compression tests were performed:

    i)   Symmetrical load test (Figure 6.6a);

    ii)   Single side load test (Figure 6.8a,b).

During the symmetrical load test, the block was compressed between two metal plates (Figure 6.6a). This test was performed to check if the strain gauges worked correctly and gave the same signal response, since the load was equally distributed across the surface. The test was completed using displacement control. The input force and displacement profiles are shown in the results section (Figure 6.6 b,c).

During the single side load test, the block was compressed via a rectangular metal fixture approximately at 21.25mm distance from the cavity (Figure 6.8 a,b). The single side load test was performed to observe strain gauge response when force is applied only to one side of the block. The test was completed in force control. The applied input force profile is shown in the results section (Figure 6.8c,d).

During all strain gauge measurements, the data was only assessed qualitatively. For the initial proof of concept testing, it was only of interest to observe whether the strain signal is changing and whether the strain signal pattern is aligned with the applied input force.

6.2.3 Results

The strain gauge signal output, recorded during the symmetrical load test, are shown in Figure 6.6d. The negative strain signal represents compression. Figure 6.6b shows that the specimen was loaded with varying displacement profile, which also created a corresponding varying force profile from 500 to 4000 N (Figure 6.6c). Figure 6.6d and Figure 6.7 shows that the output voltage profile of both strain gauges directly follows the force profile. This indicates that both strain gauges recorded the deformation of both half shells. Additionally, both strain gauges gave nearly identical signal.
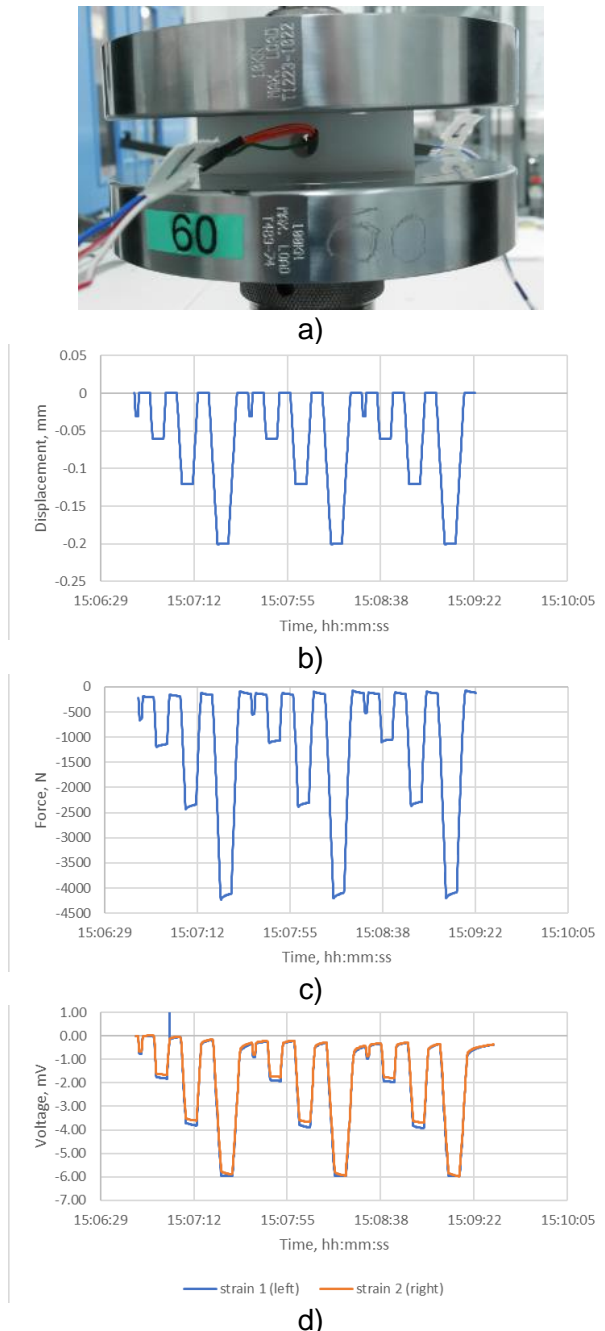
Figure 6.6 Symmetric load test a) setup, b) the displacement input, c) the force output, and d) the output voltage from the strain gauges. The negative strain signal represents compression.
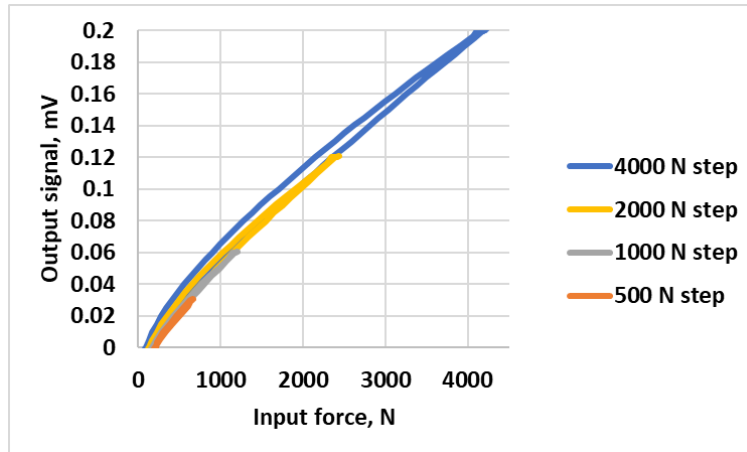
Figure 6.7 Strain gauge output signal shows linear relation to the input force.

The strain gauge output signal, recorded during the single side load test, is shown in Figure 6.8e and Figure 6.8f. Figure 6.8c and Figure 6.8d show that the specimen was loaded with cyclic force up to 1000 N. Figure 6.8e and Figure 6.8f show that the strain gauge signal changed polarity, which was dependant on the load placement. The strain gauge on the directly loaded side gave a positive signal (tension), while the opposite strain gauge gave a negative signal (compression). The relation between the output voltage profile and the input force profile was not always linear as shown in Figure 6.8g,h. Figure 6.8e shows a signal drop for the left strain gauge when it reaches +0.2 mV, during the left side loading.
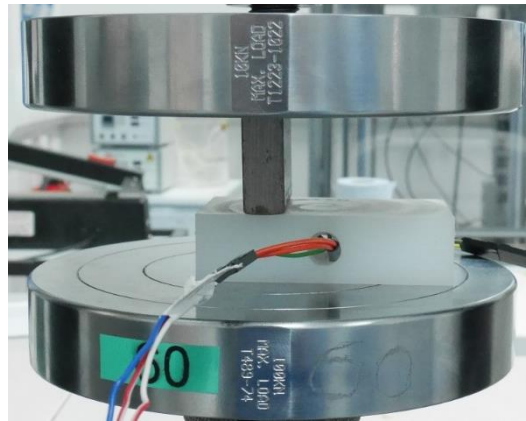
a) Left side loading setup

b) Right side loading setup
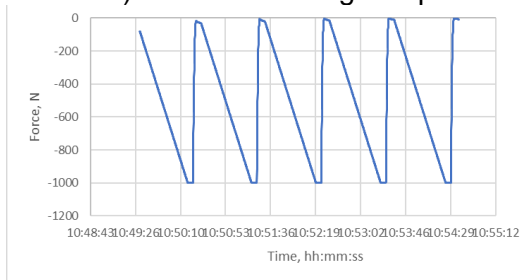
c)
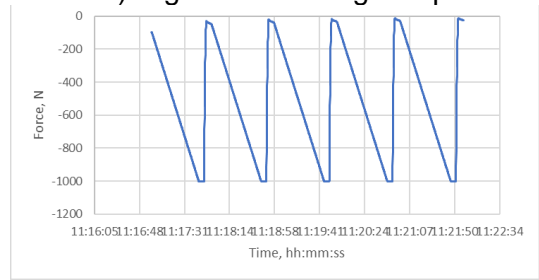
d)
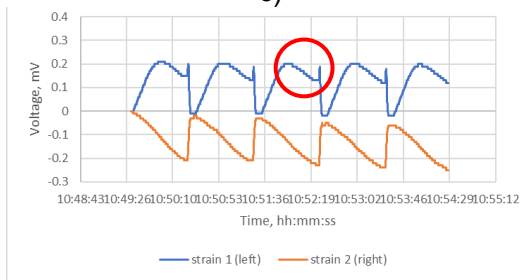
e)
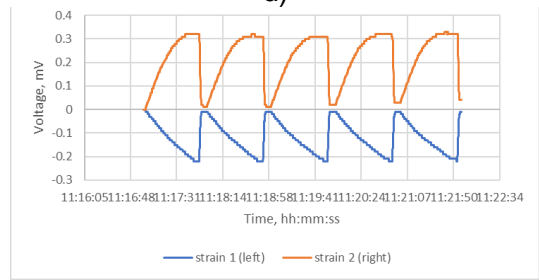
f)
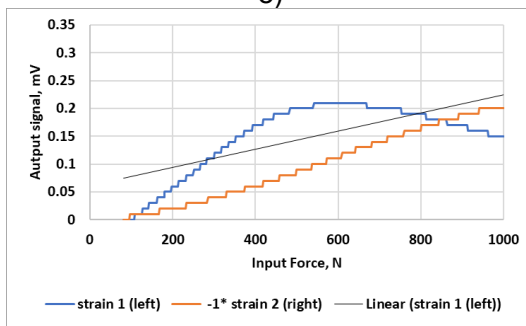
g)
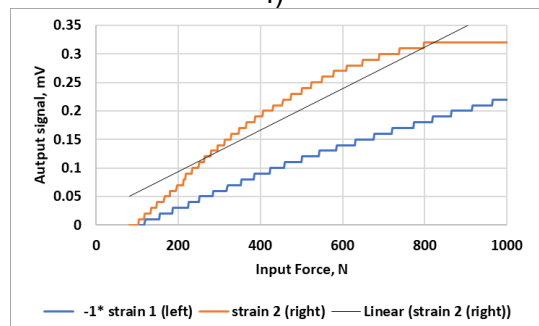
h)

Figure 6.8 Single side load test a,b) setup, c,d) the input force,
e,f) the output voltage from the strain gauges, g.h) relation between the input force and
the output signal. Signal drop highlighted with red circle.

6.2.4 Discussion

The axial compression test on a 20 x 45 x 75 mm rectangular block was performed to assess the conceptual idea of sensor placement in the intercondylar area.

The symmetrical load test showed that both strain gauges gave nearly identical voltage signals under equal loading conditions. This test also showed that the output strain gauge signal is directly proportional to the input loading profile.

The single side load test showed a difference in the strain gauge loading both in signal strength and the signal polarity. It was expected to see a change in signal strength, with the loaded side showing higher signal. Both strain gauges showed a signal increase which corresponds to the input force profile. However, on the loaded side not only was the signal strength increased (Figure 6.8f), but the signal polarity was also reversed. This indicated that the half capsule on the loaded side is deformed under tension, while the opposite half capsule is under compression. The signal polarity change could be a beneficial feature, since it allows to distinguish the left-sided loading from the right-side loading. Figure 6.8e shows a signal drop for the left strain gauge when it reaches +0.2 mV. It is unknown what caused the drop in signal, however, similar signal drop was also observed in the further tests, which seemed to be related to combined deformation in both S-I and M-L direction (further discussed in chapter 0).

The single side load test resulted in a weaker strain gauge signal, which was about 10 times smaller compared to the symmetric load results at 1000 N force. This indicates that indirect strain measurements will have a disadvantage of a reduced signal strength, which would also reduce the accuracy of force measurements.

In conclusion, this preliminary test supported the proposed design idea to place sensors in the intercondylar area. The results showed that it could be possible, firstly, to indirectly measure load applied to the articular surface with sensors placed in the intercondylar area and, secondly, to make measurements through shells made of UHMWPE without gluing strain gauges directly to the tibial insert.

6.3 Proof of concept with SS316 shells

It was of interest to test whether capsule shell could be made any other material than UHMWPE. Due to manufacturing limitations the UHMWPE half shells could only be machined with a maximum inner diameter of 6 mm (wall thickness of 2 mm) without deforming the capsule during CNC machining. Consequently, limiting the volume available to fit electronic circuitry. Therefore, it was of interest to investigate whether strain gauge signal could be recorded if the half shells were made of another medical grade material, such as, stainless steel grade SS316.

Two half shells made of SS316 were machined with outer diameter of 9.9 mm, inner diameter of 9 mm and length of 30 mm. Both shells had one strain gauge attached (1000 Ω resistance) to the internal surface at 90° to the longitudinal axis. Strain gauges were glued on with Loctite brush on super glue. After attaching the strain gauges, both shells were pressed inside the GMK Primary CR tibial insert (size S3/10) with approximately a 10 mm hole (Figure 6.9). Even though, a drill with a diameter of 10 mm was used, the drilled hole showed some deviations from the expected geometry, as shown in Figure 6.10. The shells were rotated to face one half of the insert, the approximate sensor location is shown in Figure 6.11. The strain gauge signal was recorded with a custom circuit board and a custom Matlab script, developed by electronics engineer Thomas Carpenter [189] from the iSMART project team. The Matlab script measured change in strain gauge resistance. Previously used Arduino Uno circuit board (shown in Figure 6.5) was replaced with a custom circuit board (made by Thomas Carpenter) to help Thomas with the development of a new circuit board.

a)   b)
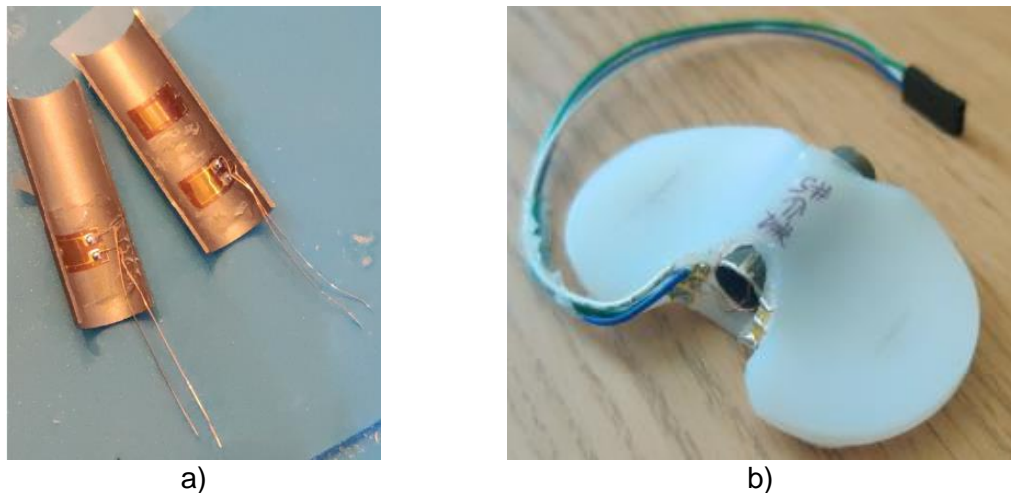
Figure 6.9 Images of SS316 half shells a) with attached strain gauges (aligned in S-I direction) and b) inserted into the tibial insert (GMK Primary CR S3/10).

a)   b)
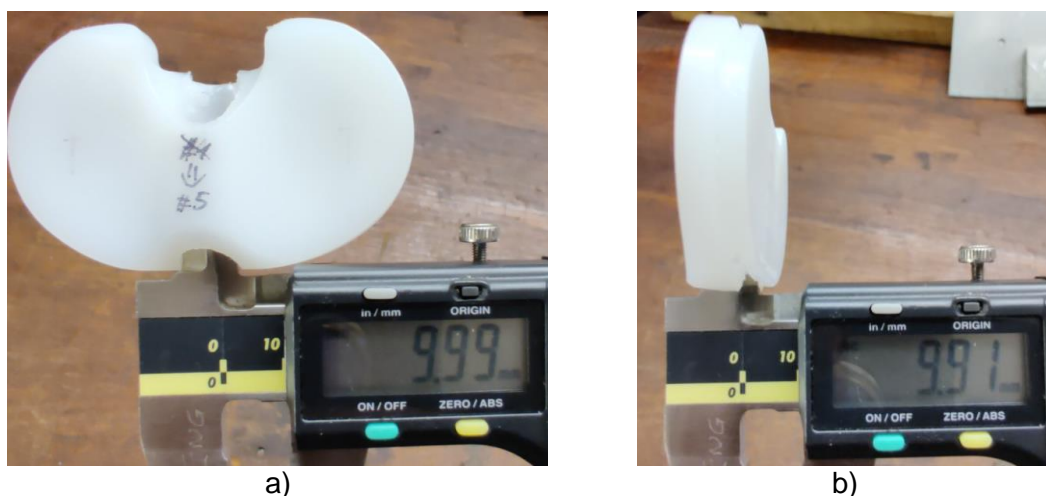
Figure 6.10 Example hole width for one specimen a) in M-L direction was approximately 9.99 mm and b) in S-I direction approximately 9.91 mm inserted into the tibial insert (GMK Primary CR S3/10).
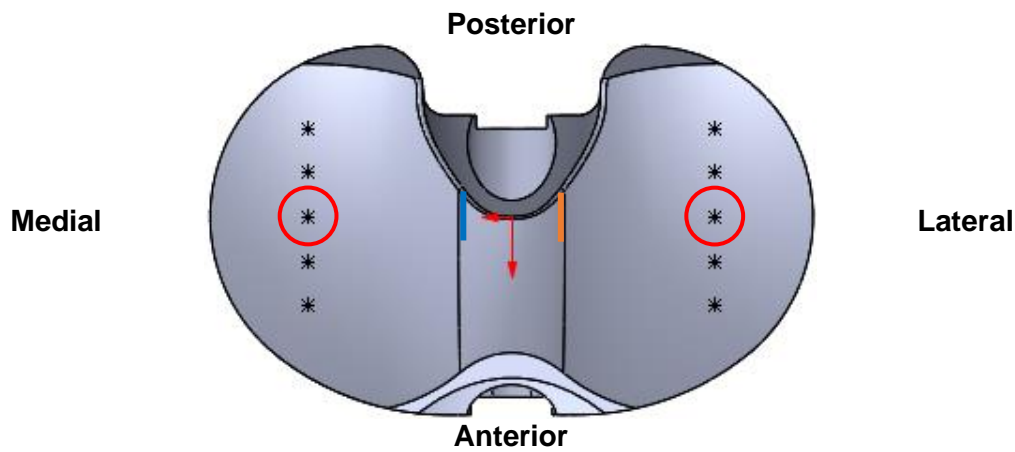
Figure 6.11 Example illustration of approximate strain gauge location (orange and blue line) and the location of applied loading at the dwell point (red circles). Strain gauges aligned in S-I direction.

An axial compression test was performed by loading the tibial insert with a femoral component (Figure 6.12). The applied force was cyclically increased from 10 N to 100 N, 500 N, 1 kN, 2 kN, 3 kN, 4 kN, 5 kN, and 6 kN.
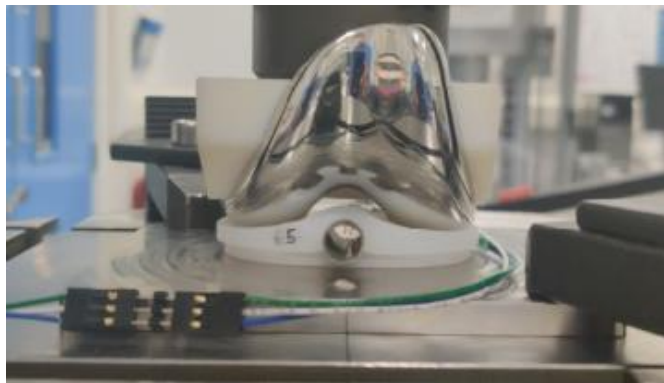
Figure 6.12 Test setup with the SS316 half shells.

6.3.1 Results

Strain measurements were recorded from both half shells. The measurements showed that the output signal profile of both strain gauges follows the input force profile. The increase in force also increased the strain gauge output signal. However, the strain signal was not directly proportional to the input force and indicated both tensile and compressive strains (Figure 6.13).

a)

b)

c)
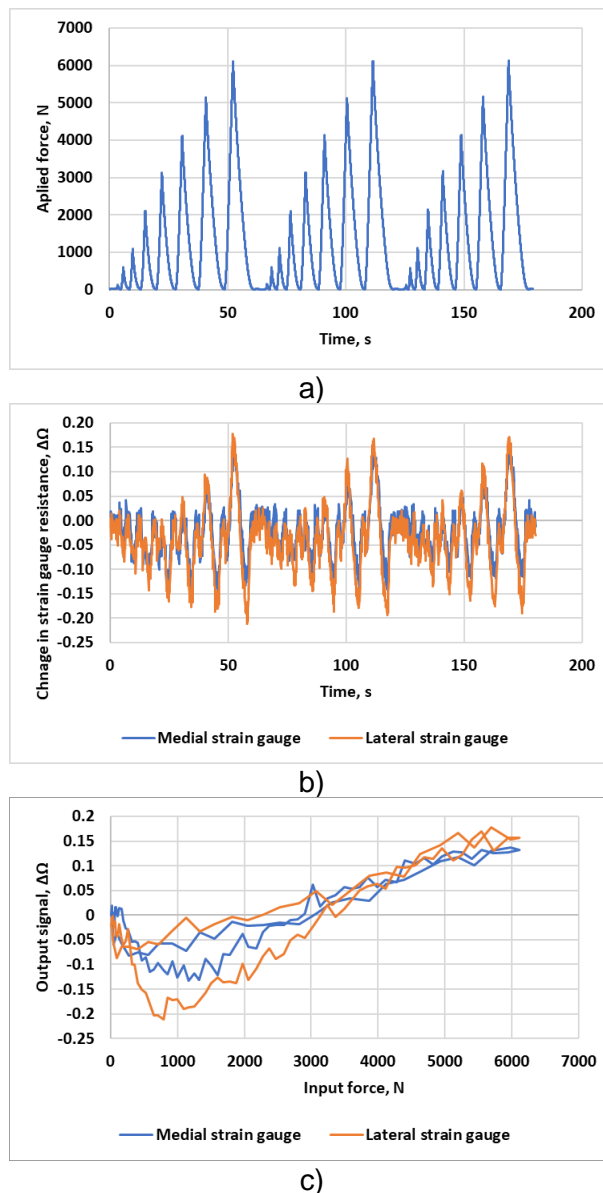
Figure 6.13 Example data a) of the input force, and b) the medial and lateral strain gauge signal output recorded from two strain gauges each attached to one shell made of SS316, and c) relation between the output signal and the input force.

6.3.2 Discussion

This test proved that strain measurements could be obtained by attaching strain gauges to a rigid metal shell made of medical grade SS316. The measurements revealed a pattern where the strain signal gradually increased with larger forces. However, the used capsule design did not provide uniform signal since strain gauges showed both compressive and tensile strains. Since there strain signal was not directly proportional to the input force, it would make it difficult to perform force estimations with this particular strain gauge setup. No further testing was performed to modify SS316 capsule design and improve strain gauge measurements. During the preparation of the half shells, it was difficult to both glue and orient the strain gauges, therefore more efficient potting method was developed.

6.4 Proof of concept with potted strain gauges

In order to both simplify strain gauge assembly and also seal the electronic components a new manufacturing technique was used. Supervisor Bernard H. van Duren came with the idea that strain gauges could be glued on a 3D-printed frame, and the frame could be placed inside a resin mould and potted with a liquid resin (Figure 6.14).

a)	b)	c)	d)
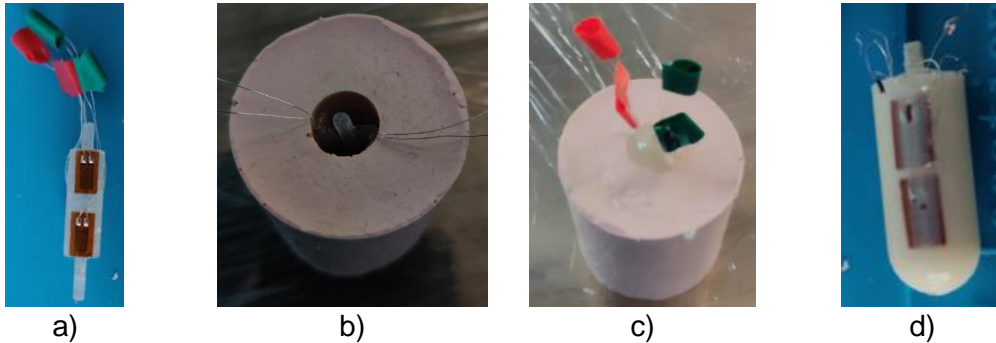
Figure 6.14 During potting procedure a) strain gauges were glued on a 3D-printed frame (aligned in A-P direction), b) the frame was placed inside the mould with diameter of 10 mm, c) the mould was filled with liquid self-curing resin, and d) then a solid capsule was removed and pushed inside the tibial insert.

The potting could be performed both with self-curing polymethyl methacrylate (PMMA) and polyurethane (PU) resin. For initial studies, a CENTRI™ BASE Cold Cure (WHW Plastics, UK) self-curing resin consisting of PMMA was used, because it had dental bone cement properties. However, due to potting difficulties, for later studies the PMMA resin was replaced with PU resin Polycraft SG2000 (MB Fiberglass, Northern Ireland), since PU resin ensured less shrinking (Figure 6.15), was easier to pour, and could be safely used in a home environment for prototyping. The curing temperature was not recorded whilst potting the PMMA and PU resin.

a)	b)
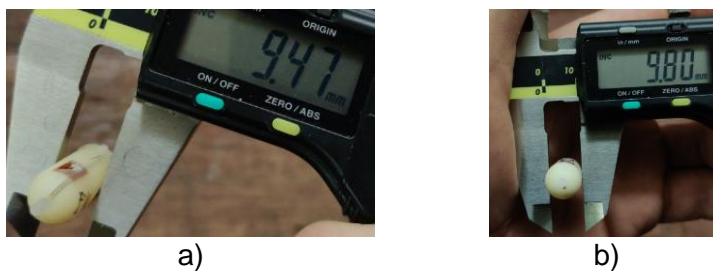
Figure 6.15 When using the same mould with diameter of 10 mm a) the capsule made of PMMA resin showed larger shrinkage down to diameter of 9.47 mm whilst b) the capsule made of PU resin shrank only to diameter of 9.80 mm.

The strain gauge (120 Ω) measurements were made with Arduino Uno circuit board (Figure 6.5). To improve data recording, the Arduino signal was recorded directly to

Excel spread sheet by using open source script PLX-DAQ[2] [190] (version 2.11, published under alias "Net^Devil" [191]).

Axial compression test was performed by loading a simplified tibial insert replica with a femoral component (Figure 6.12). The insert replica was made of UHMWPE GUR1020 and had a simplified geometry with overall dimensions of 15 x 45 x 70 mm. The insert replica was 10 mm thick at the articulating surface and 15 mm thick at the intercondylar area with a hole diameter of 10 mm. The applied force was cyclically increased from 10 N to 100 N, 250 N, 1 kN, 3 kN, and 6 kN.

| a) | b) | c) |
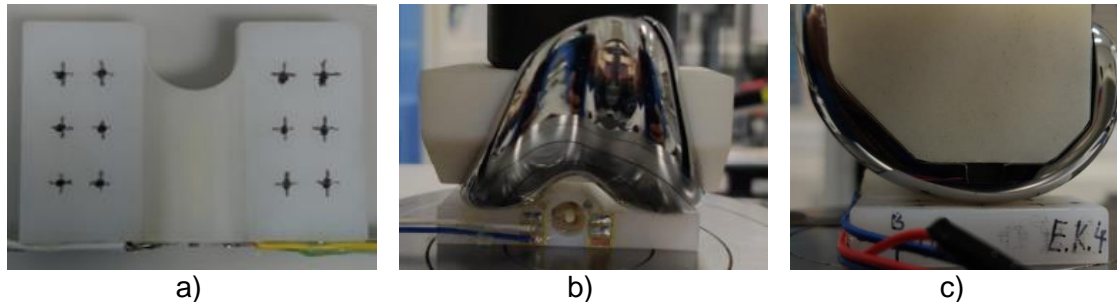
Figure 6.16 Test setup with a) a rectangular tibial insert replica potted with PMMA resin b) compressed with a femoral component c) approximately at the middle of the articulating surface.

The capsule contained four strain gauges, all being aligned in A-P direction. There was no particular rational for positioning strain gauges in A-P direction. It was simply of interest to see how strain measurements would differ from previous strain gauge measurements in S-I direction. It was also of interest to investigate whether the strain signal would change in different locations, therefore, four strain gauges were used. Two strain gauges were positioned both on medial and lateral side (Figure 6.17).
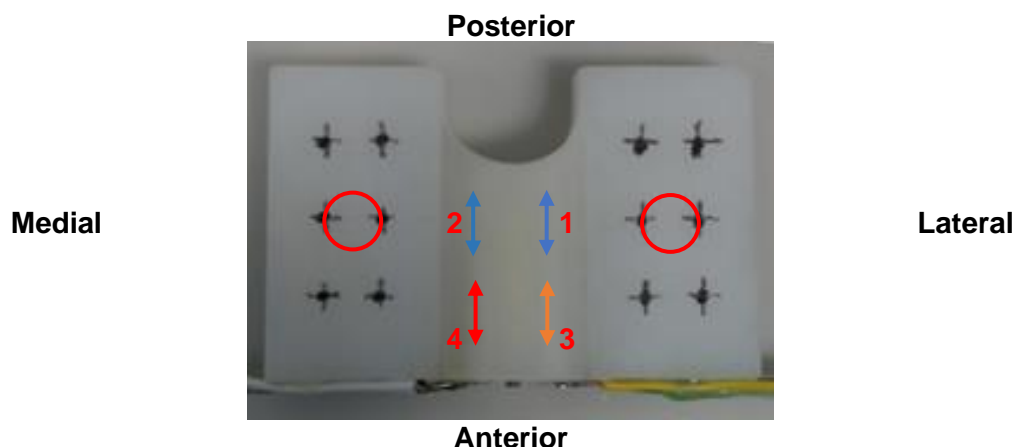
Figure 6.17 Example illustration of approximate strain gauge locations and the locations of applied loading at the dwell point (red circles). All four strain gauges were aligned in A-P direction (shown with arrows and numbers).

---

[2] PLX-DAQ download is also freely available from PARALLAX (PARALLAX, USA) website with release note stating that "API modCOMM module written by David M. Hitchens, distributed freely" and have "updates to modCOMM for 64-bit VBA by Martin Hebel".

6.4.1 Results

Strain measurements were recorded from all four strain gauges. The measurements showed that the signal output profile of all strain gauges follows the input force profile. The increase in force also increased the strain signal. However, the output strain signals were not directly proportional to the input force and some strain gauges indicated both tensile and compressive strains (Figure 6.18). No force versus voltage plot was made, since the strain signal showed obvious spikes and chaotic signal behaviour, especially for the strain gauge 3. The two posterior strain gauges positioned closer to loaded area showed stronger signal compared to the two anterior strain gauges, which were positioned further away from the loaded area.

a)

b)
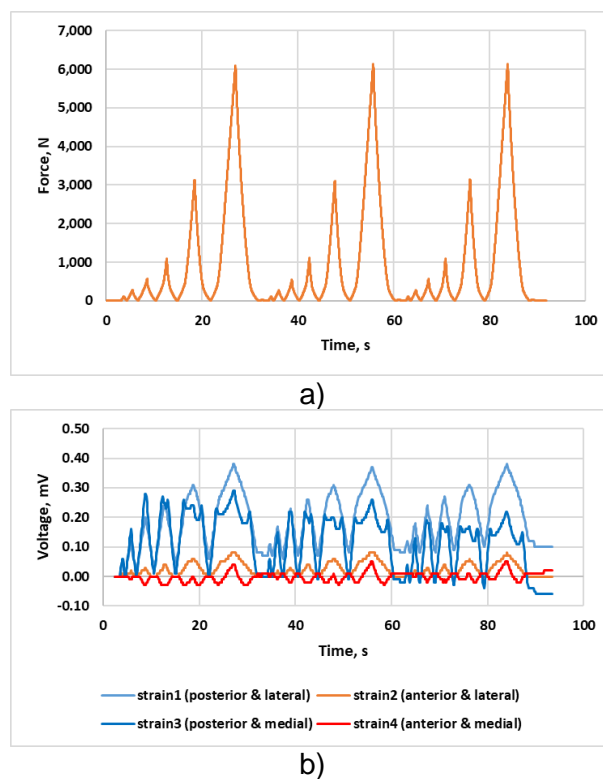
Figure 6.18 Example data b) of the input force, and c) the output voltage from the strain gauges.

6.4.2 Discussion

This test proved that strain measurements could be obtained if the strain gauges are potted inside a self-curing resin made of PMMA. Therefore, a potted resin capsule could be used as an alternative to the previously used half shell capsules to measure indirect loading. The measurements revealed a pattern where the strain signal gradually increased with larger forces. The measurements also showed that the strain gauges positioned closer to the loading point will show stronger signal, which indicated that strain gauge signal could be used to estimate the loading location in A-P direction.

However, the used capsule design did not provide uniform signal since some strain gauges showed both compressive and tensile strains. The strain signal drop was a reoccurring issue, which seemed to be related to combined deformation in both S-I and M-L direction (this is discussed in detail in chapter 0).

The curing temperature was not recorded whilst potting the PMMA and PU resin. Since UHMWPE material is sensitive to thermal treatment (see Section 1.6.2.3), in the future studies it should be considered whether curing temperature would have an effect on altering UHMWPE material properties or the geometry of the hole or the insert.

6.5 Strain gauges aligned in M-L direction

Previous tests described in sections 6.2, 6.3, and 6.4 revealed several challenges:

1. Firstly, it was difficult to push a capsule inside the tibial insert.
2. Secondly, the strain gauges were showing random non-linear signal.
3. Thirdly, it was difficult to precisely position the specimens onto the testing bed.

Therefore, several improvements were made regarding potting and test setup. The potting procedure was improved by potting strain gauges directly inside the tibial insert (Figure 6.19) with a PU resin to ensure the best fit within the hole. Additionally, previously made FEA models (see Figure 5.9) indicated that the capsule is mostly deformed in the M-L direction. Therefore, during strain gauge assembly, four strain gauges were glued on a 3D-printed replica of electronic components, placed in the centre of the capsule instead of the outer walls, and aligned in M-L direction (see Figure 6.20 and Figure 6.21).

a)   b)   c)
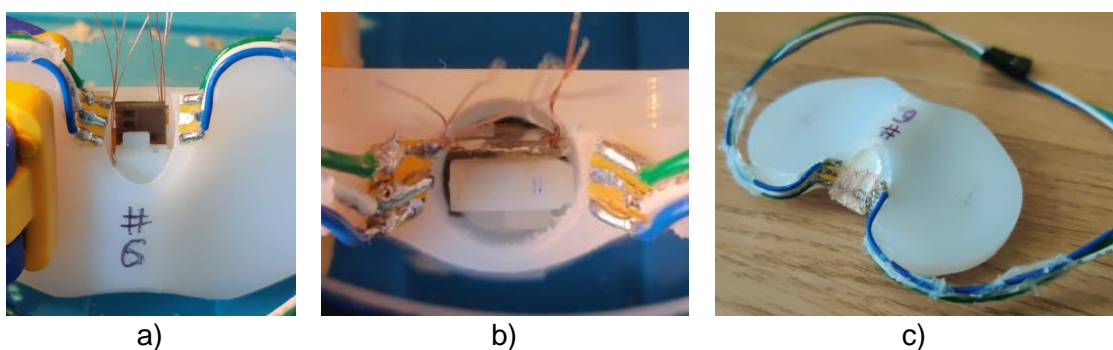
Figure 6.19 Example image showing a,b) strain gauge location before potting and c) tibial insert after potting with PU resin.

a)   b)

Figure 6.20 Example image from a) inferior view and b) side view, showing four strain gauges aligned in M-L direction and attached to a 3D-printed replica of electronic components.
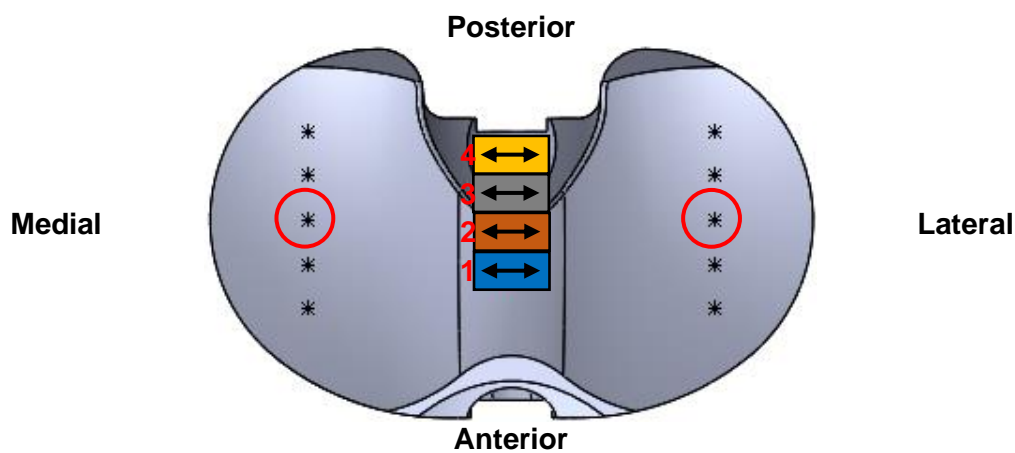
Figure 6.21 Example illustration of approximate strain gauge location and the location of applied loading at the dwell point (red circles). Strain gauges aligned in M-L direction (shown with arrows).

The experimental test setup on the Instron 3366 machine was improved by improving fixturing. The tibial insert positioning precision was improved by creating a custom metal tray fixture. The tray fixture had the geometrical features of the tibial tray with anterior and posterior locking mechanism (Figure 6.22). The positioning in A-P and M-L direction was controlled by aligning the tibial fixture with drawn reference lines on the Instron base (previously described in Section 4.2.11) as shown in Figure 6.23. The dwell point was used as the zero coordinate for A-P position. Two locking plates were used to replicate a locking mechanism and prevent tibial insert from lifting whilst being loaded.

| a) | b) |
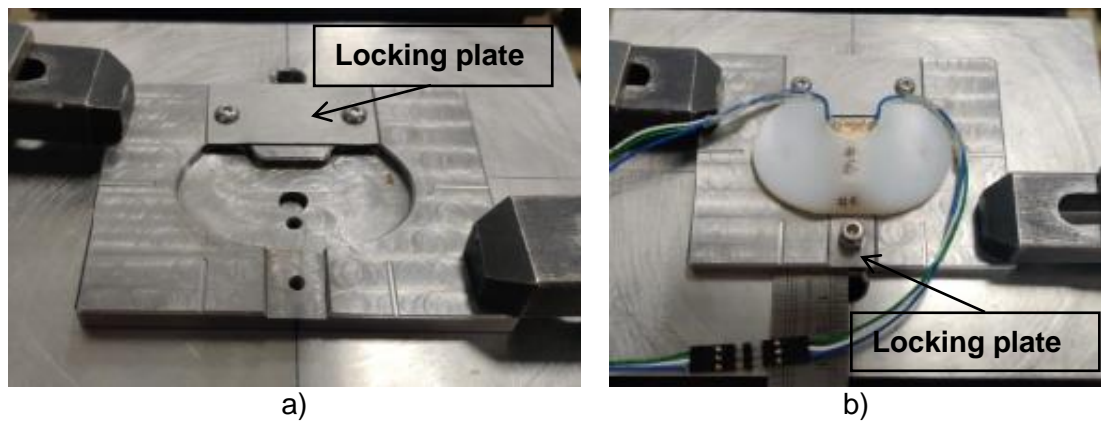
Figure 6.22 Custom made tibial tray fixture shown a) empty with attached posterior locking plate and b) with a tibial insert secured with anterior and posterior locking plate.
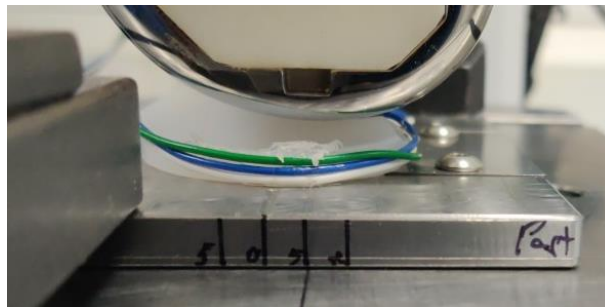
Figure 6.23 Example image showing the tibial insert positioned 5 mm posteriorly from the dwell point. Dwell point was the zero coordinate for A-P position.

Axial compression test was performed by loading a GMK Primary tibial insert size S3/10 with a left femoral component size S3. The force was applied in four locations along the A-P direction to assess signal differences between all strain gauges: 5 mm anterior from the dwell points, at the dwell points, 5 mm and 10 mm posteriror from the dwell points. The applied force was cyclically increased from 10 N to 100 N, 500 N, 1 kN, 2 kN, 3 kN, 4 kN, 5 kN, and 6 kN. This test used 1000 Ω strain gauges and signal was recorded with the custom MatLab script.

6.5.1 Results

Strain measurements were recorded from all four strain gauges. The measurements showed that the signal output profile of all strain gauges followed the input force profile. The strain signal could be qualitatively distinguished and recognised for seven force peaks between 500 N to 6 kN. Strain gauges aligned in M-L direction showed the best output signal alignment with the input force. Each strain gauge showed different signal strength depending upon load position along the A-P direction (Table 6.1). For example, strain gauge No. 1 positioned at the anterior side showed the largest signal of around -5Ω when force was applied 5 mm anterior from the dwell point and showed the smallest signal of around -0.5Ω when force was applied 10 mm posterior from the dwell point.

Table 6.1. Signal output from four strain gauges aligned in M-L as a result of applied input force. Each strain gauge shows different signal strength dependant on the loading location.

Input force

Loading location	Strain gauge output
5 mm anterior from dwell points.	

| **At dwell points.** | |

| **5 mm posterior from dwell points.** | |

| **10 mm posterior from dwell points.** | |
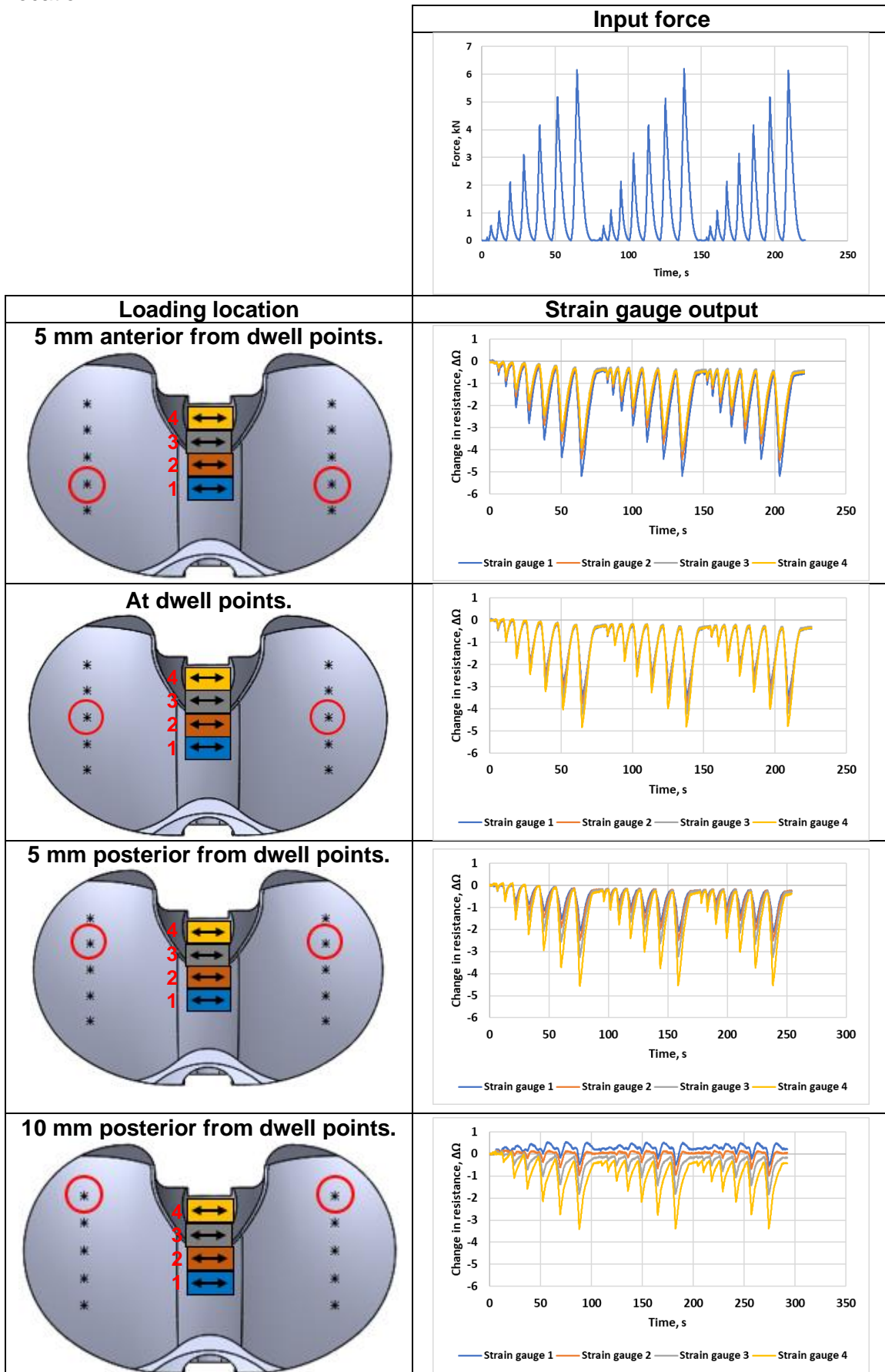
All four strain gauges showed signal directly proportional to the input force, when force was applied 5 mm anterior, at dwell point, and 5 mm posterior from dwell point. However, when force was applied 10 mm posterior, then strain gauge No. 1 showed non-linear signal relation. Figure 6.24 shows an example relation between the input force versus the strain gauge output signal.

a)   b)
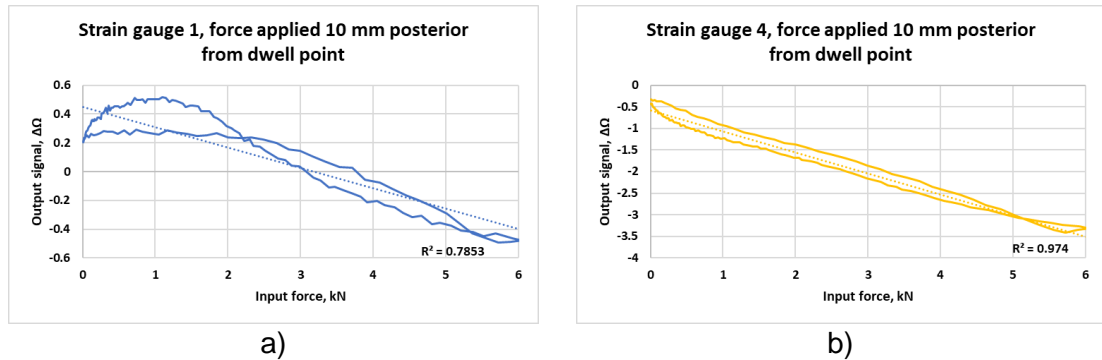
Figure 6.24 Example of relation between the input force and the strain gauge output signal when strain gauges are aligned in M-L direction and the axial force is applied 10 mm posterior from the dwell point. A) strain gauge No. 1 shows non-linear relationship, and b) strain gauge No. 4 shows linear relationship.

6.5.2 Discussion

This test proved that strain measurements could be obtained if the strain gauges are potted inside a self-curing resin made of PU. The measurements revealed a pattern where the strain signal was directly proportional to the applied force. The measurements also showed that the strain gauges positioned closer to the loading point will show stronger signal, which further indicated that strain gauge signal could be used to estimate the loading location in A-P direction. The configuration with four strain gauges position in the centre and aligned in M-L direction (Figure 6.21) provided the best signal output when compared to all others strain gauge configurations.

During this test it was observed that there were almost no noticeable strain gauge signal inconsistencies due to signal drop. The poor strain gauge signal from the previous tests could be explained by unnoticed specimen damage. During previous testing with a simplified tibial insert replica it was noticed that the insert replica did not have a perfectly flat bottom face due to machining inaccuracies (Figure 6.25). Having a small gap a the bottom of the insert replica resulted in aditional bending deformation in S-I direction. Therefore, the non uniform strain gauge signal was likely caused by the combined deformation in both S-I and M-L direction.
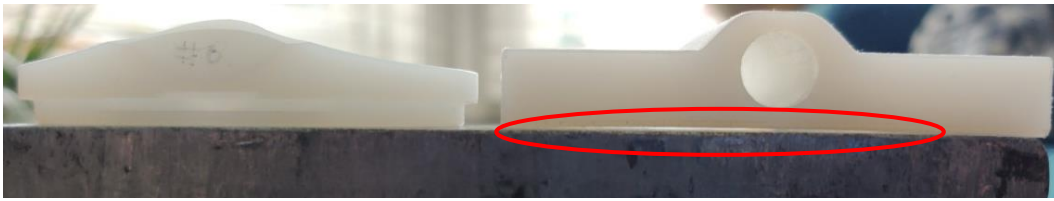
Figure 6.25 Front view of the GMK Primary CR tibial insert (left) and the simplified tibial insert replica (right). The simplified replica did not have a flat bottom face. The red circle highlights the gap where light is shining through.

6.6 Loading with different pressure

Previous test results (from section 6.5) showed that it could be possible to recognise different loading applied at the articulating surfaces in different locations along the A-P direction. Therefore, further testing was performed to analyse whether it is possible to recognise different pressures applied to the medial and lateral articulating surface.

For this test a GMK Primary CR size S4/17 (minimum thickness of 13 mm) tibial insert was used. Four strain gauges were potted with PU resin. All strain gauges were aligned in S-I direction. Two strain gauges were positioned both on medial and lateral side (Figure 6.26). This test used 1000 Ω strain gauges and signal was recorded with the custom MatLab script.
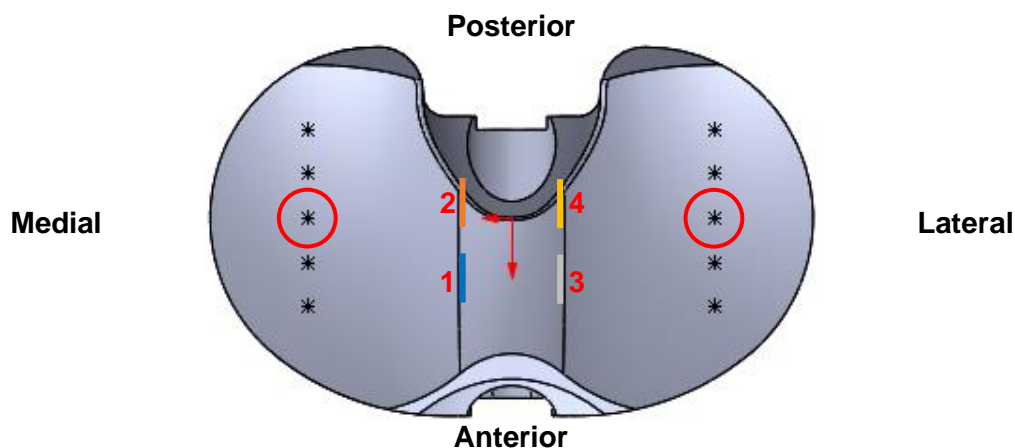
Figure 6.26 Example illustration of approximate strain gauge location. Strain gauges aligned in S-I direction.

Two compression tests were performed:
    i)   Single articular surface loading (Figure 6.27).
    ii) Double articular surface loading with different pressure (Figure 6.28).

During the single articular surface loading a sphere with diameter of 32 mm was placed on one of the articulating surfaces (Figure 6.27). This test setup is similar to the

previously described test shown in Figure 6.8. This simplified test simulated an isolated varus valgus stress test as it would be performed by a clinician.

a)   b)
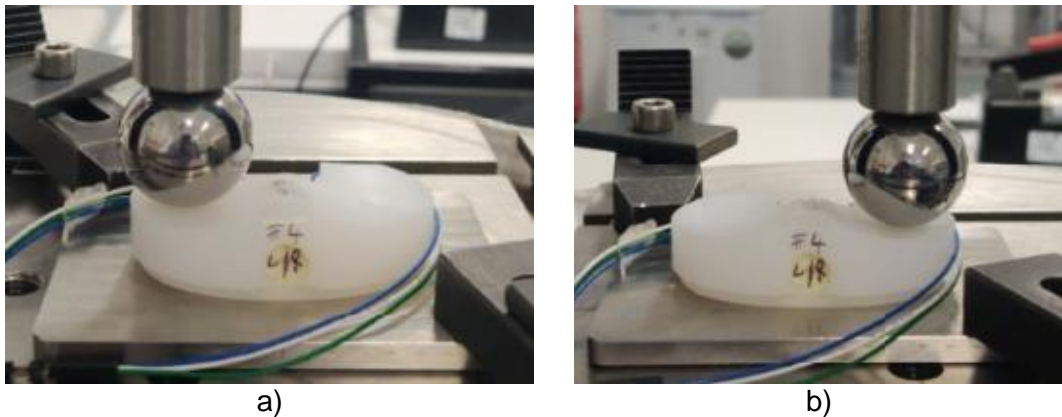
Figure 6.27 Test setup with the axial force applied to either a) medial or b) lateral articulating surface.

During the double articular surface loading the same amount of force was applied on both articulating surfaces using different contact areas. It was of interest to find out whether strain gauges at the intercondylar area would be able to distinguish differences between the loading applied at the medial and lateral articulating surface. This simplified test simulated a daily loading scenario when both femoral condyles are applying different forces which result in different contact pressures [192]. Due to Instron 3366 machine limitations, it was not possible to simultaneously apply different forces on both articulating surfaces, since it would require two independent pistons to apply two independent forces simultaneously. As an alternative solution, one loading piston could apply the same force on two different contact areas, thus applying different pressures. Difference in applied pressure was created by placing a metal bolt with approximate diameter of either 9 mm or 13 mm on each of the articulating surfaces (Figure 6.28).

a)   b)
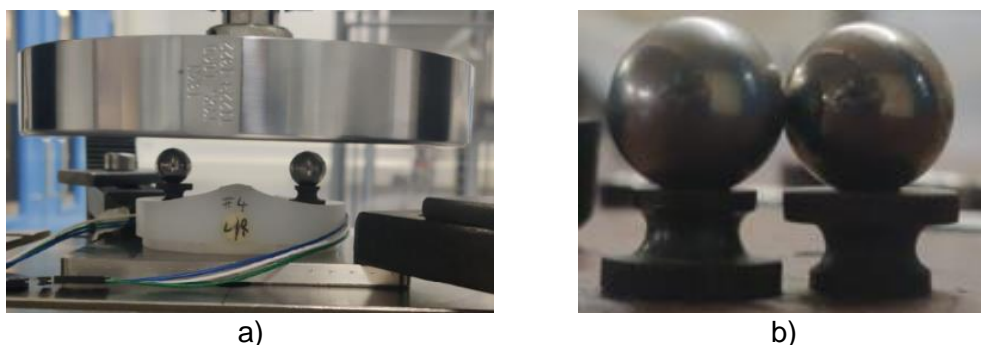
Figure 6.28 Test setup with a) different pressure applied to both articulating surfaces b) by using two identical bolts with different diameters on each side.

6.6.1 Results

The single side loading test showed different strain gauge signal depending on side was loaded. Strain gauge No.4 showed opposite signal polarity between the two loading scenarios (Figure 6.29).

a)   b)
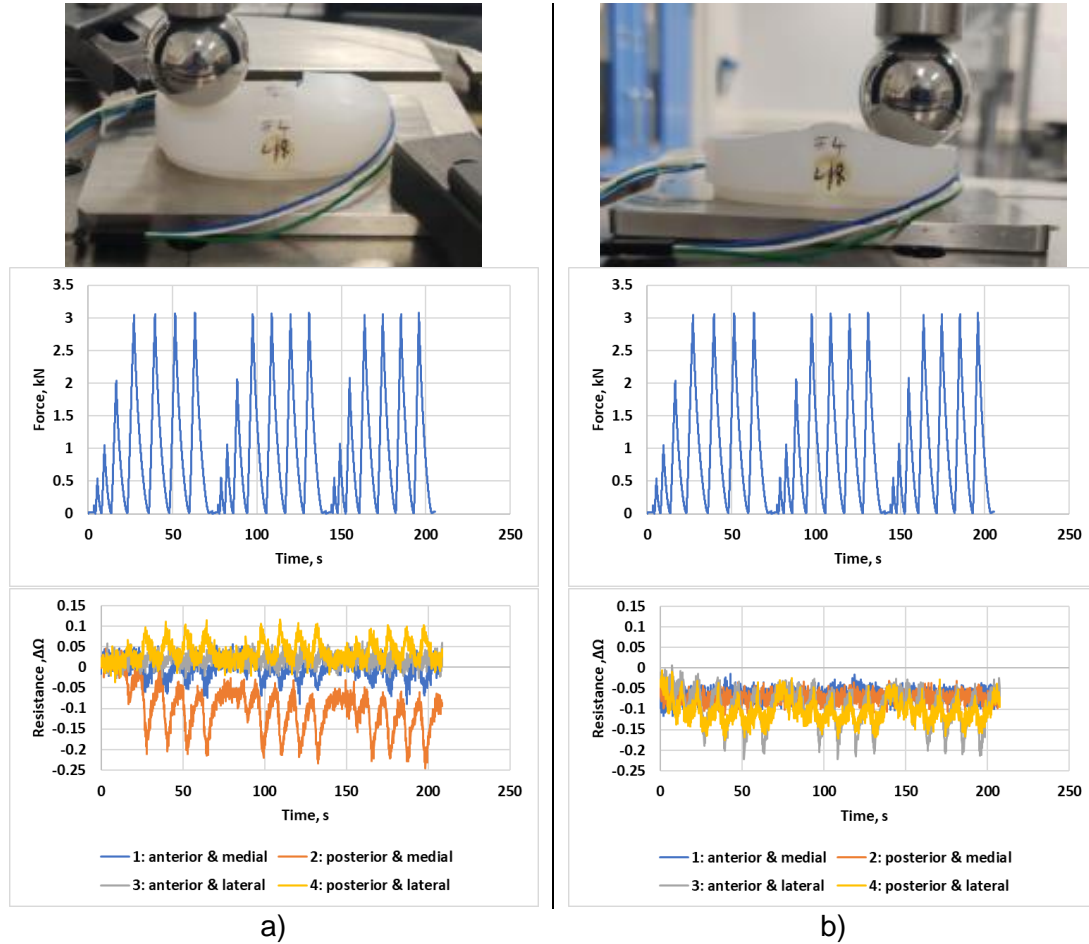
Figure 6.29 Strain gauge signal when load is applied only to a) medial or b) lateral side.

Test specimen: GMK Primary CR size S4/17 (minimum thickness of 13 mm).

When different pressure was applied on both articulating surfaces, no noticeable difference could be seen in strain gauge signal between the two loading scenarios (Figure 6.30). It must be also noted that it was unexpected to see that the strain signal has a negative signal polarity. Since strain gauges were aligned in S-I direction, it was expected to see positive signal polarity, similar to another test result shown in Table 6.3. It is unknown what caused the negative signal polarity shown in Figure 6.30. One explanation could be, that the results were affected by the increased thickness of the tibial insert, since Figure 6.30 shows data for the insert size S4/17 with 13 mm minimum thickness, whilst Table 6.3 shows data for the insert size S3/10 with 7 mm minimum thickness.
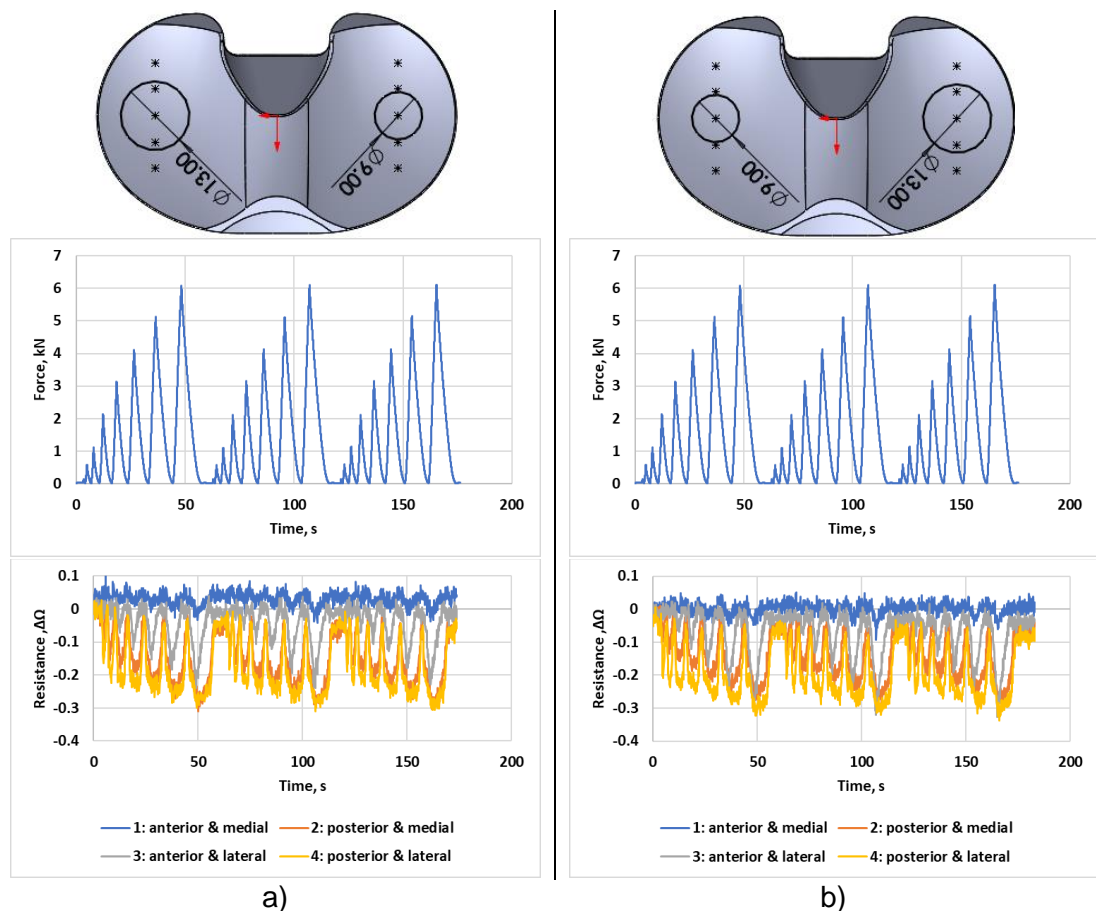
Figure 6.30 Strain gauge signal when smaller pressure is applied only to a) medial or b) lateral side. Test specimen: GMK Primary CR size S4/17 (minimum thickness of 13 mm).

6.6.2 Discussion

Strain gauges showed a unique signal pattern by changing the signal polarity when isolated force was applied to only one of the articulating surfaces. This signal pattern maybe could be used to identify different knee joint load during a varus valgus test.

No noticeable signal difference could be observed when different pressure was applied on both articulating surfaces, which has been noticed also in the FEA models. These preliminary results did not provide evidence that strain gauges positioned at the

intercondylar area could be used to differentiate medial and lateral condyle pressure during walking or other daily activities. Previously described FEA models (see Table 5.9 and Table 5.10) also did not show strain patterns which could be used to differentiate medial and lateral condyle pressure.

Figure 6.30 showed unexpected negative strain signal polarity, when positive polarity was expected instead. It was not investigated what caused the negative signal polarity, but one possible explanation could be the increased thickness of the tibial insert.

6.7 Tibial insert loading with missing support

It was of interest to investigate whether strain gauge data could be used to indicate different clinical failure modes. Whilst rarely occurring, one significant failure mode is tibial tray fracture, which could be caused by combination of factors, for example, falling, loss of bone support due to osteoporosis, and eccentric loading [83]. Such implant failure would cause pain and further implications due to metallosis and revision surgery. Therefore, it was of interest to simulate worst case loading conditions when there is partially missing bone under the tibial insert.

Initial proof of concept testing was performed without using Instron 3366 machine. During testing, a tibial insert was positioned on two metal plates. The two metal plates were misaligned to simulate a partially missing support at the bottom of the tibial insert: full support, quarter support missing, or half support missing. Then axial force was manually applied at the dwell points via a femoral component (Figure 6.31). For this study, strain gauges were aligned in M-L direction as shown in Figure 6.21, since previous test results showed that it is an optimal configuration.

a)   b)

Figure 6.31 Test setup without laboratory equipment for axial loading. The tibial insert was positioned a) on two misaligned plates to mimic different conditions with missing support b) and then the axial force was manually applied at the dwell points.

Afterwards, one of the loading conditions was repeated with laboratory equipment. Instron 3366 test machine was used to apply axial force with only half of the tibial tray

supported as shown in (Figure 6.32). For this study, strain gauges were aligned in M-L direction as shown in Figure 6.21.
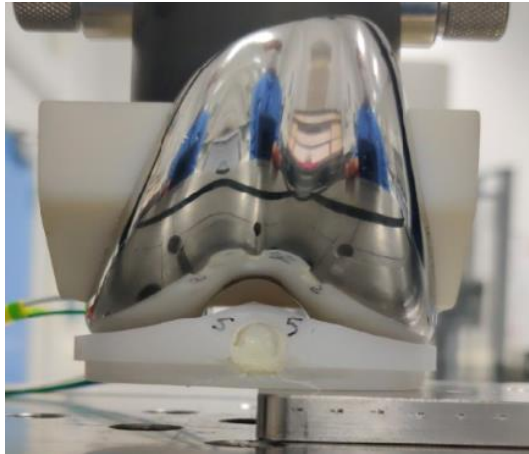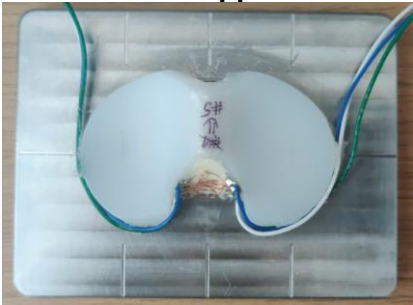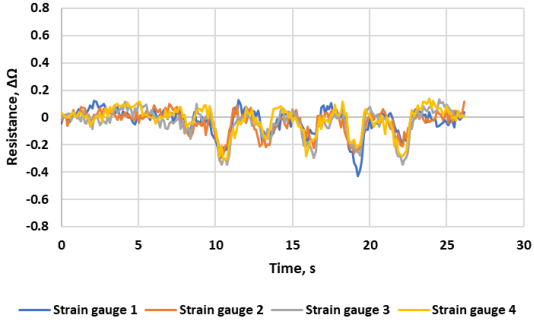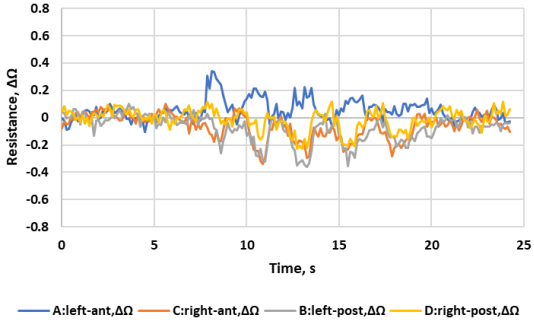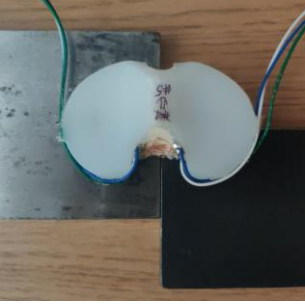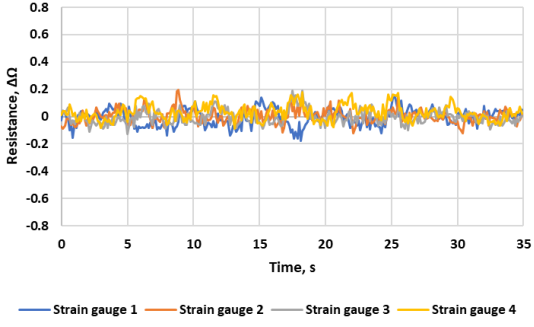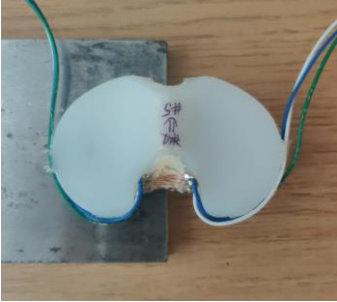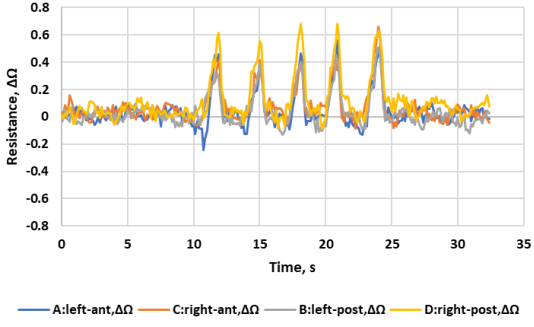
Figure 6.32 Test setup on the Instron 3366 test machine with only half of the tibial tray supported.

6.7.1 Results

The results from the proof-of-concept testing are shown in Table 6.2. The preliminary results showed different strain gauge signal for each of the four scenarios with missing support. Depending on the loading some scenario strain gauges changes signal polarity from negative to positive.

Table 6.2. The effect of the missing support under the tibial insert on the strain gauge signal.

Tibial insert support	Corresponding strain gauge signal pattern under axial loading (strain gauge alignment per Figure 6.21)
Full support	
Missing posterior quarter support	
Missing anterior quarter support	
Missing half support	

The results from the laboratory testing are shown in Figure 6.33. The preliminary results showed that three out of four strain gauges had positive signal polarity.

a)

b)

c)
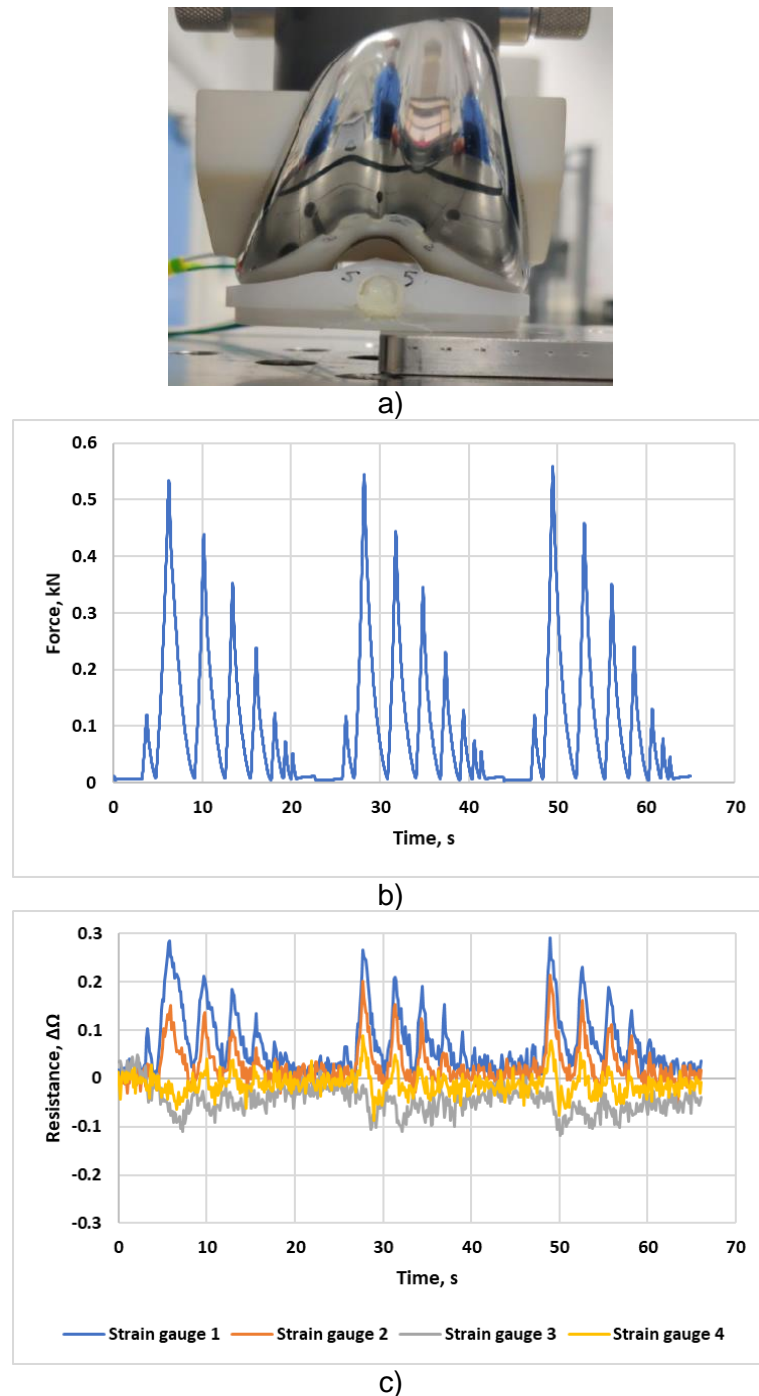
Figure 6.33 Test setup a) with only half of the tibial tray supported, b) the axial force input, and c) the strain gauge output signal.

6.7.2 Discussion

During the proof-of-concept testing, it was observed that strain gauges could potentially provide useful information about a clinical failure, such as, tibial bone loss. Strain gauges aligned in M-L direction showed a unique signal pattern. Under normal loading conditions, all strain gauges showed negative signal, whilst when support was partially

removed, some of the strain signals changed to positive signal polarity, which could be explained by the bending deformation which would induce tensile strain.

However, the presented strain gauge prototype has a limited practical application. To observe the unique signal polarity change, at least a quarter of the support had to be removed. Most probably, the bone loss must be extended far enough to cause bending near strain gauges in order to cause tensile deformation.

6.8 Tibial tray loading with missing support

As a continuation of the previous test described in section 6.7, it was of interest to investigate whether strain gauge data could be used to recognise a loading condition when there is partially missing bone under the metal tibial tray.

During test preparation, a tibial insert with embedded strain gauges was placed inside the tibial tray. Tibial tray was placed into a custom metal fixture to recreate a condition when there is missing support. The metal fixture supported only the lateral half of the tibial tray. The lateral side of the tray was fixed in the custom fixture with a bone cement (Figure 6.34b).

a)   b)
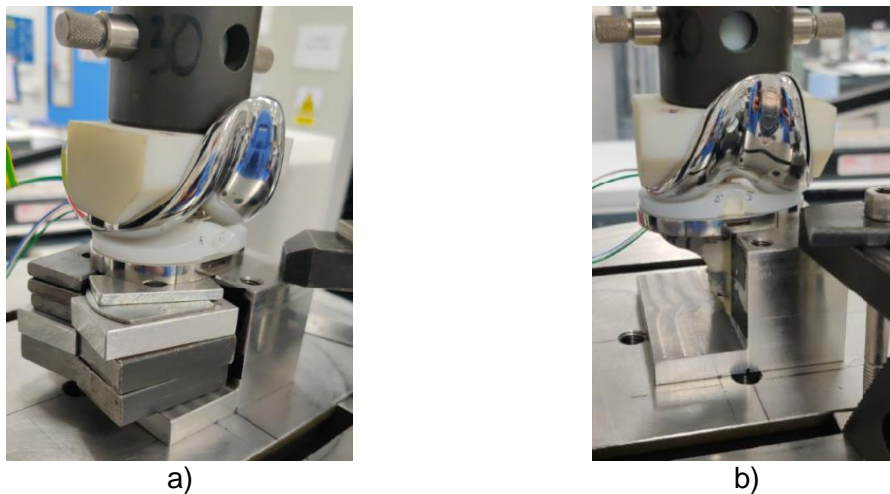
Figure 6.34 Test setup with the bottom of the tibial tray having a) a full support and b) a half support.

During testing, two fixation conditions were compared: full support (Figure 6.34a) and half support (Figure 6.34b) representing the worst-case scenario. The full support was achieved by stacking metal plates under the overhanging lateral side. Both support scenarios were tested with two strain gauge configurations: four strain gauges aligned in S-I direction (Figure 6.26) and four strain gauges aligned in M-L direction (Figure 6.21). Axial force was applied at the dwell points via a femoral component. The applied force was cyclically increased with Instron machine from 10 N to 100 N, 500 N, 1 kN, 2 kN, 3 kN, 4 kN, 5 kN, and 6 kN. This test used 1000 Ω strain gauges and signal was recorded with the custom MatLab script.

6.8.1 Results

Signal was recorded from all strain gauges (Table 6.3). All strain gauge signals were directly proportional to the input force. No unique signal differences were noticed between the two loading conditions: with full and half tray support.

Additionally, none of the strain gauges showed signs of signal polarity change. Strain gauges aligned in S-I direction showed only positive signal polarity with maximum change in resistance approximately 1.2 Ω. Strain gauges aligned in M-L direction showed only negative signal polarity with maximum change if resistance approximately 2.5 Ω.

Table 6.3. Strain gauge signals during loading scenario with full and half support under the tibial tray. Data shown both for S-I and M-L strain gauge alignment. Test specimen: GMK Primary CR size S3/10 (minimum thickness of 7 mm).

Strain gauge alignment and loading area	Full tray support (see Figure 6.34a)	Half tray support (see Figure 6.34b)
S-I direction		
M-L direction		
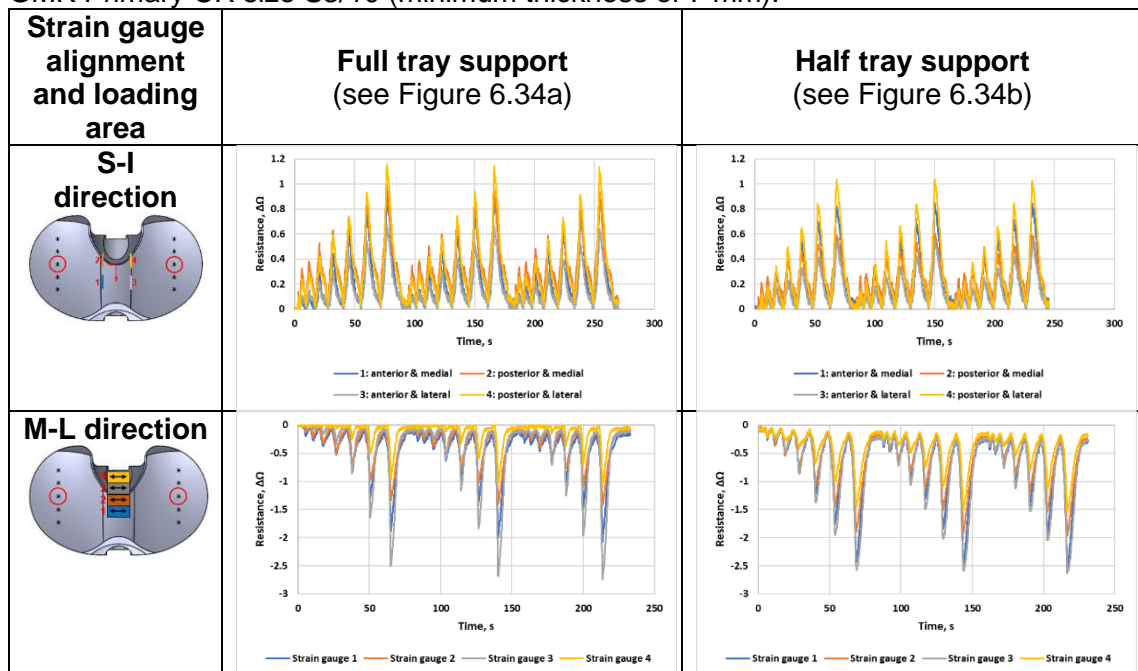
6.8.2 Discussion

After analysing strain gauge data from S-I and M-L alignment, no signal difference could be distinguished between the testing scenario with full and half tray support. Results from half support showed some variations in strain signal strength, but such variations could have been also caused by differences in axial loading or loading applied in different A-P position. Therefore, there was no unique signal pattern which would allow to differentiate the two support scenarios.

Since the tibial insert is fully supported by a much stiffer tibial tray, the applied force was not enough to cause tibial tray to bend. Accordingly, strain gauges from both

configurations could not change signal polarity due to bending deformation, as it was previously observed during a test without a tibial tray (section 6.7).

These results confirmed the FEA predictions that the capsule is compressed in M-L direction. Strain gauges aligned in S-I direction had a weaker signal with positive polarity, whilst strain gauges aligned in M-L direction had a stronger signal with negative polarity. This indicated that the capsule was primarily compressed in the M-L direction and, due to Poisson's effect, the capsule was expanding in S-I direction. The ratio between the maximum S-I and M-L strain gauge signal strength was approximately 0.48.

6.9 Discussion

This PhD thesis section has presented various test methods to analyse strain signal response due to high axial forces of up to 6000 N, and with various loading scenarios by changing A-P position, pressure on medial and lateral articulating surface, or implant support. In comparison, a few other studies have used instrumented tibial insert where strain gauges were embedded directly under the articulating surfaces [12, 68, 122, 193]. These studies have only shown that it could be possible to measure the total axial force and separate forces under medial and lateral articulating surface. In these studies, equal force was applied on both femoral condyles, therefore their test methods could not recreate loading scenarios with different force or pressure applied on both articulating surfaces. These studies also did not consider other potential applications, such as, detecting clinical failure modes. One study used a robotic knee simulator and applied different forces up to 950 N at different flexion angles in one fixed position and showed a close match between the strain gauge signal and applied total force [68]. However, this study did not show how strain signal would change at high forces or during a complex motion with varying flexion angle, A-P displacement, and I-E rotation. Another experimental study tested strain gauges with axial force up to 3100 N and it demonstrated strain signal non-linearity and insensitivity to small forces due to material creep [122]. The strain signal amplitude and pattern could have been affected by the interference/clearance fit between the capsule and the hole. The effect of interference fit on the strain signal was not investigated, but it should be considered in future studies.

The relation between the output strain and the input force was only assessed qualitatively by observing whether the output strain signal pattern is aligned in time and shape with the input force pattern. In the future studies, quantitative comparison could be done by plotting the output strain versus the input force.

6.10 Summary

Laboratory experiments revealed that it is possible to detect change in strain signal when strain gauges are placed at the intercondylar area. The change in strain could be recorded with four different encapsulation methods: by using shells made of UHMWPE, shells made of SS316, by potting in PMMA resin, and potting in PU resin.

The laboratory results showed that strain gauges placed in the centre of the capsule and aligned in the M-L direction give the strongest signal, which also confirms previously made FEA predictions (see Section 5.3.3). During axial compression tests with Instron 3366 materials testing machine three different signal patterns were observed: by changing axial force, by changing loading point in A-P direction, and by applying force only to one articulating surface. However, these results were obtained in controlled testing environment with isolated axial force. In more realistic loading condition with varying loads and joint kinematics it may be more difficult to distinguish strain gauge signal patterns. Therefore, further experimental studies should be performed on a knee simulator to analyse the strain gauge signal.

7   Experimental fatigue to failure study

7.1 Introduction

This chapter relates to research Objective 1 (fulfil the design requirements), Objective 3 (develop test methods), Objective 6 (testing with modified insert), and Objective 7 (testing with sensors). Specifically, this chapter assesses the safety of a smart tibial insert. This Section presents the preliminary physical fatigue test results, which investigate whether a hole at the intercondylar area would show any signs of damage, which could cause electronic component failure or be potentially harmful to the patient.

7.2 Cantilever bending test

7.2.1 Introduction

Modern tibial inserts are subjected to wear, plastic deformation, fracture, and dislocation (see Figure 1.14). In particular, one retrieval study has shown an extreme damage mode where the tibial insert broke in half at the intercondylar area [83]. The retrieved implants showed that both tibial tray and tibial insert fractured along the sagittal plane. The tibial tray, AMK Total Knee System (DePuy, USA), had a centralising stem, but it did not have two side keels to provide structural support against cantilever bending.

This retrieval study was used as the worst-case scenario for the proposed smart tibial insert design, because fracture at or near the intercondylar area could potentially release the electronic components within patient's body and cause further harm. It was of interest to investigate, whether such failure mode would be possible when using GMK Primary tibial tray with side keels (ribs) together with the modified tibial insert.

7.2.2 Materials and methods

In order to investigate whether the modified tibial insert could fracture at the intercondylar cavity a test method was created to simulate worst-case loading scenario. A fatigue to failure test method was developed by adapting ISO 14879-1 [194] and ASTM F1800 [114] test standards. These standards have been used in medical industry to prove that the tibial tray designs have sufficient strength to withstand fatigue fracture under cantilever bending, but they do not give guidance on how to test tibial inserts. In this PhD study, these test standards were further adapted to allow testing both the tibial insert and the tibial tray together.

The test was performed on GMK Primary tibial insert and tibial tray. The tibial insert was modified with an intercondylar hole, which accommodated four embedded strain

gauges aligned in M-L direction (as shown in Figure 6.20 and Figure 6.21) and sealed with PU resin. To recreate cantilever bending, tibial tray was placed into a custom block fixture which supported only the lateral half of the tibial tray. Bone cement CENTRI™ BASE Cold Cure (WHW Plastics, UK) was used to fix the tibial tray to the inferior surface. Bone cement was also used to create a cast with a negative shape of the tibial insert. The cast was placed on top of the tibial insert and then fixated with a metal plate. Four bolts were used to fixate the metal plate to the block fixture, therefore firmly clamping both the tibial tray with the tibial insert (Figure 7.1 and 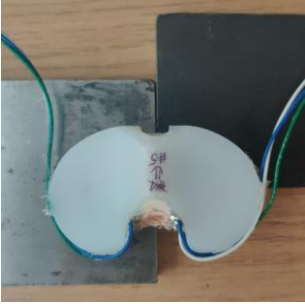Figure 7.2). This setup simulated the worst-case scenario where both the tibial insert and the tibial tray is subjected to a cantilever bending due to bone loss. Depending on the implant design, this loading scenario could potentially cause both component fracture at or near the intercondylar area.
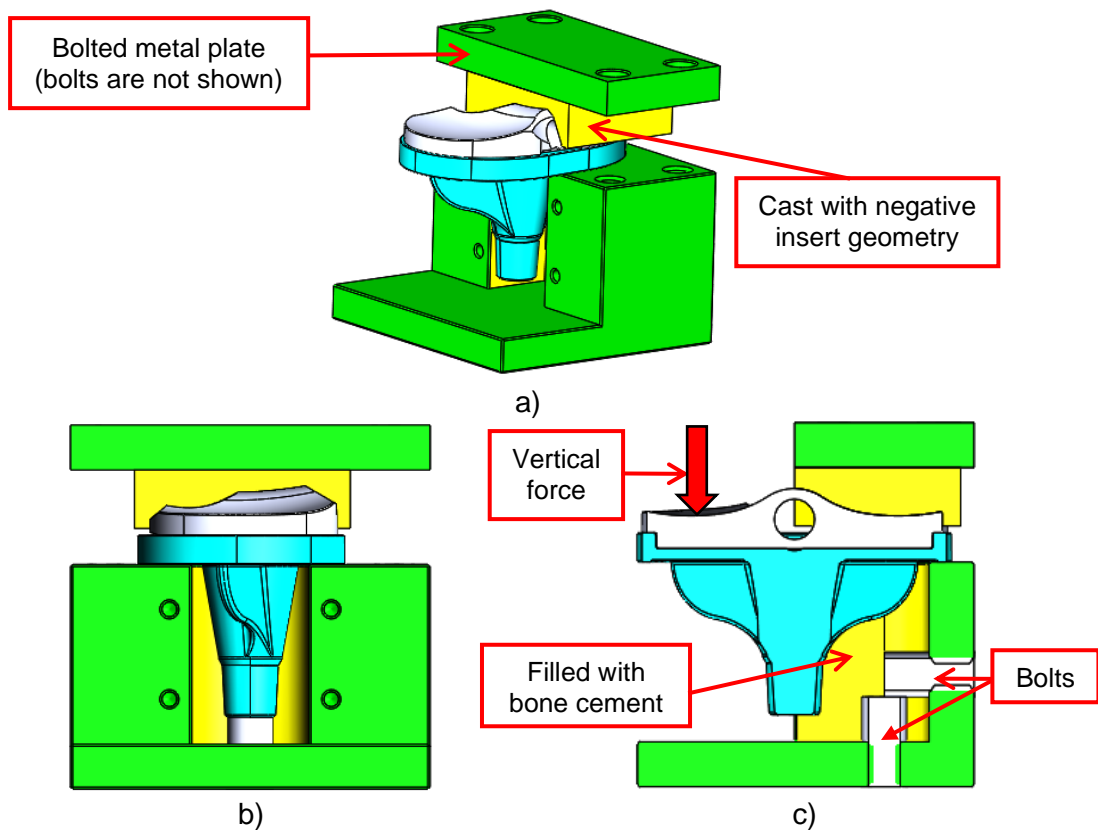
Figure 7.1 Cantilever bending test setup illustration in a) isometric view, b) side view in sagittal plane, and c) section view in coronal plane.

a)   b)
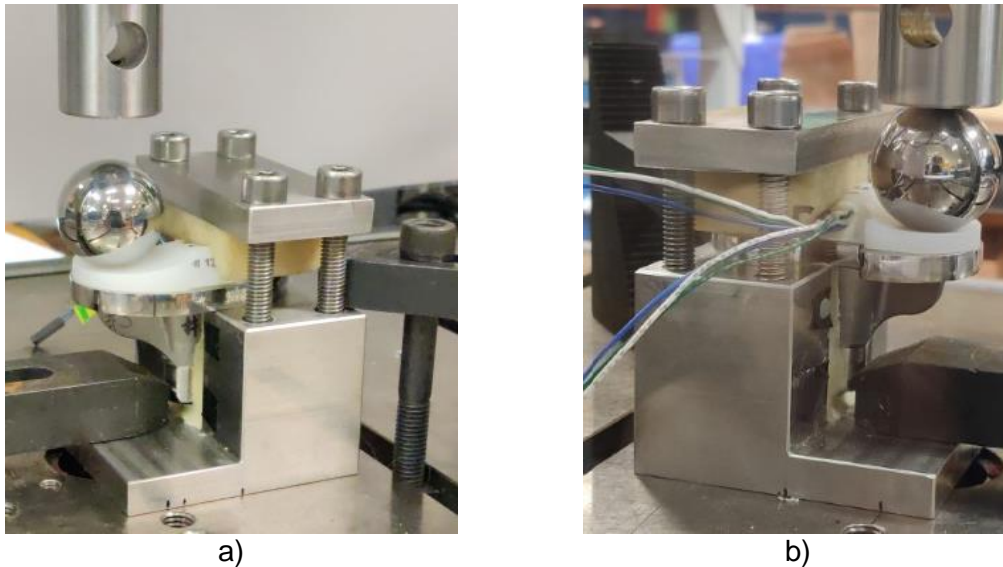
Figure 7.2 Cantilever bending test setup a) anterior view, b) posterior view with the load applied at the dwell point.

Electropulse E10000 (Instron®, USA) materials testing machine (with 10 kN load cell) was used for applying cyclic load at high force and frequency of 10 Hz. The Force was applied via a metal sphere with diameter of 32 mm (Figure 7.2). This test used 1000 Ω strain gauges and strain signal was recorded with the custom MatLab code.
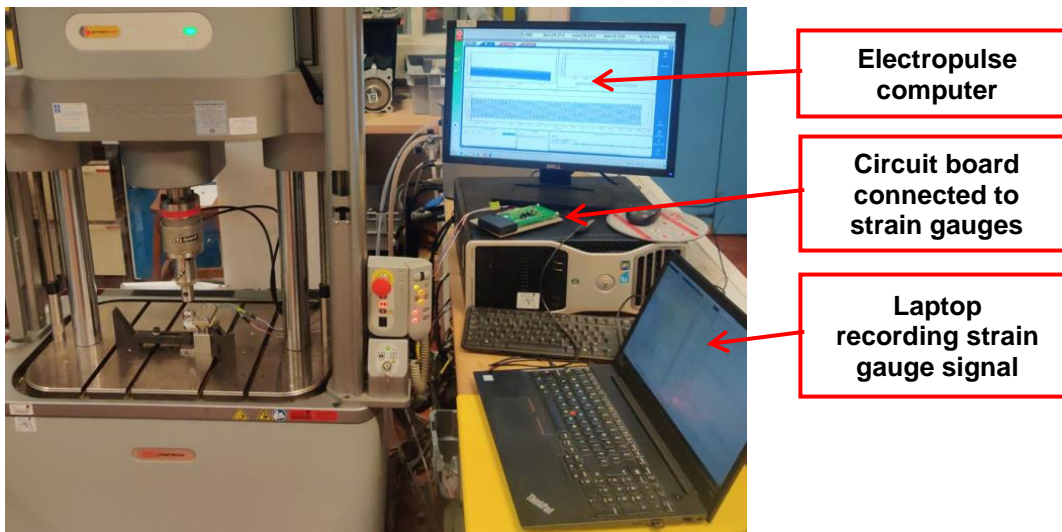
Figure 7.3 Cantilever bending test equipment setup.

The ASTM F2083-12 [115] test standard states that tibial insert must withstand at least 10 million cycles with no failures using a maximum load of 900 N, whilst other studies have also suggested using a maximum load of 2000 N [116, 117, 195] or 4000 N [116].

Following testing steps were executed:

1) Force was applied with minimum to maximum load ratio of 1:10.
2) Cyclic loading was applied for 10 million cycles (MC) at 10 Hz frequency. Peak force and peak displacement were measured for every cycle.

3) The test was stopped after one of the criteria was met:
   a. if 10 million cycles were completed, or
   b. if displacement exceeded 5 mm.
4) At the end of each test the specimen was assessed for any signs of damage. If tibial insert showed no damage at the intercondylar area, then test was repeated with higher loads to accelerate implant failure.

The cantilever fatigue test was performed three times on one test specimen, in order to fracture the tibial tray and exceed the 5 mm displacement. The first test of 10 MC was performed to confirm if GMK Primary implants can withstand the minimum worst-case loading requirement. All subsequent tests were performed only to cause a visible fracture. Therefore, at every repeated test the applied force or loading location was changed to accelerate implant failure:

1. Test 1: cyclic force was applied from 200 N to 2000 N at the dwell point for 10 million cycles.
2. Test 2: to accelerate implant failure, cyclic force was applied from 400 N to 4000 N [116] at the dwell point for 10 million cycles.
3. Test 3: to further accelerate implant failure, cyclic force was applied from 400 N to 4000 N posteriorly by 10 mm from the dwell point (Figure 7.4) until tibial tray was displaced by 5 mm.
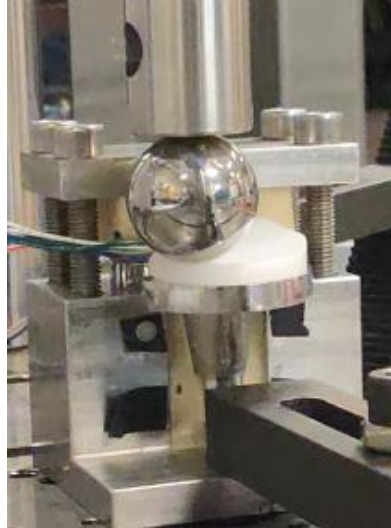
Figure 7.4 Cantilever bending test 3 with vertical force applied 10 mm posterior from the dwell point.

At the test planning stage, it was unknown which failure modes would be observed. Therefore, prior to testing, a prediction of potential failure modes and their clinical impact were considered (see Table 7.1). This table was used a checklist during specimen inspections at the end of each test.

Table 7.1. Potential test outcomes and their clinical interpretation.

	Potential test outcome	Clinical interpretation of the test outcome
1	Tibial insert fractures at the intercondylar cavity.	Electronics are exposed, which could physically harm the patient.
2	Tibial insert fractures away from the intercondylar cavity.	Electronics are not exposed, no harm to patient due to electronics.
3	Tibial insert does not fracture.	Electronics are not exposed, no harm to patient due to electronics.
4	Tibial insert does not fracture, but intercondylar area has cracks.	Electronics could be exposed if more fatigue cycles were applied, which could physically harm the patient.
5	Tibial insert does not fracture, but intercondylar area has plastic deformation.	Electronics are not exposed, but sensor measurement precision could be affected. No physical harm to patient, but could give misleading data.
6	Tibial insert does not fracture, but the capsule is easy to remove from the cavity by hand.	The capsule with electronics could fall outside the implant, which could physically harm the patient.

7.3 Results

7.3.1 Test 1 results

On completion of the first test (cumulative 10 MC), both the tibial tray and the tibial inserts showed no cracks. Tibial insert showed no cracks or plastic deformation at the intercondylar area. Tibial insert only showed plastic deformation caused by the indentation with the metal sphere at the dwell point (Figure 7.6a). Additionally, the tibial insert showed backside wear with burnishing scars appearing under the loaded area and under the intercondylar area (Figure 7.6a). The polyurethane (PU) capsule created debris at the posterior side, which was caused by rubbing against the metal tibial tray (Figure 7.5).

a)   b)   c)
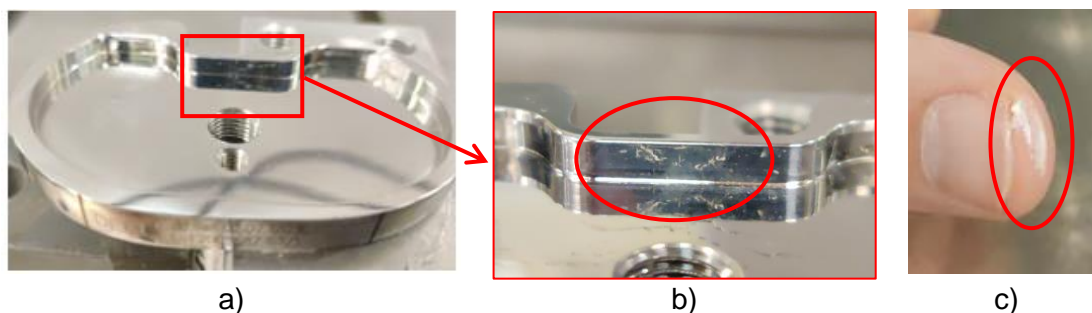
Figure 7.5 After completing test 1, a) no tibial tray damage was observed, b,c) debris from the PU capsule was found at the posterior side where the PU capsule was in contact with the metal tray.

<div align="center">a)   b)</div>

Figure 7.6 After completing test 1, the tibial insert showed a) plastic deformation (red circle) due to indentation with the metal sphere and b) patches with glossy burnished surface (black dotted line) indicating backside wear.

During testing, it was not possible to record complete strain gauge signal shape, because Matlab script recording was limited to 21.5 Hz sampling frequency. Since the test was performed at 10 Hz frequency, the sampling frequency was not sufficient to capture the entire strain signal pattern per each loading cycle. Therefore, only average strain signal could be assessed. The average strain gauge signal strength is shown in Figure 7.7 . During testing, strain gauge signal remained mostly unchanged. Only after completing 8.5 MC the signal from strain gauge 3 changed from approximately -4.0 $\Delta\Omega$ to -3.5 $\Delta\Omega$.
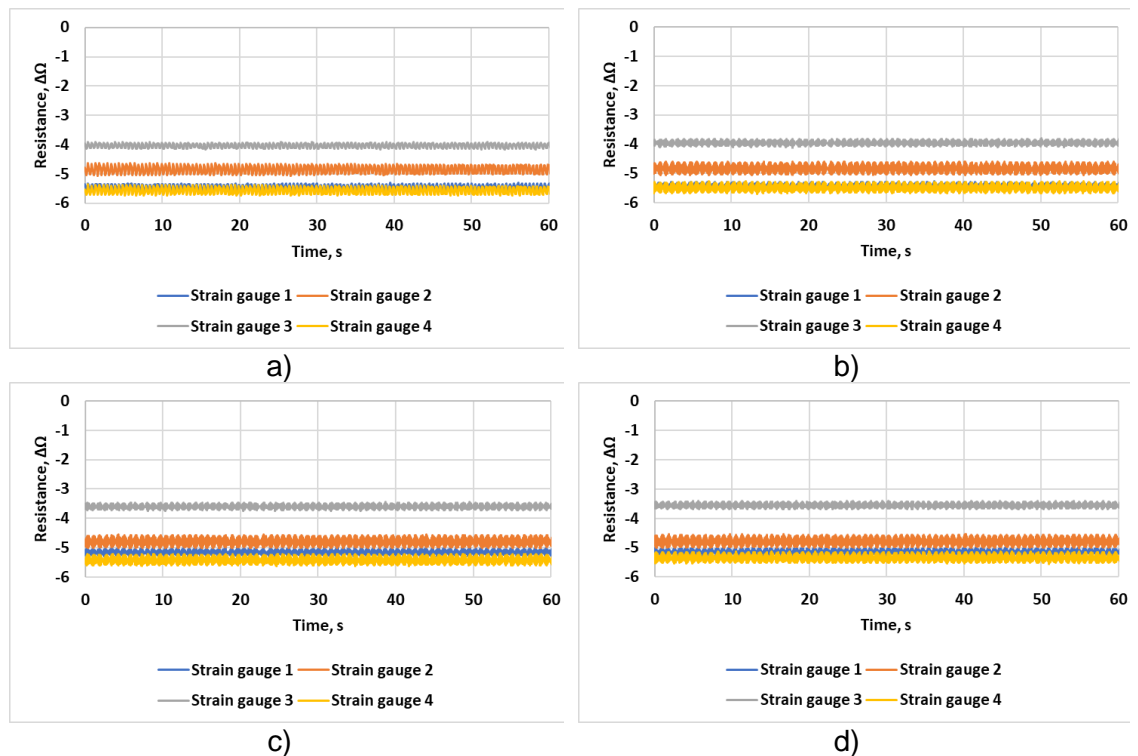
Figure 7.7 Strain gauge signal during cantilever fatigue test 1 a) after 6.1 MC, b) after 7.7 MC, c) after 8.5 MC, and d) after 9.7 MC.
Note: $\Delta\Omega$ = strain gauge resistance Ω – 1000 Ω reference resistor.

7.3.2 Test 2 results

After completing the second test (cumulative 20 MC), the tibial tray showed cracks at the posterior side (Figure 7.8). Tibial tray showed no cracks on the anterior side (Figure 7.9). Tibial insert showed no cracks at the intercondylar area. Tibial insert was slightly bent since it had no longer a flat bottom surface (Figure 7.11). Tibial insert showed increased plastic deformation caused by the indentation with the metal sphere at the dwell point (Figure 7.12a). Tibial insert also showed increased backside wear with burnishing scars appearing under the loaded area and under the intercondylar area (Figure 7.12b). PU debris was again found posteriorly on the tibial tray (Figure 7.10).

a)   b)

c)   d)
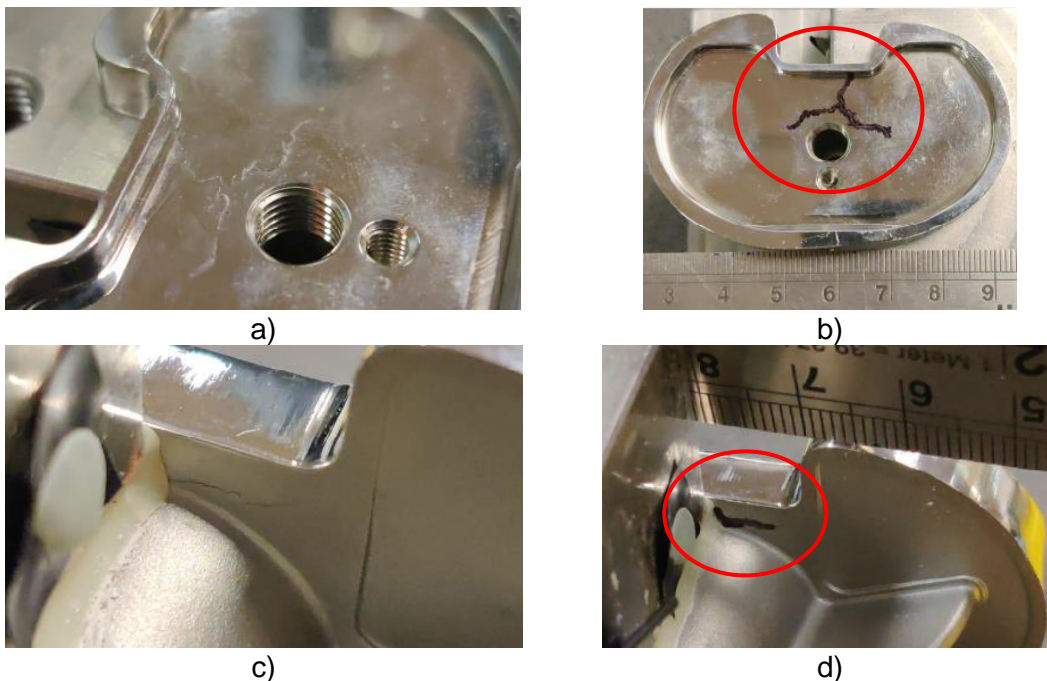
Figure 7.8 After completing test 2, the tibial tray showed a crack at the posterior side, visible both a,b) on the top surface and c,d) on the bottom surface.
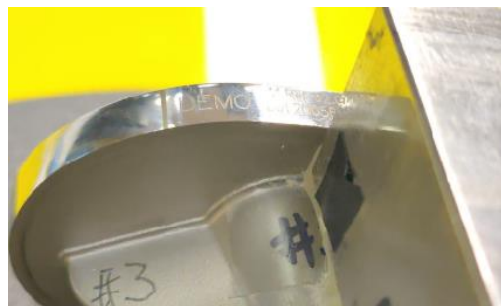
Figure 7.9 No cracks on the bottom surface, anterior side.

a)   b)

Figure 7.10 After completing test 2, debris from the PU capsule was found at the posterior side where the PU capsule was in contact with the metal tray. Images show debris a) before and b) after wiping off.
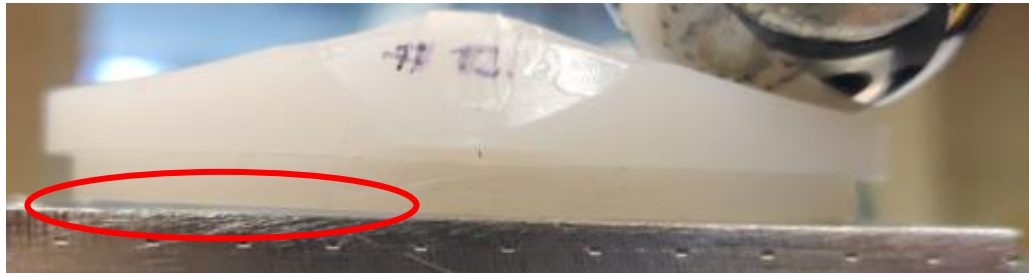
Figure 7.11 After completing test 2, the tibial insert did not have a flat bottom surface.

a)   b)
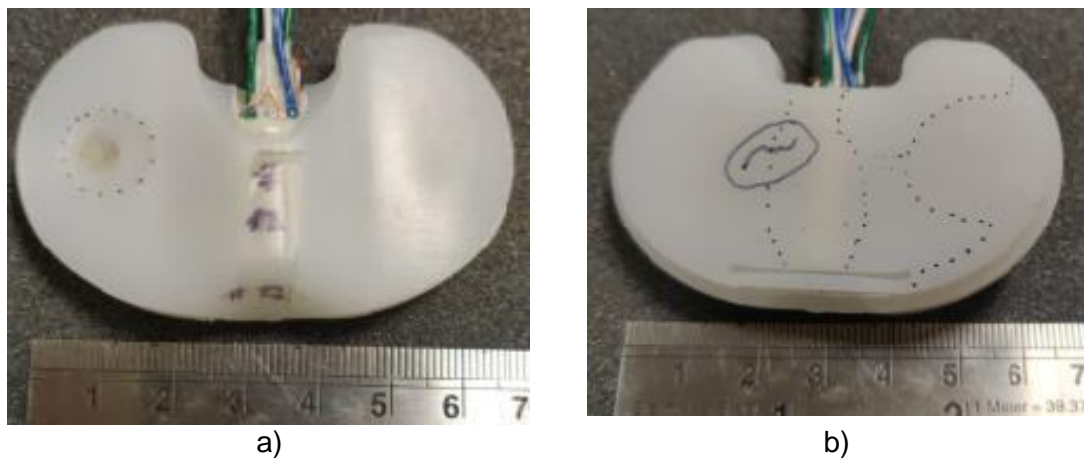
Figure 7.12 After completing test 2, the tibial insert showed a) larger plastic deformation due to indentation with the metal sphere and b) larger patches with glossy burnished surface (dotted line) indicating backside wear and a scar (solid line) created by the tibia tray crack line.

During testing, strain gauge signal remained mostly unchanged. Only strain gauge 3 had showed a slowly drifting average signal of -5.6 ΔΩ, -5.1 ΔΩ, and -4.3 ΔΩ after completing 3.5 MC, 6.1 MC, and 8.7 MC respectively (Figure 7.13).

a)   b)

c)   d)
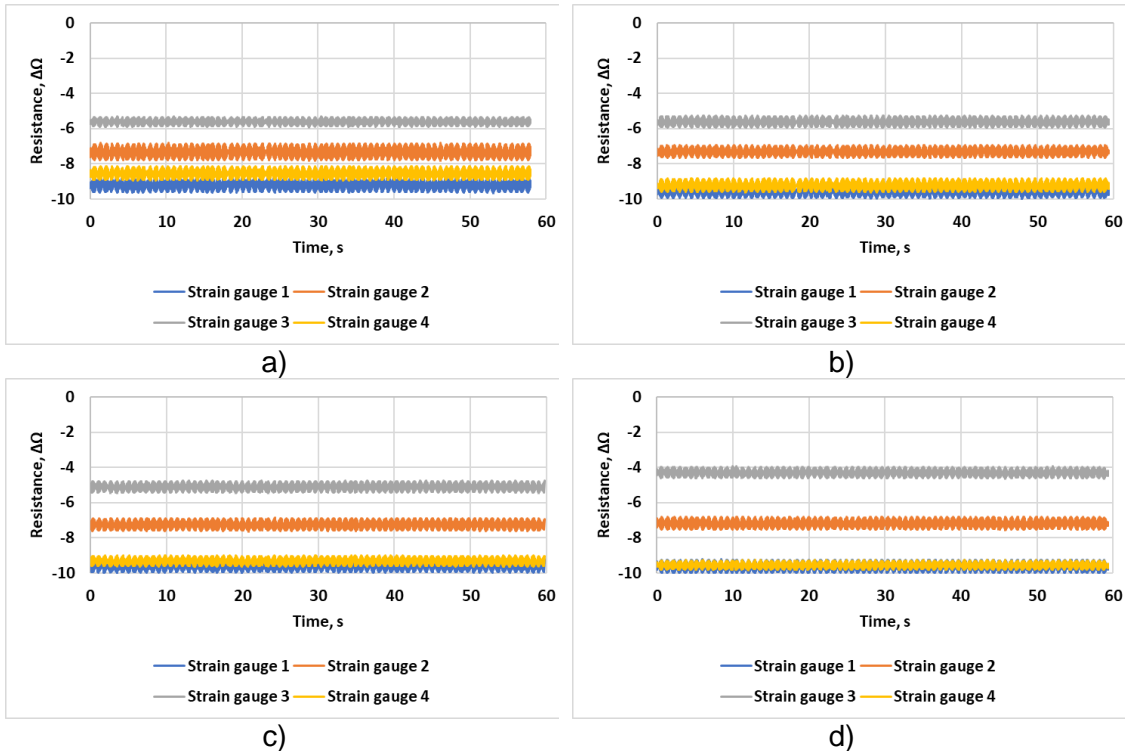
Figure 7.13 Strain gauge signal during cantilever fatigue test 2 after completing
a) 0.9 MC, b) 3.5 MC, c) 6.1 MC, and d) 8.7 MC.
Note: ΔΩ = strain gauge resistance – 1000 Ω reference resistor.

7.3.3 Test 3 results

The third test was stopped after completing additional 3.7 MC (cumulative 23.7 MC) because the tibial tray fractured and was vertically displaced by more than 5 mm (Figure 7.14). Tibial tray showed fractures both at the posterior and anterior side with loose large metal chunks and small metal debris (Figure 7.15). The tibial insert showed no cracks within the intercondylar area or anywhere else on the superior and inferior surfaces. The tibial insert was bent along the line corresponding to where the tibial tray fractured (Figure 7.16). The inferior surface of the tibial insert had a long scar line across the insert created by the tibia tray crack line. The tibial insert developed small gaps between the PU capsule and the intercondylar hole (Figure 7.17). Nevertheless, the capsule remained firmly fixed inside the tibial insert and could not be pulled out.
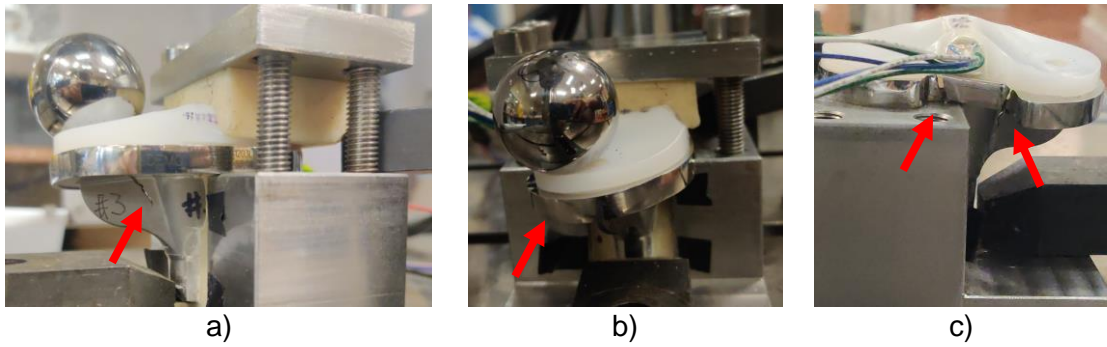
Figure 7.14 During test 3 the tibial tray fractured and deformed as shown (with red arrow) in a) anterior view, b) side view, and c) posterior view.
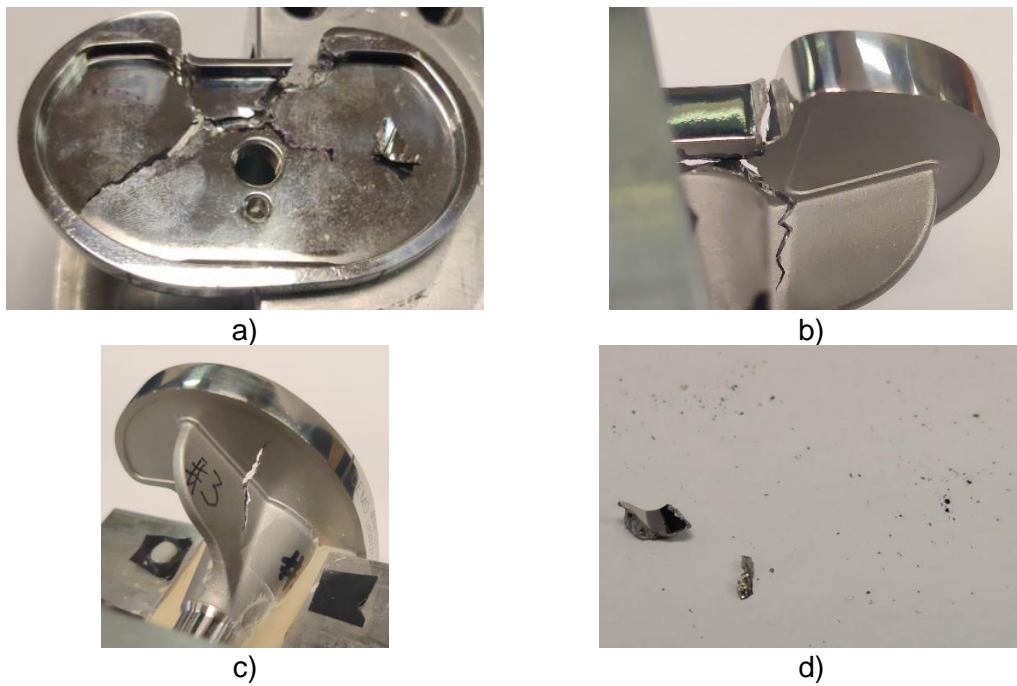
Figure 7.15 During test 3 the tibial tray showed a,b) fractures both at the posterior and c) anterior side d) with loose metal chunks and metal debris.

a)

b)

c)

d)
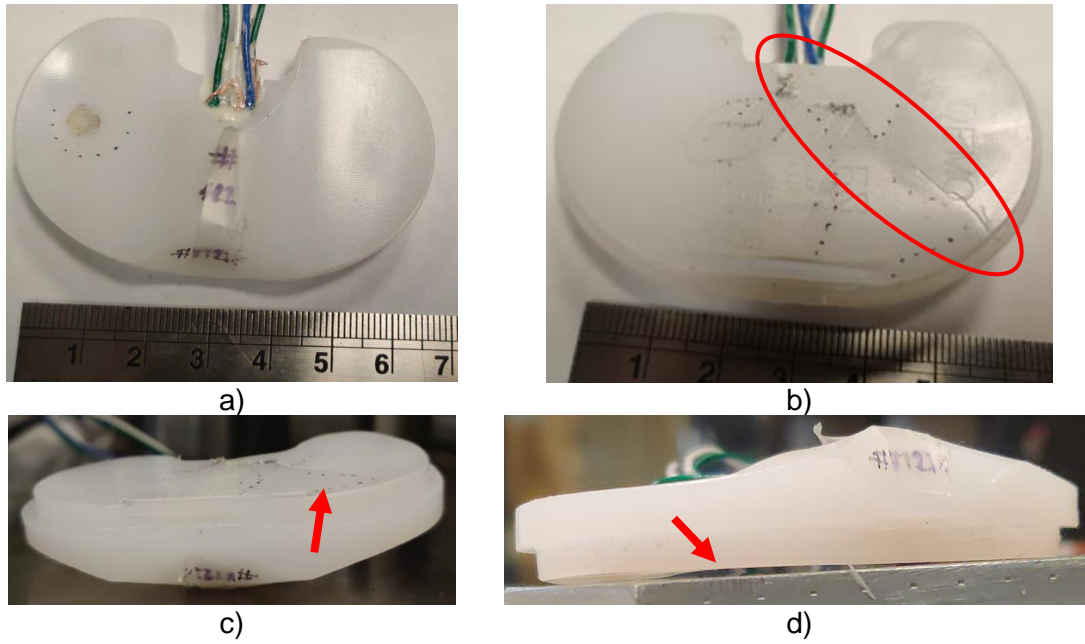
Figure 7.16 During test 3 the tibial insert showed a,b) no cracks on the top or bottom surface. Tibial insert had b) a scar line along the insert created by the tibia tray crack line and c,d) tibial insert was bent at the area where the tibial tray fractured

a)   b)   c)
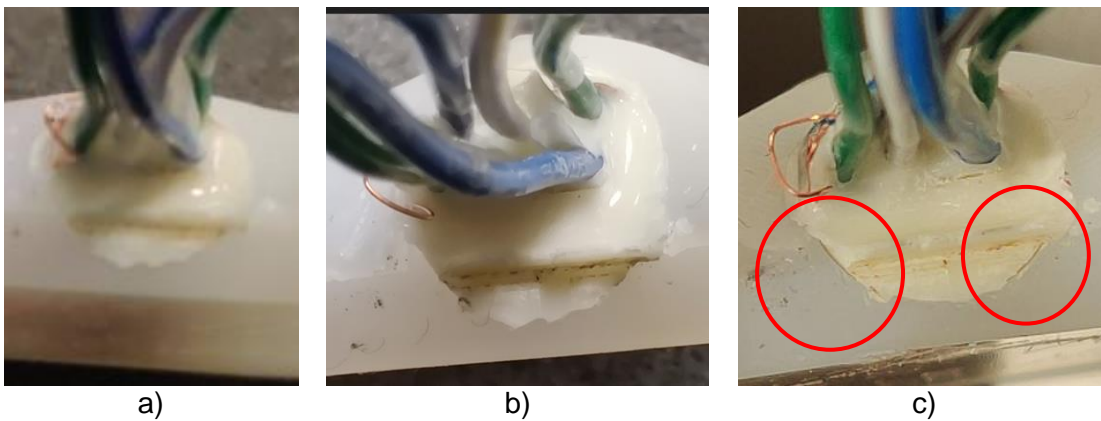
Figure 7.17 Back view of the PU capsule after completing a) test 1, b) test 2, and c) test 3. Small gaps were observed only after stopping test 3.

All four strain gauges remained fully functional after the tibial tray fractured and deformed. During testing, all strain gauges showed a slowly drifting average signal (Figure 7.18). The posterior strain gauge No. 1 showed the largest signal drift of 3.7 ΔΩ (Table 7.2).
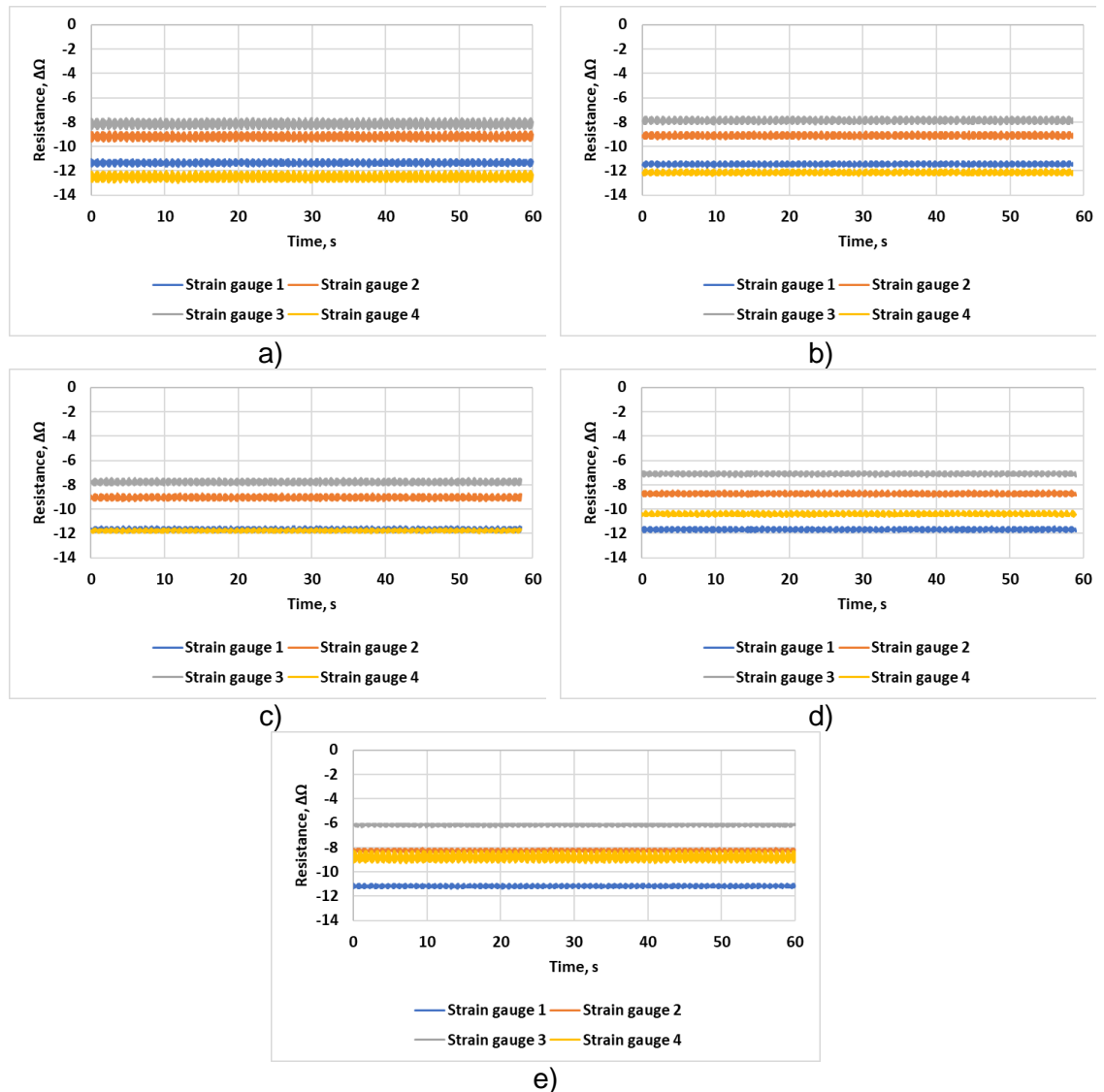
Figure 7.18 Strain gauge signal during cantilever fatigue test 3 after completing a) 0.005 MC, b) 0.7 MC, c) 1.8 MC, d) 2.7 MC, and e) 3.4 MC.
Note: ΔΩ = strain gauge resistance – 1000 Ω reference resistor.

Table 7.2. Strain gauge signal during test 3 at different time points.

	Average strain gauge signal value, ΔΩ			
	Strain gauge 1 (most anterior)	Strain gauge 2	Strain gauge 3	Strain gauge 4 (most posterior)
0.005 MC	-11.4	-9.2	-8.1	-12.5
0.7 MC	-11.5	-9.1	-7.9	-12.1
1.8 MC	-11.7	-9.0	-7.8	-11.8
2.7 MC	-11.7	-8.7	-7.1	-10.4
3.4 MC	-11.2	-8.2	-6.2	-8.8
Total signal drift	0.5	1.0	2.0	3.7

Strain gauge signal was compared from recordings taken before starting test 1 and after stopping test 3. Two most posterior strain gauges No. 3 and No. 4 changed signal polarity to positive, indicating that the strain gauges are loaded under tension (Figure 7.19).

a)   b)
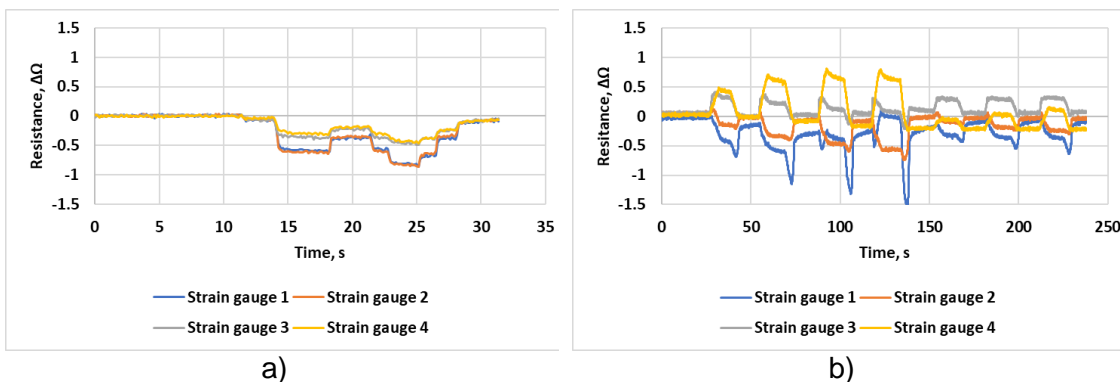
Figure 7.19 Strain gauge signal a) before starting test 1 and b) after stopping test 3. After test 3 strain gauges No. 3 and No. 4 showed positive signal polarity when loading with a fractured tibial tray. Note: positive "+" sign indicates strain gauge extension.

7.3.4 Discussion

A new test method was developed to analyse tibial insert fracture under the cantilever loading. In this study ASTM F1800 [114] standard was adapted and a custom fixture was developed which allowed testing a tibial insert placed inside a tibial tray. This study method was specifically developed to recreate worst-case loading conditions which could potentially cause tibial insert fracture at or near the intercondylar area, which has been clinically observed on other implant design [83].

The United States Food and Drug Administration (FDA) recommends using the test method described in ASTM F1800 [114] standard with at least one specimen surviving 10 million cycles to provide reasonable assurance of the tibial tray safety [92]. ASTM F1800 requires maximum axial load of only 900 N. In the current study the tibial tray

together with a tibial insert were subjected with force of 2000 N for 10 million cycles, without showing any cracks or fractures either to the tibial tray or the tibial insert.

Nevertheless, during testing, some safety concerns were observed regarding the proposed electronic component potting technique with PU resin. The PU capsule was not sealed at the posterior side and had a direct contact with the metal tibial tray, which resulted in creation and scattering of PU debris. In clinical scenario, if PU debris were released into the synovial fluid, then it could potentially cause aseptic loosening or third body wear. These observations suggest that a capsule made of PU or PMMA resin should not be directly exposed to any components which could scratch of the surface of the resin. As one of the solutions, potting with resin could still be potentially used for encapsulation of electronic components, however, the manufacturing process should be improved so that the potted capsule would be fully sealed by a layer of UHMWPE. For example, this could be achieved with UHMWPE compression moulding techniques. Alternatively, injection moulding techniques with polyetheretherketone (PEEK) should be also considered.

The FDA also recommends performing implant failure analysis [92]. Given the tibial tray did not fracture in test 1, the cantilever fatigue testing was repeated two more times. To accelerate implant failure, during test 2, the load was increased to 4000 N and, during test 3, the bending moment was increased by applying load 10 mm posterior from the dwell point. As a result, tibial tray fractured and was displaced by more than 5 mm after accumulated total of 23.7 million cycles. Even though the tibial tray fractured, the tibial insert was only plastically deformed and displayed no signs of cracking or fracture. The tibial insert was predominantly deformed only at the loading area where the tibial tray fractured. The hole at the intercondylar area showed signs of deformation by revealing small gaps near the capsule, but the PU capsule remained firmly fixed inside the tibial insert. This failure mode indicated that the tibial insert is protected by the tibial tray. Regarding the cantilever loading scenario, it can be assumed if the tibial tray is undamaged then the tibial insert will also remain undamaged. However, the tibial insert damage should be only considered together with the tibial tray. If a different tibial tray design would have been used, then potentially other failure modes could be observed. No other publications were found to compare tibial insert damage under cantilever loading.

All four strain gauges remained fully functional throughout testing. However, it must be noted that strain gauge signal was only indicative. No calibration methods were developed to assess strain measurement accuracy or precision. Therefore, strain signal was only used to analyse the existence of signal, different strain patterns, and relative comparison between the strain gauges. During all three fatigue tests some of

the strain gauges showed a drifting signal, which could potentially indicate damage caused to the tibial tray. However, signal drifting could have also been caused by the electronic circuit board malfunction, which would require further investigation. A unique signal pattern was observed after comparing strain gauge data with measurements performed before starting test 1 and after stopping test 3. After test 3, two posterior strain gauges, which were near the area where the tibial tray was fractured, showed signal polarity change. This indicates that strain gauges embedded inside the tibial insert could indirectly detect fracture of the tibial tray, showing a potential benefit to detect a clinical failure mode. However, the practical application is limited for such measurements with the currently used strain gauge configuration. Firstly, tibial tray fracture is a rare occurrence. Secondly, tibial tray fracture must be close to the strain gauges and must cause bending deformation of the tibial insert.

A few studies have used instrumented tibial insert where strain gauges were embedded directly under the articulating surfaces [12, 68, 122, 193]. However, these studies did not consider tibial insert safety issues due to design modifications nor the potential applications to defect implant failure, such as, tibial tray or tibial insert fracture.

7.4 Summary

A new test method was developed to assess tibial insert damage under worst-case cantilever loading scenario by adapting ASTM F1800 standard. Tibial insert showed no cracks at the intercondylar hole or anywhere else after applying 2000 N for 10 million loading cycles. However, during testing, the capsule made of PU resin created debris which could potentially cause harm to the patient. Therefore, the potting procedure of the electronic components should be further improved.

The tibial tray fractured and was displaced by more than 5 mm after accumulated total of 23.7 MC. However, the tibial insert showed no fracture or sign of cracks even after 23.7 MC. Tibial insert only deformed at the area where the tibial tray fractured. Tibial insert also showed deformation at the intercondylar hole, but the PU capsule remained fixed inside the tibial insert.

All strain gauges remained fully functional throughout testing even after the tibial tray fractured. Strain gauge measurements showed a signal pattern change in response to the tibial tray fracture.

These study results indicate that it could be safe to place electronic components at the intercondylar area, if the manufacturing procedure is further improved to mitigate debris

release from the PU capsule. The strain gauge signals could also provide clinical benefit, for example by indirectly detecting tibial tray fracture.

8   Experimental wear and deformation simulation study on Total Knee Replacement

8.1 Introduction

When designing instrumented tibial insert it is important to understand the modes of damage. When tibial insert is exposed to dynamic loads and motions the tibial inserts is experiencing two modes of damage: particle removal due to wear and plastic deformation. Wear debris can induce osteolysis causing aseptic loosening [196]. Plastic deformation would change surface geometry which could have further negative effect on wear rate [93], knee joint kinematics [40], and quadriceps muscle force [42].

Knee simulators can be used to expose tibial insert to dynamic loads and motions, allowing to observe and assess the cumulative damage (wear and plastic deformation) over multiple millions of cycles. This chapter describes a knee simulation study performed on two tibial insert designs (original insert and modified insert with a through hole). To assess the damage, gravimetric measurements were performed to calculate wear rate and coordinate measuring machine (CMM) measurements were performed to calculate change in geometry.

The aim of this study was to subject two different designs of tibial inserts under the same loading conditions within a knee simulator, then measure damage and make a direct comparison. If both the original and modified tibial insert would show similar wear rate and similar deformation, then it would indicate that insert's performance has not changed even after modification. However, if the wear rate or geometry would differ, then it would indicate that the long-term performance could be different, for example, by affecting long term wear or knee joint kinematics.

8.2 Materials

This study was carried out with GMK Primary knee implants (Medacta International, Switzerland): size S3/10 cruciate retaining tibial insert (with minimal thickness of 7 mm) made of unirradiated GUR 1020 UHMWPE, size 3 left femoral component and tibial tray. This study was performed with two groups: original and modified tibial inserts (Figure 8.1). In total 8 tibial insert specimens were used (6 study specimens and 2 soak controls). Both groups consisted of 3 test specimens (n=3) and one control specimen. In the original group no modifications were made to the tibial inserts, whilstin the modified group the tibial inserts had a hole with a 10 mm diameter, as described in previous chapters.

a)   b)
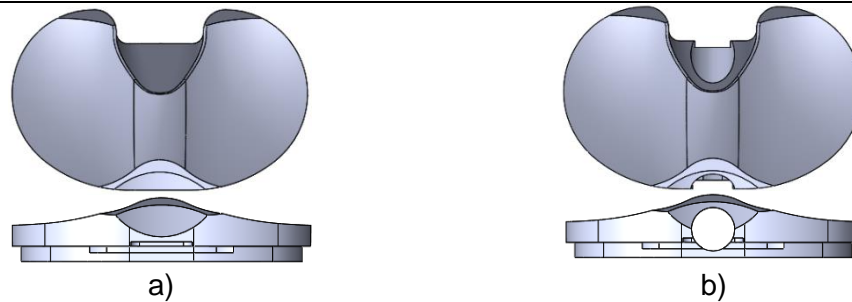
Figure 8.1. Top and front view of a) the original and b) the modified tibial insert with a
through hole (10 mm diameter).

The tibial inserts under investigation were modified by milling a through hole in the
anterior-posterior (A-P) direction at the intercondylar area (Figure 8.2). A through hole
was chosen instead of the posterior hole with a metal cylinder (previously described in
Section 5.4.4) to simplify the cleaning process and ensure that no serum or water
residue would remain inside the hole, which would cause inaccuracies in gravimetric
measurements.

Figure 8.2. Milling setup to cut a through hole at the intercondylar area of the tibial
insert.

During the experimental knee simulator study following equipment was used:

1. Knee simulator (Prosim 6-station deep flexion knee simulator, Simulation
   Solutions, UK) No. 6 (KS6) with 5 degrees of freedom (DoF) allowing superior-
   inferior (S-I), anterior-posterior (A-P), internal-external (I-E), flexion-extension
   (F-E), and abduction-adduction (A-A) motion or loading. Medial-lateral (M-L)
   axis was fixed (Figure 8.4).
2. Digital microbalance Mettler XP205 (Mettler Toledo, USA).
3. CMM Legex 322 (Mitutoyo, Japan).
4. Panasonic Lumix GF7 digital camera (Panasonic, Japan)
5. Digital microscope Alicona Infinite Focus with Laboratory Measurement Module
   version 6.6.12 (Alicona Imaging, Austria).

A lubricant was used for the knee simulator. The lubricant was 25% bovine serum (Life Technologies, New York, USA) in 0.04% sodium azide solution (Severn Biotech Ltd, Worcestershire, UK) and was changed approximately every 0.33 million cycles. The simulation was performed in ambient room temperature.

8.3 Methods

8.3.1 Experimental knee simulation

Prior to initiating the experimental knee simulation, load cells and displacement sensors were calibrated for each station. During calibration, the axial force reading deviated within ±11.2 N and the A-P displacement reading deviated within ±0.38 mm. After calibration, a check was performed to ensure that the knee simulator fixture alignment was not deviating from the zero position by more than ±0.5 mm in A-P translation and more than ±0.5° in I-E and F-E rotation.

Experimental knee simulation involved cleaning, loading, and measurement steps. Knee simulator was used to perform 3 million loading and motion cycles. Knee simulator setup is shown in (Figure 8.3 and Figure 8.4).

Knee implants placed inside a bag with bovine serum

Soak control
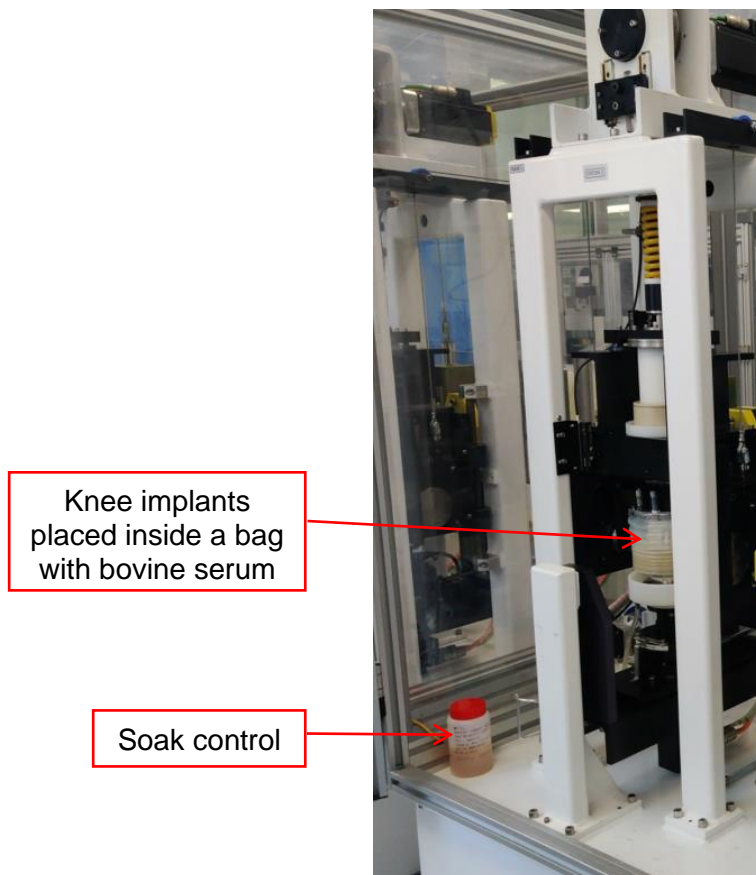
Figure 8.3. Knee simulator KS6 setup.
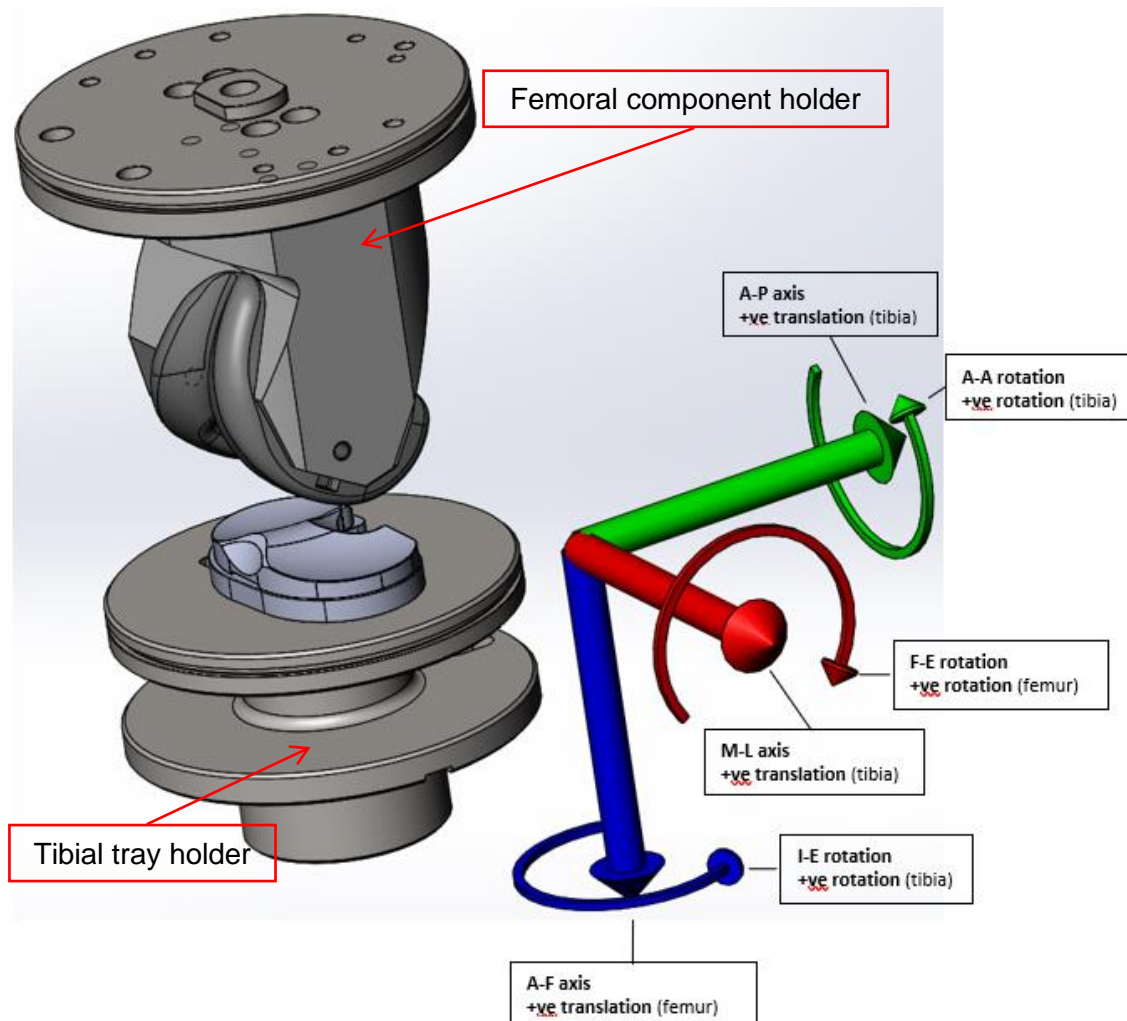
Figure 8.4. Illustration of implant placement inside the knee simulator KS6. Note: KS6
could control only 5 DoF (M-L displacement was fixed).

Previously described FEA models were used to decide which standardised loading
condition would cause damage closer to the intercondylar area of the tibial insert (see
Section 5.6). FEA models showed that daily loading conditions per ASTM F3141 [49]
test standard resulted in higher stresses near the intercondylar area, which could
cause larger damage. However, KS6 simulator could not be used to apply
ASTM F3141 profiles, since it had no capability to apply M-L load. KS6 have been
designed to apply loading and motion profiles per ISO 14243-3:2014 [109] standard for
walking in displacement control and per ISO 14243-1:2009 [108] standard for walking
in load control. ISO 14243-1 predicted high stress areas closer to the intercondylar
area (Figure 8.5). Therefore, ISO 14243-1 profile for load control was chosen as an
input for the knee simulator, to cause higher wear and plastic deformation near the
intercondylar area.

a)   c)
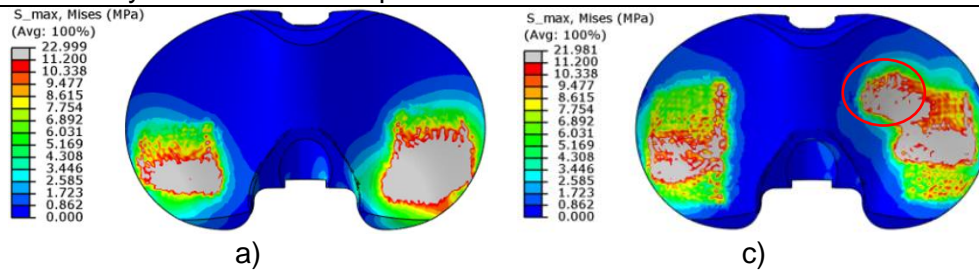
Figure 8.5. FEA models for walking per a) ISO 14243-3:2014 and b) ISO 14243-1:2009
standard, showing von Mises stress (MPa) value over all frames of full gait phase. The
grey area shows values above the true yield stress of 11.2 MPa. Red circle highlights
that ISO 14243-1:2009 applied loading closer to the intercondylar area.

During knee simulator calibration, it was discovered that KS6 has a fault, and one of
the stations could not apply load control to the tibial component, however all 6 stations
could work in displacement control. In order to recreate the necessary loading
conditions near the intercondylar area, the ISO 14243-1:2009 profile was adapted and
applied with displacement control instead of load control parameters.

To adapt the ISO 14243-1:2009 for displacement control, the necessary kinematic
parameters for I-E rotation and A-P displacement were calculated from the FEA
simulation performed with load control parameters (load control waveforms are shown
in Figure 4.37). Then the calculated kinematic I-E and A-P waveforms were imported
into Excel and further simplified, by manually smoothing out the profiles (see Figure
8.6), since KS6 simulator could not accommodate sudden changes in direction. Knee
simulator was not able to suddenly accelerate/decelerate or reverse direction, therefore
all small curves and sharp peaks needed to be replaced with an averaged curve, which
would accommodate more gradual acceleration and deceleration. Finally, the original
axial load and F-E rotation waveforms together with the simplified I-E and A-P
kinematic waveforms were trialled on the KS6 simulator to confirm that KS6 can
execute these input waveforms. The FEA and knee simulator studies were performed
with the same size and geometry tibial inserts (GMK Primary CR S3/10).

a)   b)
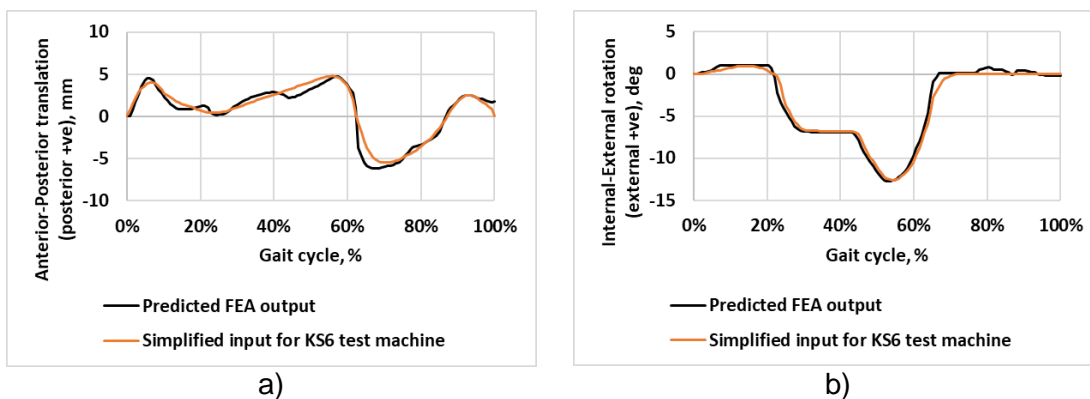
Figure 8.6. Kinematic waveforms for ISO 14243-1:2009 a) A-P displacement and b) I-E
rotation predicted with FEA and simplified for the KS6 input.

The FEA model was repeated with the simplified kinematic profiles to check that the
tibial insert was still deformed in the same locations. The FEA models with original load
control parameters and simplified KS6 displacement control parameters showed similar
contour plots for Von Mises stress and plastic deformation (Figure 8.7).

a)   b)
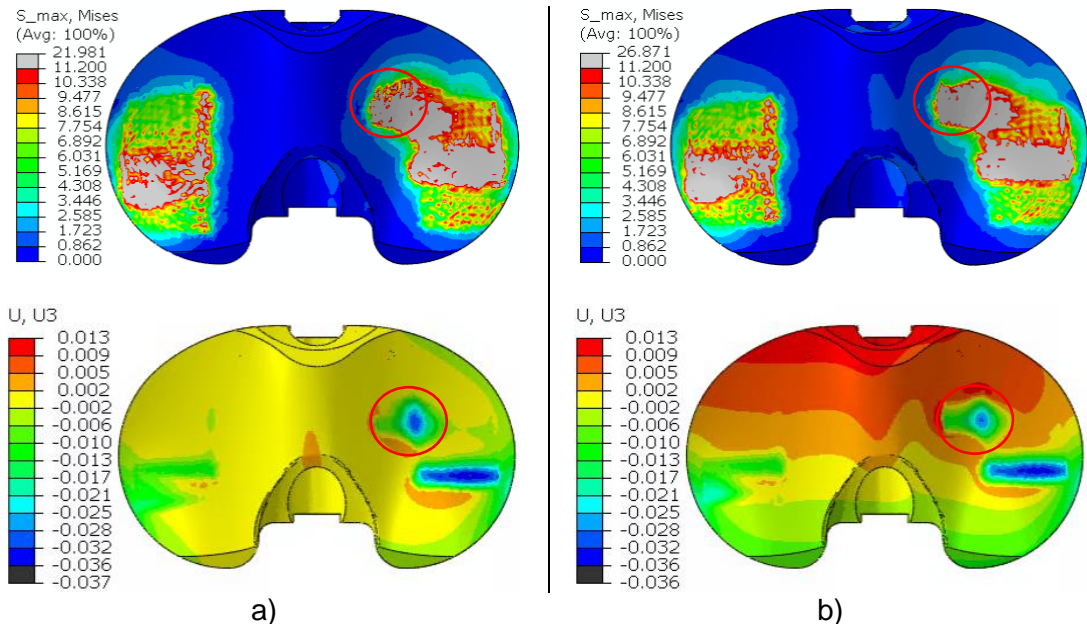
Figure 8.7. FEA contour plots with Von Mises stress (MPa) and axial plastic
deformation (mm) predicted for the ISO 14243-1:2009 a) with load control and b) with
simplified KS6 input for displacement control. Red circle highlights the applied loading
close to the intercondylar area.

Throughout the study, tibial inert damage was assessed with two different
measurement methods: gravimetric and surface geometry measurements. Differences
in wear rates were assessed with gravimetric measurements, whilst differences in
surface geometry were assessed with CMM measurements. Gravimetric and CMM
measurements were taken prior starting the study and after completing every 1 million
cycles (MC).

A number of preparations were completed prior starting knee simulations on KS6:

1. Preparation of metal tibial trays:

    1.1. Rectangular holes were cut in the metal tibial trays to allow pushing out the
        tibial inserts, when inserts needed to be removed for the gravimetric
        measurements (Figure 8.8a).

    1.2. Each tibial insert was placed in and taken out of the tibial tray at least 5 times
        in order to deform the anterior locking mechanism and to remove any loose
        strands of material from the tibial insert (Figure 8.9), because the tibial tray had
        a sharp edge on the anterior and posterior locking mechanism.

    1.3. Sharp edge was removed on the tibial tray at the anterior locking mechanism (Figure 8.8b) by grinding off ≈0.4 mm, to reduce further loss of material whilst inserting and removing the tibial insert from the tibial tray.

2. Tibial trays and femoral components were cemented into KS6 holders (Figure 8.4).

3. Tibial and femoral component alignment was visually checked by covering femoral component with a thin layer of Microset 101FF black dye (Microset Products, UK) and bringing tibial and femoral component into contact at 0° flexion. The black marks on the tibial inserts visualised whether the femoral condyles are approximately positioned over the dwell points on both articulating surfaces.

4. Pre-study pictures were taken of the tibial insert top surface to take a note of any existing scratch marks.

5. Tibial inserts were pre-soaked for 2 weeks in purified water to accommodate for mass changes due to fluid adsorption, and then dried for at least 48 hours in the gravimetric room to acclimatise prior taking gravimetric measurements.

6. Whilst inserts were drying, at least five CMM measurements were performed and different time intervals:

    6.1. In the morning and afternoon on the first drying day.

    6.2. In the morning and afternoon on the second drying day.

    6.3. Before the gravimetric measurement on the third day.

7. Only then pre-study gravimetric measurements were taken.

a)   b)
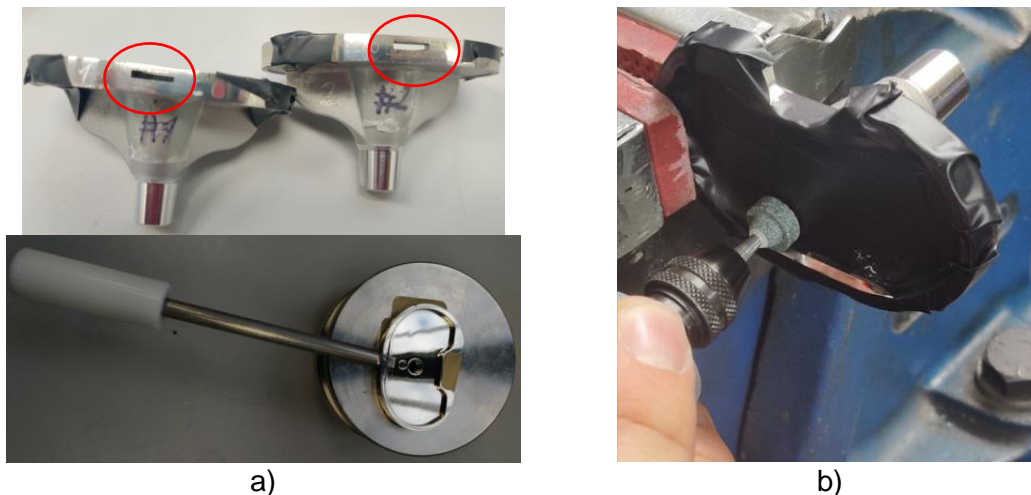
Figure 8.8. Tibial tray was prepared by a) cutting a square hole so the tibial insert could be pushed out with a flat end screwdriver, and b) the anterior locking mechanism was dulled to reduce tibial insert damage during removal.

a)   b)
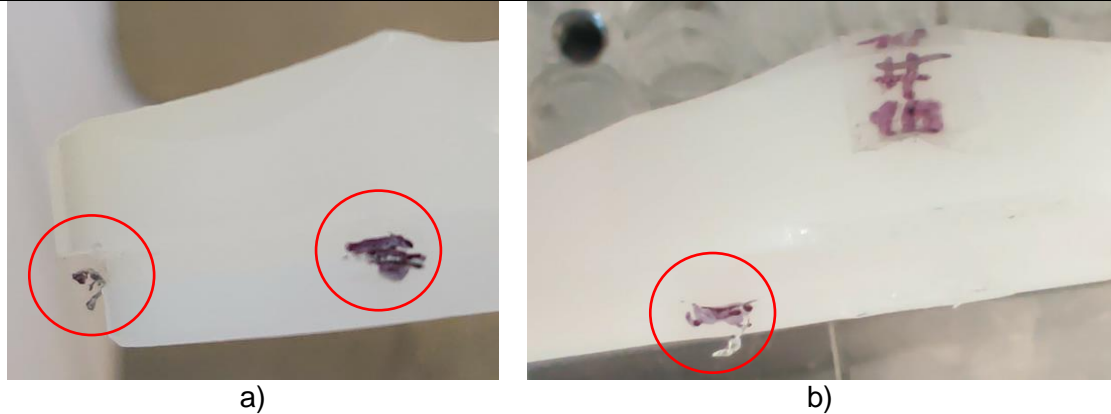
Figure 8.9.Example image of loose strands of material at the a) posterior and b)
anterior locking mechanism. The red circle highlights the areas where material was cut
off by the tibial tray.

Study procedure:

1. During simulation with KS6:

    a. Output profiles were checked daily to ensure that the output profiles were
       still within ±5% range of the input profile (Figure 8.16).

    b. Bovine serum lubricant was changed approximately every 5 days
       (approximately after 333,333 cycles).

2. After performing 1 MC on a knee simulator, all specimens were cleaned and then
   dried for at least 48 hours in the gravimetric room.

3. Gravimetric measurements were performed after drying.

4. CMM measurements were performed after gravimetric measurements.

5. After finishing the measurements, pictures were taken of the tibial insert surface.
   Wear scars were marked with a permanent pen, which were afterwards cleaned off
   with isopropanol.

6. At the end of every million cycles the specimens were moved to a different testing
   station on KS6 to accommodate for loading and motion differences between each
   station as shown in Figure 8.16.

7. This procedure was repeated until 3 million cycles were completed.

8.3.2 Gravimetric measurements

Wear of each test specimen was assessed by calculating change in mass. Tibial insert
mass was measured before starting the knee simulator study and after completing
every 1 MC. An additional measurement was performed after completing 1.45 MC
because the study had to be paused due to laboratory closure. The average mass of
each specimen was calculated from five consecutive measurements which did not
differ by more than 0.1 mg. Change in mass was calculated by subtracting test

measurements from the pre-test measurements. Change in mass of test specimens was further corrected by subtracting the change in mass from control specimen for its group to compensate for changes due to liquid sorption.

Wear volume per each test specimen was calculated using a density of 0.934 mg/mm^3 for the UHMWPE GUR1020 material [197]. The gravimetric measurement setup is shown in Figure 8.10. The XP205 digital microbalance had accuracy of 0.015 mg at low load [198].

Figure 8.10. Gravimetric measurement setup.

8.3.3 CMM measurements

CMM measurements with Legex 322 were performed on soaked tibial inserts before starting the knee simulator study and after completing every gravimetric measurement.

CMM accuracy was checked every day before performing measurements by measuring a ceramic calibration sphere. The daily calibration checks showed that CMM accuracy was within 0.0015 mm from nominal dimension. CMM probe (probe code A-5000-3553) with diameter of 3 mm and stem length of 21 mm was used.

A bespoke metal tray fixture (Figure 8.11) was used to maintain consistent specimen positioning throughout measurements. The tray fixture had a cut-out which replicated the tibial tray geometry to match the inferior geometry of the tibial insert. The same tray fixture was used throughout the study for all test specimens to improve measurement repeatability by providing consistent reference points. Tray fixture was bolted to the CMM bed to eliminate fixture misalignment during specimen assembly.
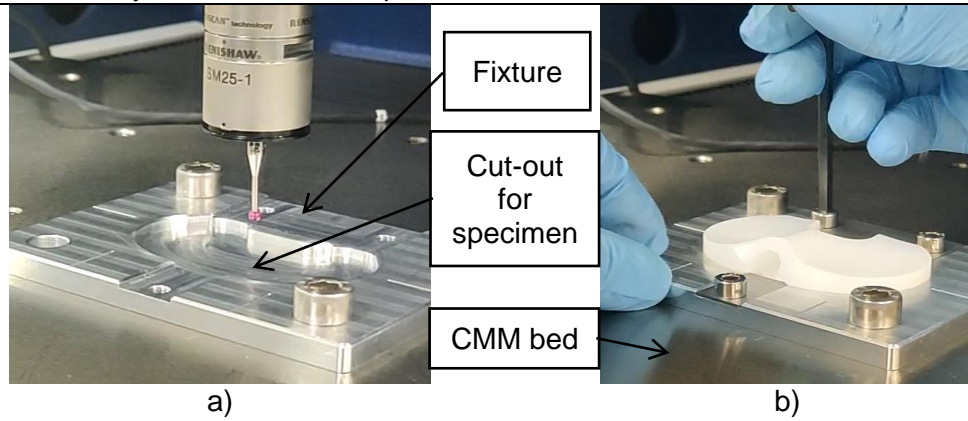
Figure 8.11. Fixture for holding tibial insert specimens a) without insert and b) with insert.

CMM was used to measure top surface geometry in M-L direction at 0.2 mm intervals for all tibial inserts (Figure 8.12). CMM trace lines were taken at 3 mm intervals in A-P direction across the entire top surface (Figure 8.13 and Figure 8.14). Trace lines were spaced out with 3 mm intervals to reduce the measurement time to approximately 10 minutes per specimen. The tibial insert point of origin was assumed in the centre of the tibial insert at the bottom face colinear with the dwell points (Figure 8.14).
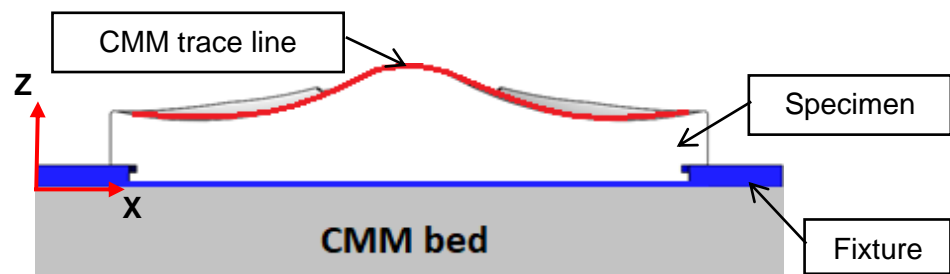
Figure 8.12. Example illustration in frontal cut view of the tibial insert positioned in the bespoke fixture (red lines indicate the CMM trace line geometry).
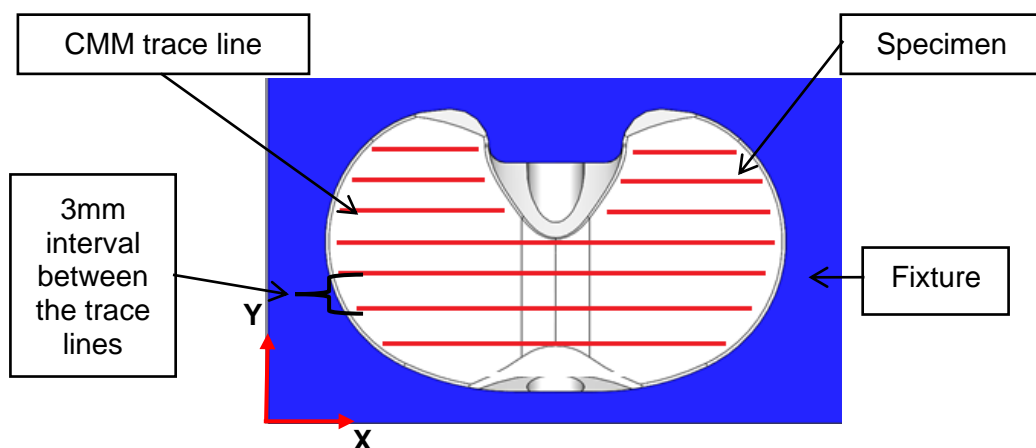
Figure 8.13. Example illustration in top view of modified tibial insert positioned in the bespoke fixture. The surface topology trace lines (in red) are measured by CMM in M-L direction.

a)   b)
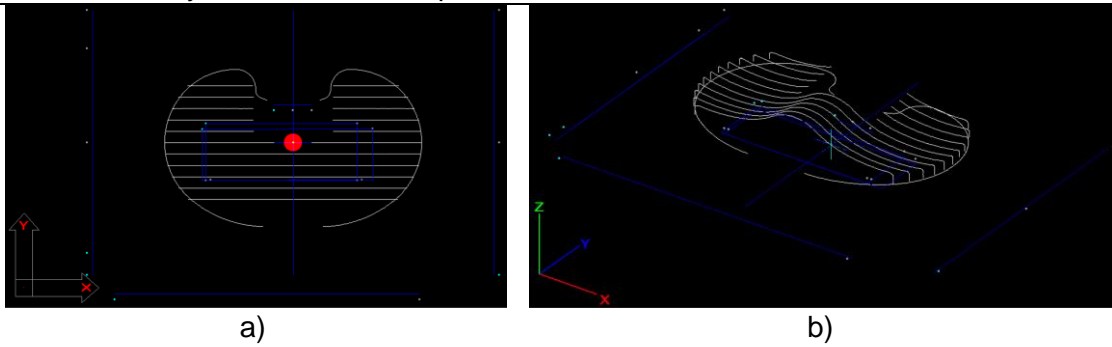
Figure 8.14. Example image of CMM trace lines from a) top view and b) isometric view.
Point of origin is shown with the red dot.

Once the studying was completed, the point clouds obtained from the CMM were
analysed in MATLAB (R2019a, MathWorks, USA) to determine the location and size of
the surface damage of the tibial insert.

8.3.3.1 CMM measurement precision

CMM measurement and fixturing method was validated by calculating CMM
measurement precision. Measurement imprecisions could be caused by material
expansion/shrinking or tibial insert misalignment within the fixture due to repetitive
assembling. Therefore, undamaged tibial insert specimens were remeasured six times
during different time periods, to calculate measurement variation caused by changes in
the ambient environment and due to manual handling.

Specific measurement points were chosen across the tibial insert superior surface. The
height measurements were taken at the lowest point on each articulating surface for
every measured trace line (Figure 8.15). Each measurement point served as a sample
which was remeasured six times during the pre-study measurement stage. Then
standard deviation (SD) was calculated per each sample, and pooled SD (also called
as pooled variance [199]) was calculated across all of the sample SDs. Since the
number of measurements were the same for each sample, a simplified pooled SD
equation was used (Equation 1).
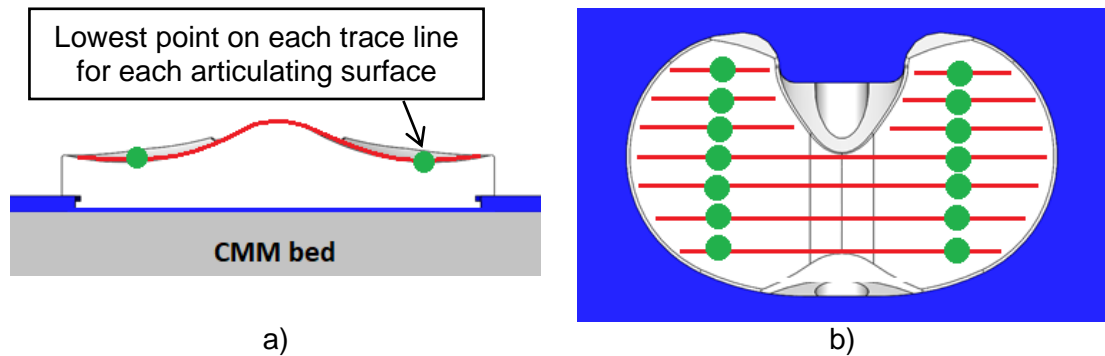
Figure 8.15. To calculate measurement precision, pooled standard deviation was
calculated by measuring the height values of the lowest point (green dot) at each
articulating surface for every measured trace line. Illustration from a) side view and b)
superior view.

S_{Pooled}: pooled standard deviation
S: standard deviation for each
measurement point
k: number of measurements
points

$$S_{Pooled} = \sqrt{\frac{S_1^2 + S_2^2 + \cdots + S_k^2}{k}}$$

Equation 4:
Pooled standard
deviation

Pre-study measurement data resulted in pooled SD of 0.007 mm. The measurement
precision was calculated as three pooled SD of 0.020 mm, therefore following the
empirical rule than 99.7% of data points of height variations are captured within 0.020
mm. Accordingly, any geometrical height deviations within ±0.020 mm could not be
distinguishable from specimen misalignment, expansion, or other surface artefacts.
Only surface height deviation outside ±0.020 mm was considered as an actual
deformation caused by the KS6 knee simulator.

8.3.4 Wear scar images

Digital camera images were taken at 0 MC, 1 MC, 2 MC, and 3 MC on a knee
simulator. Images were taken with Panasonic Lumix GF7 digital camera. Wear scars
were manually marked with a permanent marker on both the superior and inferior
surface. The wear contour was outlined with a solid line and the glossy burnished
surface was filled in with stripes.

Additionally, digital microscope images were taken with Alicona Infinite Focus after
completing 3 MC to better visualise the wear scars on the superior surface of the tibial
inserts (Figure 8.20), which were not visible on digital camera images. Alicona settings:
only coaxial light was used with brightness of 700 µs, contrast of 4.0, vertical resolution
of 410 nm, and lateral resolution of 23.48 µm. Each image took aproximately 14 hours
of scanning.

8.4 Results

8.4.1 Knee simulator output profiles

KS6machine was able to maintain output profiles for all six stations mostly within ±5%
of the input profile (Figure 8.16). KS6 simulator struggled to maintain output profiles
within the ±5% range for axial force between 0-20% of the gait cycle and for A-P
displacement between 0-20% and 65-70% of the gait cycle.
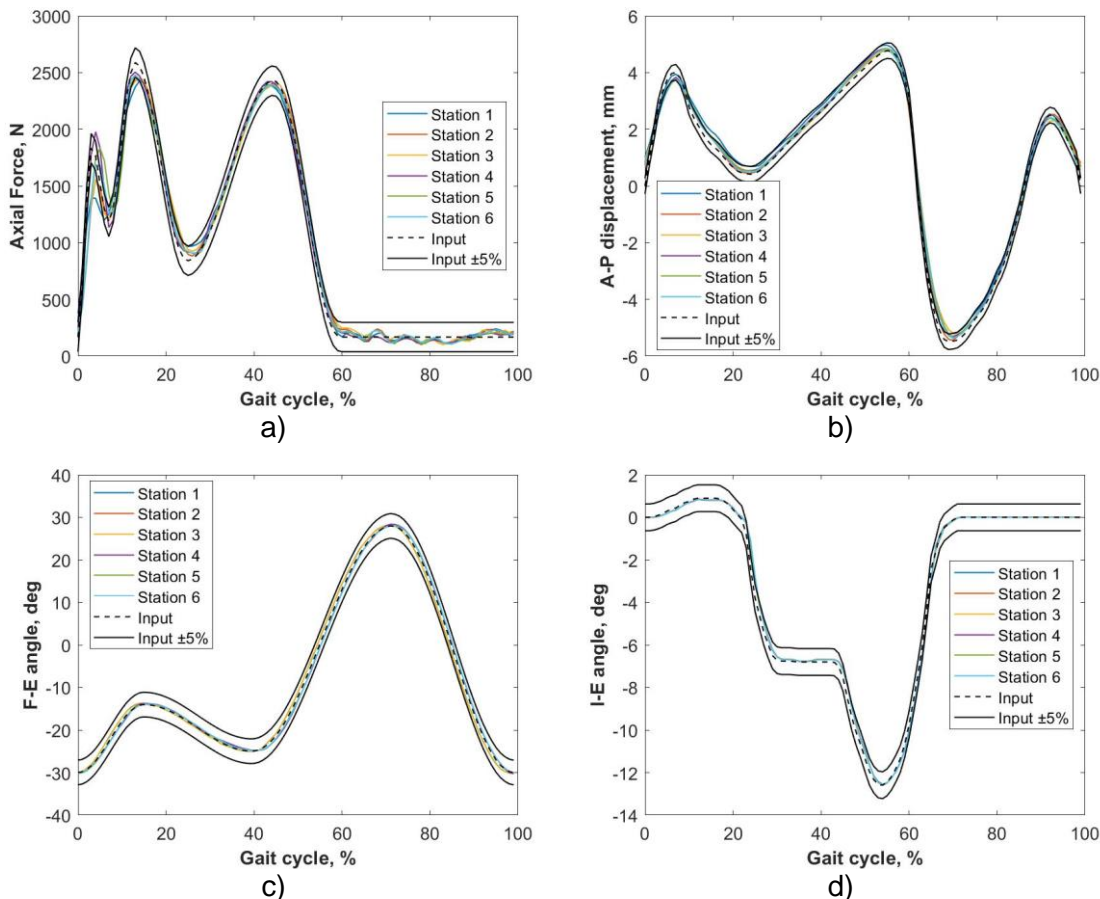
Figure 8.16. KS6 output profiles for a) axial force, b) A-P displacement, c) F-E angle,
and d) I-E angle.

8.4.2 Gravimetric measurements

Volumetric wear was calculated after completing 1 MC, 1.45 MC, 2 MC, and 3 MC on a
knee simulator. The average wear rate with 95% confidence interval (CI) for the original
and modified tibial insert group was 10.22 ± 5.04 mm³/MC and 11.71 ± 12.11 mm³/MC
respectively (Figure 8.17). Student's unpaired two sample t-test with significance taken
at $p<0.05$ showed no statistically significant difference between the two groups at 3 MC
with p-value 0.65 (Table 8.1). The group with modified tibial inserts showed larger
variation in wear volume compared to the group with original inserts. Modified
specimen No. 21 showed the smallest wear rate of 6.42 mm³/MC, whilst modified

specimen No. 23 showed the largest wear rate of 16.02 mm^3/MC among all six test
specimens from both groups after 3 MC (Figure 8.18).

Table 8.1. Cumulative wear volume at each measurement interval.

	Wear volume, mm^3						Average group 1, mm^3	Average group 2, mm^3	p-value between group 1 & 2
	Group 1 (with through hole)			Group 2 (original)					
MC	No.21	No.22	No.23	No.24	No.25	No.26			
0-1	4.73	18.16	10.10	14.59	13.07	10.81	11.00	12.82	-
0-1.45	8.16	22.24	20.94	23.03	17.65	12.75	17.11	17.81	-
0-2	12.40	27.56	29.68	30.60	23.30	17.22	23.21	23.71	-
0-3	18.84	39.25	46.86	35.96	29.89	25.62	34.98	30.49	0.65
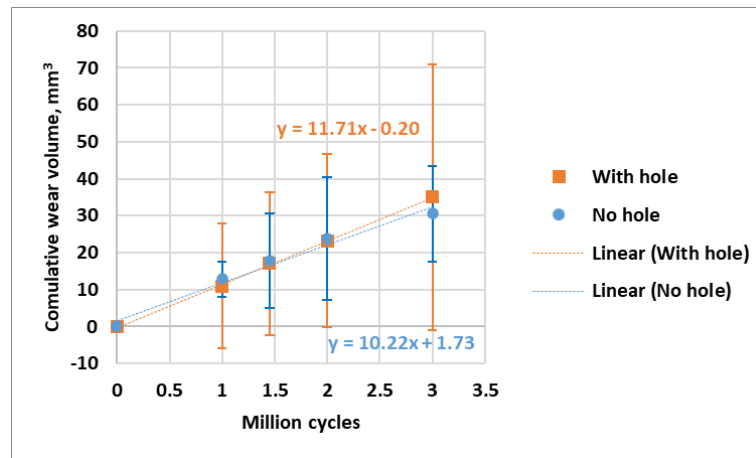
Figure 8.17. GMK Primary unirradiated UHMWPE GUR1020 cumulative average wear
volume over 3 MC with 95% CI. Note: zero wear was assumed at the beginning of the
study.
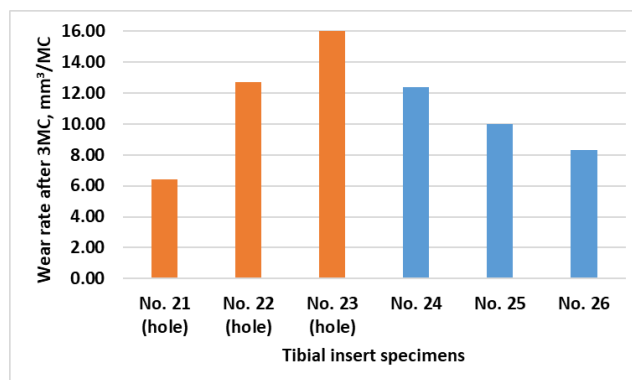
Figure 8.18. GMK Primary unirradiated UHMWPE GUR1020 wear rate per each
original and modified test specimen after 3 MC.

8.4.3 CMM measurements

The surface deviation (caused by wear and plastic deformation) was calculated for
each tibial insert by subtracting the averaged undeformed geometry, obtained from
pre-study measurements, from the deformed geometry at each MC (Table 8.2). All
specimens showed maximum surface deviation on the medial condyle positioned

anterior from the dwell point, with maximum deviation up to 0.40 mm after completing 3

MC. All tibial inserts showed different surface deviation depth and contour location,

matching the wear scar images shown in Table 8.5 and Figure 8.20. Additionally, the

surface deviation contour plots visualised plastic deformation around the implant

perimeter outside the wear scar regions, which is further described in Figure 8.21.

Table 8.2. CMM contour plots of axial surface deviation for each tibial insert top surface
geometry after 1 MC, 2 MC, and 3 MC compared to pre-study geometry.
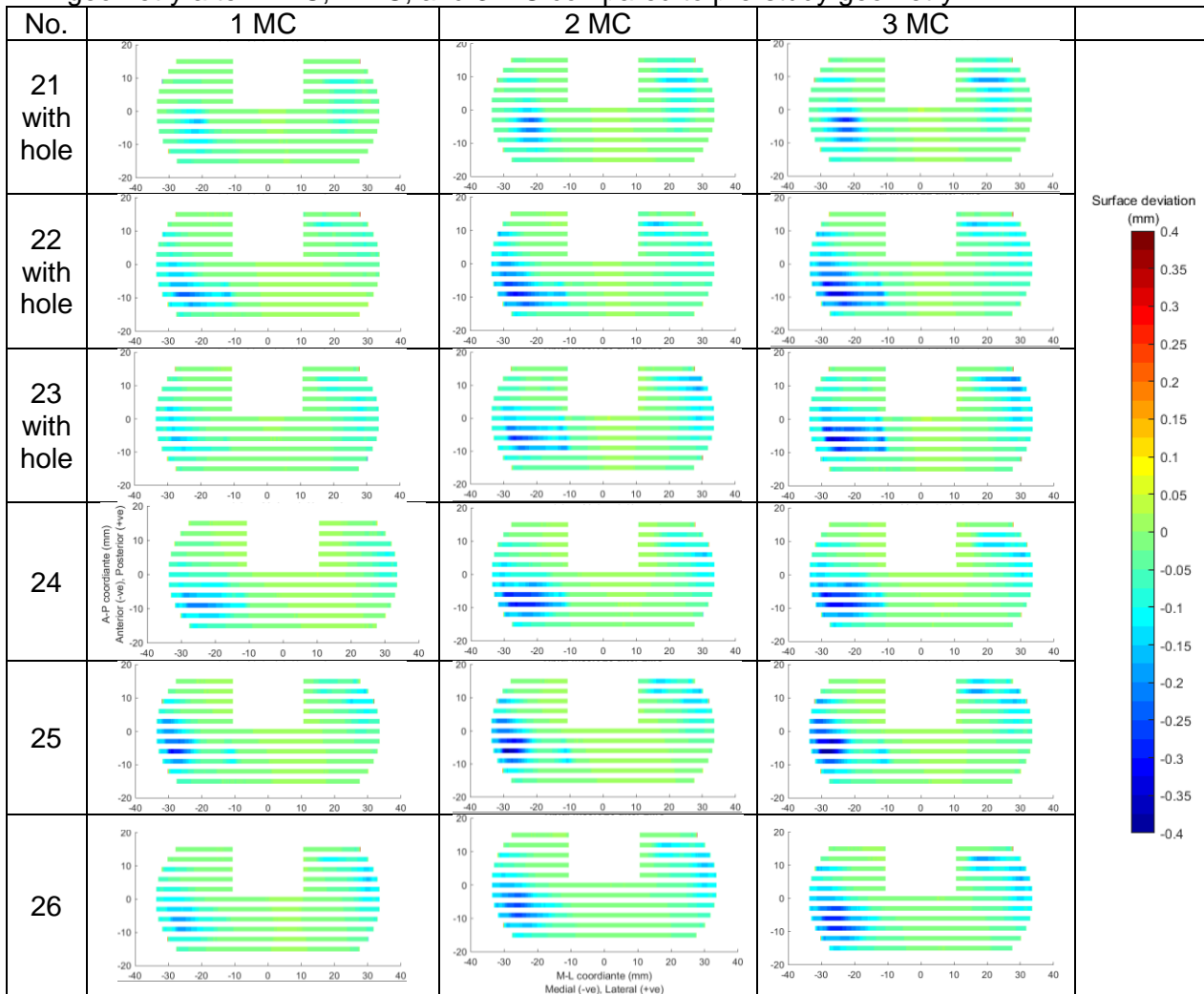
Whilst Table 8.2 illustrates surface deviation also at the intercondylar area, it is difficult

to distinguish the exact magnitude of the deviation from the coloured contour plots.

Therefore,

Table 8.3 shows data regarding the surface deviation for the intercondylar area above the hole (within ±5 mm M-L from the origin).

Table 8.3. Minimum, maximum, and mean surface deviation above the hole
(within ±5 mm M-L from the origin) for each tibial insert at 3 MC.

Specimen No.		Min, mm	Max, mm	Mean, mm
21	With	-0.016	0.029	0.007
22	10 mm	-0.029	0.022	0.004
23	hole	-0.025	0.029	0.009
24		-0.016	0.010	0.000
25	Original	-0.015	0.017	0.003
26		-0.027	0.001	-0.011

Additionally, surface deviation at the far medial side is shown in Table 8.4, ranging

between -0.068 mm and -0.208 mm, because it indicates tibial insert plastic

deformation outside the wear scar.

Table 8.4. Minimum surface deviation at the far medial side (between -34 mm
and -32 mm M-L from the origin) for each tibial insert at 3 MC.

Specimen No.		Min, mm
21	With	-0.068
22	10 mm	-0.165
23	hole	-0.123
24		-0.168
25	Original	-0.208
26		-0.162

8.4.4 Wear scar images

Digital images of wear scar contour outlines at the superior and inferior surface after
each MC are shown in Table 8.5 and Table 8.6 respectively. Digital images show
different wear scar location on all tibial inserts. As a common feature the wear scars on
the medial side are larger compared to the lateral side.

Table 8.5. Tibial insert wear scars on the superior surface at each measurement
interval for modified insert (No 21-23) and original inserts (No 24-26). Wear scars were
outlined with a solid line. Burnished surface areas were filled in with stripes.
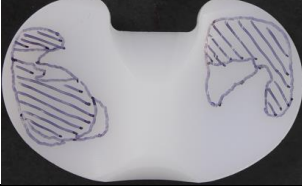
No.	1 MC	2 MC	3 MC
21 with hole			
22 with hole			
23 with hole			
24			
25			
26			

Table 8.6. Tibial insert wear scars on the inferior surface at each measurement interval
for modified insert (No 21-23) and original inserts (No 24-26). Wear scars were outlined
with a solid line. Burnished surface areas were filled in with stripes.

No.	1 MC	2 MC	3 MC
21 with hole			
22 with hole			
23 with hole			
24			
25			
26			

Some tibial inserts also showed noticeable wear scars at the bottom of the side lip
(Figure 8.19), which indicated that the tibial insert side faces could deform and be
pressed against the side rims of the metal tibial trays predicted by FEA models shown
in Figure 4.32.

a)   b)

Figure 8.19. Example images of backside wear scars after 3 MC on tibial insert
specimen a) No. 23 and b) No. 25. Red circles highlight the wear scars at the bottom
side face.

Digital images in Table 8.5 and Table 8.6 only show the approximate wear scar contour outline. Additional images with Alicona microscope were taken after 3 MC to better visualise the worn areas and show sign of scratching, pitting, and burnishing on the superior surface.

a) No. 7 (control)   e) No. 27 (control)

b) No. 21   f) No. 24

c) No. 22   g) No. 25

d) No. 23   h) No. 26
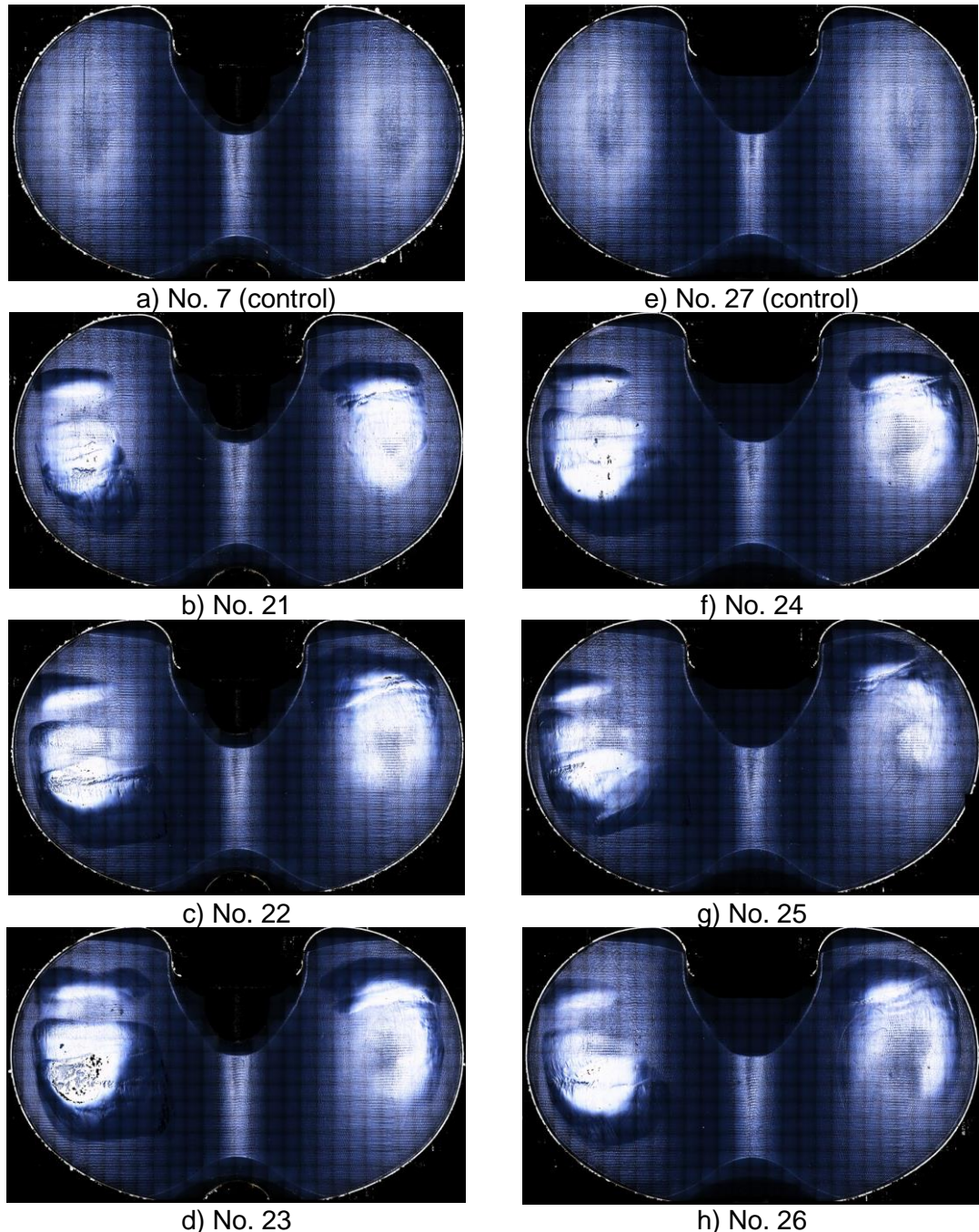
Figure 8.20. Wear scar images of a-d) modified (hole diameter of 10mm) and e-h) original tibial inserts, taken with Alicona digital microscope after completing 3 MC on a knee simulator, showing original machining marks and marks of scratching, pitting, and burnishing.

Images taken with digital camera and Alicona microscope could not visualise any signs of deformation outside the wear scar. However, after making side by side comparison of CMM contour plots and Alicona images, it could be observed that the tibial insert was deformed also outside the wear scar area (Figure 8.21). For example, CMM data indicated that the medial side lips of the tibial insert have been deflected by up to -0.208 mm as shown in Table 8.4. This deformation was considered to be real, because it was outside the limit of ±0.020 mm, which represents the precision of this CMM measurement method, and some inserts also showed signs of the backside wear as shown in Figure 8.19.
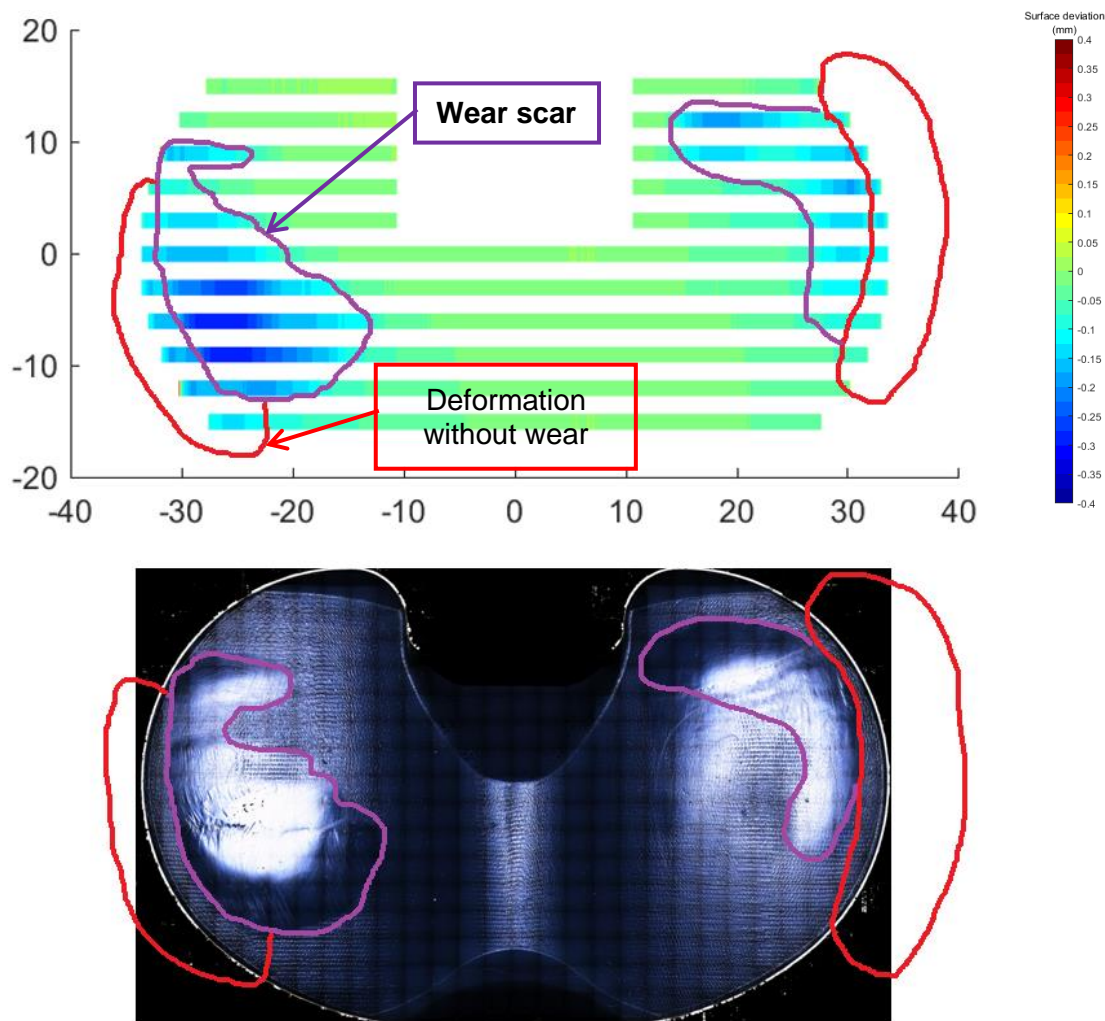
Figure 8.21. Example comparison between a CMM image and a digital photography for tibial insert specimen No. 26 after 3 MC. Both the CMM image and the digital photography can be misleading. CMM image was useful for visualising deformation depth, but it could not distinguish areas without wear. For example, deformation (highlighted with a red line) is not part of the wear scar (highlighted with a purple line). Digital photography was useful for visualising wear scar area; however, other deformed areas might still look undamaged.

8.4.5 Discussion

The measured wear rates and 95% confidence intervals with unirradiated UHMWPE GUR1020 under ISO 14243-1:2009 in displacement control were 10.22 ± 5.04 mm^3/MC for original inserts and 11.71 ± 12.11 mm^3/MC for modified inserts and fell within the range of other published studies. Study by Okazaki et al. with unirradiated UHMWPE GUR1020 under ISO 14243-1:2009 in load control showed volumetric wear rate of 15.1 ± 1.2 mm^3/MC [200]. Studies performed at the University of Leeds with gamma vacuum foil irradiated UHMWPE GUR1020 showed wear rates of 4.0 ± 3.1 mm^3/MC, 9.7 ± 3.7 mm^3/MC, and 22.6 ± 5.1 mm^3/MC when tested with ISO 14243-3 displacement control in "low", "intermediate", and "high" kinematic conditions [201].

No statistical difference was observed between the volumetric wear rate of the two groups, Student's unpaired two sample t-test at 3 MC had p-value of 0.65. However, group with modified inserts showed larger variation in wear volume compared to original inserts. Calculated confidence intervals were probably larger due to a small group size of 3 specimens (n=3) whilst other studies used 6 specimens (n=6). Furthermore, the variations between the two groups may have been affected due to motion and loading differences between each knee simulator station, due to material loss caused by sharp edges on the tibial tray, and due to specimen misalignment during cementing.

CMM measurements taken after 3 MC showed maximum surface deviation up to 0.40 mm. No matching publications could be found on geometry measurements with tibial insert made of UHMWPE GUR1020 under ISO 14243-1 loading. A study with unirradiated GUR1050 insert under ISO 14243-3 loading showed up to 0.30 mm deviation after 2 MC [202]. A study with GUR1020 irradiated with 30 kGy vitamin E stabilised insert under "High100" loading showed over 0.30 mm deviation after 2.5 MC [19]. A study with unirradiated conventional polyethylene insert under ISO 14243-3 loading combined with healthy patient kinematics after 3 MC approximated maximum lateral and medial surface deviation of 0.78 mm and 0.45 mm respectively [106].

During cementing stage, tibial inserts were randomly misaligned (Figure 8.23) from the intended position (Figure 8.22) which changed the wear scar pattern. Therefore, wear scar CMM measurements between the two groups could not be directly compared. Nonetheless, CMM measurements allowed to assess the surface deviation at the area of interest above the intercondylar area. Even though the loading areas were randomised, the knee simulator was still able to create surface damage (surface deviation caused by wear and plastic deformation) near the medial side of intercondylar area. Both original (No. 24 and No. 25) and modified (No. 22 and No. 23) tibial insert

specimens showed damage approximately 10 mm from the origin on the medial side. After 3 MC the intercondylar area (±5 mm from the M-L symmetry line) for all six tibial inserts showed average surface deviation ranging between -0.011 mm and 0.009 mm, which was within the measurement precision of ±0.020 mm and could not be distinguished from the measurement artefacts. This indicates that the 10 mm hole did not significantly affect the way how tibial insert deformed at the intercondylar area.

CMM measurements revealed surface deviation on the far medial and lateral side of the tibial insert as previously predicted by the FEA models (see Figure 4.32**)**. Across all specimens the minimum surface deviation on the far medial side ranged between -0.068 mm and -0.208 mm, which matches the approximate gap size of 0.20 mm (previously described in Section 4.2.12) between the side face of the tibial insert and tibial tray. This illustrates that the tibial insert can deform also at areas which are not under direct loading. A different study performed with a micro-CT has previously shown that geometry change could occur across all surfaces of the tibial inserts, such as, the articular surface, backside surface, sides, and locking mechanism [106].

8.4.6 Limitations

Due to the technical problems with KS6, the knee simulator loading was performed in displacement control. Therefore, the study results could not be used to validate dynamic FEA models. This study method could be improved in future by performing load control profiles per ISO 14243-1:2009 as originally intended. Additionally, this study could be further improved by performing load control profiles per ASTM F3141, since dynamic FEA models (see Figure 5.17) indicated larger damage at the intercondylar area.

Several difficulties were discovered during this knee simulator study. The tibial trays had sharp edges, which scratched the tibial insert. During simulation each KS6 station applied slightly different motion and loading profile. During the cementing stage all tibial trays were differently positioned.

As a precaution, prior to starting the study all tibial inserts were assembled and disassembled multiple times to remove all loose strands, and the anterior edge of the tibial trays were dulled. However, there is a possibility that additional material was scratched off during studying, which could have increased the wear rate. To mitigate the different loading conditions between each KS6 station all specimens were attached to a different station after every million cycles.

During the calibration stage, it was ensured that the knee simulator holders maintain
translation position within ±0.5 mm and rotation position with ±0.5° from the zero
position. During cementing stage, an existing standard operating procedure was
followed. However, specimen misalignment during cementing could not be mitigated
due to lack of guiding fixtures. Inadvertently, human error was introduced, causing tibial
insert misalignment (Figure 8.23) from the intended position (Figure 8.22). The M-L
position varied approximately from 3.8 mm to 6.0 mm from the target 4.7 mm. The A-P
position varied approximately from 9.4 mm to 11.5 mm from the target 12.0 mm. The
I-E rotation varied approximately from 0.5° to 4.0° from the target 0.0°. Due to implant
misalignment each tibial insert was loaded in a different location, which most likely
changed the contact mechanics for each specimen and therefore may have resulted in
different wear rates.
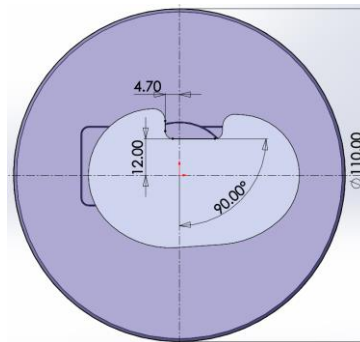
Figure 8.22. Ideal tibial tray position on the knee simulator tray holder.
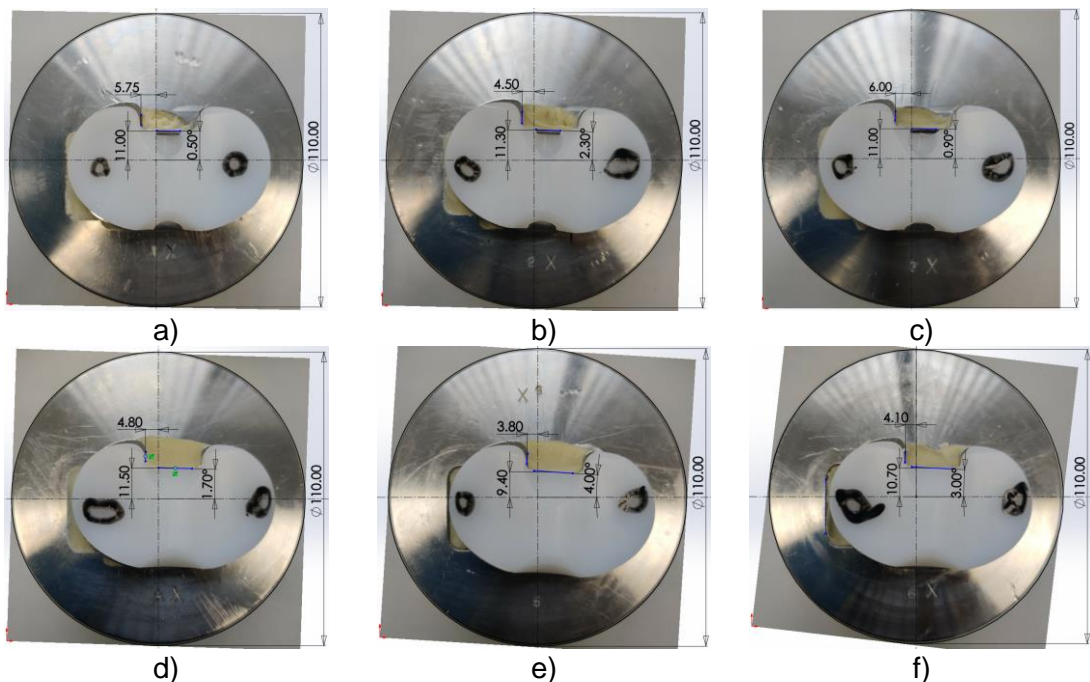
Figure 8.23. Tibial tray position after cementing a-f) specimens No. 21 to 26 on the
knee simulator tray holder No. 1 to 6 respectively. Note: dimensions were
approximated by manually scaling the image within SolidWorks.

Tibial insert misalignment could not be mitigated for this study. Prior to cementing an attempt was made to create a 3D-printed cementing guide (Figure 8.24a). The cementing guide was necessary to improve the placement repeatability by restricting A-P and M-L alignment and in I-E rotation. Unfortunately, the cementing guide was unsuccessful because the tray holder had no geometrical features on the outer surface to provide necessary fixation and restrict I-E rotation. Therefore, the cementing technique had to be done by following the existing standard operating procedure which relied on alignment check with the "naked eye". However, for the future studies the cementing technique could be improved by using a 3D-printed guide. This could be accomplished by drilling two small holes on the top of the tray holder, which then could be used as fixation and reference points for any 3D-printed guide design.

a)   b)
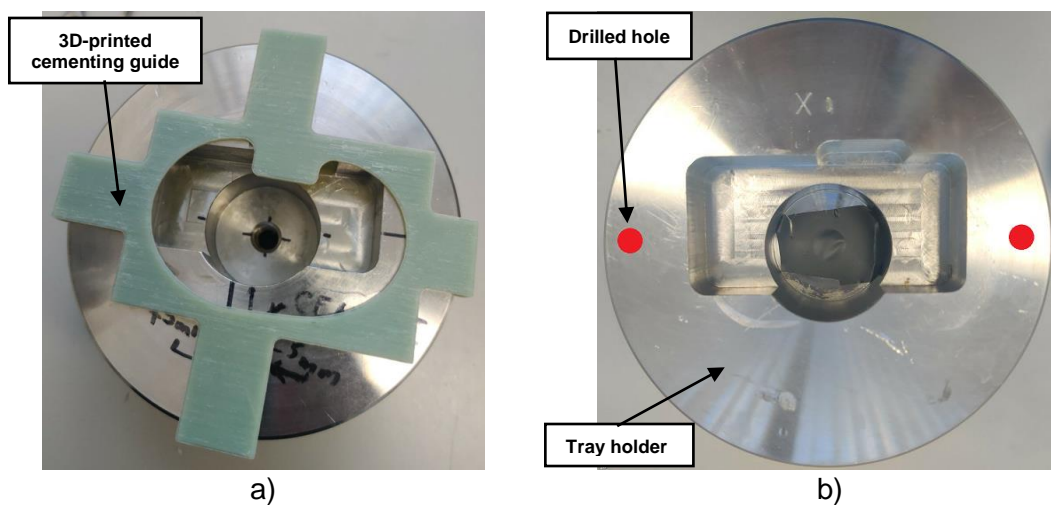
Figure 8.24. An attempt was made to design a) a 3D-printed cementing guide which would help with alignment during the cementing procedure. However, the 3D-fixture could not be used because the tray holder had no geometrical features to restrict I-E rotation. A potential solution could be to b) drill two holes (shown as red dots) on the top surface to provide fixating points for any 3D-printed guide.

During CMM measurements the trace lines were spaced out in A-P direction with 3 mm intervals to reduce the measurement time to 10 minutes. This CMM method did not measure the entire surface of the tibial insert, therefore it had missing data regarding surface deviation. This CMM method was developed only to perform direct comparison between two groups which were loaded in identical conditions. Unfortunately, loading conditions differed for all specimen in both groups and it was not possible to directly compare CMM results.

8.5 Conclusion

The results obtained from the laboratory experiment on a knee simulator gave an indication that there was no influence on surface wear rate in this short term 3 million

cycle study due to the hole in the tibial insert, which could be then used to fit in
electronics and sensors. After performing 3 MC in displacement control with an
adapted ISO 14243-1:2009 loading profile following observations were made:

1. The wear rate between the two groups (original insert and modified insert with a
   10 mm hole) had no statistical difference. However, it must be noted that this
   study used a small group size of 3 specimens (n=3) and modified inserts
   showed larger wear variation.
2. CMM measurement showed no noticeable deformation at the intercondylar
   area. All specimens from both groups showed mean surface deviation at the
   intercondylar area within ±0.020 mm, which could not be distinguished from the
   measurement artefacts.
3. CMM measurements revealed surface deviation on the far medial and lateral
   side of the tibial insert as previously predicted by the FEA models.

This study provides only preliminary results. Further knee simulator studies should be
performed in load control per ASTM F3141 standard on a tibial insert with embedded
electronics, to replicate various scenarios of human gait and cause larger damage near
or at the intercondylar area, to assess the differences in wear rates, and to investigate
whether any damage is caused to the embedded electronics.

9 Overall discussion and future work

9.1 Introduction

The aim of this PhD research was to investigate how to modify a conventional tibial insert design to incorporate sensors and electronic components whilst ensuring patient safety. A novel design approach was developed, by sealing electronic components into a PU capsule and placing only at the intercondylar area of the tibial insert.

To date, only metal implant components have been successfully modified to develop smart knee implants for clinical use [54, 64]. Smart implants made of metal have several limitations: enlarged dimensions require additional bone resection, interference with electromagnetic signal, higher cost of manufacturing, and unavailability of different designs which limits the practical application. To overcome the limitations of metal components, other research groups tried developing a smart tibial insert [10-12], but their studies focused only on electronic component development and did not address mechanical design, manufacturing limitations, and safety issues. Therefore, this PhD research presented methodologies on how to develop smart tibial inserts by resolving the mechanical design challenges.

Experimental studies were carried out using GMK Primary CR TKR manufactured by Medacta International. The tibial insert was made of unirradiated GUR 1020 UHMWPE. In most experimental tests a modified insert was compared with the original conventional insert. A conventional tibial insert was modified by drilling a 10 mm hole at the intercondylar area and placing a capsule within the hole. The experimental studies investigated whether design modifications had any effect on tibial insert performance, specifically, by changing contact pressure, deformation, and wear. The effect on contact pressure was found using a Tekscan pressure sensor. The effect on deformation was determined by height gauge and CMM measurements. Finally, wear rates were compared by performing gravimetric measurements during a 3 MC knee simulator study.

Computational FEA models were developed using Abaqus CAE 2017 to model TKR within the experimental simulator under both static and dynamic loading. The static FEA model was validated by comparing the plastic deformation and contact pressure results with the experimental data. The static FEA model was then used to optimise the design of modified tibial insert, embedded capsule, and strain gauge orientation. Static FEA model was also used to develop dynamic FEA models simulating different daily activities, such as, walking, jogging, pivot turn, crossover turn, stairs ascend, stair descend, and sit to stand to sit. However, the dynamic FEA model was not further

validated with experimental knee simulator data, due to technical problems with the knee simulator.

No previous study on smart tibial inserts has investigated mechanical performance and modes of damage, such as, plastic deformation, wear, and fracture. The use of both experimental and computational methods allowed analysing a number of different manufacturing methods, optimal strain gauge position, damage caused to tibial insert due to different daily activities, and potential safety issues.

9.2 Computational Methods

Both static and dynamic FEA models were developed in order to analyse tibial insert performance. The intended purpose for using FEA models was to help with design decisions before performing experimental studies.

Static FEA models were validated with experimental results for contact pressure and plastic deformation at the dwell point. The finding showed good agreement between the static FEA model predictions and the experimental measurements with two tibial inserts. The static FEA model predicted a unique loading pattern with edge loading on the far medial and lateral side, which was also experimentally observed on Tekscan film measurements with both specimens. The Tekscan pressure contact area differed by no more than 10% from the static FEA prediction. Literature shows that K-scan 4000 film could overestimate up to 20% [150], therefore the FEA prediction falls within this range. The peak contact pressures for both insert specimens differed by up to 6% from the static FEA prediction. Other studies have achieved results within 10% of the predicted value for contact area and contact pressure measurements [121, 151]. The laboratory experiment measured 30 μm deformation with +/-5 μm accuracy, which was close to the static FEA prediction of 38 μm. In comparison, a different study achieved 8% accuracy by implementing a dynamic nonlinear viscoelastic FEA model with time-dependent relaxation [152]. The FEA predictions were close to the laboratory experiment results and showed realistic deformation pattern, which indicate that implant geometry was sufficiently defined and appropriate material properties were chosen.

The static FEA models were further used to optimise smart tibial insert design and to analyse the feasibility of strain gauge measurements. Both FEA and experimental results showed no significant difference in contact pressure and plastic deformation between original and modified tibial inserts under axial loading at the dwell point. The FEA finding indicated that a cylindrical capsule could be used to provide the biggest volume for electronic circuitry when compared to bullet and pill shape capsule designs.

Both FEA and experimental studies showed that a capsule placed at the intercondylar area would be mostly compressed in the M-L direction, therefore, strain gauges should be aligned in M-L direction to give stronger signal. Both FEA and experimental studies showed that strain patterns within the capsule correspond to changes in axial forces and to changes in loading location along A-P direction.

During this PhD research an attempt was made to also develop and validate dynamic FEA models. This is the first study presenting detailed methodology for developing dynamic FEA models to simulate CR TKR in daily loading scenarios per ASTM F3141-17a [49] standard. Heavy loading data for a 100 kg subject were used to simulate walking, pivot turn, crossover turn, stairs ascend, stair descend, and sit to stand to sit. Only one other publication was found performing FEA per ASTM F3141, but it was created for PS TKR and used average instead of heavy loading data among other simplifications [167]. This PhD research discussed the challenges of developing dynamic FEA model, because ASTM F3141 standard does not provide clear guidance on how to simulate soft tissue constraints. Without adequate constraints, the FEA models showed unrealistic kinematics resulting in femoral component dislocation (see Figure 4.38), which would not happen during normal in-vivo walking conditions and would not allow performing experimental studies on a knee simulator. Therefore, this study compiled relevant literature and presented a table (see Table 4.8) with spring stiffness values, which could be used to replicate realistic soft tissue constraints within a knee simulator. When comparing FEA models for ISO 14243-1/3 and ASTM F3141 standard conditions, the ASTM models revealed larger contact areas, stresses, deformations, and different contact patterns, therefore indicating that all available loading patterns should be considered when performing either experimental or computational studies.

The dynamic FEA models were not validated with dynamic experimental tests due to technical issues with the knee simulator. Furthermore, the presented dynamic FEA models did not consider the inertia effects. For example, the FEA models did not consider the mass or the friction of the friction within an experimental knee simulator, nor different time periods were considered. However, the dynamic FEA results were similar to other studies reporting maximum contact pressures ranging from 29 to 62 MPa [148, 169-173].

9.3 Experimental Methods

Experimental knee simulator study was performed on two different tibial insert design groups: original conventional tibial insert and modified tibial insert with a through hole

of 10 mm diameter at the intercondylar area. Both test groups were subjected to loading conditions per adapted ISO 14243-1:2009 in displacement control.

The measured wear rates and 95% confidence intervals with unirradiated UHMWPE GUR1020 under ISO 14243-1:2009 in displacement control for original and modified inserts were 10.22 ± 5.04 mm^3/MC and 11.71 ± 12.11 mm^3/MC respectively. These findings were within the range of another published study with wear rate of 15.1 ± 1.2 mm^3/MC under ISO 14243-1:2009 in load control [200]. No statistical difference was observed between the volumetric wear rate of the two groups with Student's unpaired two sample t-test at 3 MC having p-value of 0.65. However, confidence intervals were probably larger due to a small group size of 3 specimens (n=3) whilst other studies used 6 specimens (n=6).

CMM measurements taken after 3 MC on a knee simulator showed maximum surface deviation up to 0.40 mm for ISO 14243-1 loading. Other published studies have showed maximum surface deviation between 0.30 mm after 2 MC [202] and 0.78 mm after 3 MC [106] for ISO 14243-3 loading. CMM measurements showed no significant deformation at the intercondylar area for both groups showed average surface deviation between -0.011 mm and 0.009 mm, which could not be distinguished from the CMM measurement artefacts. CMM measurements also revealed that tibial insert could be deformed in areas that are not subjected to direct loading, which has been previously reported in another study [106].

Experimental fatigue to failure cantilever bending test method was developed to simulate worst-case failure mode by fracturing the modified tibial insert together with a tibial tray, which has been previously reported in one retrieval study [83]. A fatigue to failure test method was developed by adapting ISO 14879-1 [194] and ASTM F1800 [114] test standards. This was a novel test method adaptation with no publications to compare with. The results showed that one tibial insert placed inside a tibial tray could withstand 10 MC with maximum cyclic force of 2000 N without showing any signs of tibial tray damage, which surpassed the minimum requirement for the clinical TKR implants to withstand 10 MC at 900 N per ASTM F2083-12 [115]. Therefore, indicating that the used GMK Primary TKR design is unlikely to fail in a manner which would expose the electronic component to the human body. In order to fracture the tibial tray, the axial force had to be increased to 4000 N and applied for additional 13.7 MC. After causing tibial tray fracture, the modified tibial insert showed deformation at the intercondylar hole, but the PU capsule remained fixed inside the tibial insert. However, during testing, the capsule made of PU resin created debris which could cause harm to the patient. All four strain gauges remained fully functional throughout testing even

after the tibial tray fractured and showed a signal pattern change in response to the tibial tray fracture.

9.4 Limitations

Static FEA experimental validation study was limited to plastic deformation measurements only at one point (dwell point). The validation study did not consider different flextion angles and loading locations. Tekscan pressure sensors had less accuracy due to less resolution compared to FEA models.

Dynamic FEA models for daily activities were not validated, therefore dynamic FEA models could not be used to perform parametric optimisation to enlarge the hole at the intercondylar area and increase the available volume for electronic circuitry.

Experimental strain gauge studies did not show strain signal pattern during complex loading scenarios, for example, when subjected to motions and loads within a knee simulator.

The experimental knee simulator study could be performed only in displacement control due to technical problems. Therefore, knee simulator results could not be used to validate dynamic FEA. Knee simulator study results showed large variations for wear rates and damaged contact area, which made it difficult to compare the differences in damage caused to the original and modified tibial insert group.

9.5 Conclusions

This PhD research completed all set aims and objectives. This research provided preliminary evidence to confirm the hypothesis that the intercondylar area has minimal or no effect on the structural strength for the tibial insert. The results obtained from the modified tibial inserts indicated that the wear rate was not affected, there were no signs of plastic deformation which could affect joint kinematics, and the implant fracture is unlikely due to the support provided by the metal tibial tray. Therefore, the intercondylar area could be potentially repurposed to contain embedded sensors and electronics.

This study presented a methodology to developed static FEA model for TKR and validate static FEA for contact pressure and plastic deformation. The static FEA models were further used to analyse and optimise the tibial insert design to incorporate sensors and electronic circuitry. This study also presented a methodology for developing dynamic FEA models to simulate TKR motion and loading within experimental knee simulator, but no experimental studies were performed to validate dynamic FEA.

Both FEA and experimental studies have shown that axial force could be approximated with strain gauge measurements taken at the intercondylar area. Furthermore, strain gauges do not need to be directly glued onto the tibial insert surface. Strain gauged can be sealed within a capsule, which is placed inside the tibial insert with an interference fit. Strain gauge measurements could be obtained even when the capsule was made of four different materials: UHMWPE half shells, SS316 half shells, PMMA and PU resin.

The experimental studies for knee simulator and fatigue to failure cantilever bending gave preliminary evidence that it could be safe to place electronic components at the intercondylar area, if the manufacturing procedure for encapsulation was further improved. The only observed significant failure mode was the generation of PU debris due to capsule contact with the metal tray.

Computational and experimental studies have also indicated that strain gauge measurements could also provide clinically relevant data, for example, by approximating the total axial load applied by the femoral component or by indirectly detecting tibial tray fracture.

This study presented following suggestion for the mechanical design of instrumented tibial insert:

1) All electronical components should be placed at the intercondylar area to reduce the risk of affecting wear rates and kinematics for TKR.
2) The external dimension should not be changed to prevent unnecessary bone resection, implant design changes, or changes to the surgical procedure.
3) All electronic components should be placed within a sealed capsule to prevent the exposure to human body.
4) The capsule could be made of various materials, but it is suggested to surround the capsule with UHMWPE due to the risk of generating debris from the capsule.
5) Whilst cylindrical capsule provided the largest useful volume, other capsule shapes could also be used.
6) Encapsulated strain gauges showed the strongest signal when aligned in M-L direction.
7) Instrumented tibial insert performance should be analysed by simulating TKR under different daily activity scenarios.
8) In the current study showed that a capsule with 10 mm diameter could be used, but it should not limit conducting further studies to find larger volume.

9.6 Future Work

This study presented initial design requirements for instrumented implant development, which were set at the beginning of this PhD research. Design requirements are always changing and evolving with time; therefore, the requirements should be reassessed and modified for each individual research projects to comply with particular the stakeholders' needs.

This study has shown a method for validating static FEA for TKR. Dynamic FEA models should be improved by adding mass and changing the loading time. Further work must be done to create a validation method with a knee simulator for dynamic FEA. Once dynamic FEA is validated, the drilled hole shape could be parametrically optimised to increase the free volume for the electronic components.

This study presented a manufacturing method to modify a tibial insert with a drilled posterior hole with diameter of 10 mm. In this study the posterior hole was filled with a PU resin, which caused problems with PU debris due to contact with the metal tray. Future work must be done to improve manufacturing method, for example, by surrounding the PU capsule with a thin layer of UHMWPE during compression moulding or by finding a different method to prevent PU capsule contact with the metal components.

This study presented experimental methods to analyse strain gauge response when loaded with only axial force. The experimental methods should be further improved to analyses strain gauge response when simultaneously loading with multiple forces and torques, for example, by applying I-E torque on the Electropulse E10000 materials testing machine, or by applying loading and motion with the knee simulator machine.

This study presented experimental knee simulator study in displacement control comparing an original tibial insert with a drilled tibial insert. Further knee simulator studies should be performed in load control to analyse differences in kinematics along the differences in deformation and wear rates. In further studies original tibial insert design should be compared with a finalised design of a wireless smart tibial insert. Preferably, knee simulator studies should be performed with ASTM F3141 standard to add M-L force and cause larger damage (plastic deformation and wear) near the intercondylar area. Additionally, standard operating procedures should be further improved regarding specimen alignment to minimise test condition variation between each knee simulator station.

This study has suggested to analyse smart tibial insert performance and safety by examining wear rates, deformation, and fracture risk. Further studies should be performed to analyse other potential risks and usability, for example, it would be of

interest to perform studies with magnetic resonance imaging machine to assess whether any harm could be caused to the patient if strong magnetic fields would force the implant to move, levitate, or heat up or whether the electronic circuitry would get damaged.

Most importantly, future research must be practical instead of academical, if the intention is to develop a commercial medical device. Researchers must not only consider academic aspects. Before even starting the research, researchers must first communicate and understand the challenges of medical device manufacturers, then the limitations of medical device regulations, the necessity of patents before publications, the hospital challenges, and patient needs. Commercial product, compared to published research, is more likely to benefit patients.

10 Bibliography

1.   Human anatomy planes. National Cancer Institute.

2.   Losina E, Thornhill TS, Rome BN, Wright J, Katz JN. The dramatic increase in total knee replacement utilization rates in the United States cannot be fully explained by growth in population size and the obesity epidemic. JBJS. 2012;94(3):201-207. doi: 10.2106/JBJS.J.01958. PubMed PMID: 22298051.

3.   NJR. National Joint Registry for England, Wales, Northern Ireland and the Isle of Man: 15th Annual Report. 2018.

4.   Inacio MCS, Paxton EW, Graves SE, Namba RS, Nemes S. Projected increase in total knee arthroplasty in the United States – an alternative projection model. Osteoarthr Cartil. 2017;25(11):1797-1803. doi: https://doi.org/10.1016/j.joca.2017.07.022.

5.   Kurtz SM, Ong KL, Lau E, Widmer M, Maravic M, Gómez-Barrena E, et al. International survey of primary and revision total knee replacement. Int Orthop. 2011;35(12):1783-1789. doi: https://doi.org/10.1007/s00264-011-1235-5. Epub 2011/03/15. PubMed PMID: 21404023.

6.   Schwartz AM, Farley KX, Guild GN, Bradbury TL. Projections and Epidemiology of Revision Hip and Knee Arthroplasty in the United States to 2030. The Journal of Arthroplasty. 2020;35(6, Supplement):S79-S85. doi: https://doi.org/10.1016/j.arth.2020.02.030.

7.   Evans JT, Walker RW, Evans JP, Blom AW, Sayers A, Whitehouse MR. How long does a knee replacement last? A systematic review and meta-analysis of case series and national registry reports with more than 15 years of follow-up. The Lancet. 2019;393(10172):655-663. doi: https://doi.org/10.1016/S0140-6736(18)32531-5.

8.   Australian Orthopaedic Association National Joint Replacement Registry (AOANJRR). Hip, Knee & Shoulder Arthroplasty: 2019 Annual Report. Adelaide: AOA, 2019.

9.   Torrão JND, dos Santos MPS, Ferreira JAF. Instrumented knee joint implants: innovations and promising concepts. Expert Review of Medical Devices. 2015;12(5):571-584. doi: https://doi.org/10.1586/17434440.2015.1068114.

10.   Crescini D, Sardini E, Serpelloni M, . An Autonomous Sensor for Force Measurements in Human Knee Implants. Procedia Chem. 2009;1(1):718-721. doi: https://doi.org/10.1016/j.proche.2009.07.179.

11.   Crescini D, Sardini E, Serpelloni M, . Design and test of an autonomous sensor for force measurements in human knee implants. Sens Actuator A Phys. 2011;166(1):1-8. doi: https://doi.org/10.1016/j.sna.2010.12.010.

12.   Simoncini M. Design and integration of an instrumented knee prosthesis. PhD thesis 2014.

13.   Clarke HD, Scott WN, Insall JN, Pedersen HB, Math KR, Vigorita VJ, et al. Anatomy. Insall & Scott Surgery of the Knee, 5th edition, chapter 1. Philadelphia: Elsevier Health Sciences; 2012.

14.   Taylor WR, Schütz P, Bergmann G, List R, Postolka B, Hitz M, et al. A comprehensive assessment of the musculoskeletal system: The CAMS-Knee data set. Journal of Biomechanics. 2017;65:32-39. doi: https://doi.org/10.1016/j.jbiomech.2017.09.022.

15.   Halder A, Kutzner I, Graichen F, Heinlein B, Beier A, Bergmann G. Influence of Limb Alignment on Mediolateral Loading in Total Knee Replacement: In Vivo Measurements in Five Patients. JBJS. 2012;94(11):1023-1029. doi: 10.2106/jbjs.K.00927. PubMed PMID: 00004623-201206060-00007.

16.   Chen Z, Jin Z. Prediction of in-vivo kinematics and contact track of total knee arthroplasty during walking. Biosurface and Biotribology. 2016;2(3):86-94. doi: https://doi.org/10.1016/j.bsbt.2016.08.002.

17.   Popoola OO, Yao JQ, Johnson TS, Blanchard CR. Wear, delamination, and fatigue resistance of melt-annealed highly crosslinked UHMWPE cruciate-retaining knee inserts under activities of daily living. Journal of Orthopaedic Research. 2010;28(9):1120-1126. doi: 10.1002/jor.21104.

18.   Schwiesau J, Fritz B, Kutzner I, Bergmann G, Grupp TM. CR TKA UHMWPE wear tested after artificial aging of the vitamin E treated gliding component by simulating daily patient activities. Biomed Res Int. 2014;2014:567374-567374. doi: 10.1155/2014/567374. Epub 2014/11/20. PubMed PMID: 25506594.

19.   Grupp TM, Fritz B, Kutzner I, Schilling C, Bergmann G, Schwiesau J. Vitamin E stabilised polyethylene for total knee arthroplasty evaluated under highly demanding activities wear simulation. Acta Biomaterialia. 2017;48:415-422. doi: https://doi.org/10.1016/j.actbio.2016.10.031.

20.   Saxby DJ, Modenese L, Bryant AL, Gerus P, Killen B, Fortin K, et al. Tibiofemoral contact forces during walking, running and sidestepping. Gait & Posture. 2016;49:78-85. doi: https://doi.org/10.1016/j.gaitpost.2016.06.014.

21.   Bergmann G, Bender A, Graichen F, Dymke J, Rohlmann A, Trepczynski A, et al. Standardized loads acting in knee implants. PLoS One. 2014;9(1):e86035-e86035. doi: 10.1371/journal.pone.0086035. PubMed PMID: 24465856.

22.   Messier SP, Pater M, Beavers DP, Legault C, Loeser RF, Hunter DJ, et al. Influences of alignment and obesity on knee joint loading in osteoarthritic gait. Osteoarthr Cartil. 2014;22(7):912-917. doi: 10.1016/j.joca.2014.05.013. Epub 2014/05/21. PubMed PMID: 24857973.

23.   Kumar D, Manal KT, Rudolph KS. Knee joint loading during gait in healthy controls and individuals with knee osteoarthritis. Osteoarthr Cartil. 2013;21(2):298-305. doi: https://doi.org/10.1016/j.joca.2012.11.008.

24.   Worsley P, Stokes M, Barrett D, Taylor M. Joint loading asymmetries in knee replacement patients observed both pre- and six months post-operation. Clinical Biomechanics. 2013;28(8):892-897. doi: https://doi.org/10.1016/j.clinbiomech.2013.07.014.

25.   Kutzner I, Küther S, Heinlein B, Dymke J, Bender A, Halder AM, et al. The effect of valgus braces on medial compartment load of the knee joint – in vivo load measurements in three subjects. Journal of Biomechanics. 2011;44(7):1354-1360. doi: https://doi.org/10.1016/j.jbiomech.2011.01.014.

26.   Lundberg HJ, Ngai V, Wimmer MA. Comparison of ISO Standard and TKR patient axial force profiles during the stance phase of gait. Proceedings of the Institution of Mechanical Engineers, Part H: Journal of Engineering in Medicine. 2012;226(3):227-234. doi: 10.1177/0954411911431650. PubMed PMID: 22558837.

27.   Winby CR, Lloyd DG, Besier TF, Kirk TB. Muscle and external load contribution to knee joint contact loads during normal gait. Journal of Biomechanics. 2009;42(14):2294-2300. doi: https://doi.org/10.1016/j.jbiomech.2009.06.019.

28.   D'Lima DD, Steklov N, Patil S, Colwell CW, Jr. The Mark Coventry Award: in vivo knee forces during recreation and exercise after knee arthroplasty. Clin Orthop Relat R. 2008;466(11):2605-2611. doi: https://doi.org/10.1007/s11999-008-0345-x. Epub 2008/06/19. PubMed PMID: 18563502.

29.   Messier SP, Gutekunst DJ, Davis C, DeVita P. Weight loss reduces knee-joint loads in overweight and obese older adults with knee osteoarthritis. Arthritis & Rheumatism. 2005;52(7):2026-2032. doi: 10.1002/art.21139.

30.   Kurtz SM. 8 - The Origins and Adaptations of UHMWPE for Knee Replacements. In: Kurtz SM, editor. UHMWPE Biomaterials Handbook (Third Edition). Oxford: William Andrew Publishing; 2016. p. 106-122.

31.   Kurtz SM, Zagorski M. 3 - Packaging and Sterilization of UHMWPE. In: Kurtz SM, editor. UHMWPE Biomaterials Handbook (Third Edition). Oxford: William Andrew Publishing; 2016. p. 21-32.

32.   Kaivosoja E, Tiainen VM, Takakubo Y, Rajchel B, Sobiecki J, Konttinen YT, et al. 7 - Materials used for hip and knee implants. In: Affatato S, editor. Wear of Orthopaedic Implants and Artificial Joints: Woodhead Publishing; 2013. p. 178-218.

33.   Medacta. GMK Primary [accessed 2020 May 15]. Available from: https://www.medacta.com/EN/gmk-primary.

34.   Kurtz SM. 9 - The Clinical Performance of UHMWPE in Knee Replacements. In: Kurtz SM, editor. UHMWPE Biomaterials Handbook (Third Edition). Oxford: William Andrew Publishing; 2016. p. 123-144.

35.   ISO. ISO 16087:2013 Implants for surgery — Roentgen stereophotogrammetric analysis for the assessment of migration of orthopaedic implants.

36.   van IJsseldijk EA, Valstar ER, Stoel BC, de Ridder R, Nelissen RGHH, Kaptein BL. Measuring polyethylene wear in total knee arthroplasty by RSA: Differences between weight-bearing and non-weight-bearing positioning. Journal of Orthopaedic Research. 2014;32(4):613-617. doi: https://doi.org/10.1002/jor.22579.

37.   Losina E, Katz JN. Total knee arthroplasty on the rise in younger patients: are we sure that past performance will guarantee future success? Arthritis Rheum. 2012;64(2):339-341. doi: 10.1002/art.33371. PubMed PMID: 22252374.

38.   Nam D, Nunley RM, Barrack RL. Patient dissatisfaction following total knee replacement. BJJ. 2014;96-B(11_Supple_A):96-100. doi: https://doi.org/10.1302/0301-620x.96b11.34152.

39.   Gunaratne R, Pratt DN, Banda J, Fick DP, Khan RJK, Robertson BW. Patient Dissatisfaction Following Total Knee Arthroplasty: A Systematic Review of the Literature. The Journal of Arthroplasty. 2017;32(12):3854-3860. doi: https://doi.org/10.1016/j.arth.2017.07.021.

40.   Uvehammer J, Kärrholm J, Brandsson S, Herberts P, Carlsson L, Karlsson J, et al. In vivo kinematics of total knee arthroplasty: Flat compared with concave tibial joint surface. Journal of Orthopaedic Research. 2000;18(6):856-864. doi: 10.1002/jor.1100180603.

41.   Ardestani MM, Moazen M, Jin Z. Contribution of geometric design parameters to knee implant performance: Conflicting impact of conformity on kinematics and contact mechanics. The Knee. 2015;22(3):217-224. doi: https://doi.org/10.1016/j.knee.2015.02.011.

42.   Koh Y-G, Nam J-H, Kang K-T. Effect of geometric variations on tibiofemoral surface and post-cam design of normal knee kinematics restoration. Journal of Experimental Orthopaedics. 2018;5(1):53. doi: 10.1186/s40634-018-0167-z.

43.   Li Y, Wang S, Wang Y, Yang M. Does Kinematic Alignment Improve Short-Term Functional Outcomes after Total Knee Arthroplasty Compared with Mechanical Alignment? A Systematic Review and Meta-analysis. J Knee Surg. 2018;31(01):078-086. doi: 10.1055/s-0037-1602136. Epub 01.05.2017.

44.   Chen C, Li R. Cementless versus cemented total knee arthroplasty in young patients: a meta-analysis of randomized controlled trials. J Orthop Surg Res. 2019;14(1):262-262. doi: 10.1186/s13018-019-1293-8. PubMed PMID: 31426816.

45.   Longo UG, Ciuffreda M, Mannering N, D'Andrea V, Cimmino M, Denaro V. Patellar Resurfacing in Total Knee Arthroplasty: Systematic Review and Meta-Analysis. The Journal of Arthroplasty. 2018;33(2):620-632. doi: 10.1016/j.arth.2017.08.041.

46.   Verra WC, Boom LGHvd, Jacobs WCH, Schoones JW, Wymenga AB, Nelissen RGHH. Similar outcome after retention or sacrifice of the posterior cruciate ligament in total knee arthroplasty. Acta Orthop. 2015;86(2):195-201. doi: 10.3109/17453674.2014.973329. Epub 2014/10/17. PubMed PMID: 25323799.

47.   Young T, Dowsey MM, Pandy M, Choong PF. A Systematic Review of Clinical Functional Outcomes After Medial Stabilized Versus Non-Medial Stabilized Total Knee Joint Replacement. Front Surg. 2018;5:25-25. doi: 10.3389/fsurg.2018.00025. PubMed PMID: 29696144.

48.   Kaufman KR, Kovacevic N, Irby SE, Colwell CW. Instrumented implant for measuring tibiofemoral forces. Journal of Biomechanics. 1996;29(5):667-671. doi: https://doi.org/10.1016/0021-9290(95)00124-7.

49.   ASTM F3141-17a, Standard Guide for Total Knee Replacement Loading Profiles. West Conshohocken, PA: ASTM International; 2017.

50.   O'Connor C, Kiourti A. Wireless Sensors for Smart Orthopedic Implants. Journal of Bio- and Tribo-Corrosion. 2017;3(2):20. doi: https://doi.org/10.1007/s40735-017-0078-z.

51.   Karipott SS, Veetil PM, Nelson BD, Guldberg RE, Ong KG. An Embedded Wireless Temperature Sensor for Orthopedic Implants. IEEE Sensors Journal. 2018;18(3):1265-1272. doi: https://doi.org/10.1109/JSEN.2017.2780226.

52.   Pritchett JW. Heat Generated by Knee Prostheses. Clinical Orthopaedics and Related Research®. 2006;442:195-198. doi: https://doi.org/10.1097/01.blo.0000183739.50869.bb. PubMed PMID: 00003086-200601000-00031.

53.   Liu X, Berger JL, Ogirala A, Mickle MH. A Touch Probe Method of Operating an Implantable RFID Tag for Orthopedic Implant Identification. IEEE Transactions on Biomedical Circuits and Systems. 2013;7(3):236-242. doi: https://doi.org/10.1109/TBCAS.2012.2201258.

54.   Meswania JM, Taylor SJG, Blunn GW. Design and characterization of a novel permanent magnet synchronous motor used in a growing prosthesis for young patients with bone cancer. Proceedings of the Institution of Mechanical Engineers, Part H: Journal of Engineering in Medicine. 2008;222(3):393-402. doi: https://doi.org/10.1243/09544119JEIM247.

55.   OrthopedicDesign&Technology. First Knee Replacement Surgery with Persona IQ Smart Knee: Orthopedic Design & Technology; 2022 [accessed 2022 Jul-29].

Available from: https://www.odtmag.com/contents/view_breaking-news/2021-10-13/first-knee-replacement-surgery-with-persona-iq-smart-knee/.

56.   ZimmerBiomet. Persona IQ [accessed 2022 Jul-29]. Available from: https://www.zimmerbiomet.com/en/products-and-solutions/specialties/knee/persona-iq.html.

57.   Taylor SJG, Walker PS. Forces and moments telemetered from two distal femoral replacements during various activities. Journal of Biomechanics. 2001;34(7):839-848. doi: https://doi.org/10.1016/S0021-9290(01)00042-2.

58.   D'Lima DD, Patil S, Steklov N, Slamin JE, Colwell CWJ. THE CHITRANJAN RANAWAT AWARD: In Vivo Knee Forces after Total Knee Arthroplasty. Clin Orthop Relat R. 2005;440:45-49. doi: https://doi.org/10.1097/01.blo.0000186559.62942.8c. PubMed PMID: 00003086-200511000-00010.

59.   D'Lima DD, Patil S, Steklov N, Chien S, Colwell CW. In vivo knee moments and shear after total knee arthroplasty. Journal of Biomechanics. 2007;40:S11-S17. doi: https://doi.org/10.1016/j.jbiomech.2007.03.004.

60.   Heinlein B, Kutzner I, Graichen F, Bender A, Rohlmann A, Halder AM, et al. ESB clinical biomechanics award 2008: Complete data of total knee replacement loading for level walking and stair climbing measured in vivo with a follow-up of 6-10 months. Clinical Biomechanics. 2009;24(4):315-326. doi: https://doi.org/10.1016/j.clinbiomech.2009.01.011.

61.   Kirking B, Krevolin J, Townsend C, Colwell CW, D'Lima DD. A multiaxial force-sensing implantable tibial prosthesis. Journal of Biomechanics. 2006;39(9):1744-1751. doi: https://doi.org/10.1016/j.jbiomech.2005.05.023.

62.   Heinlein B, Graichen F, Bender A, Rohlmann A, Bergmann G. Design, calibration and pre-clinical testing of an instrumented tibial tray. Journal of Biomechanics. 2007;40:S4-S10. doi: https://doi.org/10.1016/j.jbiomech.2007.02.014.

63.   Holmberg J, Alexander L, Rajamani R, Bechtold JE. Battery-Less Wireless Instrumented Knee Implant. Journal of Medical Devices. 2013;7(1). doi: https://doi.org/10.1115/1.4023412.

64.   Cushner F, Schiller P, Gross J, Mueller JK, Hunter W. A total knee arthroplasty prosthesis capable of remote patient monitoring. Orthopaedic Proceedings. 2021;103-B(SUPP_9):18-18. doi: https://doi.org/10.1302/1358-992x.2021.9.018.

65.   Cushner FD, Sculco PK, Long WJ. The Talking Knee Is a Reality: What Your Knee Can Tell You After Total Knee Arthroplasty. Journal of Orthopaedic Experience & Innovation. 2022.

66.   Graichen F, Arnold R, Rohlmann A, Bergmann G. Implantable 9-Channel Telemetry System for In Vivo Load Measurements With Orthopedic Implants. IEEE

Transactions on Biomedical Engineering. 2007;54(2):253-261. doi: 10.1109/TBME.2006.886857.

67.   Morris B, D D'Lima D, Slamin J, Kovacevic N, W. Arms S, P. Townsend C, et al. e-Knee: Evolution of the Electronic Knee Prosthesis: Telemetry Technology Development. JBJS. 2001;83-A Suppl 2:62-66. doi: 10.2106/00004623-200100021-00013.

68.   Forchelet D, Simoncini M, Arami A, Bertsch A, Meurville E, Aminian K, et al. Enclosed electronic system for force measurements in knee implants. Sensors (Basel). 2014;14(8):15009-15021. doi: 10.3390/s140815009. PubMed PMID: 25196007.

69.   Safaei M, Anton SR. Self-Powered Multifunctional Instrumented Knee Implant. ASME. 2018(51951):V002T006A008. doi: 10.1115/SMASIS2018-8078. PubMed Central PMCID: PMCSmart Materials, Adaptive Structures and Intelligent Systems.

70.   D'Lima DD, Patil S, Steklov N, Colwell CW, Jr. The 2011 ABJS Nicolas Andry Award: 'Lab'-in-a-knee: in vivo knee forces, kinematics, and contact analysis. Clin Orthop Relat R. 2011;469(10):2953-2970. doi: https://doi.org/10.1007/s11999-011-1916-9. Epub 2011/05/20. PubMed PMID: 21598121.

71.   Almouahed S, Hamitouche C, Stindel E, Roux C, editors. New trends in instrumented knee prostheses. 2008 3rd International Conference on Information and Communication Technologies: From Theory to Applications; 2008 7-11 April 2008.

72.   Camp J, F. Graboyes R. Us Medical Devices: Choices and Consequences. SSRN Electronic Journal. 2018. doi: 10.2139/ssrn.3191321.

73.   Arami A, Simoncini M, Atasoy O, Hasenkamp W, Ali S, Bertsch A, et al., editors. Instrumented prosthesis for knee implants monitoring. 2011 IEEE International Conference on Automation Science and Engineering; 2011 24-27 Aug. 2011.

74.   Baronio G, Luciano V, Sardini E, Serpelloni M. Design considerations of an electromechanical generator implanted in human total knee prosthesis. International Journal of Mechatronics and Manufacturing Systems. 2013;6(3):270-284. doi: 10.1504/ijmms.2013.056453. PubMed PMID: 56453.

75.   Ibrahim A, Jain M, Salman E, Willing R, Towfighian S. A Smart Knee Implant Using Triboelectric Energy Harvesters. Smart Materials and Structures. 2018. doi: https://doi.org/10.1088/1361-665X/aaf3f1.

76.   Mentink MJA. Measurement of bearing load in unicompartmental knee arthroplasty using an instrumented knee bearing. PhD Thesis 2014.

77.   Regulation (EU) 2017/745 of the European Parliament and of the Council of 5 April 2017 on medical devices, amending Directive 2001/83/EC, Regulation (EC) No 178/2002 and Regulation (EC) No 1223/2009 and repealing Council Directives 90/385/EEC and 93/42/EEC (Text with EEA relevance.).

78.   Kurtz SM. 2 - From Ethylene Gas to UHMWPE Component: The Process of Producing Orthopedic Implants. In: Kurtz SM, editor. UHMWPE Biomaterials Handbook (Third Edition). Oxford: William Andrew Publishing; 2016. p. 7-20.

79.   Scott CEH, Eaton MJ, Nutton RW, Wade FA, Evans SL, Pankaj P. Metal-backed versus all-polyethylene unicompartmental knee arthroplasty. Bone & Joint Research. 2017;6(1):22-30. doi: 10.1302/2046-3758.61.Bjr-2016-0142.R1.

80.   Rajamäki A, Niemeläinen M, Junnila M, Lehtovirta L, Karsikas M, Ponkilainen V, et al. Thicker polyethylene inserts (≥ 13 mm) increase the risk for early failure after primary cruciate-retaining total knee arthroplasty (TKA): a single-centre study of 7643 TKAs. Knee Surgery, Sports Traumatology, Arthroscopy. 2023;31(3):1018-1025. doi: 10.1007/s00167-022-07189-8.

81.   Muratoglu OK, Bragdon CR. 15 - Highly Cross-Linked and Melted UHMWPE. In: Kurtz SM, editor. UHMWPE Biomaterials Handbook (Third Edition). Oxford: William Andrew Publishing; 2016. p. 264-273.

82.   Spece H, Schachtner JT, MacDonald DW, Klein GR, Mont MA, Lee G-C, et al. Reasons for Revision, Oxidation, and Damage Mechanisms of Retrieved Vitamin E-Stabilized Highly Crosslinked Polyethylene in Total Knee Arthroplasty. The Journal of Arthroplasty. 2019;34(12):3088-3093. doi: https://doi.org/10.1016/j.arth.2019.07.018.

83.   Kang JY, Lee YS. Same-Level Fracture of the Tibial Metal Tray and Polyethylene Insert After Total Knee Arthroplasty. Orthopedics. 2016;39(4):e787-789. doi: 10.3928/01477447-20160513-03. PubMed PMID: 27203415.

84.   Li AE, Sneag DB, Miller TT, Lipman JD, Padgett DE, Potter HG. MRI of Polyethylene Tibial Inserts in Total Knee Arthroplasty: Normal and Abnormal Appearances. American Journal of Roentgenology. 2016;206(6):1264-1271. doi: 10.2214/AJR.15.15107.

85.   Teeter MG, McAuley JP, Naudie DD. Fracture of Two Moderately Cross-Linked Polyethylene Tibial Inserts in a TKR Patient. Case Rep Orthop. 2014;2014:491384-491384. doi: 10.1155/2014/491384. Epub 2014/01/08. PubMed PMID: 24511401.

86.   Currier BH, Currier JH, Franklin KJ, Mayor MB, Reinitz SD, Van Citters DW. Comparison of Wear and Oxidation in Retrieved Conventional and Highly Cross-Linked UHMWPE Tibial Inserts. The Journal of Arthroplasty. 2015;30(12):2349-2353. doi: https://doi.org/10.1016/j.arth.2015.06.014.

87.   Bei Y, Fregly B. The relationship between contact pressure, insert thickness, and mild wear in total knee replacements. CMES-COMPUTER MODELING IN ENGINEERING & SCIENCES. 2004;6:145-152.

88.   Collier JP, Mayor MB, McNamara JL, Surprenant VA, Jensen RE. Analysis of the Failure of 122 Polyethylene Inserts From Uncemented Tibial Knee Components.

Clinical Orthopaedics and Related Research®. 1991;273:232-242. PubMed PMID: 00003086-199112000-00034.

89.   Bartel DL, Bicknell VL, Wright TM. The effect of conformity, thickness, and material on stresses in ultra-high molecular weight components for total joint replacement. JBJS. 1986;68(7):1041-1051. PubMed PMID: 00004623-198668070-00010.

90.   Pijls BG, Van der Linden-Van der Zwaag HMJ, Nelissen RGHH. Polyethylene thickness is a risk factor for wear necessitating insert exchange. Int Orthop. 2012;36(6):1175-1180. doi: 10.1007/s00264-011-1412-6.

91.   Institution TBS. BS EN ISO 21536:2009+A1:2014. Non-active surgical implants. Joint replacement implants. Specific requirements for knee-joint replacement implants. 2009.

92.   FDA. Knee Joint Patellofemorotibial and Femorotibial Metal/Polymer Porous-Coated Uncemented Prostheses - Class II Special Controls Guidance Document for Industry and FDA 2003/2018 [accessed 2020 May 14]. Available from: https://www.fda.gov/medical-devices/guidance-documents-medical-devices-and-radiation-emitting-products/knee-joint-patellofemorotibial-and-femorotibial-metalpolymer-porous-coated-uncemented-prostheses.

93.   Koh Y-G, Jung K-H, Hong H-T, Kim K-M, Kang K-T. Optimal Design of Patient-Specific Total Knee Arthroplasty for Improvement in Wear Performance. Journal of Clinical Medicine. 2019;8:2023. doi: 10.3390/jcm8112023.

94.   MatOrtho. SAIPH Knee System [accessed 2020 January 28]. Available from: https://www.matortho.com/products/saiph-knee-system/.

95.   Corin_group. Global APEX Knee™ Reconstruction System [accessed 2020 January 28]. Available from: https://www.coringroup.com/assets/product-resources/apex/GKL-014-Global-Apex-Knee-System-Brochure-REV-0.pdf.

96.   Kobayashi H, Mitsugi N, Mochida Y, Taki N, Akamatsu Y, Aratake M, et al. Mid-term results of stryker® scorpio plus mobile bearing total knee arthroplasty. Sports Medicine, Arthroscopy, Rehabilitation, Therapy & Technology. 2012;4(1):38. doi: 10.1186/1758-2555-4-38.

97.   Zimmer. Zimmer®NexGen® Trabecular Metal™ Monoblock Tibial Components Surgical Technique Addendum 2012 [accessed 2020 May 15]. Available from: https://www.zimmerbiomet.com/content/dam/zimmer-biomet/medical-professionals/000-surgical-techniques/knee/zimmer-nexgen-trabecular-metal-monoblock-tibial-components-surgical-technique.pdf.

98.   Klein GR, Levine HB, Hartzband MA. Removal of a Well-Fixed Trabecular Metal Monoblock Tibial Component. The Journal of Arthroplasty. 2008;23(4):619-622. doi: https://doi.org/10.1016/j.arth.2007.05.004.

99.   Biomet. The Oxford® Partial Knee [accessed 2020 January 28]. Available from: http://www.biomet.com/web_accents/biomet_products/oxfordSignature.cfm.

100.   MedicalEXPO. Biomet, Vanguard XP [accessed 2020 January 28]. Available from: https://www.medicalexpo.com/prod/biomet/product-74862-695258.html.

101.   Conformis. iTotal [accessed 2020 January 28]. Available from: https://www.conformis.com/custom-made-knee-implants/products/itotal/.

102.   Harman MK, DesJardins J, Benson L, Banks SA, LaBerge M, Hodge WA. Comparison of polyethylene tibial insert damage from in vivo function and in vitro wear simulation. J Orthop Res. 2009;27(4):540-548. doi: 10.1002/jor.20743. Epub 2008/10/22. PubMed PMID: 18932244.

103.   Haider H. 32 - Tribological Assessment of UHMWPE in the Knee. In: Kurtz SM, editor. UHMWPE Biomaterials Handbook (Third Edition). Oxford: William Andrew Publishing; 2016. p. 599-634.

104.   Mendenhall S. 2008 Hip and Knee Implant Review. Orthopedic Network News. 2008 August 10.

105.   Bowden AE, Bergström J. 39 - Computer Modeling and Simulation of UHMWPE. In: Kurtz SM, editor. UHMWPE Biomaterials Handbook (Third Edition). Oxford: William Andrew Publishing; 2016. p. 753-771.

106.   Teeter MG, Parikh A, Taylor M, Sprague J, Naudie DD. Wear and Creep Behavior of Total Knee Implants Undergoing Wear Testing. The Journal of Arthroplasty. 2015;30(1):130-134. doi: https://doi.org/10.1016/j.arth.2014.08.001.

107.   AMTI. ADL Knee Simulator 6-Station Joint Simulator [accessed 2023 May 07]. Available from: https://www.amti.biz/product/knee-simulator/.

108.   ISO. ISO 14243-1:2009+A1:2020. Implants for surgery. Wear of total knee-joint prostheses. Loading and displacement parameters for wear-testing machines with load control and corresponding environmental conditions for test.

109.   ISO. ISO 14243-3:2014+A1:2020. Implants for surgery. Wear of total knee-joint prostheses. Loading and displacement parameters for wear-testing machines with displacement control and corresponding environmental conditions for test.

110.   Abdelgaied A, Fisher J, Jennings LM. A comprehensive combined experimental and computational framework for pre-clinical wear simulation of total knee replacements. Journal of the Mechanical Behavior of Biomedical Materials. 2018;78:282-291. doi: https://doi.org/10.1016/j.jmbbm.2017.11.022.

111.   ASTM F2003-02(2015), Standard Practice for Accelerated Aging of Ultra-High Molecular Weight Polyethylene after Gamma Irradiation in Air. West Conshohocken, PA: ASTM International; 2015.

112.   ASTM F2777-16, Standard Test Method for Evaluating Knee Bearing (Tibial Insert) Endurance and Deformation Under High Flexion. West Conshohocken, PA: ASTM International; 2016.

113.   EndoLab. [accessed 2020 February 19]. Available from: https://www.endolab.org/default.asp.

114.   ASTM F1800-19e1, Standard Practice for Cyclic Fatigue Testing of Metal Tibial Tray Components of Total Knee Joint Replacements. West Conshohocken, PA: ASTM International; 2019.

115.   ASTM F2083-12, Standard Specification for Knee Replacement Prosthesis. West Conshohocken, PA: ASTM International; 2012.

116.   Villa T, Migliavacca F, Gastaldi D, Colombo M, Pietrabissa R. Contact stresses and fatigue life in a knee prosthesis: comparison between in vitro measurements and computational simulations. Journal of Biomechanics. 2004;37(1):45-53. doi: https://doi.org/10.1016/S0021-9290(03)00255-0.

117.   Ahir SP, Blunn GW, Haider H, Walker PS. Evaluation of a testing method for the fatigue performance of total knee tibial trays. Journal of Biomechanics. 1999;32(10):1049-1057. doi: https://doi.org/10.1016/S0021-9290(99)00094-9.

118.   Fish J, Belytschko T. Introduction. A First Course in Finite Elements. Chichester: Wiley; 2007. p. 1-9.

119.   Anderson AE, Ellis BJ, Weiss JA. Verification, validation and sensitivity studies in computational biomechanics. Computer methods in biomechanics and biomedical engineering. 2007;10(3):171-184. doi: 10.1080/10255840601160484. PubMed PMID: 17558646.

120.   Bergmann G, Graichen F, Rohlmann A, Westerhoff P, Heinlein B, Bender A, et al. Design and Calibration of Load Sensing Orthopaedic Implants. Journal of Biomechanical Engineering. 2008;130(2). doi: 10.1115/1.2898831.

121.   Pegg EC, Murray DW, Pandit HG, O'Connor JJ, Gill HS. Fracture of mobile unicompartmental knee bearings: A parametric finite element study. Proceedings of the Institution of Mechanical Engineers, Part H: Journal of Engineering in Medicine. 2013;227(11):1213-1223. doi: 10.1177/0954411913494326. PubMed PMID: 23940210.

122.   Hasenkamp W, Thevenaz N, Villard J, Bertsch A, Arami A, Aminian K, et al. Design and test of a MEMS strain-sensing device for monitoring artificial knee implants. Biomedical Microdevices. 2013;15(5):831-839. doi: 10.1007/s10544-013-9770-z.

123.   ASTM F3161-16, Standard Test Method for Finite Element Analysis (FEA) of Metallic Orthopaedic Total Knee Femoral Components under Closing Conditions. West Conshohocken, PA: ASTM International; 2016.

124.   ASTM F3334-19, Standard Practice for Finite Element Analysis (FEA) of Metallic Orthopaedic Total Knee Tibial Components. West Conshohocken, PA: ASTM International; 2019.

125.   Kurtz SM. 1 - A Primer on UHMWPE. In: Kurtz SM, editor. UHMWPE Biomaterials Handbook (Third Edition). Oxford: William Andrew Publishing; 2016. p. 1-6.

126.   ACNIS_INTERNATIONAL. POLYMERS [accessed 2020 06-Jan]. Available from: http://www.acnis-titanium.com/en/polymers/.

127.   Medacta. GMK Primary product range [accessed 2020 06-Jan]. Available from: https://www.medacta.com/EN/gmk-primary.

128.   Malito LG, Arevalo S, Kozak A, Spiegelberg S, Bellare A, Pruitt L. Material properties of ultra-high molecular weight polyethylene: Comparison of tension, compression, nanomechanics and microstructure across clinical formulations. Journal of the Mechanical Behavior of Biomedical Materials. 2018;83:9-19. doi: https://doi.org/10.1016/j.jmbbm.2018.03.029.

129.   Bianchi F, rinaldi S, Quagliana I, Siccardi F. Polyethylene in TKA: do we really need cross-linked polyethylene? MORE Journal. 2011;01.

130.   Ansari F, Gludovatz B, Kozak A, Ritchie RO, Pruitt LA. Notch fatigue of ultrahigh molecular weight polyethylene (UHMWPE) used in total joint replacements. Journal of the Mechanical Behavior of Biomedical Materials. 2016;60:267-279. doi: https://doi.org/10.1016/j.jmbbm.2016.02.014.

131.   Zheng X, Wu K, Wang J, Ma L, Yu J, Xu J. Mechanical characteristics of medical grade UHMWPE under dynamic compression. Journal of Materials Science: Materials in Medicine. 2019;30(5):50. doi: 10.1007/s10856-019-6254-6.

132.   Lu Y-C, Wu C-Y, Chang T-K, Huang C-H, Huang C-H. Elastoplastic behavior of highly cross-linked and vitamin E-stabilized polyethylene – A biomechanical study. Clinical Biomechanics. 2018;59:152-158. doi: https://doi.org/10.1016/j.clinbiomech.2018.09.021.

133.   Johnston HE. The Effect of Surgical Alignment and Soft Tissue Constraints on the Kinematics, Contact Pressure and Wear of a Total Knee Replacement. PhD thesis. [PhD thesis]. Leeds: University of Leeds; 2019.

134.   Aherwar A, Singh A, Patnaik A. Current and future biocompatibility aspects of biomaterials for hip prosthesis. AIMS Journal. 2016;3:23-43. doi: 10.3934/bioeng.2016.1.23.

135.   ABAQUS documentation. Contact constraint enforcement methods in Abaqus/Standard. [accessed 2022 Jul 14]. Available from: https://abaqus-docs.mit.edu/2017/English/SIMACAEITNRefMap/simaitn-c-

contactconstraints.htm#:~:text=The%20default%20constraint%20enforcement%20met hod,overclosure%20relationship%20is%20in%20effect.

136.   Budynas R, Nisbett K. Shigley's Mechanical Engineering Design. 9th edition: McGraw-Hill Higher Education; 2010.

137.   Smith&Nephew. JOURNEY II XR Measurements [accessed 2020 Jun 05]. Available from: https://www.smith-nephew.com/global/assets/pdf/products/surgical/journeyii-xr-specs.pdf.

138.   Stryker. RESTORIS® MCK MultiCompartmental Knee System [accessed 2020 Jun 05]. Available from: https://www.strykermeded.com/media/1708/restoris-mck-technical-data-sheet.pdf.

139.   Medacta. MOTO® Medial Partial Knee System [accessed 2020 Jun 05]. Available from: https://media.medacta.com/media/moto-specification-guide-9938moto11sg-rev02.pdf.

140.   Nabrdalik M, Sobociński M. Numerical analysis of stress distribution generated in spherical polyethylene inserts by knee joint endoprotheses' sleds %J Polish Journal of Chemical Technology. 2019;21(2):1-5. doi: doi:10.2478/pjct-2019-0012.

141.   ABAQUS Analysis User's Manual. ABAQUS Online Documentation: Version 6.6. Section 18.2.1 Classical metal plasticity.2006.

142.   Godest AC, Beaugonin M, Haug E, Taylor M, Gregson PJ. Simulation of a knee joint replacement during a gait cycle using explicit finite element analysis. Journal of Biomechanics. 2002;35(2):267-275. doi: https://doi.org/10.1016/S0021-9290(01)00179-8.

143.   Abaqus. Abaqus Analysis User`s Manual 6.10. Chapter 25.1.4 Three-dimensional solid element library [accessed 2023 Jan 03]. Available from: http://130.149.89.49:2080/v6.10/books/usb/default.htm?startat=pt06ch25s01ael03.html .

144.   Abaqus. Abaqus Analysis User`s Manual 6.11. Chapter 27.1.1 Solid (continuum) elements [accessed 2023 Jan 03]. Available from: http://130.149.89.49:2080/v6.11/books/usb/default.htm?startat=pt06ch27s01alm01.html.

145.   Abaqus. Abaqus Analysis User`s Manual 6.6. Chapter 21.1.4 Section controls [accessed 2023 Jan 03]. Available from: https://classes.engineering.wustl.edu/2009/spring/mase5513/abaqus/docs/v6.6/books/usb/default.htm?startat=pt06ch21s01aus90.html.

146.   ABAQUS Analysis User's Manual. ABAQUS Online Documentation: Version 6.6-1. Section 29.2.11.2006.

147.   Jahani F. Modelling of dynamic edge loading in total hip replacements with ceramic on plyethylene bearings. PhD Thesis. [PhD Thesis]: University of Leeds; 2017.

148.   Liu F, Wang M, Wang J, Du W. The influence of frontally flat bearing design on contact mechanics and kinematics in total knee joint replacements. Tribology International. 2019;136:23-30. doi: https://doi.org/10.1016/j.triboint.2019.03.006.

149.   Lee K-Y, Pienkowski D. Viscoelastic recovery of creep-deformed ultra-high molecular weight polyethylene (UHMWPE). ASTM special technical publication. 1998;1307:30-36.

150.   Drewniak EI, Crisco JJ, Spenciner DB, Fleming BC. Accuracy of circular contact area measurements with thin-film pressure sensors. Journal of Biomechanics. 2007;40(11):2569-2572. doi: https://doi.org/10.1016/j.jbiomech.2006.12.002.

151.   Khosravipour I, Pejhan S, Luo Y, Wyss UP. Customized surface-guided knee implant: Contact analysis and experimental test. Proceedings of the Institution of Mechanical Engineers, Part H: Journal of Engineering in Medicine. 2017;232(1):90-100. doi: 10.1177/0954411917744586.

152.   Chen P, Colwell C, D'lima D. A Nonlinear Viscoelastic Finite Element Model of Polyethylene. Molecular & Cellular Biomechanics. 2011;8(2):135.

153.   Bitter T, Khan I, Marriott T, Lovelady E, Verdonschot N, Janssen D. The effects of manufacturing tolerances and assembly force on the volumetric wear at the taper junction in modular total hip arthroplasty. Computer Methods in Biomechanics and Biomedical Engineering. 2019;22(13):1061-1072. doi: 10.1080/10255842.2019.1627524.

154.   Institution BS. BS EN 22768-1:1993, ISO 2768-1:1989. General tolerances. Tolerances for linear and angular dimensions without individual tolerance indications. 1989.

155.   OrthoLoad. Standard Loads Knee Joint 2014 [accessed 2020 Nov 05]. Available from: https://orthoload.com/test-loads/standard-loads-knee-joint/.

156.   Abaqus. Abaqus Analysis User`s Manual 6.6. Chapter 2.4 Comparison of implicit and explicit procedures [accessed 2023 Feb 17]. Available from: https://classes.engineering.wustl.edu/2009/spring/mase5513/abaqus/docs/v6.6/books/gsa/default.htm?startat=ch02s04.html.

157.   Abaqus. Abaqus Analysis User`s Manual 6.6. Chapter 3.1 Types of problems suited for ABAQUS/Explicit [accessed 2023 Feb 17]. Available from: https://classes.engineering.wustl.edu/2009/spring/mase5513/abaqus/docs/v6.6/books/gsx/default.htm?startat=ch03s01.html.

158.   Research Computing at the University of Leeds. ARC Acknowledgement [accessed 2022 Sep 28]. Available from: https://arcdocs.leeds.ac.uk/usage/acknowledgement.html.

159.   Research Computing at the University of Leeds. ARC3. Available from: https://arcdocs.leeds.ac.uk/systems/arc3.html.

160.   MILLER RH, EDWARDS WB, BRANDON SCE, MORTON AM, DELUZIO KJ. Why Don't Most Runners Get Knee Osteoarthritis? A Case for Per-Unit-Distance Loads. Medicine & Science in Sports & Exercise. 2014;46(3):572-579. doi: 10.1249/mss.0000000000000135. PubMed PMID: 00005768-201403000-00018.

161.   Abaqus. Abaqus Analysis User`s Manual 6.6. Chapter 7. Linear Dynamics 7.1 Introduction [accessed 2023 Feb 24]. Available from: https://classes.engineering.wustl.edu/2009/spring/mase5513/abaqus/docs/v6.6/books/gsa/default.htm?startat=ch07s01.html.

162.   Abaqus. Abaqus Analysis User`s Manual 6.14. 6.3.2 Implicit dynamic analysis using direct integration [accessed 2023 Jan 03]. Available from: http://130.149.89.49:2080/v6.14/books/usb/default.htm?startat=pt03ch06s03at07.html.

163.   Piziali RL, Seering WP, Nagel DA, Schurman DJ. The function of the primary ligaments of the knee in anterior-posterior and medial-lateral motions. Journal of Biomechanics. 1980;13(9):777-784. doi: https://doi.org/10.1016/0021-9290(80)90239-0.

164.   Völlner F, Pilsl U, Craiovan B, Zeman F, Schneider M, Wörner M, et al. Stability of knee ligament complex of Thiel-embalmed cadaver compared to in vivo knee. Journal of the Mechanical Behavior of Biomedical Materials. 2017;71:392-396. doi: https://doi.org/10.1016/j.jmbbm.2017.04.009.

165.   Markolf K, Mensch J, Amstutz H. Stiffness and laxity of the knee--the contributions of the supporting structures. A quantitative in vitro study. JBJS. 1976;58(5):583-594. PubMed PMID: 00004623-197658050-00001.

166.   Haider H, Walker P, DesJardins J, Blunn G. Effects of Patient and Surgical Alignment Variables on Kinematics in TKR Simulation Under Force-Control. Journal of Astm International. 2006;3. doi: 10.1520/JAI100248.

167.   Wang X-H, Bi Z, Dong X, Hu S-Y, Xu L-j, Cheng C-K. Increasing the height of the anterior lip on a tibial insert in a posterior stabilized knee prosthesis has little effect on the wear rate. Med Eng Phys. 2021;91:48-53. doi: https://doi.org/10.1016/j.medengphy.2021.03.007.

168.   Maag C, Cracaoanu I, Langhorn J, Heldreth M. Total knee replacement wear during simulated gait with mechanical and anatomic alignments. Proceedings of the Institution of Mechanical Engineers, Part H: Journal of Engineering in Medicine. 2021;235(5):515-522. doi: 10.1177/0954411921991269. PubMed PMID: 33522419.

169.   D'Lima DD, Steklov N, Fregly BJ, Banks SA, Colwell Jr. CW. In vivo contact stresses during activities of daily living after knee arthroplasty. Journal of Orthopaedic Research. 2008;26(12):1549-1555. doi: https://doi.org/10.1002/jor.20670.

170.   Bartel DL, Rawlinson JJ, Burstein AH, Ranawat CS, Flynn WFJ. Stresses in Polyethylene Components of Contemporary Total Knee Replacements. Clinical

Orthopaedics and Related Research®. 1995;317:76-82. PubMed PMID: 00003086-199508000-00012.

171.   Kurtz SM, Bartel DL, Rimnac CM. Postirradiation Aging Affects Stress and Strain in Polyethylene Components. Clinical Orthopaedics and Related Research®. 1998;350:209-220. PubMed PMID: 00003086-199805000-00029.

172.   Mell SP, Fullam S, Wimmer MA, Lundberg HJ. Finite element evaluation of the newest ISO testing standard for polyethylene total knee replacement liners. Proceedings of the Institution of Mechanical Engineers, Part H: Journal of Engineering in Medicine. 2018;232(6):545-552. doi: 10.1177/0954411918770700. PubMed PMID: 29658386.

173.   Chen Z, Zhang J, Gao Y, Chen S, Zhang X, Jin Z. Effects of interference assembly of a tibial insert on the tibiofemoral contact mechanics in total knee replacement. Proceedings of the Institution of Mechanical Engineers, Part H: Journal of Engineering in Medicine. 2019;233(9):948-953. doi: 10.1177/0954411919859905. PubMed PMID: 31234760.

174.   Schwiesau J, Schilling C, Utzschneider S, Jansson V, Fritz B, Blömer W, et al. Knee wear simulation under conditions of highly demanding daily activities – Influence on an unicompartmental fixed bearing knee design. Med Eng Phys. 2013;35(8):1204-1211. doi: https://doi.org/10.1016/j.medengphy.2012.12.015.

175.   Pruitt LA, Ansari F, Kury M, Mehdizah A, Patten EW, Huddlestein J, et al. Clinical trade-offs in cross-linked ultrahigh-molecular-weight polyethylene used in total joint arthroplasty. Journal of Biomedical Materials Research Part B: Applied Biomaterials. 2013;101B(3):476-484. doi: https://doi.org/10.1002/jbm.b.32887.

176.   Completo A, Fonseca F, Simões JA. Finite Element and Experimental Cortex Strains of the Intact and Implanted Tibia. Journal of Biomechanical Engineering. 2007;129(5):791-797. doi: 10.1115/1.2768382.

177.   Oosterom R, van Ostayen RAJ, Antonelli V, Bersee HEN. Effect of Interface Conditions between Ultrahigh Molecular Weight Polyethylene and Polymethyl Methacrylate Bone Cement on the Mechanical Behaviour of Total Shoulder Arthroplasty. Proceedings of the Institution of Mechanical Engineers, Part H: Journal of Engineering in Medicine. 2005;219(6):425-435. doi: 10.1243/095441105x34455. PubMed PMID: 16312102.

178.   Shi W, Li XY, Dong H. Improved wear resistance of ultra-high molecular weight polyethylene by plasma immersion ion implantation. Wear. 2001;250(1):544-552. doi: https://doi.org/10.1016/S0043-1648(01)00636-6.

179.   Halloran JP, Petrella AJ, Rullkoetter PJ. Explicit finite element modeling of total knee replacement mechanics. Journal of Biomechanics. 2005;38(2):323-331. doi: https://doi.org/10.1016/j.jbiomech.2004.02.046.

180.   Willing R, Kim IY. A holistic numerical model to predict strain hardening and damage of UHMWPE under multiple total knee replacement kinematics and experimental validation. Journal of Biomechanics. 2009;42(15):2520-2527. doi: https://doi.org/10.1016/j.jbiomech.2009.07.008.

181.   Bischoff JE, Dharia MA, Hertzler JS, Schipper ON. Evaluation of Total Ankle Arthroplasty Using Highly Crosslinked Ultrahigh-Molecular-Weight Polyethylene Subjected to Physiological Loading. Foot & Ankle International. 2019;40(8):880-887. doi: 10.1177/1071100719847645. PubMed PMID: 31091414.

182.   Brockett CL, Abdelgaied A, Haythornthwaite T, Hardaker C, Fisher J, Jennings LM. The influence of simulator input conditions on the wear of total knee replacements: An experimental and computational study. Proceedings of the Institution of Mechanical Engineers, Part H: Journal of Engineering in Medicine. 2016;230(5):429-439. doi: 10.1177/0954411916645134. PubMed PMID: 27160561.

183.   Pandey RM. Approaches to sample size calculation in comparative studies. The Indian Journal of Pediatrics. 1999;66(4):533-538. doi: 10.1007/BF02727163.

184.   Jones SR, Carley S, Harrison M. An introduction to power and sample size estimation. Emerg Med J. 2003;20(5):453-458. doi: 10.1136/emj.20.5.453. Epub 2003/09/05. PubMed PMID: 12954688; PubMed Central PMCID: PMCPMC1726174.

185.   Rapuri VR, Clarke HD, Spangehl MJ, Beauchamp CP. Five Cases of Failure of the Tibial Polyethylene Insert Locking Mechanism in One Design of Constrained Knee Arthroplasty. The Journal of Arthroplasty. 2011;26(6):976.e921-976.e924. doi: https://doi.org/10.1016/j.arth.2010.07.013.

186.   Sanders AP, Raeymaekers B. The effect of polyethylene creep on tibial insert locking screw loosening and back-out in prosthetic knee joints. Journal of the Mechanical Behavior of Biomedical Materials. 2014;38:1-5. doi: https://doi.org/10.1016/j.jmbbm.2014.06.002.

187.   von Keudell A, Agrawal K, Rubash HE. Atraumatic Late Screw Loosening of the Tibial Polyethylene Insert Locking Mechanism in a Constrained Knee Arthroplasty: A Case Report. The Orthopaedic Journal at Harvard Medical School. 2016;17:93-98.

188.   Vasiljeva K. Ksenija Vasiljeva ORCID 0000-0002-2049-6491 [accessed 2023 Feb 27]. Available from: https://orcid.org/0000-0002-2049-6491.

189.   Carpenter T. Thomas Carpenter ORCID 0000-0001-5676-1739 [accessed 2023 Feb 27]. Available from: https://orcid.org/0000-0001-5676-1739.

190.   PARALLAX. PLX-DAQ 2020 [updated 2021 Dec 01; accessed 2023 Jan 16]. Available from: https://www.parallax.com/package/plx-daq/.

191.   NetDevil. PLX-DAQ version 2 - now with 64 bit support! (and further new features) [Arduino forum]. 2016 [accessed 2023 Jan 16]. Open source software].
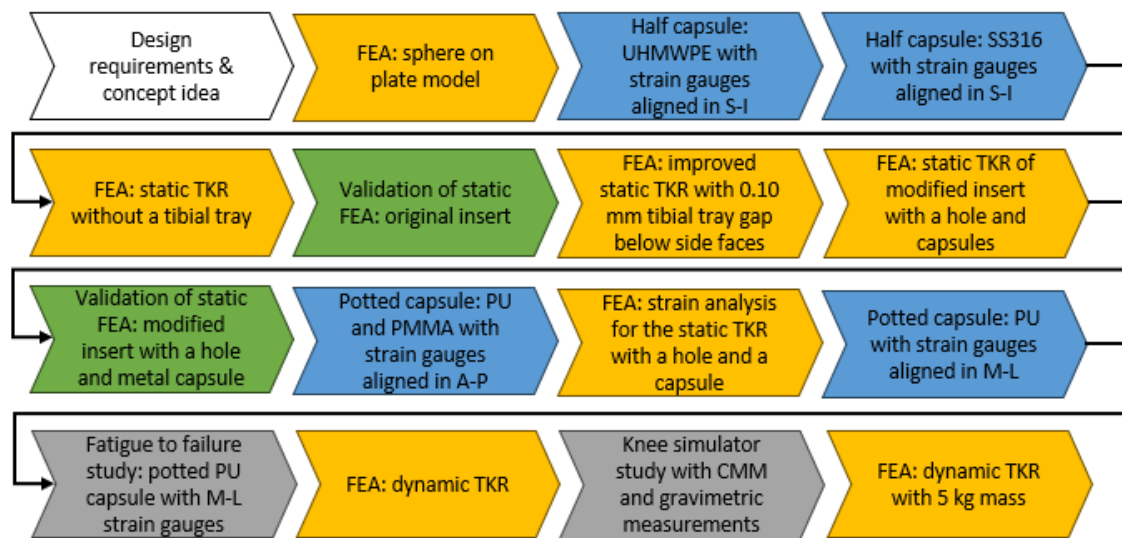
Available from: https://forum.arduino.cc/t/plx-daq-version-2-now-with-64-bit-support-and-further-new-features/420628.

192.   Rossom Sv, Smith CR, Thelen DG, Vanwanseele B, Assche DV, Jonkers I. Knee Joint Loading in Healthy Adults During Functional Exercises: Implications for Rehabilitation Guidelines. Journal of Orthopaedic & Sports Physical Therapy. 2018;48(3):162-173. doi: 10.2519/jospt.2018.7459. PubMed PMID: 29308697.

193.   Arami A, Simoncini M, Atasoy O, Ali S, Hasenkamp W, Bertsch A, et al. Instrumented Knee Prosthesis for Force and Kinematics Measurements. IEEE Transactions on Automation Science and Engineering. 2013;10(3):615-624. doi: 10.1109/TASE.2012.2226030.

194.   ISO. ISO 14879-1:2020. Implants for surgery. Total kneejoint prostheses. Determination of endurance properties of knee tibial trays.

195.   Ahir SP. Development of clinically relevant testing methods for the fatigue performance for tibial trays. Doctoral thesis.: University College London (University of London); 2004.

196.   Kandahari AM, Yang X, Laroche KA, Dighe AS, Pan D, Cui Q. A review of UHMWPE wear-induced osteolysis: the role for early detection of the immune response. Bone Res. 2016;4:16014. doi: 10.1038/boneres.2016.14. Epub 2016/07/29. PubMed PMID: 27468360; PubMed Central PMCID: PMCPMC4941197.

197.   Okazaki Y. Effects of fine microstructures and precipitates of laser-sintered Co–28Cr–6Mo alloy femoral components on wear rate of UHMWPE inserts in a knee joint simulator. Journal of the Mechanical Behavior of Biomedical Materials. 2020;112:103998. doi: https://doi.org/10.1016/j.jmbbm.2020.103998.

198.   MettlerToledo. Operating Instructions Excellence Plus Analytical Balances XP Models - Part 1 [accessed 2023 Jan 12]. Available from: https://www.mt.com/dam/P5/labtec/02_Analytical_Balances/03_XP/03_Documentations/03_Operating_Instructions/OI_XP_Analytical_Part_1_EN.pdf.

199.   Dodge Y. The concise encyclopedia of statistics. Page 427 Pooled Variance: Springer Science & Business Media; 2008.

200.   Okazaki Y, Hosoba M, Miura S, Mochizuki T. Effects of knee simulator control method and radiation dose on UHMWPE wear rate, and relationship between wear rate and clinical revision rate in National Joint Registry. Journal of the Mechanical Behavior of Biomedical Materials. 2019;90:182-190. doi: https://doi.org/10.1016/j.jmbbm.2018.09.034.

201.   Fisher J, McEwen H, Tipper J, Jennings L, Farrar R, Stone M, et al. Wear-simulation analysis of rotating-platform mobile-bearing knees. Orthopedics. 2006;29(9):S36.
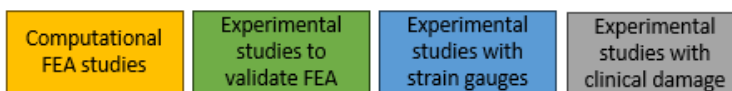
202.   Affatato S, Valigi MC, Logozzo S. Wear Distribution Detection of Knee Joint Prostheses by Means of 3D Optical Scanners. Materials. 2017;10(4):364. PubMed PMID: doi:10.3390/ma10040364.

11 Appendix A

This flow chart approximately visualises the chronological order of the performed computional and experimental studies. The most important thing to notice is that FEA models were used in conjuction with laboratory experiments and have been continously improved throughout the PhD research. FEA models were sometimes improved after making real life observations, for example, during the first validation experiment it was observed that there is a small gap under the side faces of the tibial insert. In other instances, FEA models helped to inform the experimental study and to improve the implant design. For example, during the initial experiments, strain gauges were aligned in S-I and A-P direction, but only after analysing strain with FEA models, it was discovered that strain gauges should be aligned in M-L direction.

12 Appendix B, CV

Edgars Kelmers

Enthusiastic mechanical engineer with both industry and academic experience in R&D. Inventor and designer of medical devices. During PhD developed a commercial smart knee implant (**patent pending**). Passionate about new product development. Excited for a new industry challenge to apply my talent and improve patient outcomes.

LinkedIn:

linkedin.com/in/edgars-kelmers/

Current location: Leeds, UK

(EU citizen, UK settled status)

Competencies

- Medical Devices
- Manufacturing & Prototyping
- 3D-printing
- New Product Development
- Multidisciplinary R&D
- CAD & FEA
- Training
- Project Management
- ISO 13485
- ISO 60601-1

IT knowledge

Nastran NX	●●●●○
SolidWorks	●●●●●
Abaqus	●●●●○
Ansys	●●○○○
MatLab	●●●●○
Python	●●○○○
Arduino UNO	●●○○○
CMM/Metrology	●●●●○

Hobbies

Calisthenics Gym Hiking & being active

Product Development Experience

CAE/Design Engineer   **Apr 2023 – Present**

Cerca Magnetics, Nottingham, UK

- **Medical Device Development** – Developing a novel OPM MEG diagnostics device in compliance with FDA and MDR requirements.
- **CAE** – FEA and CAD model development in Simcenter NX.
- **Prototyping & Testing** — Prototype development and laboratory testing.

PhD research: Smart Implant Design   **Oct 2018 – Nov 2023**

Institute of Medical and Biological Engineering (iMBE), Leeds, UK

Research title: Mechanical Design of Instrumented Tibial Insert for TKR

Supervisors: Prof. H. Pandit, Dr. B. van Duren, Prof. R. Wilcox, Prof. L. Jennings

- **Product Development** – I helped developing a novel commercial product from a concept to a functional prototype. Was responsible for mechanical design.
- **CAD** – Made 2D technical drawings and 3D models in SolidWorks.
- **FEA** – Structural stress, strain, deformation analysis, and parametric optimisation. Created non-linear dynamic FEA and validation methods.
- **Testing** – Developed accelerated testing methods.
- **Metrology** – CMM, 3D-microscope, gravimetric balance, pressure sensors.
- **Funding** – Helped securing a further investment from industrial partner.
- **Project & Time Management** – Developed a medical device within budget and time targets. Analysed market and competitors, researched patents, FDA applications, and ISO/ASTM standards. Communicated with electronics engineers, manufacturing, surgeons, academics, and clients.

Industry Experience

Finite Element Analysis Engineer (internship)   **Nov 2021 – Nov 2021**

Medacta International, Castel San Pietro, Switzerland

- **FEA** – Created FEA in Ansys and 3Dexperience to replicate component loading under standardised ISO and ASTM tests to comply with European regulations.
- **Consulting** – Documented FEA software bugs and technical limitations, communicated with software suppliers, compared 3Dexperience with Ansys and Abaqus. Developed FEA modelling tutorials in Word, PowerPoint, and video.

R&D Test Engineer - Biomechanics   **Jan 2016 – Jul 2018**

DePuy Synthes, Leeds, UK

- **Test Lab** – Wrote reports, performed destructive tests and failure analysis on metal and polymer products for cyclic fatigue, torque, impact, surface damage, welding strength. Worked on CMM. Worked in ISO 13485 certified laboratory.
- **CAD** – Made 3D models in (SiemensNX) and designed custom fixtures manufactured with CNC milling and 3D-printing.
- **Training** – Taught my laboratory colleagues how to design fixtures with CAD. Taught graduate scheme students how to use test machines and perform tests.
- **Health & Safety** – Assisted in H&S audits, organised laboratory and made COSHH assessments to ensure laboratory safety.

Edgars Kelmers

Additional skills

Full clean UK driver's licence.

Languages:
- English (Fluent)
- Russian (Good)
- Latvian (Native)
- German (Beginner)
- Ukrainian (Beginner)

Education

MSc Medical Engineering (*Distinction, 1ˢᵗ Class*)   **Sep 2018 – Dec 2020**

University of Leeds, UK

- **FEA** – Studied non-linear FEA of contact mechanics, composite materials, viscoelastic deformation.
- **Business** – Studied business innovation and medical technologies.

ERASMUS study placement   **Aug 2013 – Aug 2014**

KU Leuven, Belgium

Mechanical Design Project: CT-compatible manipulator for foot biomechanics analysis

Supervisors: Prof. Jos Vander Sloten, Dr. Tassos Natsakis

- **MSc** – Studied Biomechanics. I designed and built a prototype of a CT compatible device fully made of polymers, which could withstand human body weight.
- **CAD & Prototyping** – Within 12 months created 2D (AutoCAD) and 3D (SolidWorks) models, built and tested a functional prototype. Purchased parts and materials to build a prototype within a £5,000 budget.
- **Manufacturing** – Made parts by turning, laser cutting, and 3D-printing.
- **Team work** – Collaborated with electrical and mechanical engineers, clinicians, and academics (supervisor Jos Vander Sloten).

BEng & BSc in Medical Physics & Engineering (88.6%)   **Sep 2010 – Dec 2014**

Riga Technical University, Latvia

- **Mechanical engineering** – Studied CAD, Materials Science, Medical Equipment Design and Manufacturing along other subjects.

Skills and Qualifications

- **FEA** – Abaqus, Nastran NX, Ansys, CATIA 3Dexperience.
- **CAD** – SolidWorks (CSWA certificate), Simcentre NX, AutoCAD.
- **PLM & QMS**—Teamcenter NX, Greenlight Guru.
- **Coding** – Matlab, Python, Arduino Uno.
- **CMM** – Mitutoyo MCOSMOS, ZEISS Calypso, Alicona Infinite Focus.
- **Med-Tech** – ScanIP, Materialise Mimics, OpenSim.
- **3D printing** – Formlabs SLA, Bambu Lab FDM, PolyJet.

Patent

- 2022 patent application: An implantable device and charging module for powering the same (**GB2210781.7**).

Publications

- **E. Kelmers**, et al. "Smart Knee Implants: An Overview of Current Technologies and Future Possibilities." *Indian Journal of Orthopaedics* (2022): 1-8.
- Contributed to: H. Boey, et al. "Combination of 4D CT scanning and a foot manipulator device to measure individual foot kinematics during simulated gait." *Orthopaedic Proceedings*. Vol. 99. No. SUPP_1. Bone Joint J, 2017.

Volunteering

Volunteered for the Red Cross Youth organisation (Aug 2011 - Aug 2013). Visited local schools and taught students first aid. Performed first aid demonstrations in public events, judged in competitions, and taught in a summer camp.